

High fidelity mechanical and loss modelling of an interior permanent magnet traction machine for electrical vehicles

Guanhua Zhang

A thesis submitted for the degree of Doctor of Philosophy

Department of Electronic and Electrical Engineering

The University of Sheffield, UK

December 2023

Abstract

High-performance permanent magnet electrical machines have become the leading machine technology in the electric vehicle market due to their combination of high efficiency and high-power density. However, their design optimisation involves complex and often strongly coupled mechanical, electromagnetic and thermal behaviour. Of the many possible topologies of permanent magnet machines, interior (IPM) machines have become the favoured machine type as they offer advantages in field weakening, a contribution from reluctance torque and the ability to retain the magnets within the rotor core without the need in many cases for a separate containment sleeve. However, the trade-off between electromagnetic and mechanical performance is especially important in IPMs because of the use of thin bridge-sections within the rotor core. This thesis reports on detailed design study into the mechanical and electromagnetic optimisation of an 8-pole, 100kW IPM machine with a base speed of 4,000rpm and an extended speed range up to 12,000rpm and makes extensive use of structural and electromagnetic finite element analysis to identify a preferred design. The other aspect of IPM performance which is investigated in this thesis is the influence of high frequency converter switching on the iron loss in the machine. An analysis methodology is developed and applied to an IPM machine with combines a SIMULINK model with pre-calculated finite element characteristics of the machine to predict detailed localised element-by-element flux density variations in the cores of an IPM machine which includes realistic representation of switching events. The effect of current ripple and the grounding of the star-point is investigated. These high frequency flux density waveforms are then used as the basis for estimating the effect of high frequency current ripple on iron loss. This aspect includes a detailed investigation of the limitations of different analytical and numerical models for solving the diffusion equation with 3D eddy current finite element simulations providing a baseline against which to test various models. This aspect of the research results in a time-stepped finite difference representation of 1D eddy current flow in laminations and is applied at full machine level as post-processing tool. The thesis concludes with some experimental measurements of core loss with switching ripple which demonstrates the value of including lamination level eddy current effects in loss predictions.

Acknowledgements

During my PhD student period, I would like to express my appreciation to my supervisor, professor Geraint Jewell, for his invaluable and continuous support, patience and responsibility. I learned a lot from the working experience with my supervisor including wealth knowledge, research skills and logical thinking, these all supporting me to overcome the difficulties in this journey and will be my treasures in the future career.

I received much help from others, and I would like to thank Edward Stone, Jason Ede, Reece Eblet, David Hewitt for their support. In addition, Dr Xiao Chen also helped me a lot when I had difficulties and many thanks for this.

I would also like to thank my friends who have accompanied me over the past four years, especially Jiamiao, who have enriched my life, I enjoy the time with them and hope everyone has a bright future.

Finally, I would like to express my thanks to my parents for their love, trust and support. This all brings me here.

Contents

Abstract	1
Acknowledgements	2
Contents	3
List of symbols	7
Chapter 1 Introduction	14
1.1 Background to electrified transportation	14
1.1.1 Electrical machine performance requirements	15
1.2 Machine topologies	16
1.2.1 Induction machines	17
1.2.2 Brushless permanent magnet machines	21
1.2.3 Reluctance machines.....	25
1.2.4 Summary of machine topologies.....	26
1.3 Key magnetic materials in permanent magnet synchronous machines	26
1.3.1 Stator and rotor core materials	27
1.3.2 Permanent magnet materials	28
1.3.3 Conducting material	28
1.4 Loss prediction	28
1.4.1. Importance of loss predictions	28
1.4.2 Steinmetz equation and derivatives.....	29
1.4.3 Loss separation model.....	31
1.5 Thesis structure	32
References	34
Chapter 2: Design optimisation of an interior permanent magnet machine	43
2.1 Introduction	43
2.1.1 Interior permanent magnet machine topologies and features.....	43
2.1.2 Performance specification.....	45
2.2 IPM machine electrical and electromagnetic design	46
2.2.1 Initial sizing	46
2.2.2 Alternative winding configurations	46
2.2.3 Calculation of open-circuit phase back-emf	48
2.2.4 Cogging torque.....	49
2.2.5 Torque performance.....	49
2.3 Combined mechanical and electromagnetic optimisation of 30 slot / 8 pole IPM machine ...	50
2.3.1 Baseline machine dimensions and performance	50

2.2.2 Material properties and mechanical properties	52
2.3.3 Influence of interference fit of shaft	53
2.3.4 Rotor design and Optimal ratio	55
2.3.5 Influence of hub diameter	59
2.3.6 Influence of magnet shape	64
2.4 Summary of final design.....	67
Reference	69
Chapter 3: High frequency switching effects in PM machines	71
3.1 Introduction.....	71
3.2 Calculation of machine electrical parameters	72
3.2.1 Prediction and representation of self-inductance and mutual-inductance.....	72
3.2.2 Prediction and representation the phase resistance	77
3.2.3: Prediction and representation of the open-circuit back-EMF waveform	77
3.3 Simulation model for a PMSM driven by a hysteresis band current controlled converter ...	78
3.3.1 Overall drive architecture.....	78
3.3.2 Operating principles of hysteresis band controllers	79
3.3.3 System model.....	80
3.3.3.1 Switching signal generation sub-system	81
3.3.3.2 Calculation of mutually coupled voltage	82
3.3.3.3 Back-emf generator.....	83
3.4 Significance of machine star-point connection.....	83
3.4.1 Introduction to star-point grounding	83
3.4.2 Grounded star connection	84
3.4.3 Floating star connection.....	86
3.5 Prediction of current waveforms with switching effects	87
3.5.1 Grounded star-point	87
3.5.2 Floating star-point.....	91
3.6 Calculation of high frequency flux density waveforms	94
Reference	98
Chapter 4 Iron loss prediction in electrical machines	99
4.1 Conventional iron loss prediction models for electrical machines	99
4.1.1 Hysteresis loss.....	99
4.1.2 Excess loss prediction model	101
4.1.3 Classical resistance-limited model for predicting eddy current loss	103
4.1.4 Total loss calculation	106
4.2 Iron loss prediction for high frequency switching	106
4.2.1 Idealised saw-tooth current ripple test case	106

4.2.2 Grounded star connection electrical machine	109
4.2.3 Floating star connection electrical machine.....	112
4.3 Summary.....	115
Reference	116
Chapter 5: Iron loss calculation considering skin effect.....	117
5.1 Introduction.....	117
5.2 Diffusion equation models for predicting eddy currents in a thin lamination	118
5.2.1 Formulation of the general form of the diffusion equation.....	118
5.2.2 Solution of complex diffusion equation.....	120
5.3 Three-dimensional finite element modelling of a reference lamination.....	123
5.3.1 Model configuration.....	123
5.3.2 Magnetostatic calculations.....	126
5.3.3 Transient time-stepped eddy current calculations.....	128
5.4 Analytical solution of the diffusion equation for linear magnetic materials	130
5.4.1 Direct use of the diffusion equation for predicting one-dimensional eddy current field redistribution.....	130
5.4.2 Layered analytical solution to diffusion equation.....	131
5.4.3 Modelling non-sinusoidal excitation through harmonics in linear materials	134
5.5 Non-linear solution of the diffusion equation.....	138
5.6 Finite difference time-stepped method for a one-dimensional numerical post-processing model	147
5.6.1 The finite difference method.....	147
5.6.2 Test case for finite difference method on a linear problem	150
5.7 Development of the non-linear finite difference one-dimensional post-processing method.	153
5.8 Establishing surface magnetic field strength for a 1D finite difference eddy current model from flux density waveforms.....	157
5.9 Machine level iron loss calculations including the effects of high frequency switching and skin effect.	161
5.9.1 Introduction.....	161
5.9.2 Machine details and operating conditions.....	161
5.10 Summary.....	165
Reference	166
Chapter 6: Experimental testing and validation.....	168
6.1 Introduction.....	168
6.2 Toroidal core testing with sinusoidal excitation.....	168
6.2.1 Measurement equipment for sinusoidal excitation	168
6.2.2 Sample winding	169
6.2.3 Preparation of test sample	170

6.2.4 Method for predicting losses in the toroid sample	172
6.2.5 Loss measurements with sinusoidal excitation	173
6.3 Toroidal core testing with switching waveform	175
6.3.1 Test apparatus	175
6.3.2 Calculating loss density from the measured waveforms	177
6.4 Manufacture of a demonstrator IPM machine	182
6.5 Summary.....	184
Reference	185
Chapter 7: Conclusions and Future Work	186
7.1 Main conclusions.....	186
7.2 Key contributions to knowledge	188
7.3 Future work.....	188
7.3.1 Experiment validation of iron loss at machine level	188
7.3.2 Experiment validation of mechanical modelling for rotor of high speed IPM machine	188
7.3.3 Enhancement to the electromagnetic performance by adjusting hub diameter.....	189
7.3.4 Switching loss modelling of converters	189
7.3.5 Enhancement to the eddy current loss model.....	189
APPENDIX.....	190
PYTHON script to export <i>B</i> and <i>H</i>.....	190
MATLAB script to process exported <i>B</i> and <i>H</i>.....	191

List of symbols

Symbol	Explanation	Unit
Chapter 1		
A	Cross section area of thin lamination	m^2
B_s	Peak induction of sinusoidal excitation	T
d	Lamination thickness	m
f_{eq}	Equivalent frequency of MSE model	Hz
f_r	Fundamental frequency of periodic waveform	Hz
G	Dimensionless coefficient of eddy current	
k	Material parameter	
k_{eddy}	Eddy current coefficient	
k_{excess}	Excess loss coefficient	
k_h	Hysteresis coefficient	
P_{eddy}	Eddy current loss per unit mass	W/kg
P_{excess}	Excess current loss per unit mass	W/kg
P_{GSE}	Average iron loss power per unit volume of GSE model	W/mm ³
P_{iGSE}	Average iron loss power per unit volume of iGSE model	W/mm ³
P_{iron}	Total iron loss power per unit volume	W/mm ³
P_{MSE}	Average iron loss power per unit volume of MES model	W/mm ³
P_{OSE}	Average iron loss power per unit volume of OSE model	W/mm ³
T	Period of excitation waveform	s
V_0	Parameter refers to statistical distribution properties of anomalous eddy currents	
x	Steinmetz coefficient form material permeability	
α	Induction exponents for frequency of Steinmetz parameters	
β	Induction exponents for magnetic of Steinmetz parameters	

θ	Phase angle of excitation waveform	$^{\circ}$
ρ	Electrical resistivity	$\Omega \cdot m$
σ	Electric conductivity	S/m
ΔB	Peak-to-peak amplitude of magnetic induction	T

Chapter 2

E	Young's modulus	Pa
E_c	Young's modulus of core	Pa
E_s	Young's modulus of shaft	Pa
h_1	Rotor bridge thickness	m
h_2	Magnets separation	m
L_d	d axis inductance	H
L_q	q axis inductance	H
P_i	Contact pressure	Pa
r_{ci}	Inner radius of rotating solid annulus	m
r_{co}	Outer radius of rotating solid annulus	m
ν	Poisson's ratio	
β	Angle between the magnets within one pole	$^{\circ}$
δ_i	Interference level	m
ρ	Density	kg/m^3
$\sigma_{\theta,core}$	Hoop stress in the rotor core at the inner bore	Pa
ω	Rotating angular velocity	rad/s
Δr_{ci}	Radial growth at the inner radius of core	m
Δr_{so}	Radial growth at the outer radius of shaft	

Chapter 3

B_{ij}	Flux density for i th element at j th time	T
E_{ph}	Phase back EMF	V
HB	Hysteresis band width	
i_a	Phase A actual current	A
i_a^+	Current in rising period	A
i_a^-	Current in dropping period	A

i_a^*	Phase A command current	A
i_b	Phase B actual current	A
i_b^*	Phase B command current	A
i_c	Phase C actual current	A
i_c^*	Phase C command current	A
I_j	Current at j th time	A
I_{ph}	Phase current	A
L	Load inductance	H
L_a	Phase A self-inductance	H
L_b	Phase B self-inductance	H
L_c	Phase C self-inductance	H
L_{ph}	Phase self-inductance	H
M_{ab}	Mutual inductance between phase A and phase B	H
M_{ac}	Mutual inductance between phase A and phase C	H
M_{ba}	Mutual inductance between phase B and phase A	H
M_{bc}	Mutual inductance between phase B and phase C	H
M_{ca}	Mutual inductance between phase C and phase A	H
M_{cb}	Mutual inductance between phase C and phase B	H
N_{ph}	Phase coil number of turns	
Q_1 to Q_6	Converters of three phase bridge	
R	Load resistance	Ω
t_1	Current rising period	s
t_2	Current dropping period	s
T_c	Single current reversed region	s
V_a	Phase A back EMF	V
V_b	Phase B back EMF	V
V_c	Phase C back EMF	V
$V_{coupling}$	Phase coupling voltage	V
V_{DC}	DC voltage of hysteresis band control drive	V
V_{muA}	Phase A induced coupling voltage	V
ΔI	Current variation between ripple current and purely sinusoidal current	A

Φ_{ph}	Phase flux-linkage	Wb
-------------	--------------------	----

Chapter 4

B	Average flux density	T
B_m	Peak amplitude of flux density	T
B_{max}	Peak flux density amplitude	T
B_x	Flux density in x axis	T
d	Lamination thickness	m
E	Induced electric field	V/m
f	Frequency	Hz
G_{mo}	Eddy current damping factor for an active magnetic object	
G_w	Eddy current damping factor of 180° moving wall	
H_x	Magnetic field strength in x axis	A/m
H_e	Eddy counter field of the moving wall	A/m
J	Current density	A/m ²
k_{exc}	Excess loss coefficient	
k_h	Material hysteresis coefficient	
K	Hysteresis loss coefficient	
L	Width of lamination	m
M_s	Saturation magnetisation	A/m
\hat{n}	Effective number of magnetic objects	
n_{mo}	Number of active magnetic objects at same time	
n_w	Number of individual activated domain wall	
N_{mlp}	Number of minor loop	
P_c	Eddy current power loss density	W/kg
P_e	Excess loss power density	W/kg
P_h	Hysteresis loss density	W/kg
S	Cross-section area of lamination	m ²
T	Period	s
v	Domain wall velocity	
V_o	Parameter related to the effective active magnetic objects to the eddy current counter field	

α_h	Material hysteresis coefficient	
δ	Density	kg/m ³
σ	Electric conductivity	S/m
$\dot{\phi}_w$	Flux rate provided by the domain wall movement	
ΔB_i	Flux density variation for i th minor loop	T

Chapter 5

b	Half thin lamination thickness	m
B	Magnetic flux density	T
h	Space separation between two successive mesh point	m
h_l	Layer thickness within the thin lamination	m
H	Magnetic field strength	A/m
H_{10}	Magnetic field strength at boundary line 10	A/m
H_9	Magnetic field strength at boundary line 9	A/m
H_r	Radial magnetic field strength	A/m
H_s	Surface magnetic field strength	A/m
H_z	Magnetic field strength in z axis	A/m
I	Current	A
I_a	Supply current	A
j	Imaginary unit	
J	Current density	A/m ²
K_1, K_2	Coefficients determined by boundary condition	
M	Material magnetization	A/m
n	Number of turns for transformer lamination model	
p	Time interval between two successive transient magnetic field strength	s
r	Parameter for writing convenience	
α	Complex propagation constant	
β	Initial constant of finite difference method	
δ	Skin depth	
μ	Magnetic permeability	H/m
μ_0	Vacuum permeability	H/m
μ_{ini}	Initial permeability for finite difference method	H/m

μ_{max}	Peak permeability for finite difference method	H/m
μ_r	Relative permeability	
σ	Electric conductivity	S/m
φ	Flux-linkage	Wb
φ_m	Peak amplitude of flux-linkage	Wb
χ_m	Magnetic susceptibility	
ω	Rotating angular velocity	rad/s
$\Delta\theta$	Phase shift between the successive boundary lines or layers	°
\emptyset	Flux-linkage	Wb
\emptyset_m	Peak amplitude of flux-linkage	Wb

Chapter 6

A	Cross section area of the toroidal sample	m ²
B	Magnetic flux density	T
D_i	Inner diameter of toroid	m
D_{mean}	Mean diameter of toroid	m
D_n	Mean diameter for nth segment of toroid	m
D_o	Outer diameter of toroid	m
e_B	Induced voltage in search coil of toroid	V
e_s	Search coil emf	V
h	Thickness of the sample	m
h_l	Thickness of individual lamination	m
H	Magnetic field strength	A/m
H_{mean}	Mean magnetic field strength for toroid	A/m
H_n	Magnetic field strength for nth segment	A/m
i	Current	A
i_d	Drive coil current	A
l_m	Mean path length of toroidal core flux path	m
m	Mass of the toroidal sample	kg
N_B	Number of turns on search coil of the toroidal sample	
N_H	Number of turns on drive coil of the toroidal sample	
N_l	Number of laminations in toroid	

P_e	Average electrical input power over one cycle	W/m ³
P_{fe}	Average of loss per kg	W/kg
T	Period of power supply	s
V_1	Measured voltage in drive coil of toroid	V
V_2	Measured voltage in search coil of toroid	V
ρ	Density of the material	kg/m ³
ϕ	Flux-linkage	Wb

Chapter 1 Introduction

1.1 Background to electrified transportation

Greenhouse gases (GHG) and the associated warming of the planet are becoming a worldwide issue of concern. A report from the United States Environmental Protection Agency (EPA) found that transportation contributed 28% of 2021 GHG emissions in the US. This is the largest single source of GHG emissions [1]. These emissions come predominantly from the consumption of fossil fuel by various vehicle types. The future development of transportation systems increasingly requires reductions in fossil fuel use and GHG emissions. Electrified transportation systems are the favoured choice due to sustainability and zero emissions [2]. Research has shown that the dominant source of air pollution in urban areas are passenger vehicles, which is the focused of this thesis [3]–[5]. According to the different degrees of electrification, EVs can be divided into hybrid electric vehicles (HEVs), plug-in hybrid electric vehicles (PHEVs), extended-range electric vehicles (EREVs) and pure-electric vehicles (EV). HEVs come with various degree of electrification in combination with internal combustion engines (ICEs), with electrical ratings that can be 20%-50% of the total vehicle power [6]. The degree of electrification is increased in PHEVs and EREVs particularly in the battery, which increases system efficiency. In addition, they provide longer pure-electric operating range of ~65kms with plug-in charging. For pure-electric vehicles, the propulsion is supplied only by the electric drive-train and the energy may come from battery although there are on-going developments in hydrogen fuel cell powered vehicles. The number of EVs on the market continues to grow as shown in Figure 1.1.

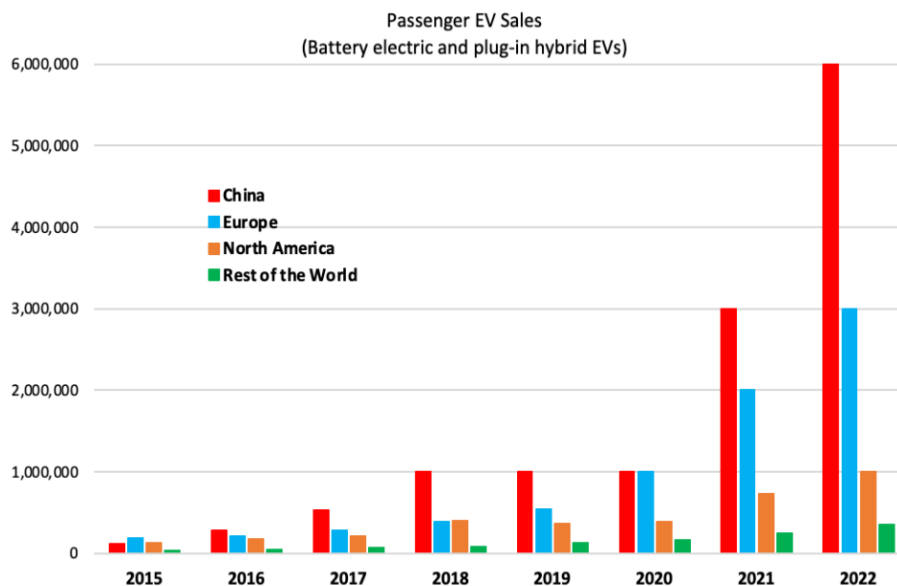


Figure 1.1 Passenger electric vehicle sales worldwide (Source: [7])

1.1.1 Electrical machine performance requirements

The efficiency of electrical machines in EVs is typically around 90% and above over much of their operating range [8] which is much higher than the 30% or so of modern ICEs. Hence, electric machines have significant potential for reducing energy consumption as well as reducing emissions. In pure EVs, the efficiency of the electrical machine has a proportional impact on the range of the vehicle for a particular battery size. Hence, although efficiencies of electrical machines are already around 90%+ and much higher than ICEs there is still interest in further increasing efficiencies beyond current levels.

Several studies have identified the requirements for the electric machines used in the EVs [9]–[11]. These include, high power-to-weight ratio, power delivery with very little lag, high efficiency, high reliability and robustness especially and low cost. A typical specification for a pure EV is shown in Table 1.1, in this case for a Tesla Model Y [12].

Table 1.1 Performance specification for Tesla Model Y (Source: [12])

Parameter	Value
Type	PMSM
Power	258 kW
Total electric torque	527 Nm
Top Speed	217 km/h
Acceleration 0 to 100 km/h	5.1 s
Curb weight	2025 kg
Max towing capacity weight	1588 kg
Aerodynamic drag coefficient	0.8
Wheelbase	287.5 cm
Power-weight output ratio	0.13 kW/kg

Although the performance of a machine is often described in terms of power, it is important to note that the requirements of an actual is specified in terms of a torque speed curves for continuous and peak short-term ratings. A typical EV torque-speed requirement is shown in Figure 1.2 along with the corresponding power-speed characteristics.

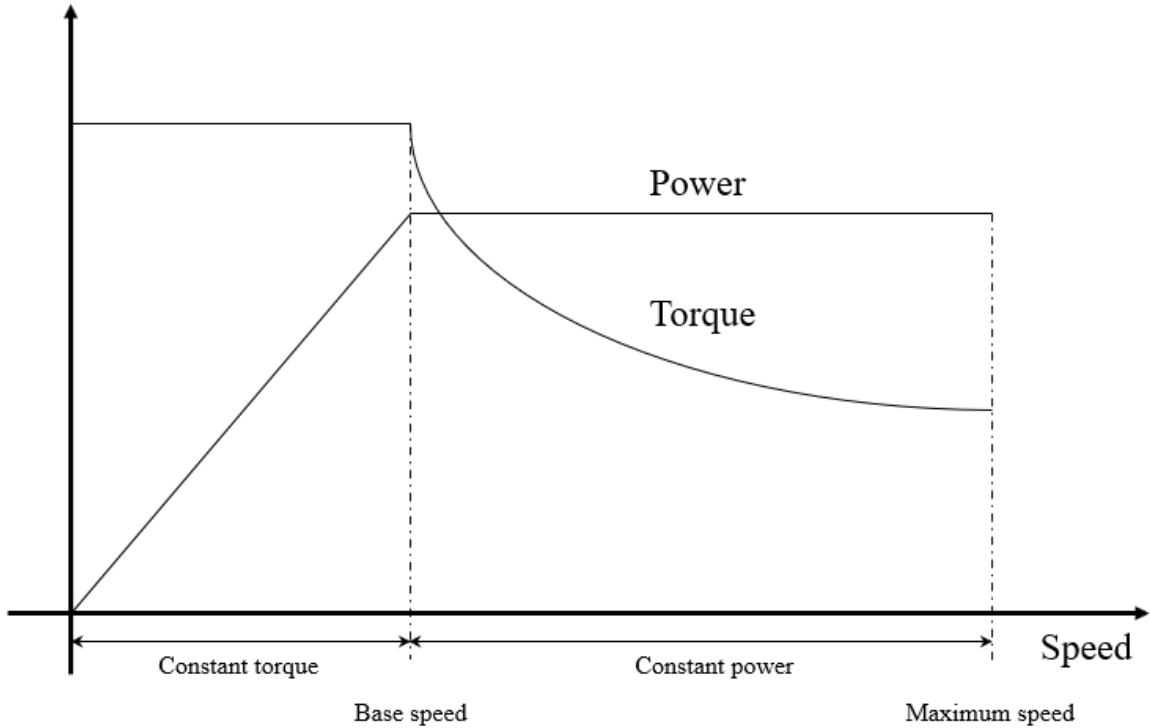


Figure 1.2 Typical operating characteristics for an EV application

During operation, the EV machine needs to produce a peak short-term torque during hard acceleration, climbing and hard braking. This peak torque is generally 5 to 10 times the cruising torque [13]–[15]. The characteristic in Figure 1.2 includes a constant torque region during which the machine power and speed has linear relationship until the speed reaches the base speed. Beyond the base speed, the machine operates in a constant power region. During this operating mode, field-weakening is used to reduce the torque with the increasing machine operating speed to maintain constant power. This type of characteristic is used to minimise the power converter rating even though the machine itself may well be capable of delivering the rated torque right up to the maximum speed.

1.2 Machine topologies

There are a range of different types of machines used in commercial EVs as shown in Table 1.2 which summarises a published survey of motor types in EVs up to 2020 [16]. As can be seen, brushless permanent magnet synchronous machines (PMSM in Table 1.2) dominate this survey.

Table 1.2 Survey of electrical machine types in commercial EVs up to 2020 (Source: [16])

EV Model	Power (kW)	Motor Type	Year
Mahindra e2o Plus	19-30	IM	2016
Renault Kangoo ZE	44	PMSM	2011
Mitsubishi i-MiEV	47	PM	2010
Volkswagon E-up	60	PMSM	2019
Renault Zoe	65	PMSM	2012
LandRover	70	SRM	2013
Renault Fluence Z.E.	70	PMSM	2012
Nissan Leaf	80	PMSM	2010
BJEV EC5	80	PMSM	2019
Hyundai Ioniq Electric	88	PMSM	2016
Hyundai Kona	88-150	PMSM	2018
BYD E6	90	PMSM	2014
BMW i3	125	PMSM	2013
Xpeng G3	139	PMSM	2018
Mercedes-Benz EQC	150*2	IM	2019
BJEV EU5	160	PMSM	2018
Tesla Model X	193-375	IM	2015
Tesla Model 3	211-340	PMSM	2020
Tesla Model S	235-568	IM	2012
NIO EC6	320	PMSM	2020
NIO ES6	320	PMSM	2020

Although brushed DC machine have been used in low performance electric vehicles for many years [17] they are not a technology which is being used in mass-market EVs today due to low power density, limited speed range, maintenance requirements and low efficiency. Many of these limitations result from the use of brushes and commutators. There are a few examples of low performance drivetrains such as Dynavolt system introduced by the French Peugeot Citroen [18], [19] but in general brushed DC machines are not considered to be a competitive technology in modern EVs. The next sections review the main competing technologies of brushless permanent magnet (PM), induction (IM) and reluctance machines.

1.2.1 Induction machines

Induction machines, which are also called asynchronous machines, can be classified according to the rotor winding type. The most common type of rotor winding consists of a series of solid bars (usually aluminium but sometimes copper in higher efficiency machines) which are connected by solid end-rings to form what it often called a squirrel cage rotor. An

example of a small squirrel cage rotor from an industrial machine is shown in Figure 1.3. This shows the complete rotor, the rotor laminations and the cage with the core removed to show the geometry. The example shown is a cast aluminium cage which is typical of industrial machines. For EV applications, copper cages with higher mass and cost are often preferred because of their higher efficiencies. An example of a 26kW (120 Nm at 2020 rpm) induction machine with a copper squirrel cage rotor designed for electrical vehicle traction application [20] is shown in Figure 1.4. The other type of rotor, which is far less common, is a wound rotor which is usually used in combination with slip rings to connect external resistors to improve starting torque. A schematic of a wound rotor induction machine with external starting resistors is shown in Figure 1.5.



Figure 1.3 Typical cast aluminium squirrel cage rotor from an industrial induction machine
(Source: [21])



Figure 1.4 26 kW induction machine with copper rotor (Source: [20])

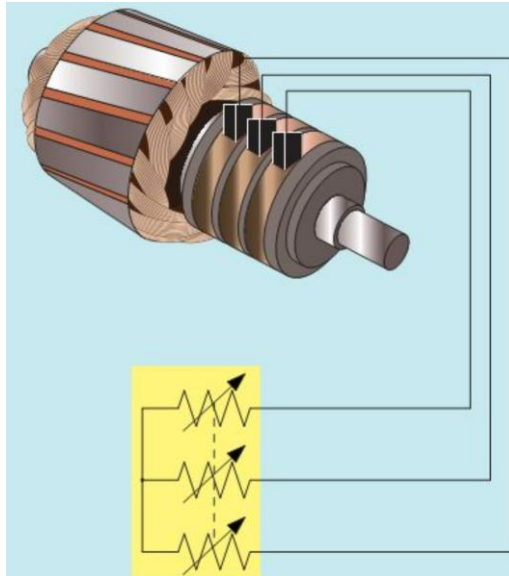


Figure 1.5 Schematic of a typical wound rotor for an induction machine (equipped with slip rings and external starting resistors) (Source: [22])

For EV applications, squirrel cage induction machines have been used by some EV manufacturers as the electric propulsion technology due to their reliability, ruggedness, low manufacturing cost, low maintenance and ability to operate in harsh environments [23]. Although it was shown previously in Table 1.2 that permanent magnet machines tend to dominate the market, induction machines are still being developed for EV applications [9], [24].

Figure 1.6 shows a typical operating envelope of an induction machine when driven from a power inverter. At speeds below the base speed, the IMs vector controller can realise constant torque. Beyond the base speed, IMs operate in a constant power mode up to limit, which is realised by a field weakening control strategy. Eventually a further reduction in torque occurs when the machine is operated in an extended high-speed range. The efficiency of an IM is relatively high when operating at high speed and low torque. However, when IMs are operating in the low speed and high torque region, the efficiency is lower, because of increased rotor losses [25].

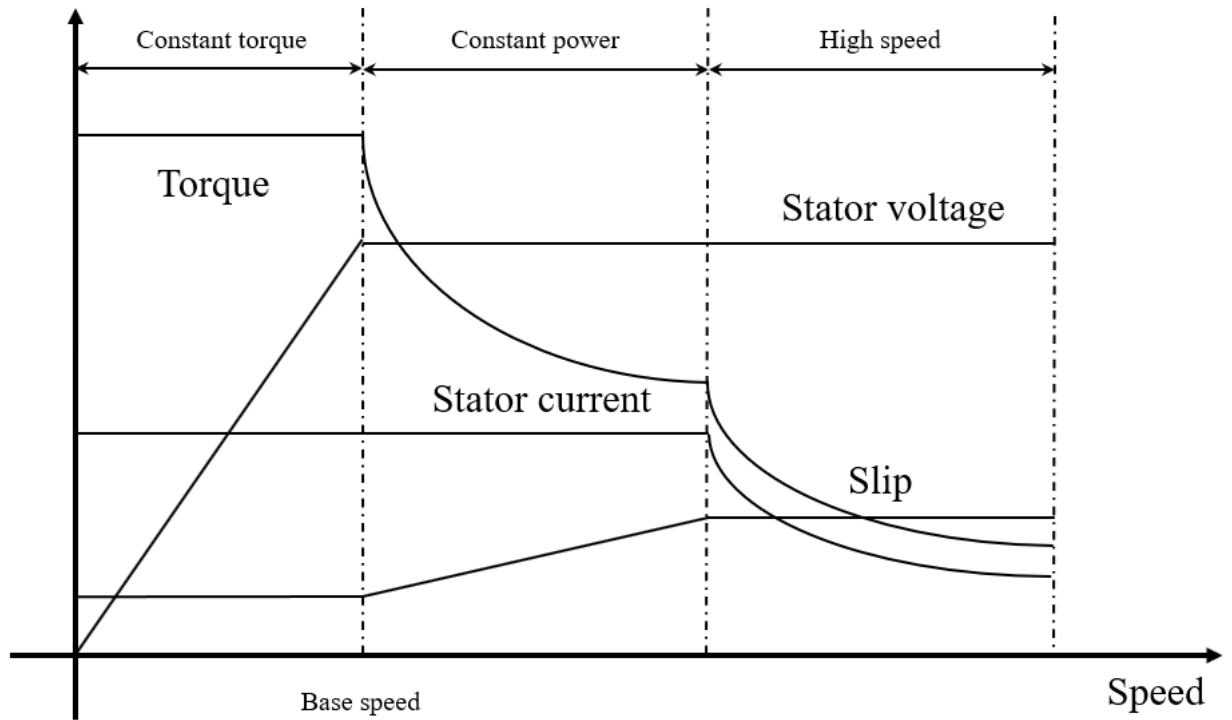
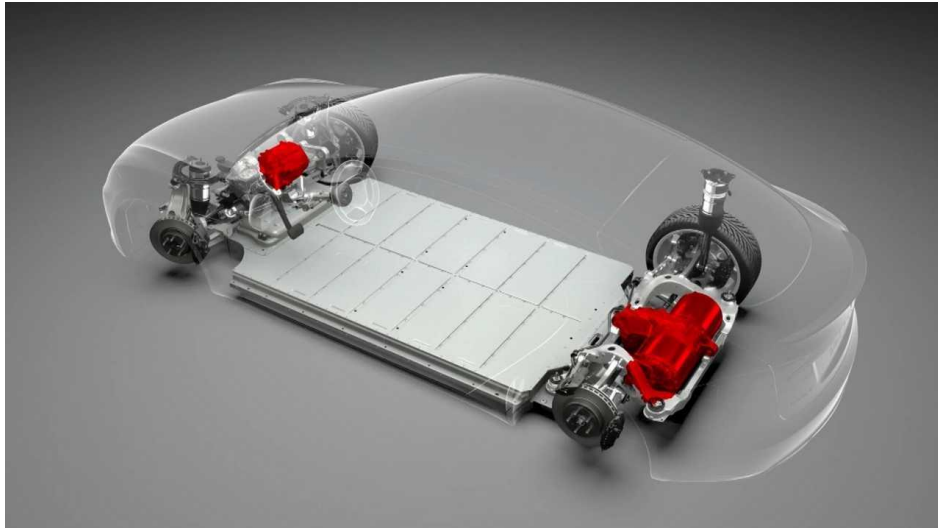


Figure 1.6 Typical operating envelope of an inverter fed induction machine

Although IMs have been adopted by various EVs manufacturers, they still have many drawbacks such as low efficiency, low power factor and low power inverter utilisation, which has hindered their application for higher power levels and high-speed machines in EVs [23], [26], [27]. EVs which are on the market with asynchronous induction machines include the Audi e-Tron SUV, Mercedes-Benz EQC, Tesla Model S, 3, X and Y and VW Group MEB. Among these examples, the Tesla model series and VW Group MEB use induction machine only in their front axles [28]. Figure 1.7 shows the Tesla model X dual motor design, which illustrates that its front motor is an AC induction machine and rear motor is AC permanent magnet synchronous motor.



Front motor: Induction machine

Rear motor: PM machine

Figure 1.7 Tesla model X dual motor configuration (Source: [29], [30])

1.2.2 Brushless permanent magnet machines

As shown previously in Table 1.2 brushless PM machines are the preferred technology for EV drivetrains for most vehicle manufacturers. Within the category of brushless permanent machines there are so-called brushless DC machines and brushless AC machines (also called PM synchronous machines or PMSM). Both types are sometimes referred to as electronically commutated machines since the polarity of the current in the windings is controlled by an external power converter. These two types of brushless PM machine are not as different as their names suggest. Brushless DC machines have trapezoidal back-emfs and are fed with a 120° quasi square-wave current waveform while brushless AC or PMSM machines have sinusoidal back-emfs and are fed with sinusoidal currents. In principle, a brushless DC machine can be operated with a sinusoidal current and vice versa, but there would be some loss of performance if a machine is operated in a different current mode from the one it was designed for.

The currents supplied to brushless PM machines are synchronised with rotor position rather than time and they can accommodate load changes within their rated capability without

any issues over stability and stalling as is the case with conventional synchronous machines in which the currents are synchronised with time. The need to synchronise the current waveform with position means that many high performance drive-trains, particularly those which require high starting torque, need some form of rotor position sensor such as encoders or resolvers. In order to reduce cost, there has been interest and research into sensorless control systems which use measurements of electrical quantities to estimate rotor position [31].

Brushless PM machines have the advantages of high torque and power densities, high efficiency and are usually the lightest machine technology to meet a particular power requirement. As a consequence, they are well suited to demanding applications such as in-wheel direct drive [32]–[36]. However, due to the fixed nature of the magnetic field produced by the magnets, their field-weakening capability is limited, which in turn limits the speed range with constant torque. Adopting a field weakening control strategy allows the operating speed to be extended to 3 to 4 times the base speed [23], [36]–[44]. In addition, high d-axis current during the field weakening process increases risk of irreversible demagnetisation.

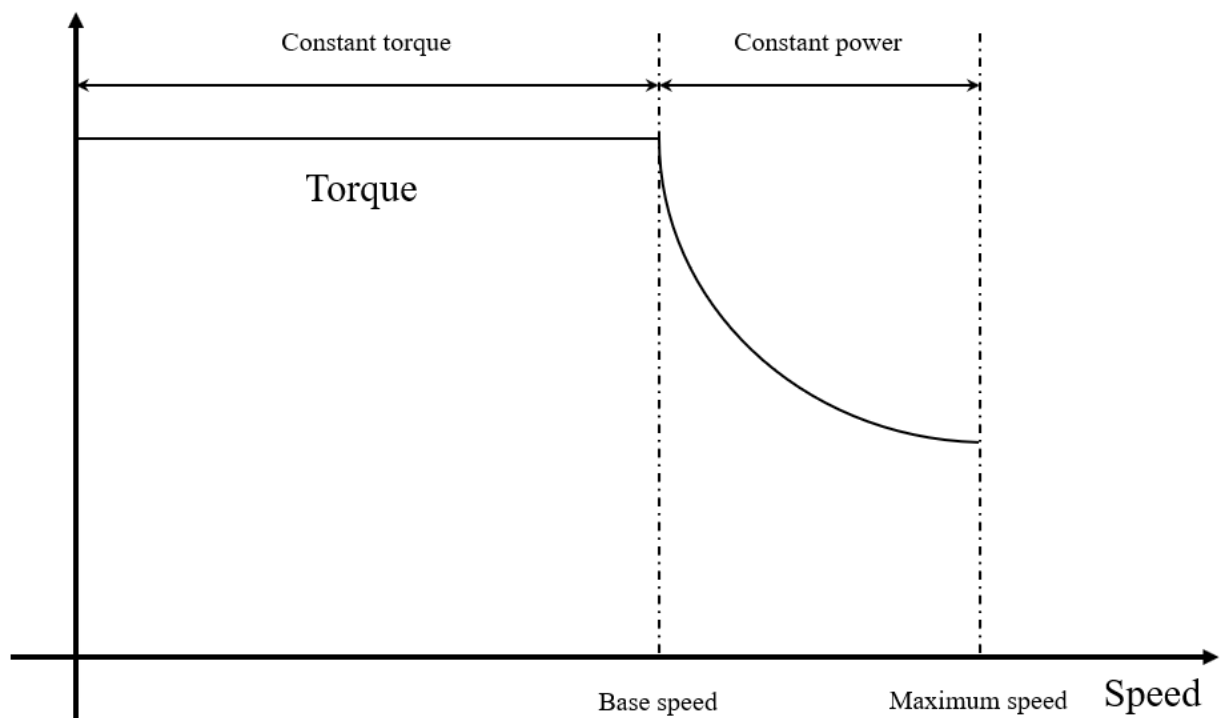


Figure 1.8 Typical PM machine torque-speed curve

One further sub-division of PM brushless machines is whether the machine has an internal or external rotor as shown in Figure 1.9. Most machines have internal rotors because the mechanical arrangement is much simpler, and it is easier to extract heat from an external stator.

However, some applications such as in-hub wheel drives are well-suited to external rotor machines.

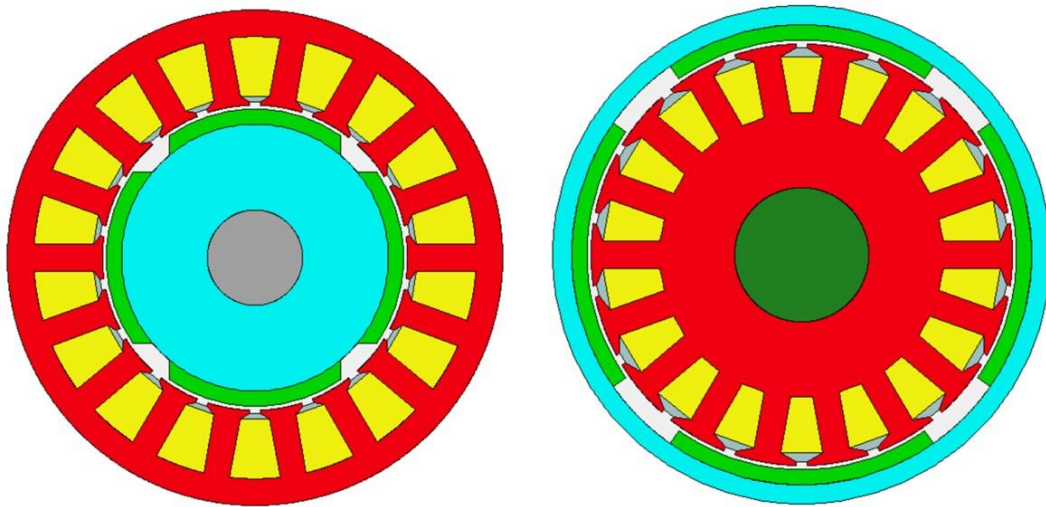


Figure 1.9 Internal and external rotor permanent magnet machines

Another significant difference between PM machines is the arrangement of rotor magnets on the rotor core. Although there are many variations within each category (as shown later in chapter 3 for interior PM machines), the main categories of rotor magnet arrangements are surface-mounted PMs (SPM), inset magnets and interior permanent magnet (IPM) as shown in Figure 1.10.

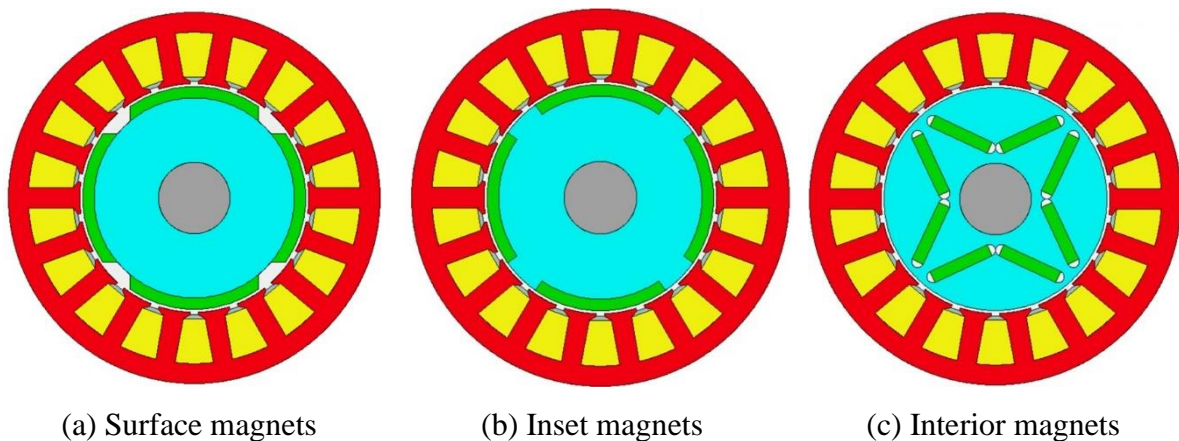


Figure 1.10 Different rotor magnet arrangements

As the speed of electrical machines increase, retaining the magnets on the rotor becoming a problem, and some form of high-strength mechanical sleeves are required around the rotor [45]. There is a growing interest in attaching the magnets on the stator alongside the coils [46]. Machine topologies with stator-mounted PMs include doubly salient PM (DSPM) machines, flux reversal PM (FRPM) machines and flux switching PM (FSPM) machines. Among these

three machines, FSPM offers some promise with relatively higher torque and power densities, and a near sinusoidal back-emf. An example of a 12 slot, 10 pole and 4 phase FSPM is shown in Figure 1.11.

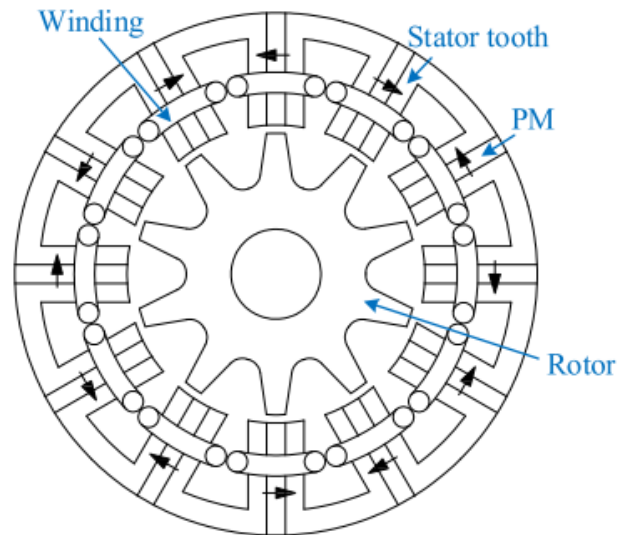


Figure 1.11 3-phase FSPM machine with 12 slots, 10 poles (Source: [45])

Depending on its structure, FSPM machines can have a very robust rotor, similar in shape to a switched reluctance rotor as shown previously in Figure 1.11. This type of rotor can withstand high mechanical loads which makes them suitable for high-speed applications. The stator core has a complicated structure made up of laminated U-shaped segments structure. Rectangular blocks of permanent magnets of alternating polarity are located in between each pair of U-shaped stator core modules. The location of the PMs in the stator means that less space is available for the stator winding and hence the electric loading is lower than an equivalent conventional PMSM which tends to result in reduced torque density. Moreover, FSPM tend use a larger quantity of permanent magnets for a given machine size and power rating and hence the cost is also increased.

Numerous studies on the torque density of FSPM have been published [47]–[49] which show they can be competitive in terms of torque density in small machines (sub kW) but tend to be less competitive in sizes for traction machines [50]. Of the many types of PMSM rotor structures, interior permanent magnet rotors are the preferred topology for EV drives due to the combination of simple and low-cost magnet geometry, self-containment of the magnets with the rotor core (see chapter 2), a useful contribution from reluctance torque and extended field-weakening capability. These features of IPMs are discussed in more detail in chapter 2.

1.2.3 Reluctance machines

Reluctance machine contains no permanent magnets or conductors on the rotor and relies on producing reluctance torque with a laminated silicon iron rotor which has a particular geometry to enhance rotor saliency. Reluctance machine can be classified into synchronous reluctance machine (SynRM) and switched reluctance machine (SRM) which are shown with Figure 1.12. Most high performance SynRM has a fairly conventional three-phase stator using sinusoidally distributed winding while an SRM has a much more salient stator geometry with concentrated coils.

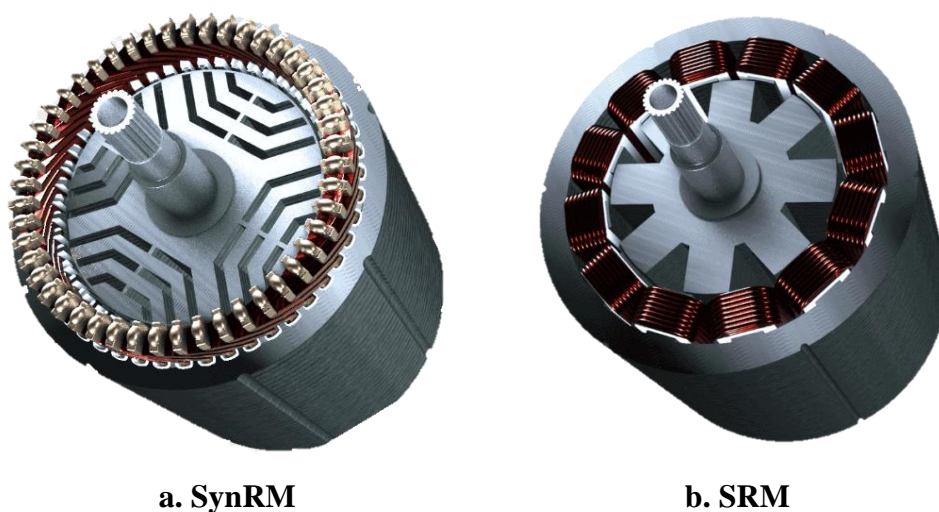


Figure 1.12 Synchronous reluctance machine and switched reluctance machine (Source: [51])

SynRMs have the drawback of low saliency ratio and power factor [52] and have not been adopted in high volume commercial applications although there are some development programmes to improve their competitiveness [53]–[55]. The key challenges are managing saturation which can limit peak power capability and the low power factor of this type of machine which affects the converter rating and cost.

SRMs have attracted more interest from researchers and vehicle manufacturers [56]–[65]. SRMs offer a potentially low-cost and a reasonably torque density solution, and independent phase windings with low mutual coupling which is useful for fault-tolerance [66]. The phase independence and fault tolerance capabilities could be enhanced further by utilizing a converter with two switches when the machine is applied with unipolar excitation current source. When a single phase encounters a short circuit condition, the machine can still operate but with reduced torque. Hence, it is claimed that SR machines have high fault tolerance capabilities,

simple structure, no high cost permanent magnets and high speed operating capability [3]. In addition, the performance of SRM are attractive for EVs, which benefits from its much smaller end winding, more isolated phase coupling, lower rotor loss, higher torque and power density [66].

A published study compared an SRM with a PM machine of same power rating. This concluded that the SRM was around 50% larger than the PM machine due in large part to a significant proportion of the stator winding current providing the magnetising current, with only the remainder for torque generation [57]. A further drawback is that although an SRM could be a low-cost machine in high volumes, it requires expensive and non-standard power converters and controllers to satisfy the requirement for more complex supply waveforms and more accurate rotor position control. Moreover, SRMs are recognized for having high torque ripple, high acoustic noise and high electromagnetic interference [67]. The ECOMmodore from Holden is amongst the limited number of EVs that have adopted an SRM as their propulsion drive is [23].

In summary, although SynRMs and SRMs have some very attractive features for EV drives, as a total system package they have tended to lose out to PMSMs with almost all manufacturers.

1.2.4 Summary of machine topologies

The previous sections have compared the performance of three competing machine technologies which are being developed for modern EV drives. Of the three technologies, PMSMs have the highest level of performance in terms of torque density and efficiency and are the preferred machine type for most manufacturers. Some manufacturers have continued to use induction machines for reasons of cost and robustness, and there has been relatively little adoption of reluctance machines. This thesis is focused on brushless PMSMs as these are by far the most significant technology in the market.

1.3 Key magnetic materials in permanent magnet synchronous machines

Brushless permanent magnet machines contain three functional materials within most machines. These are soft magnetic materials such as Silicon iron in the stator and rotor cores, permanent magnets which are in almost all cases attached to the rotor and high conductivity

materials in the stator coils (almost always Copper but in a few cases Aluminum). These all play an important role in the performance of the machine, in particular the efficiency. This section briefly describes the key requirements for these materials from an engineering perspective.

1.3.1 Stator and rotor core materials

The stator and rotor core require materials with high magnetic permeability, high saturation flux density, low electrical conductivity and low loss when exposed to time varying fields. The selection of a particular class and grade of materials usually involve some trade-off in these properties for cost. The best magnetic properties are achieved with high Cobalt (up to 49%) content alloys, but these are very expensive materials which require complex and expensive processing. The most common material for the stator and rotor cores of medium and high-performance electrical machines is Silicon Iron since it offers a good compromise between magnetic properties (10-20% worse than Cobalt iron) and cost (50-100 times lower cost depending on grade etc).

The world consumes ~10 million tons of SiFe each year, with more than 80% being used in core material market for transformers and rotating machines [68]. The Silicon content increases the electrical resistivity and can promote mechanical strength. The silicon content in commercial core materials for machines ranges from 1% to 3.5%. Even though additions of manganese help increase the electrical permeability, it tends to increase core loss due its effect on grain and so its content is limited to 0.5% [69]. Silicon iron is available in lamination thickness down to 0.1m, although 0.35mm is the most common grade for industrial machines. Grades with thickness of 0.2mm are increasingly being used for higher speeds for machines being EVs and HEVs. These specific grades (such as NO20) can be classified as high silicon content and thin gauge SiFe alloy.

Higher silicon content than 3.5% is available in SiFe alloys with silicon content up to 6.5% being produced for high frequency transformer and inductor cores. Grades with such high Silicon content tend not to be used in electrical machines due to the higher manufacturing cost, lower saturation flux density and brittleness [70]. Thin gauge SiFe alloys are produced with lamination thickness of 0.2mm and below and is well suited to reducing the eddy current loss especially in high frequency situations since eddy current loss is proportional to the square of the thickness of the alloy sheet [71].

1.3.2 Permanent magnet materials

High-performance brushless PM machines for EVs generally use rare-earth magnets, specifically NdFeB. This class of magnets were commercialised in the 1980s [72] and are able to achieve high airgap flux densities and excellent resistance to irreversible demagnetisation. Their main drawbacks are the high cost and the temperature sensitivity of the magnetic properties.

1.3.3 Conducting material

The properties of the electrical conductors in the form of wire and strip which are used to manufacture the stator coil are also important in electrical machines. They have a very significant influence on the machine losses, active mass and thermal performance. Among various conductors, copper is by far the most widely used in electrical machines due to its low resistivity and price. It has the highest conductivity of non-precious metals [73] but does suffer from a relatively high temperature coefficient of resistance, with resistance increasing by ~40% per 100°C.

Aluminum has lower electrical and thermal conductivity compared to Copper but it has a much lower density which can be helpful for light-weighting [74]. There is also some cost advantage with Aluminium [75].

Beyond Aluminium, there is on-going research on other conducting materials as a potential alternative for copper such carbon nanotubes (CNTs), graphene and combination of metals and carbon nanotubes. For CNTs, in addition to the advantage of high electrical conductivity and relatively low density, they also have good thermal conductivity and low temperature coefficient of electrical resistivity and no skin effect. CNTs have been used in prototype machines [76], [77]. Arguably the most useful new material that might have some uptake in high performance machine is a the mixture of the copper and CNTs [73] although there are still major challenges over cost and mechanical properties.

1.4 Loss prediction

1.4.1. Importance of loss predictions

The accurate prediction of losses in electrical machines is critical to their design, particularly for high efficiency. The main sources of loss in an electrical machine are winding losses (which can include high frequency skin and proximity losses) and losses in the stator

and rotor cores. Magnet losses caused by induced eddy current in the rotor magnets loss can have a dramatic effect on performance [78] but tend to form a small proportion of the overall machine. Of the three loss mechanisms, iron loss remains the loss with the greatest uncertainties due to the very complex phenomena involved. This has led to the development of many models to suit different conditions and various components of these models have evolved to form the main elements of tools which are incorporated into different design and modelling packages. The ability to account for various effects in improving [79] but there remain several aspects on which improvements still need to be made. One of these is the integration of high frequency switching effects into loss models. There have been several published models for incorporating switching effects including very simple additional terms into the loss separation model [80], and a more comprehensive model based on solution of the diffusion equation, a topic that will be returned to in chapter 5. The integration of high frequency switching events in iron loss model is the main, but not only, focus of this thesis.

Prior to considering the specific case of high frequency switching events, it is useful to review the main models used for iron loss.

1.4.2 Steinmetz equation and derivatives

The original Steinmetz equation (OSE) is proposed by Charles Steinmetz in 1882 to predict the hysteresis loss without considering the frequency, which is an empirical model based on a power-law equation [81]. The OSE is shown in equation (1.1).

$$P_{OSE} = kf^\alpha B_s^\beta \quad (1.1)$$

in which, P_{OSE} represents average iron loss power for unit volume; B_s is the peak induction of the sinusoidal excitation; k is the material parameter; α and β are the induction exponents for frequency and magnetic separately, which are regarded as the Steinmetz parameters. Generally used values of α range from 1-2 and β from 1.5-3 [82].

The Steinmetz parameters can be obtained by linear curve fitting for a series of measured iron loss data for sinusoidal flux density waveforms without DC bias [83]–[85]. However, the ideal sinusoidal voltage excitation source is not representative of conditions with power electronic converters, which have square wave voltage excitation [86]. A study has shown that for the same level of flux density amplitude, the iron loss generated by square waveform voltage source is lower than the iron loss powered by sinusoidal waveform voltage source [87]. In order to overcome this limitation, several updated version of Steinmetz equations have been

developed including Modified Steinmetz Equation (MSE), General Steinmetz Equation (GSE), Improved Generalized Steinmetz Equation (iGSE) [88]–[90].

The MSE is an update to solve the non-sinusoidal excitation issues when calculating the iron loss, which considering the effects of magnetization rate in OSE, the MSE can be expressed as equation (1.2).

$$P_{MSE} = (k f_{eq}^{\alpha-1} B_s^\beta) f_r \quad (1.2)$$

$$f_{eq} = \frac{2}{\Delta B^2 \pi^2} \int_0^T \left(\frac{dB(t)}{dt} \right)^2 dt$$

In which, f_r is the fundamental frequency of periodic waveform; f_{eq} is the equivalent frequency; ΔB is the peak-to-peak amplitude of magnetic induction and the $\frac{dB(t)}{dt}$ is the magnetization rate of iron loss.

However, when calculating the iron loss with a relatively low fundamental frequency, the accuracy of predicted results will decrease with increasing waveform harmonics [83], [91], [92]. To overcome the above limitations, another updated model GSE has been developed. The key equation in this model equation (1.3).

$$P_{GSE} = \frac{k_1}{T} \int_0^T \left| \frac{dB(t)}{dt} \right|^\alpha |B(t)|^{\beta-\alpha} dt \quad (1.3)$$

$$k_1 = \frac{k}{2^{\beta-\alpha} (2\pi)^{\alpha-1} \int_0^{2\pi} |\cos\theta|^\alpha |\sin\theta|^{(\beta-\alpha)} d\theta}$$

T and θ are the period and phase angle of excitation waveform respectively. However, this method still has the drawback that accuracy decreases when the excitation waveform has higher harmonics [84], [91], [93].

The iGSE is one of the most favoured iron loss calculation method due to its reliability and high accuracy contributed by considering the minor loops and calculating the iron loss corresponding to major and minor loops separately [89], [90]. It could be expressed as equation (1.4).

$$P_{iGSE} = \frac{k_1}{T} \int_0^T \left| \frac{dB(t)}{dt} \right|^\alpha |\Delta B|^{\beta-\alpha} dt \quad (1.4)$$

$$k_1 = \frac{k}{2^{\beta-\alpha} (2\pi)^{\alpha-1} \int_0^{2\pi} |\cos\theta|^\alpha d\theta}$$

The main feature of the Steinmetz equation and the various enhancement made to it are the coefficients related to frequency, which limit its accuracy in predicting iron loss when solving scenarios with high harmonic content excitation sources.

1.4.3 Loss separation model

The loss separation method is a widely used method with reasonable accuracy and it straightforward to implement [94]. The original version of the loss separation model was developed by Jordan, using the sum of the hysteresis loss and eddy loss to express the iron loss [84]. The hysteresis loss is also called static loss and eddy loss the dynamic loss. This original version of loss separation model is shown in equation (1.5).

$$P_{iron} = k_h f B_s + k_{eddy} f^2 B_s^2 \quad (1.5)$$

in which, P_{iron} represents the total iron loss is stands by; hysteresis coefficient is expressed as k_h ; eddy current coefficient is expressed as k_{eddy} and B_s is the peak amplitude of the flux density.

Bertotti extended the original loss separation model by introducing a new term to represent the excess loss, which allows to predict the iron loss under arbitrary magnetizing frequency. The Bertotti loss separation model, which will be studied in more detail in chapter 4, can be expressed by equation (1.6).

$$P_{iron} = k_h f B_s^x + k_{eddy} f^2 B_s^2 + k_{excess} f^{1.5} B_s^{1.5} \quad (1.6)$$

In which, k_{excess} is the excess loss coefficient and x is the Steinmetz coefficient which depends on the material permeability. The typical value of x is ranges from 1.5 to 2.5 [81], [95].

According to equation (1.6), Bertotti provides the expression of eddy current loss and excess loss for a lamination material, which represented by equation (1.7) and (1.8) separately.

$$P_{eddy} = \frac{\pi^2 d^2 f^2 B_s^2}{\sigma \beta} \quad (1.7)$$

$$P_{excess} = 8 \sqrt{\frac{GAV_0}{\rho}} B_s^{1.5} \sqrt{f} \quad (1.8)$$

In which, G is dimensionless coefficient of eddy current; ρ represents the electrical resistivity; d is the lamination thickness and V_0 is the parameter refers to statistical distribution properties of anomalous eddy currents [96]. However, the loss predictions from this simplified model with frequency and peak flux density assumes ideal sinusoidal excitation, which does not accommodate excitations with harmonics [94]. Nevertheless, it still could be utilized to calculate the iron loss for square waveform excitation with DC bias as suggested in [97].

The extension of the loss separation model to arbitrary waveforms through a time-stepped representation of flux density derivatives is described in detail in chapters 4 and 5.

1.5 Thesis structure

This research reported in this thesis focusses on the high fidelity mechanical and iron loss modelling for IPM machines designed for EV traction. The thesis is structured into the following chapters:

Chapter 1: This chapter sets the context for the research by discussing the background and market trends in EVs and the various machine technologies in the market. It compares the features of different machine technologies and discusses the key materials. It concludes by introducing methods for loss calculations.

Chapter 2: This chapter presents a design study for an IPM machine which combines electromagnetic and mechanical optimisation of the rotor of an IPM machine. A series of different machine features are investigated culminating in a final design of 100 kW IPM machine which forms the reference machine for subsequent chapters.

Chapter 3: A method for predicting representative flux density waveforms, including high frequency switching events, in a finite element model of a machine is described in this chapter. It combines magnetostatic finite element models of the machine at fundamental frequency to determine electric circuit parameters with a SIMULINK circuit simulation to predict the high frequency components of the current waveform and hence flux density.

Chapter 4: This chapter introduces a loss separation approach which includes the high frequency flux density waveforms to predict iron loss of the reference IPM machine using a classical resistance-limited eddy current model.

Chapter 5: This chapter explores a number of methods for incorporating eddy current redistribution and skin effect in individual laminations. A combination of analytical methods and a numerical finite difference method are considered for solving the one-dimensional diffusion equation. A three-dimensional finite element model of single lamination model is used as

provide a benchmark for the various solutions of the diffusion equation. The chapter concludes by applying various methods at machine level to demonstrate the significance of accounting for high frequency switching behaviour in finite element based iron loss models.

Chapter 6: This chapter reports on measurements on a toroidal sample to validate the models developed in previous chapters. It also introduces a demonstrator machine which was developed for machine level validation but which due to a fault in manufacture could not be tested.

Chapter 7: The main findings and conclusion for the research are discussed in this chapter.

Generally speaking, this paper made several contributions as follows:

- Illustrating the benefits and trade-offs during the IPM machine design, which combines electromagnetic and mechanical optimisation.
- Based on the designed IPM machine, developing a method relay on SIMULINK to generate corresponding switching current waveform with very short time step from finite element simulation based on standard time step durations. The generated current waveform represents the inductance variations of IPM machine with position and current.
- Several methods integrating lamination level eddy current and skin effect into practical post-processing methods are explored for linear and non-linear materials. Although there are some compromises and approximations when integrating magneto-dynamic effects into post-processing of magneto-static solutions, its overall benefits have been shown.
- Developed a post-processor based on MATLAB, which could work with commercial finite element packages.

Papers resulting from this thesis:

Guanhua Zhang, Geraint W Jewell, “Combined electromagnetic and mechanical design optimization of interior permanent magnet rotors for electric vehicle drivetrains”. [Accepted by Word Electric Vehicle Journal]

Guanhua Zhang, Geraint W Jewell, “High fidelity loss modelling of an interior permanent magnet machine for electrical vehicle traction”. [In preparation]

References

- [1] [Online], “Sources of Greenhouse Gas Emissions,” <https://www.epa.gov/ghgemissions/sources-greenhous.> .
- [2] B. Bilgin *et al.*, “Making the Case for Electrified Transportation,” *IEEE Trans. Transp. Electrif.*, vol. 1, no. 1, pp. 4–17, 2015, doi: 10.1109/TTE.2015.2437338.
- [3] L. Chang, “Comparison of AC Drives for Electric Vehicles—A Report on Experts’ Opinion Survey,” *IEEE Aerosp. Electron. Syst. Mag.*, vol. 9, no. 8, pp. 7–11, 1994, doi: 10.1109/62.311235.
- [4] Akimoto Hajime, “Overview of Policy Actions and Observational Data for PM2.5 and O3 in Japan: A Study of Urban Air Quality Improvement in Asia,” *JICA Res. Institute, Work. Pap.*, no. 137, 2017.
- [5] A. K. Amegah and S. Agyei-Mensah, “Urban air pollution in Sub-Saharan Africa: Time for action,” *Environ. Pollut.*, vol. 220, pp. 738–743, 2017, doi: 10.1016/j.envpol.2016.09.042.
- [6] S. G. Wirasingha, M. Khan, and O. Gross, “48-V electrification: Belt-driven starter generator systems,” *Adv. Electr. Drive Veh. Boca Raton, FL, USACRC Press*, 2014.
- [7] A. Razmjoo *et al.*, “A Comprehensive Study on the Expansion of Electric Vehicles in Europe,” *Appl. Sci.*, vol. 12, no. 22, 2022, doi: 10.3390/app122211656.
- [8] A. Emadi, *Advanced Electric Drive Vehicles*. 2014.
- [9] T. M. Jahns and V. Blasko, “Recent Advances in Power Electronics Technology for Industrial and Traction Machine Drives,” *Proc. IEEE*, vol. 89, no. 6, pp. 963–975, 2001, doi: 10.1109/5.931496.
- [10] A. G. Jack, B. C. Mecrow, and J. A. Haylock, “A comparative study of permanent magnet and switched reluctance motors for high-performance fault-tolerant applications,” *IEEE Trans. Ind. Appl.*, vol. 32, no. 4, pp. 889–895, 1996, doi: 10.1109/28.511646.
- [11] D. Diallo, M. E. H. Benbouzid, and A. Makouf, “A fault-tolerant control architecture for induction motor drives in automotive applications,” *IEEE Trans. Veh. Technol.*, vol. 53, no. 6, pp. 1847–1855, 2004, doi: 10.1109/TVT.2004.833610.
- [12] [Online], “Tesla Model Y Long Range AWD Specs,” <https://www.ultimatespecs.com/car-specs/Tesla/118935/Tesla-Model-Y-Long-Range-AWD.html> .

- [13] E. P. Cornell, R. H. Guess, and F. G. Turnbull, “Advanced Motor Developments for Electric Vehicles,” *IEEE Trans. Veh. Technol.*, vol. VT-26, no. 2, pp. 128–134, 1977, doi: 10.1109/T-VT.1977.23669.
- [14] T. Jahns, “Getting Rare-Earth Magnets Out of EV Traction Machines: A review of the many approaches being pursued to minimize or eliminate rare-earth magnets from future EV drivetrains,” *IEEE Electr. Mag.*, vol. 5, no. 1, pp. 6–18, 2017, doi: 10.1109/MELE.2016.2644280.
- [15] Y. Guan, Z. Q. Zhu, I. A. A. Afinowi, J. C. Mipo, and P. Farah, “Difference in maximum torque-speed characteristics of induction machine between motor and generator operation modes for electric vehicle application,” *Electr. Power Syst. Res.*, vol. 136, pp. 406–414, 2016, doi: 10.1016/j.epsr.2016.03.027.
- [16] Z. Wang, T. W. Ching, S. Huang, H. Wang, and T. Xu, “Challenges Faced by Electric Vehicle Motors and Their Solutions,” *IEEE Access*, vol. 9, pp. 5228–5249, 2021, doi: 10.1109/ACCESS.2020.3045716.
- [17] M. Guarnieri, “When cars went electric, Part 1,” *IEEE Ind. Electron. Mag.*, vol. 5, no. 2, pp. 1–2, 2011, doi: 10.1109/MIE.2011.941122.
- [18] C. Bader and W. Stephan, “Comparison of Electrical Drives for Road Vehicles,” *IEEE Trans. Veh. Technol.*, vol. VT-26, no. 2, pp. 123–128, 1977, doi: 10.1109/T-VT.1977.23668.
- [19] G. Dancygier and J. C. Dolhagaray, “Motor control law and comfort law in the Peugeot and Citroen electric vehicles driven by a DC commutator motor,” *IEE Conference Publication*, no. 456, pp. 370–374, 1998, doi: 10.1049/cp:19980553.
- [20] A. Harson, P. H. Mellor, and D. Howe, “Design considerations for induction machines for electric vehicle drives,” *IEE Conference Publication*, no. 412, pp. 16–20, 1995, doi: 10.1049/cp:19950827.
- [21] [Online], “AC INDUCTION MOTORS WITH SQUIRREL CAGE ROTORS,” <https://www.bodine-electric.com/blog/ac-induction-garmotors/>. .
- [22] [Online], “Construction of a Three-phase Induction motor,” <https://onlinestudentguide.com/three-phase-induction-motor-construction/>. .
- [23] M. Zeraoulia, M. E. H. Benbouzid, and D. Diallo, “Electric motor drive selection issues for HEV propulsion systems: A comparative study,” *IEEE Trans. Veh. Technol.*, vol. 55, no. 6, pp. 1756–1764, 2006, doi: 10.1109/TVT.2006.878719.
- [24] C. C. Chan, “The state of the art of electric and hybrid vehicles,” *Proc. IEEE*, vol. 90, no. 2, pp. 247–275, 2002, doi: 10.1109/5.989873.

- [25] S. S. Williamson, S. M. Lukic, and A. Emadi, “Comprehensive drive train efficiency analysis of hybrid electric and fuel cell vehicles based on motor-controller efficiency modeling,” *IEEE Trans. Power Electron.*, vol. 21, no. 3, pp. 730–740, 2006, doi: 10.1109/TPEL.2006.872388.
- [26] D. H. Cho, H. K. Jung, and C. G. Lee, “Induction motor design for electric vehicle using a niching genetic algorithm,” *IEEE Trans. Ind. Appl.*, vol. 37, no. 4, pp. 994–999, 2001, doi: 10.1109/28.936389.
- [27] T. Wang, P. Zheng, Q. Zhang, and S. Cheng, “Design characteristics of the induction motor used for hybrid electric vehicle,” *2004 12th Symp. Electromagn. Launch Technol.*, vol. 41, no. 1, pp. 523–527, 2004, doi: 10.1109/elt.2004.1398136.
- [28] [Online], “Different types of electric motors used in EVs,” https://www.arenaev.com/different_types_of_electric_motors_used_in_evs-news-214.php. .
- [29] [Online], “Model 3 Owner’s Manual,” https://www.tesla.com/ownersmanual/model3/en_cn/GUID-E414862C-CFA1-4A0B-9548-BE21C32CAA58.html. .
- [30] [Online], “Tesla Model 3’s motor - The Brilliant Engineering behind it,” <https://www.youtube.com/watch?v=esUb7Zy5Oio>. .
- [31] Z. Zhu and X.M. Wu, *Sensorless Control of Permanent Magnet Synchronous Machine Drives*. Wiley, 2023.
- [32] C. Espanet, J. M. Kauffmann, and R. Bernard, “Comparison of two in-wheel permanent magnet motors for military applications,” *2006 IEEE Veh. Power Propuls. Conf. VPPC 2006*, 2006, doi: 10.1109/VPPC.2006.364300.
- [33] O. Ustun, M. Yilmaz, C. Gokce, U. Karakaya, and R. N. Tuncay, “Energy management method for solar race car design and application,” *2009 IEEE Int. Electr. Mach. Drives Conf. IEMDC '09*, pp. 804–811, 2009, doi: 10.1109/IEMDC.2009.5075296.
- [34] M. Terashima, T. Ashikaga, T. Mizuno, K. Natori, N. Fujiwara, and M. Yada, “Novel motors and controllers for high-performance electric vehicle with four in-wheel motors,” *IEEE Trans. Ind. Electron.*, vol. 44, no. 1, pp. 28–38, 1997, doi: 10.1109/41.557496.
- [35] A. Lidozzi, L. Solero, F. Crescimbeni, and A. Di Napoli, “SVM PMSM drive with low resolution hall-effect sensors,” *PESC Rec. - IEEE Annu. Power Electron. Spec. Conf.*, vol. 2005, no. 1, pp. 1580–1586, 2005, doi: 10.1109/PESC.2005.1581841.

- [36] K. T. Chau, J. Z. Jiang, G. H. Chen, and X. Y. Wang, "A Novel Polyphase Multipole Square-Wave Permanent Magnet Motor Drive for Electric Vehicles," *IEEE Trans. Ind. Appl.*, vol. 30, no. 5, pp. 1258–1266, 1994, doi: 10.1109/28.315237.
- [37] J. G. W. West, "DC, induction, reluctance and PM motors for electric vehicles," pp. 77–88, 2003.
- [38] L. Tang and G. J. Su, "High-performance control of two three-phase permanent-magnet synchronous machines in an integrated drive for automotive applications," *IEEE Trans. Power Electron.*, vol. 23, no. 6, pp. 3047–3055, 2008, doi: 10.1109/TPEL.2008.2005374.
- [39] Y. P. Yang and D. S. Chuang, "Optimal design and control of a wheel motor for electric passenger cars," *SAE Tech. Pap.*, vol. 43, no. 1, pp. 51–61, 2005, doi: 10.4271/2005-01-0282.
- [40] N. A. Rahim, W. P. Hew, and A. Mahmoudi, "Axial-flux permanent-magnet brushless dc traction motor for direct drive of electric vehicle," *Int. Rev. Electr. Eng.*, vol. 6, no. 2, pp. 760–769, 2011.
- [41] C. Ma, Q. Li, L. Deng, C. Chen, Q. Liu, and H. Gao, "A novel sound quality evaluation method of the diagnosis of abnormal noise in interior permanent-magnet synchronous motors for electric vehicles," *IEEE Trans. Ind. Electron.*, vol. 64, no. 5, pp. 3883–3891, 2017, doi: 10.1109/TIE.2017.2652718.
- [42] P. Dai, W. Sun, N. Xu, Y. Lv, and X. Zhu, "Research on energy management system of hybrid electric vehicle based on permanent magnet synchronous motor," *Proc. 2016 IEEE 11th Conf. Ind. Electron. Appl. ICIEA 2016*, pp. 2345–2349, 2016, doi: 10.1109/ICIEA.2016.7603984.
- [43] T. Takahashi, M. Takemoto, S. Ogasawara, W. Hino, and K. Takezaki, "Size and Weight Reduction of an In-Wheel Axial-Gap Motor Using Ferrite Permanent Magnets for Electric Commuter Cars," *IEEE Trans. Ind. Appl.*, vol. 53, no. 4, pp. 3927–3935, 2017, doi: 10.1109/TIA.2017.2684739.
- [44] A. Athavale, K. Sasaki, B. S. Gagas, T. Kato, and R. D. Lorenz, "Variable Flux Permanent Magnet Synchronous Machine (VF-PMSM) Design Methodologies to Meet Electric Vehicle Traction Requirements with Reduced Losses," *IEEE Trans. Ind. Appl.*, vol. 53, no. 5, pp. 4318–4326, 2017, doi: 10.1109/TIA.2017.2701340.
- [45] H. Chen, A. M. El-Refaie, and N. A. O. Demerdash, "Flux-Switching Permanent Magnet Machines: A Review of Opportunities and Challenges - Part I: Fundamentals and Topologies," *IEEE Trans. Energy Convers.*, vol. 35, no. 2, pp. 684–698, 2020, doi: 10.1109/TEC.2019.2956600.

- [46] M. Cheng, W. Hua, J. Zhang, and W. Zhao, "Overview of stator-permanent magnet brushless machines," *IEEE Trans. Ind. Electron.*, vol. 58, no. 11, pp. 5087–5101, 2011, doi: 10.1109/TIE.2011.2123853.
- [47] Z. Q. Zhu and J. T. Chen, "Advanced flux-switching permanent magnet brushless machines," *IEEE Trans. Magn.*, vol. 46, no. 6, pp. 1447–1453, 2010, doi: 10.1109/TMAG.2010.2044481.
- [48] J. T. Chen and Z. Q. Zhu, "Influence of the rotor pole number on optimal parameters in flux-switching pm brushless ac machines by the lumped-parameter magnetic circuit model," *IEEE Trans. Ind. Appl.*, vol. 46, no. 4, pp. 1381–1388, 2010, doi: 10.1109/TIA.2010.2049720.
- [49] A. S. Thomas, Z. Q. Zhu, R. L. Owen, G. W. Jewell, and D. Howe, "Multiphase Flux-Switching Permanent-Magnet Brushless Machine for Aerospace Application," *IEEE Trans. Ind. Appl.*, vol. 45, no. 6, pp. 1971–1981, 2009, doi: 10.1109/TIA.2009.2031901.
- [50] Tianyi Zhu, "Investigation of Stator Mounted Permanent Magnet Machines," University of Sheffield, 2022.
- [51] [Online], "Reluctance Motor Types Overview and detailed Function," <https://oswos.com/reluctance-motor/>. .
- [52] Z. Q. Zhu and C. C. Chan, "Electrical machine topologies and technologies for electric, hybrid, and fuel cell vehicles," *2008 IEEE Veh. Power Propuls. Conf. VPPC 2008*, pp. 1–6, 2008, doi: 10.1109/VPPC.2008.4677738.
- [53] M. Murataliyev, M. Degano, M. Di Nardo, N. Bianchi, and C. Gerada, "Synchronous Reluctance Machines: A Comprehensive Review and Technology Comparison," *Proc. IEEE*, vol. 110, no. 3, pp. 382–399, 2022, doi: 10.1109/JPROC.2022.3145662.
- [54] [Online], "ABB IE5 SynRM and Drives - Powering Efficiency and Reliability Worldwide," <https://global.abb/topic/synrm-drive-package/en>. .
- [55] J. D. Widmer, R. Martin, and B. C. Mecrow, "Optimisation of an 80kW Segmental Rotor Switched Reluctance Machine for automotive traction," *Proc. 2013 IEEE Int. Electr. Mach. Drives Conf. IEMDC 2013*, pp. 427–433, 2013, doi: 10.1109/IEMDC.2013.6556132.
- [56] P. P. Acarnley, R. J. Hill, and C. W. Hooper, "Detection of Rotor Position in Stepping and Switched Motors by Monitoring of Current Waveforms," *IEEE Trans. Ind. Electron.*, vol. IE-32, no. 3, pp. 215–222, 1985, doi: 10.1109/TIE.1985.350161.

- [57] M. Ehsani, I. Husain, and A. B. Kulkarni, "Elimination of Discrete Position Sensor and Current Sensor in Switched Reluctance Motor Drives," *IEEE Trans. Ind. Appl.*, vol. 28, no. 1, pp. 128–135, 1992, doi: 10.1109/28.120221.
- [58] S. R. MacMinn, W. J. Rzesos, P. M. Szczesny, and T. M. Jahns, "Application of Sensor Integration Techniques to Switched Reluctance Motor Drives," *IEEE Trans. Ind. Appl.*, vol. 28, no. 6, pp. 1339–1344, 1992, doi: 10.1109/28.175286.
- [59] M. Ehsani and I. Husain, "New Modulation Encoding Techniques for Indirect Rotor Position Sensing in Switched Reluctance Motors," *IEEE Trans. Ind. Electron.*, vol. 41, no. 3, pp. 301–307, 1994, doi: 10.1109/41.293900.
- [60] I. Husain and M. Ehsani, "Rotor position sensing in switched reluctance motor drives by measuring mutually induced voltages," *Conf. Rec. - IAS Annu. Meet. (IEEE Ind. Appl. Soc.)*, vol. 1992-Janua, no. 3, pp. 422–429, 1992, doi: 10.1109/IAS.1992.244364.
- [61] J. Zhu, K. E. Cheng, X. Xue, and Y. Zou, "Design of a novel high-torque-density in-wheel switched reluctance motor for electric vehicles," *2017 IEEE Int. Magn. Conf. INTERMAG 2017*, vol. 1, no. 10, 2017, doi: 10.1109/INTMAG.2017.8008065.
- [62] S. Bukhari, W. Cao, K. A. Samo, Z. Liu, and S. Ansari, "Electrical Motor Drive Technologies for Green Electric Vehicle A Review," vol. 1, no. 2, pp. 1–10, 2017.
- [63] Z. Zhou *et al.*, "A segmented rotor type switched reluctance machine for BSGs of hybrid electric vehicles: Concept, design and analysis," *2017 20th Int. Conf. Electr. Mach. Syst. ICEMS 2017*, pp. 8–11, 2017, doi: 10.1109/ICEMS.2017.8056169.
- [64] N. Zabihi and R. Gouws, "A review on switched reluctance machines for electric vehicles," *IEEE Int. Symp. Ind. Electron.*, vol. 2016-Novem, pp. 799–804, 2016, doi: 10.1109/ISIE.2016.7744992.
- [65] M. Ruba and D. Fodorean, "Motor-drive solution for light electric vehicles based on a switched reluctance machine," *2016 20th IEEE Int. Conf. Autom. Qual. Testing, Robot. AQTR 2016 - Proc.*, no. 1, pp. 1–6, 2016, doi: 10.1109/AQTR.2016.7501372.
- [66] W. Cao, A. A. S. Bukhari, and L. Aarniovuori, "Review of Electrical Motor Drives for Electric Vehicle Applications," *Mehran Univ. Res. J. Eng. Technol.*, vol. 38, no. 3, pp. 525–540, 2019, doi: 10.22581/muet1982.1903.01.
- [67] D. E. Cameron, J. H. Lang, and S. D. Umans, "The Origin and Reduction of Acoustic Noise in Doubly Salient Variable-Reluctance Motors," *IEEE Trans. Ind. Appl.*, vol. 28, no. 6, pp. 1250–1255, 1992, doi: 10.1109/28.175275.

- [68] A. Krings, A. Boglietti, A. Cavagnino, and S. Sprague, “Soft Magnetic Material Status and Trends in Electric Machines,” *IEEE Trans. Ind. Electron.*, vol. 64, no. 3, pp. 2405–2414, 2017, doi: 10.1109/TIE.2016.2613844.
- [69] F. Li, H. Li, S. Zheng, J. You, K. Han, and Q. Zhai, “Impacts of modification of alloying method on inclusion evolution in RH refining of silicon steel,” *Materials (Basel)*, vol. 10, no. 10, pp. 1–8, 2017, doi: 10.3390/ma10101206.
- [70] S. Kasai, M. Namikawa, and T. Hiratani, “Recent progress of high silicon electrical steel in JFE steel,” *JFE Tech. Rep.*, vol. 21, no. 21, pp. 14–19, 2016.
- [71] H. Jiao *et al.*, “High-permeability and thin-gauge non-oriented electrical steel through twin-roll strip casting,” *Mater. Des.*, vol. 136, pp. 23–33, 2017, doi: 10.1016/j.matdes.2017.09.051.
- [72] J. J. Croat and J. Ormerod, “Chapter 1 - The history of permanent -magnets,” in *Modern Permanent Magnets*, Woodhead Publishing Series in Electronic and Optical Materials 2022, pp. 1–30.
- [73] R. M. Sundaram, A. Sekiguchi, M. Sekiya, T. Yamada, and K. Hata, “Copper/carbon nanotube composites: Research trends and outlook,” *R. Soc. Open Sci.*, vol. 5, no. 11, 2018, doi: 10.1098/rsos.180814.
- [74] P. Ramesh and N. C. Lenin, “High Power Density Electrical Machines for Electric Vehicles-Comprehensive Review Based on Material Technology,” *IEEE Trans. Magn.*, vol. 55, no. 11, pp. 1–21, 2019, doi: 10.1109/TMAG.2019.2929145.
- [75] J. D. Widmer, R. Martin, and B. C. Mecrow, “Precompressed and Stranded Aluminum Motor Windings for Traction Motors,” *IEEE Trans. Ind. Appl.*, vol. 52, no. 3, pp. 2215–2223, 2016, doi: 10.1109/TIA.2016.2528226.
- [76] J. Pyrhönen, J. Montonen, P. Lindh, J. J. Vauterin, and M. J. Otto, “Replacing copper with new carbon nanomaterials in electrical machine windings,” *Int. Rev. Electr. Eng.*, vol. 10, no. 1, pp. 12–21, 2015, doi: 10.15866/iree.v10i1.5253.
- [77] V. Rallabandi, N. Taran, D. M. Ionel, and J. F. Eastham, “Coreless multidisc axial flux PM machine with carbon nanotube windings,” *IEEE CEFC 2016 - 17th Bienn. Conf. Electromagn. F. Comput.*, vol. 3, p. 1, 2017, doi: 10.1109/CEFC.2016.7816368.
- [78] J. D. Ede, K. Atallah, G. W. Jewell, J. B. Wang, and D. Howe, “Effect of axial segmentation of permanent magnets on rotor loss in modular permanent-magnet brushless machines,” *IEEE Trans. Ind. Appl.*, vol. 43, no. 5, pp. 1207–1213, 2007, doi: 10.1109/TIA.2007.904397.

- [79] Z. Q. Zhu *et al.*, “Evaluation of Iron Loss Models in Electrical Machines,” *IEEE Trans. Ind. Appl.*, vol. 55, no. 2, pp. 1461–1472, 2019, doi: 10.1109/TIA.2018.2880674.
- [80] S. Xue *et al.*, “Iron loss model for electrical machines fed by low switching frequency inverter,” *2017 IEEE Int. Magn. Conf. INTERMAG 2017*, vol. 53, no. 11, pp. 2–5, 2017, doi: 10.1109/INTMAG.2017.8008031.
- [81] Steinmetz Chas. Proteus, “On the Law of Hysteresis,” *Trans. Am. Inst. Electr. Eng.*, vol. 20, pp. 51–57, 1902, doi: 10.1109/T-AIEE.1902.4764231.
- [82] M. Mu, F. C. Lee, and P. Mattavelli, “PhD Dissertation: High Frequency Magnetic Core Loss Study,” *Electr. Eng.*, vol. PhD Disser, pp. 1–52, 2013.
- [83] S. Yue, Y. Li, Q. Yang, X. Yu, and C. Zhang, “Comparative Analysis of Core Loss Calculation Methods for Magnetic Materials under Nonsinusoidal Excitations,” *IEEE Trans. Magn.*, vol. 54, no. 11, pp. 1–5, 2018, doi: 10.1109/TMAG.2018.2842064.
- [84] S. Muller, M. Keller, M. Maier, and N. Parspour, “Comparison of iron loss calculation methods for soft magnetic composite,” *14th Brazilian Power Electron. Conf. COBEP 2017*, vol. 2018-Janua, pp. 1–6, 2017, doi: 10.1109/COBEP.2017.8257313.
- [85] T. W. Zhou, G. Y. Zhou, G. Ombach, X. Gong, Y. C. Wang, and J. X. Shen, “Improvement of steinmetz’s parameters fitting formula for ferrite soft magnetic materials,” *1st IEEE Student Conf. Electr. Mach. Syst. SCEMS 2018*, pp. 1–4, 2019, doi: 10.1109/SCEMS.2018.8624798.
- [86] Robert Erickson, “Fundamentals of Power Electronics,” p. 282, 2008.
- [87] D. Y. Chen, “Comparisons of high frequency magnetic core losses under two different driving conditions: A sinusoidal voltage and a square-wave voltage,” *PESC Rec. - IEEE Annu. Power Electron. Spec. Conf.*, vol. 1978-Janua, pp. 237–241, 1978, doi: 10.1109/PESC.1978.7072358.
- [88] J. Reinert, A. Brockmeyer, and R. W. A. A. De Doncker, “Calculation of losses in ferro- and ferrimagnetic materials based on the modified Steinmetz equation,” *IEEE Trans. Ind. Appl.*, vol. 37, no. 4, pp. 1055–1061, 2001, doi: 10.1109/28.936396.
- [89] Venkatachalam Kapil, “Accurate prediction of ferrite core loss with nonsinusoidal waveforms using only Steinmetz parameters,” pp. 36–41.
- [90] S. Yue, Q. Yang, Y. Li, and C. Zhang, “Core loss calculation for magnetic materials employed in SMPS under rectangular voltage excitations,” *AIP Adv.*, vol. 8, no. 5, 2018, doi: 10.1063/1.5007201.
- [91] A. Krings and J. Soulard, “Overview and Comparison of Iron Loss Models for Electrical Machines,” *J. Electr. Eng.*, vol. 10, no. May 2010, pp. 162–169, 2010.

- [92] X. Yu, Y. Li, Q. Yang, S. Yue, and C. Zhang, “Loss Characteristics and Model Verification of Soft Magnetic Composites under Non-Sinusoidal Excitation,” *IEEE Trans. Magn.*, vol. 55, no. 2, pp. 1–4, 2019, doi: 10.1109/TMAG.2018.2869379.
- [93] J. Li, T. Abdallah, and C. R. Sullivan, “Improved calculation of core loss with nonsinusoidal waveforms,” *Conf. Rec. - IAS Annu. Meet. (IEEE Ind. Appl. Soc.)*, vol. 4, no. C, pp. 2203–2210, 2001, doi: 10.1109/IAS.2001.955931.
- [94] B. Ducharne, P. Tsafack, Y. A. Tene Deffo, B. Zhang, and G. Sebald, “Anomalous fractional magnetic field diffusion through cross-section of a massive toroidal ferromagnetic core,” *Commun. Nonlinear Sci. Numer. Simul.*, vol. 92, p. 105450, 2021, doi: 10.1016/j.cnsns.2020.105450.
- [95] S. Balci, I. Sefa, and M. B. Bayram, “Core material investigation of medium-frequency power transformers,” *16th Int. Power Electron. Motion Control Conf. Expo. PEMC 2014*, pp. 861–866, 2014, doi: 10.1109/EPEPEMC.2014.6980606.
- [96] D. Rodriguez-Sotelo, M. A. Rodriguez-Licea, I. Araujo-Vargas, J. Prado-Olivarez, A. I. Barranco-Gutiérrez, and F. J. Perez-Pinal, “Power Losses Models for Magnetic Cores: A Review,” *Micromachines*, vol. 13, no. 3, pp. 1–27, 2022, doi: 10.3390/mi13030418.
- [97] H. Sun, Y. Li, Z. Lin, C. Zhang, and S. Yue, “Core loss separation model under square voltage considering DC bias excitation,” *AIP Adv.*, vol. 10, no. 1, 2020, doi: 10.1063/1.5131561.

Chapter 2: Design optimisation of an interior permanent magnet machine

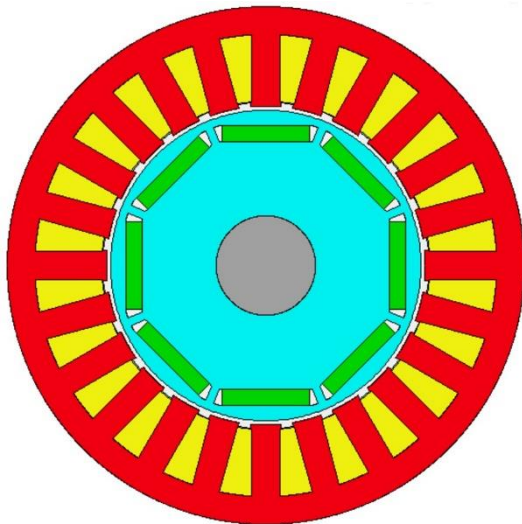
2.1 Introduction

As noted in chapter 1, permanent magnet (PM) machines have become the favoured machine technology for the vast majority of electric vehicle (EV) drivetrains due to their combination of superior power density, power factor and efficiency at rated power when compared to competing machine technologies [1]. However, maximising these performance benefits requires detailed design optimisation which must cover mechanical, electromagnetic and thermal aspects. Mechanical considerations are particularly important in high-speed machines. There is no definitive threshold beyond which machines are regarded as high-speed machines, although peripheral linear speeds beyond 100 m/s or so have been proposed as a useful definition [2]. In most high-speed machines, the mechanical loads may be sufficient to have a significant impact on the mechanical design of the rotor, and so there is often a need to trade off some electromagnetic performance to ensure a robust mechanical design. In permanent magnet machines where the rotors are not subjected to large centrifugal loads, there is a notion that torque density tends to improve with increasing rotor diameter [3]. However, in some applications, the combination of diameter and rotational speed results in large centrifugal loads within the rotor. These mechanical loads tend to push the optimum aspect ratio towards longer- and smaller-diameter machines [3].

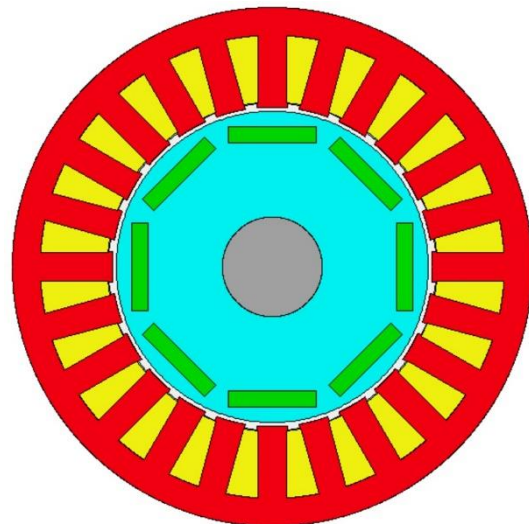
2.1.1 Interior permanent magnet machine topologies and features

Interior permanent magnet (IPM) machines in which individual magnet poles are fully enclosed within matching apertures in the rotor core have been adopted in many EV drivetrains. They are now the most widely used rotor topology in mainstream EV applications. A selection of different IPM rotor geometries is shown in Figure 2.1. The popularity of IPMs for EV applications is due to a combination of their ability to be operated readily in so-called ‘field-weakening’ mode, the scope to produce saliency torque to supplement the PM excitation torque and the scope for an IPM rotor core to provide the sole mechanical containment and support for the rotor PMs, thus simplifying rotor manufacture. If the centrifugal loading produced through a combination of the self-loading of the core and dead-weight loading from the PMs can be accommodated within the stress limits of the rotor cores, then there is no requirement to employ a separate sleeve or can on the rotor [4].

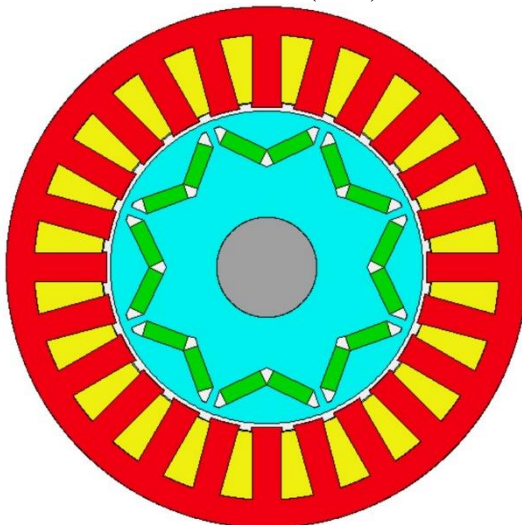
However, to exploit the self-containing capability of IPM rotor cores, it may prove necessary to thicken up critical regions of the rotor core to take the centrifugal load at acceptable levels of localized stress. The narrow regions adjacent to the airgap that close off the apertures that contain the PMs tend to be the regions of the highest mechanical stress and which require thickening up to accommodate high-speed operation. However, these are also the regions that tend to promote the leakage of the PM flux within the rotor and so thickening up these regions to accommodate centrifugal loading tends to have an adverse effect on the magnitude of the airgap flux density and, hence, the torque capability. Hence, for a given combination of torque and speed, there is likely to be an optimum rotor size and aspect ratio that yields the maximum torque density. This study seeks to investigate this design trade-off in IPM machines through the electromagnetic and mechanical optimization of the rotor of an IPM machine.



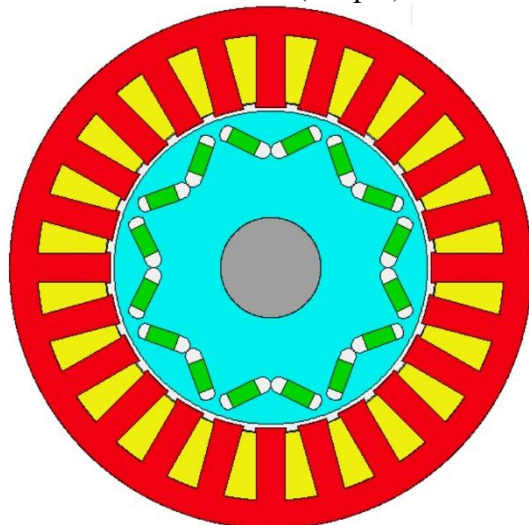
Interior flat (web)



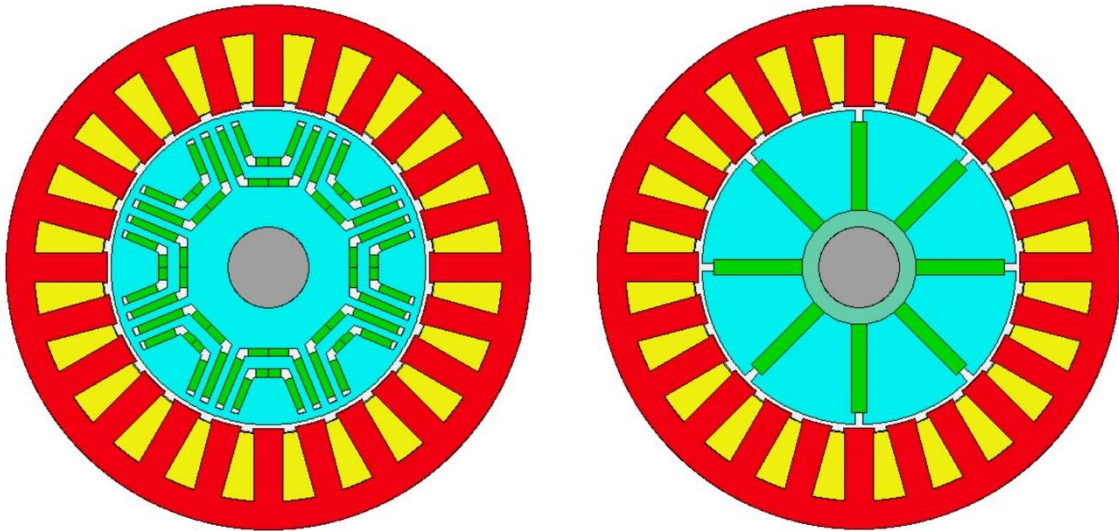
Interior flat (simple)



Interior V (web)



Interior V (simple)



Interior U-shape

Spoke

Figure 2.1 Variety of 8-pole, 24 slot IPM machines with different rotor geometries
(nomenclature for geometries based on those used in MOTORCAD)

2.1.2 Performance specification

The performance specifications of the IPM machine considered in this study are representative of a traction machine for a medium-sized, mass-market passenger vehicle, and are summarised in Table 2.1. This IPM machine adopted interior V shape permanent magnets and it will be used to provide the reference design for the ELLI research programme at the Advanced Manufacturing Research Centre for them to build the machine and a demonstrator electric drive-train will be developed to showcase novel manufacturing techniques [5]. This specification includes a flux weakening region beyond the base speed of 4,000 rpm up to the maximum speed of 12,000 rpm. From a design point of view, this field-weakening region impacts on the need to ensure there is sufficient electromagnetic capability to realise the extended speed range, e.g. the ratio of L_q to L_d , and to ensure that the rotor is sufficiently robust to operate at 12,000rpm, often with a predefined over-speed.

Table 2.1 Machine performance specifications.

Feature	Value
Rated power at base speed	100 kW
Base speed	4000 rpm
Maximum speed	12,000 rpm
Rated torque at base speed	239 Nm

2.2 IPM machine electrical and electromagnetic design

There are several major decisions which must be made in the early stages of the design of an IPM, starting with the rotor topology and pole number. Published design studies have shown that V-shaped IPM topologies tend to have superior performance compared to other IPM topologies, require less magnet volume and can withstand higher mechanical stresses [6]–[8].

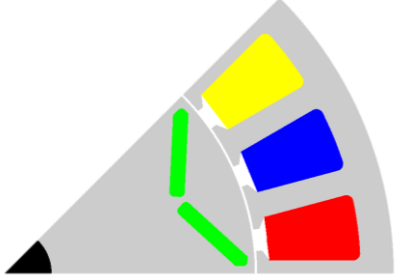
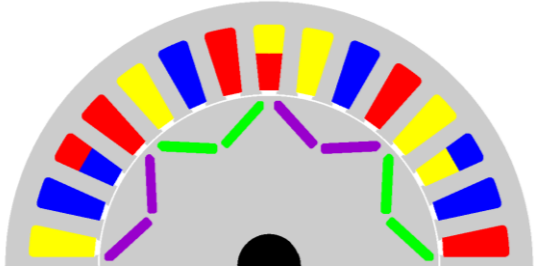

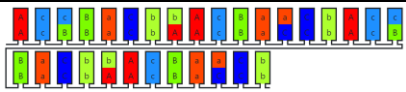
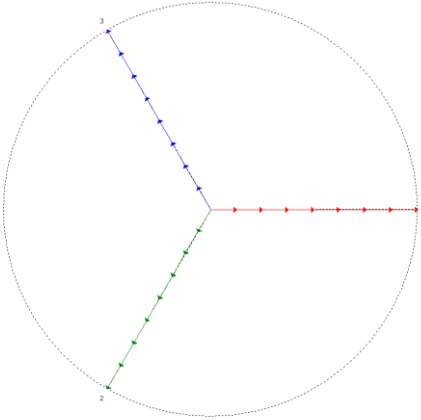
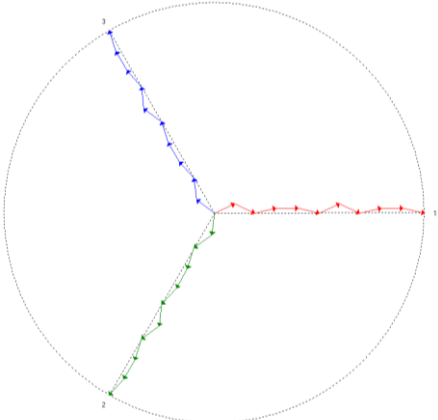
2.2.1 Initial sizing

The MOTORCAD package was used to explore various combinations of diameters and axial lengths to meet the performance specification of Table 2.1. A series of different pole numbers were explored and the best designs in terms of power density and efficiency were obtained with an 8-pole rotor. This was initially based on simple integer slot distributed winding, with 24 slots for 8 pole cases. The first baseline design had a 135mm diameter rotor and a 210 mm stator outer diameter. The axial length of 174 mm was calculated by scaling the 2D finite element predicted torque per unit length to meet the torque specification. The full details of this initial 24 slot / 8 pole design are summarised in Table 2.2.

2.2.2 Alternative winding configurations

As noted above, the initial sizing was performed for a simple 24 slot, 8-pole integer slot winding. As will be shown in this chapter, this combination results in high levels of cogging torque, significant harmonic content in the back-emf, both of which combine to produce a large torque ripple. Alternative slot numbers and winding arrangements were considered in an attempt to reduce the torque ripple while not compromising the torque and power. The other winding arrangement which was identified from options in MOTORCAD was a fractional slot distributed winding with 30 slots and 8 poles. These two IPM winding designs have been compared using the same rotor diameter of 135 mm and stator outer diameter of 210 mm. The V-shaped PM magnet rotors were identical and the airgap was fixed at 0.5 mm. The comparison was done at the 100 kW / 4,000 rpm operating point with stator rms current density of 10 A/mm² (at an assumed slot fill factor of 0.45). The details of both designs are summarised in Table 2.2. In the case of the 30 slot / 8 pole combination, the axial length of 170 mm was also established by scaling the axial length using the 2D calculated torque per unit length to meet the torque specification.

Table 2.2 Details of two studied IPM machine

	24 slots, 8 poles	30 slots, 8 poles
Layout		
Rotor diameter	135mm	135mm
Stator diameter	210mm	210mm
Axial length	174.4 mm	170 mm
Peak current	296.0 A	218.4 A
Slot area (per slot)	372.1 mm ²	274.6 mm ²
Slot area (total for machine)	8930 mm ²	8238 mm ²
Slot fill factor	0.45	0.45
Turns per slot	8	8
Current density	10 A/mm ² rms	10 A/mm ² rms
Winding layout		
Connection	Three-phase star	Three-phase star
Winding factor	1.00	0.951
Winding phasor diagram		

2.2.3 Calculation of open-circuit phase back-emf

The open circuit phase back emf was calculated for both machine designs at the rated base speed of 4,000 rpm. The phase to star-point emfs and the corresponding harmonic spectra are shown in Figure 2.2 and Figure 2.3. As can be seen, the 24-slot design has a higher peak voltage than the 30-slot design but also has more harmonic content so that the fundamental component of the 30 slot design is 336 V compared to 263 V for the 24 pole design.

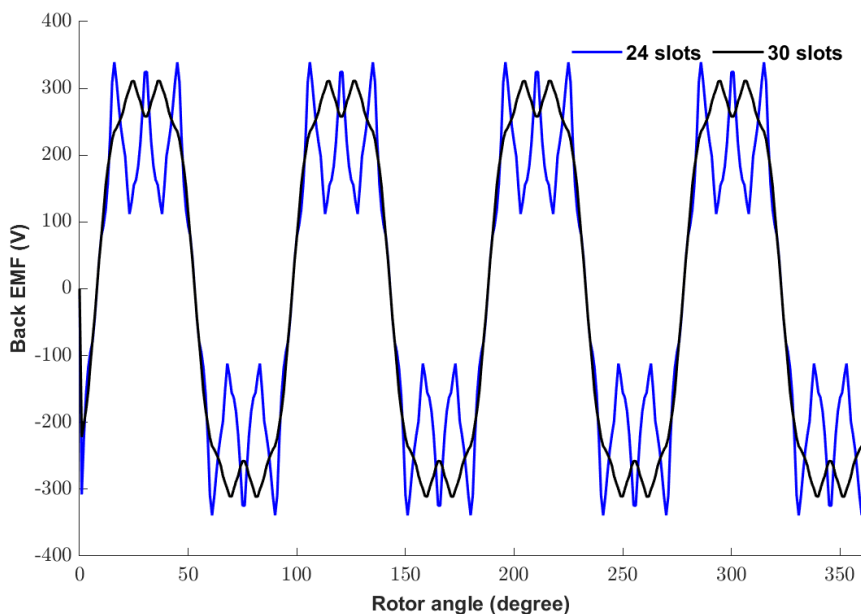


Figure 2.2 24 slots and 30 slot IPM machine back EMF under 4000 rpm, no load condition

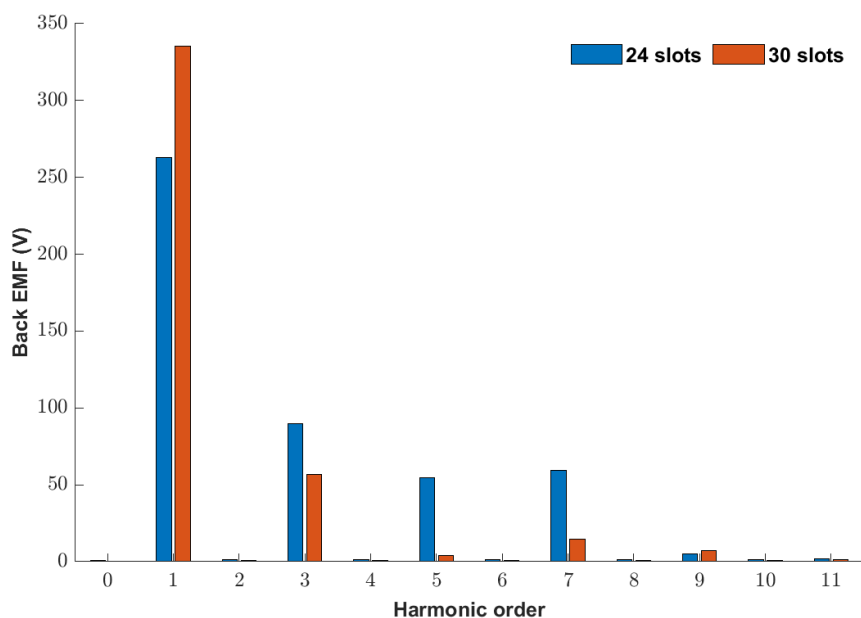


Figure 2.3 24 slots and 30 slot IPM machine FFT analysis for back EMF under 4000 rpm, no load condition

2.2.4 Cogging torque

The open-circuit cogging torque was calculated from a series of open-circuit finite element calculations. The resulting cogging torque waveforms over one mechanical rotation for the 24 slot and 30 slot designs are shown in Figure 2.4. As will be seen, the 24 slot design has much higher cogging torque with a peak of 24.8 Nm, which is ~40 times higher than the 0.64Nm peak of the 30 slot machine.

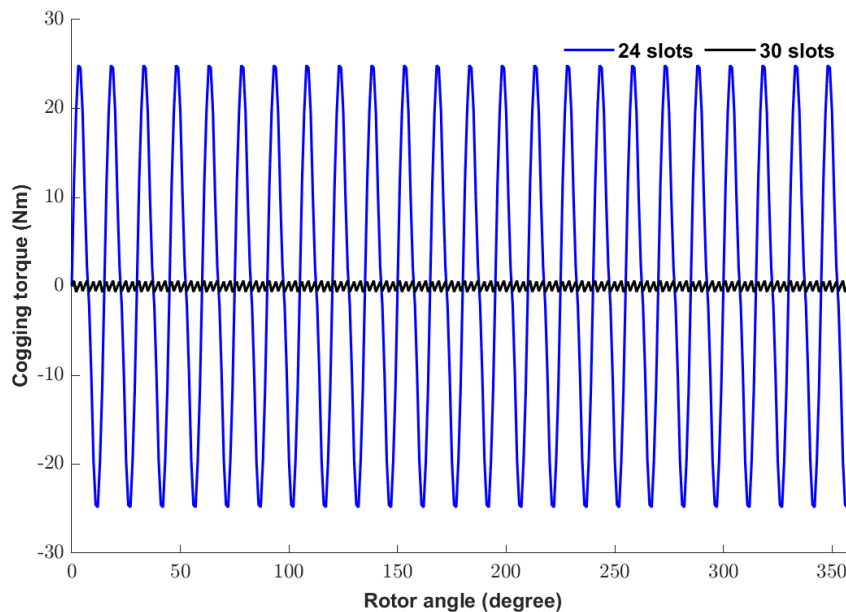


Figure 2.4 24 slots and 30 slot IPM machine design open-circuit cogging torque

2.2.5 Torque performance

The electromagnetic torque produced per unit length for these two machines at an rms current density of 10 A/mm² rms was calculated from 2D magnetostatic finite element simulation and the axial lengths scaled to produce the rated torque of 239 Nm, which corresponds to a power of 100 kW at the base speed of 4,000rpm. The torque waveforms for these two designs are shown in Figure 2.5. For 24 slot / 8 pole design, the maximum and minimum torque amplitude are 285.8 Nm and 207.4 Nm, yielding a torque ripple of 78.4 Nm. In the case of the 30 slot / 8 pole design, the maximum and minimum torque amplitudes are 251.0 Nm and 224.4 Nm giving a torque ripple of 26.6 Nm, which is ~1/3 of the torque ripple of the 24 slot/ 8 pole design. It also has a slightly lower copper loss at rated torque due to the reduced copper volume operating at the same current density.

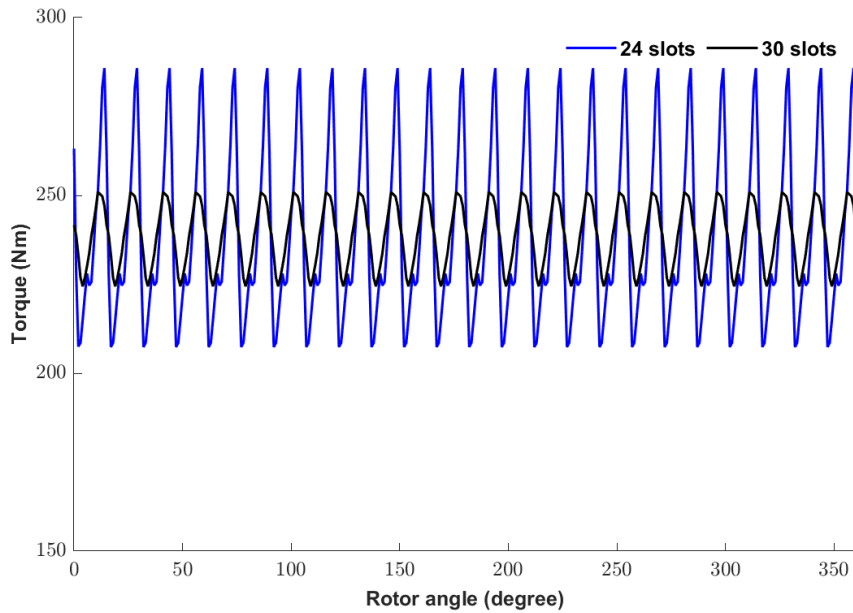


Figure 2.5 Finite element predicted torque waveform for 24 slot and 30 slot IPM machines with 8 poles and geometries detailed in Table 2.2

Because of its slightly higher torque density, lower loss and greatly reduced torque ripple, the 30 slot / 8 pole design was selected as the preferred baseline design to take forward for optimisation.

2.3 Combined mechanical and electromagnetic optimisation of 30 slot / 8 pole IPM machine

The baseline 30 slot/ 8 pole design with a rotor outer diameter of 135mm was taken as the baseline design for the combined electromagnetic and mechanical optimization. The aim of this optimization it to maximise the torque density of the machine while remaining within limits on rotor mechanical stress. An operating current density of 10 A/mm² rms and a coil packing factor were kept fixed during this optimization.

2.3.1 Baseline machine dimensions and performance

The rotor geometry adopted is the single-layer V-shaped arrangement of magnets shown in Figure 2.6. The individual geometry of the magnet pieces is profiled at their outer edges, as shown in Figure 2.7. This profiling was included to reduce mechanical stress concentrations in the surrounding rotor core. It is recognized that this shaping of the magnets has cost implications, but as shown later in this chapter, this profiling yields dividends in terms of allowing the rotor core to be shaped to reduce leakage flux within the rotor, in turn enhancing torque. The baseline machine design has an 8-pole rotor and a 30-slot stator core, which is

equipped with a fractional slot winding with the coil arrangement shown in Table 2.2. The stator and rotor core are NO20 silicon-iron, and the rotor permanent magnets are 35MGOe NdFeB grade with a room temperature remanence of 1.22 T.

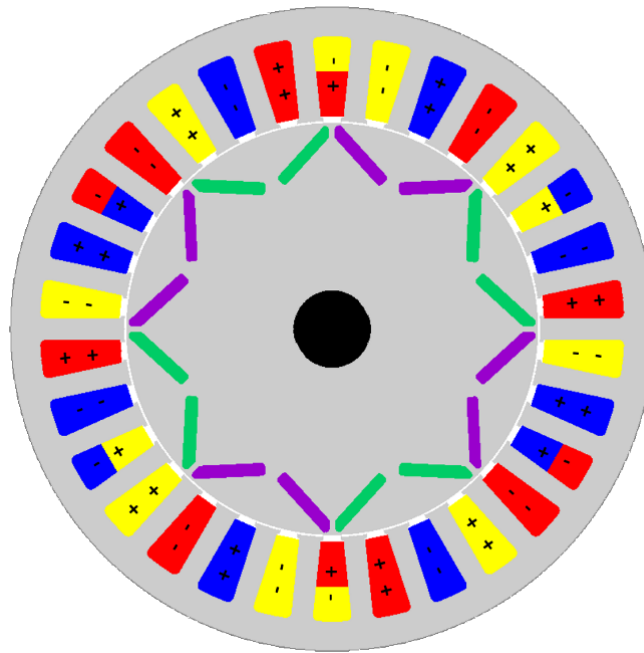


Figure 2.6. Cross-section through the baseline IPM machine.

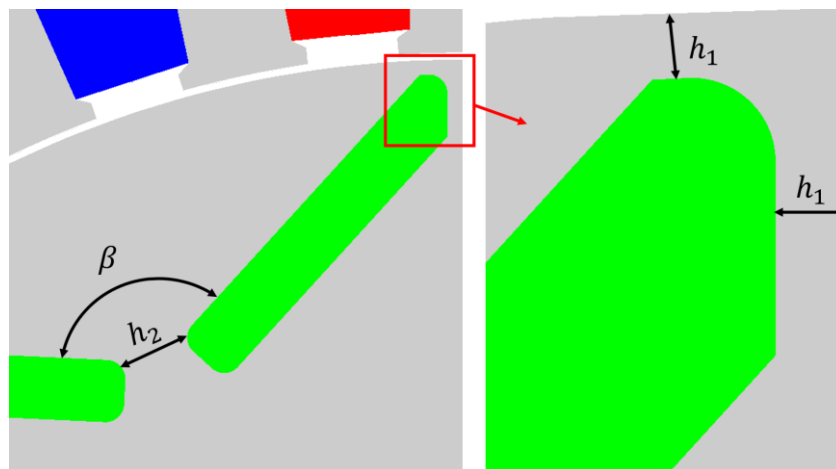


Figure 2.7 Key dimensions around the individual magnet poles.

The baseline starting design has a rotor outer diameter of 135mm. As part of the optimisation, the machine cross-section in Figure 2.6 was scaled for various rotor diameters in a systematic manner, which maintains the proportions shown in Figure 2.6. Table 2.3 shows the leading dimensions of the machine normalized by the rotor outer diameter. The normalized dimensions shown correspond to a so-called split ratio [9] of 0.64, i.e., the ratio of the rotor outer diameter to the stator outer diameter.

Table 2.3 Main machine dimensions normalized by rotor outer diameter.

Feature	Value
Rotor outer diameter	1.000
Stator outer diameter	1.556
Magnet thickness (in direction of magnetization)	0.0296
Stator tooth body width	0.0504
Shaft diameter	0.185

In all cases, the stator tooth spans an angle of 7° at the airgap, and the angle between the magnets that make up one pole (defined as β in Figure 2) is 130° . The three radii on the magnet corners shown in Figure 2.7 are set to 1 mm for the 135 mm diameter machine and then scaled in accordance with the method for other machine dimensions, with a maximum radius of 1.3 mm in the case of the 180 mm diameter rotor. The only modification to a pure scaling of the machine cross-section with the rotor diameter is a small adjustment to the stator bore diameter to maintain the same 0.5 mm mechanical airgap in all designs.

2.2.2 Material properties and mechanical properties

The microstructure and processing of most electrical steels are optimized almost entirely to achieve the highest magnetic functional properties. As a result, the mechanical properties of electrical steels tend to be modest in comparison to those of steels or other alloys optimized solely for mechanical behaviour. There are often multiple grades within the product range of a given manufacturer, and they offer some trade-off between mechanical and magnetic properties [10]. Although, in principle, this offers the opportunity to employ different grades of electrical steels in the rotor and stator cores, the utilization of electrical steels is generally poor when a single-piece stator alone is taken out of the starting strip of the material, with the region within the bore of the stator core being discarded as scrap. Improved utilization of the starting strip can be realized by taking out the rotor core from within the bore of the stator core. This may result in the use of a grade of electrical steel for the rotor core that has some trade-off in mechanical and magnetic properties to balance the different demands of the stator and rotor cores.

This study is based on NO20-1200H core material, which is a specific grade of 0.2 mm thick, non-oriented silicon-iron. This is not a grade developed specifically for its mechanical properties, but by virtue of being 0.2 mm thick, it is often adopted as a mainstream option for the stators of higher-speed machines. The manufacturer quoted that the minimum 0.2% yield

strength is 400 MPa in the rolling direction, which increases by ~2% in the transverse direction. One important consideration is the margin adopted between the design stress limit and the material yield stress. Setting this margin requires consideration of factors such as fatigue, temperature cycling and aging effects. Typically, a design stress limit of 50–60% of the manufacture-quoted yield strength would be adopted, although with extensive in-service experience and operational data, this percentage might be increased. Adopting a design stress limit that is 60% of the 0.2% yield strength of NO20 gives rise to a design stress of 240 MPa for this optimization study. The key mechanical properties adopted for the NO20 rotor core and the NdFeB rotor magnets are summarized in Table 2.4.

Table 2.4 Rotor material mechanical properties.

Feature	NO20-1200H	NdFeB
Strength	400 MPa (0.2% Yield)	80 MPa (UTS)
Young's modulus	205 GPa	160 GPa
Poisson's ratio	0.3	0.3
Density	7650 kg/m ³	7500 kg/m ³

2.3.3 Influence of interference fit of shaft

Interference fitting is widely used in powertrain components as a straightforward, reliable and low-cost means of securing shafts into hubs and cores [11]. The degree of interference employed must be carefully specified to ensure that the radial pressure exerted on the shaft by the rotor core is sufficient to transmit the electromagnetic torque. This condition must be met over the full speed and temperature range encountered in service and is usually set with a significant spare margin. However, setting the level of interference must also take account of the fact that the interference fit at the bore of the rotor core increase the stress in the remainder of the rotor core. Hence, it is important not to over-specify the interference.

A useful estimate of the minimum interference required between the shaft and the rotor core can be established from a simplified model in which the rotor is represented as a solid annulus of uniform density. For a rotating solid annulus representation of the rotor core with outer radius r_{co} and inner radius r_{ci} , the radial growth at the inner radius for a rotor of density ρ , Young's modulus E and Poisson's ratio ν when rotating at an angular velocity of ω is given by Equation (2.1) from [12]. For the smallest and largest NO20 rotor cores considered in this study, viz., 120 mm and 180 mm outer diameters, the predicted radial growths of a bore that

accommodates a 25 mm shaft are 2.2 μm and 4.9 μm , respectively, at a rated speed of 12,000 rpm.

$$\Delta r_{ci} = \frac{\rho\omega^2 r_{ci}}{4E} ((3 + \nu)r_{co}^2 + (1 - \nu)r_{ci}^2) \quad (2.1)$$

Similarly for the shaft, the change in its outer radius when rotating at an angular velocity of ω is given by

$$\Delta r_{so} = \frac{\rho\omega^2 r_{so}}{4E} ((1 - \nu)r_{so}^2) \quad (2.2)$$

For a 25 mm diameter steel shaft (with a modulus of 200 GPa and a density of 7800 kg/m³), the resulting radial growth at 12,000 rpm is a mere 0.02 μm . The difference in radial growth between the shaft and the bore of the rotor core in effect reduces the net interference at the maximum speed from the interference set at standstill. The interference at standstill must be sufficient to accommodate the differential radial growth of the rotor core while still maintaining sufficient inward radial pressure on the shaft to transmit the rated torque with an appropriate safety margin. A well-established method for calculating the contact pressure and resulting hoop stresses between interfering concentric cylinders is given in [11]. For the case of a solid shaft, the interference, δ_i , required to achieve a contact pressure between the shaft and the rotor core of P_i is given from [11] by

$$\delta_i = P_i r_{ci} \left(\frac{r_{ci}^2(-1 + \nu_c)}{E_c(-r_{co}^2 + r_{ci}^2)} + \frac{r_{co}^2(1 + \nu_c)}{E_c(r_{co}^2 - r_{ci}^2)} - \frac{r_{ci}^2(-1 + \nu_s)}{E_s r_{ci}^2} \right) \quad (2.3)$$

Taking the case of a 180 mm outer diameter rotor and assuming, for the time being, an axial length of 100 mm (an estimate of which can be obtained on an a priori basis for simple torque-sizing equations), the radial pressure required to transmit the rated torque of 239 Nm assuming a worst-case coefficient of friction of 0.2 between the shaft and the core is 12.2 MPa. This, in turn, requires a minimum net radial interference of 1.5 μm at the maximum speed, which, in turn, requires a standstill interference of 6.4 μm to allow for the 4.9 μm radial growth at 12,000 rpm. Allowing a safety factor of 2 on the interference yields a diametrical interference of 25 μm . This, in turn, generates a maximum radial pressure of 99.7 MPa at standstill. The resulting hoop stress in the rotor core at the inner bore is hence given by

$$\sigma_{\theta,core} = \frac{P_i(r_{co}^2 + r_{ci}^2)}{r_{co}^2 - r_{ci}^2} \quad (2.4)$$

This results in a maximum hoop stress within the core at standstill of 103.6 MPa, which is well within the material design limit. Although cautious in terms of the safety margin on the

interference required to transmit the torque, a diametrical interference of 25 μm between the core and the shaft is fixed for the remainder of this investigation.

2.3.4 Rotor design and Optimal ratio

Structural finite element calculations were performed using a linear elastic model (i.e., fixed modulus) within the ANSYS environment. The contact faces between the individual magnet pieces and the rotor core were represented as frictional contacts with a coefficient of friction of 0.2. A very light interference fit between the magnet and rotor core of 2 μm was employed, and the interference fit between the rotor core and the shaft was set to 25 μm for all rotor diameter combinations.

A series of rotor outer diameters between 120 mm and 180 mm (in 15 mm increments) were considered. For each rotor diameter, a total of 154 designs were modelled comprising all-inclusive combinations of designs with h_1 values from 0.4 mm to 2.5 mm in 0.1 mm steps and h_2 values from 0.8 mm to 2 mm in 0.2 mm steps. An example of the resulting von Mises stress distribution in the vicinity of the rotor magnets is shown in Figure 2.8; this case is a 135 mm diameter rotor at a maximum speed of 12,000 rpm with $h_1 = 2$ mm and $h_2 = 1$ mm. Although much of the rotor operates at stress levels below 50 MPa, as would be expected, there are regions of stress concentration at the outer tips of the magnets and in the gap between the innermost regions of the magnets. In this case, the peak localized stress is 230 MPa, which is just within the design stress limit of 240 MPa set for the NO20 rotor material.

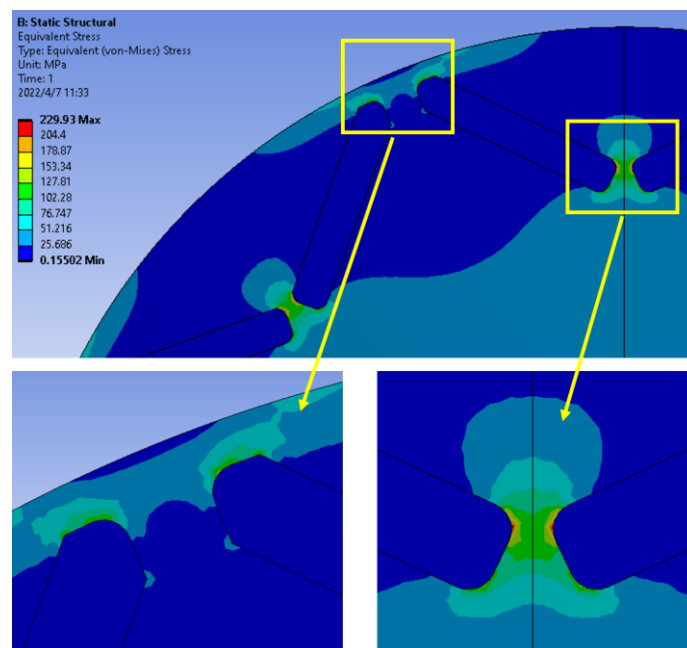


Figure 2.8 IPM von Mises stress distribution for a 135 mm diameter rotor at 12,000 rpm ($h_1 = 2$ mm; $h_2 = 1$ mm).

Taking again the example of the 135 mm diameter rotor, the variation in the maximum predicted localized stress at 12,000 rpm as a function of h_1 and h_2 for the 154 designs considered is shown in Figure 2.9. In this case, 40 combinations of h_1 and h_2 result in localized stress levels greater than the 240 MPa design stress limit set for this study.

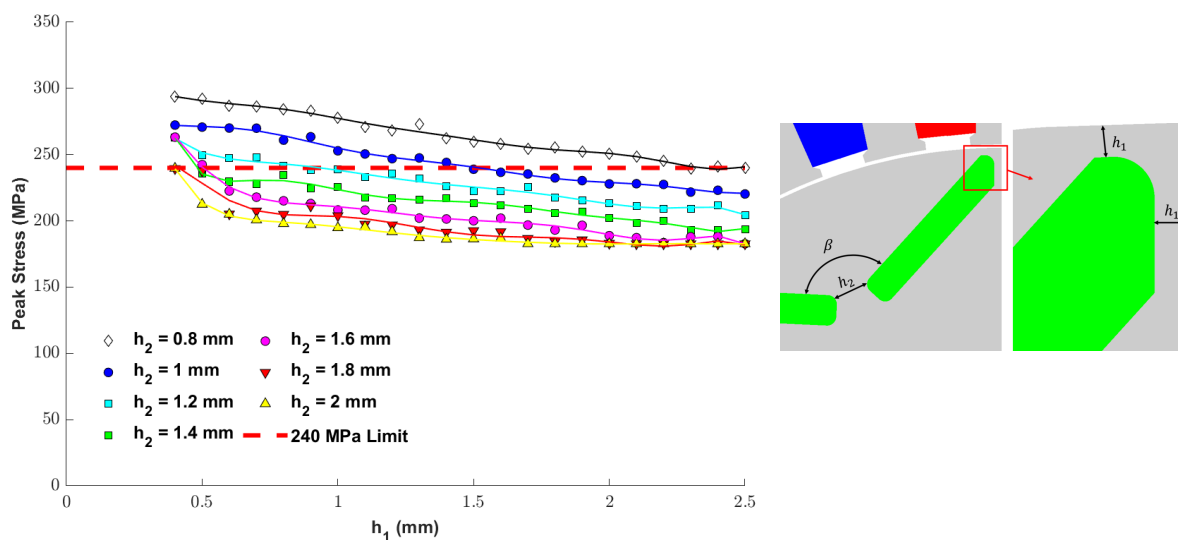


Figure 2.9 Variation in peak localized stress in a series of 135 mm outer diameter rotor designs at 12,000 rpm (core-to-shaft diametrical interference is 25 μ m in each case).

Having established the combinations of h_1 and h_2 that yield viable designs from a mechanical stress threshold perspective, the electromagnetic torque is calculated using a two-dimensional, magneto-static, non-linear finite element analysis for the specific case of a stator rms current density of 10 A/mm² (at an assumed slot fill factor of 0.45) with a current advance angle of 45° (electrical).

The resulting average torque per unit length values calculated for the 154 design combinations with a 135 mm diameter rotor are shown in Figure 5. Although 40 of these combinations are not viable mechanically, the torques that they produce are included to demonstrate the torque penalty that results from a design stress limit of 240 MPa. For this 135 mm diameter rotor, the highest predicted torque per unit length is 1498 Nm/m for the smallest combination of h_1 (0.4 mm) and h_2 (0.8 mm), although this results in a peak localized stress of 290 MPa. The highest predicted torque per unit length for a design that also results in a von Mises stress that falls within the design limit of 240 MPa is 1468 Nm/m, which is achieved for an h_1 value of 0.5 mm and an h_2 value of 1.4 mm. Scaling this torque per unit length to meet the torque specification set out in Table 2.1 yields an axial length of 162 mm for this rotor

diameter of 135 mm, in turn yielding a predicted mass for this design, including an estimate of end-winding mass of 50.6 kg, which corresponds to ~ 2 kW/kg.

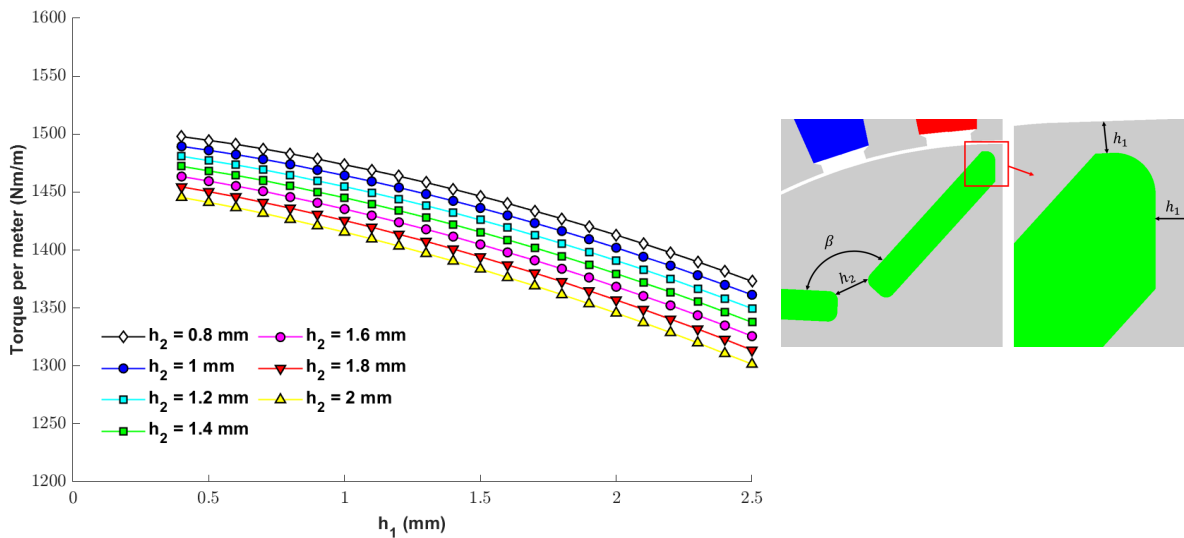


Figure 2.10 Variation in electromagnetic torque in a 135 mm diameter rotor for various combinations of h_1 and h_2

Repeating this process to establish the optimal designs for all the rotor outer diameters between 120 mm and 180 mm yields the series of designs summarized in Table 2.5, which exhibit the maximum torque per unit length within a peak design stress limit of 240 MPa at 12,000 rpm. The axial lengths of the stator and rotor cores of these designs are all scaled to produce a rated torque of 239 Nm at a stator rms current density of 10 A/mm² (at an assumed slot fill factor of 0.45).

Table 2.5 Optimized designs for different rotor diameters

	D120	D135	D150	D165	D180
h_1 (mm)	0.2	0.5	0.7	1.2	3.2
h_2 (mm)	0.7	1.4	2.9	4.6	6.9
Core axial length (mm)	224	162	125	103	99
Rotor volume (dm ³)	2.87	2.32	2.21	2.20	2.52
Machine mass (kg)	60.5	50.6	44.9	42.3	46.3
Torque density (Nm/kg)	3.93	4.70	5.30	5.63	5.14
Power density (kW/kg) at 4,000rpm	1.65	1.97	2.22	2.36	2.15

As would be expected, increasing the rotor diameter beyond 120 mm requires larger values of h_1 and h_2 to maintain the localized stress within the rotor below the 240 MPa limit.

Thickening up the rotor core beyond the end of the magnets tends to promote increased leakage flux within the rotor. It is apparent from the results presented in Table 2.5 that there is an optimum rotor diameter of 165 mm, albeit that this is specific to this combination of rotational speed, rotor core maximum stress limit, machine split ratio and current density constraints. Without mechanical stress considerations, the torque density tends to continually increase with increasing rotor diameter because of the nature of scaling with the diameter of the electric loading (Ampere turns per unit of airgap periphery). There is a further tendency for the predicted torque density to increase with diameter due to the limitations of two-dimensional finite element modelling. A two-dimensional finite element electromagnetic analysis does not account for the influence of end effects in short-axial-length machines and, hence, tends to overestimate the torque produced by machines with short axial lengths relative to diameters. The presence of an optimum in Table 2.5 is a consequence of the electromagnetic penalty, which is increasingly incurred with the need to thicken up the regions of the rotor core adjacent to the airgap to ensure that the entire rotor core remains with the specified design mechanical stress.

Figure 2.11 shows a predicted flux density distribution in the rotor and stator cores of this 165 mm diameter design at the rated torque, while Figure 2.12 shows a close-up of the von Mises stress distribution in the region around the magnet poles at 12,000 rpm. As is apparent, there is significant magnetic saturation both in regions adjacent to the airgap near the magnet tips and in the regions between the pair of magnets that make up one pole, with peak flux densities of up to ~ 3.4 T. This saturation plays an important role in limiting the magnet leakage flux within the rotor core, which would otherwise further diminish the airgap flux density. This illustrates the importance of modeling the behavior beyond saturation accurately, as this can have a significant bearing on torque in this machine, even at modest electric loading. In this regard, the representation of the magnetization characteristics is best suited to a semi-analytical model in which saturation is enforced mathematically rather than extrapolated from a series of discrete data points.

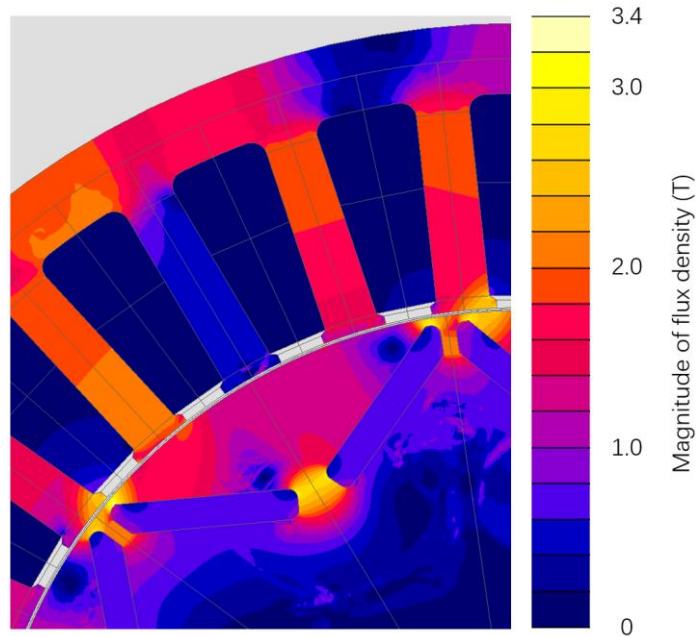


Figure 2.11 Predicted flux density distribution for the 165 mm design in Table 4

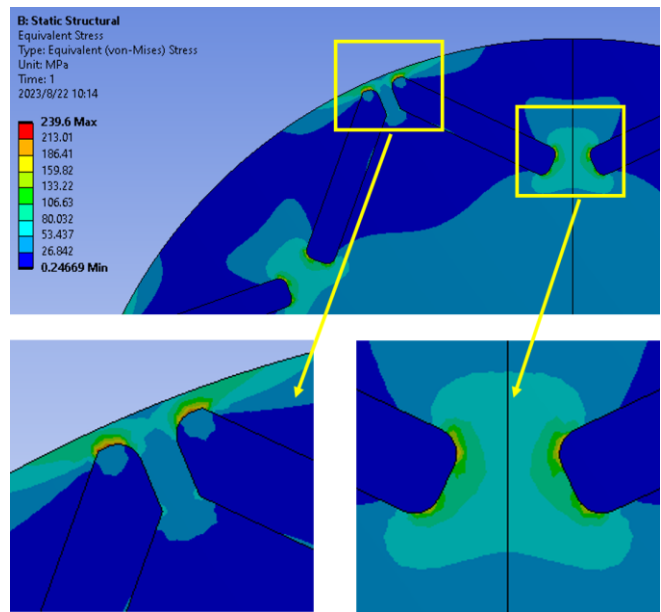


Figure 2.12 Predicted von Mises stress distribution for the 165 mm design in Table 4

2.3.5 Influence of hub diameter

The rotor designs considered up to this point are all based on scaling the cross-section of the rotor according to a fixed shaft-to-rotor diameter ratio of 0.185. This results in a range of shaft diameters between 22.2 mm and 33.3 mm for the range of rotor outer diameters considered. The remainder of the rotor cross-section is occupied entirely by the rotor core and magnets. From an electromagnetic point of view, much of the inner regions of the rotor need not be magnetic, and, indeed, the nature of the field distribution with an IPM is such that this large region of core within the magnets can promote leakage flux. Hence, employing a non-

magnetic and lightweight hub to span the region between the shaft and a slimmed down rotor core will yield dividends in terms of a reduced mass, and it may also yield some electromagnetic benefits. Taking the 165 mm rotor diameter design in Table 2.5, which offers the highest torque density of all the rotor diameters considered, a series of electromagnetic finite element predictions of average torque are performed with gradually increasing diameter of the non-magnetic hub radius, which, in electromagnetic terms, increases the bore diameter of the rotor core. The non-magnetic hub diameter is limited by the presence of the V-shaped arrangement of the magnets. For the particular arrangement adopted, the inner edges of the magnets are at a diameter of 122 mm for a 165 mm rotor outer diameter.

The resulting variation in the predicted torque with hub diameter is shown in Figure 2.13; all cases have the same rotor axial length of 103 mm. As is evident and indeed expected, over much of the range considered, the predicted torque remains unchanged from the 239 Nm predicted for the original shaft arrangement. However, as the hub diameter increases beyond 115 mm, the predicted torque starts to increase markedly, with a maximum value of 258 Nm at a rotor core inner diameter of 121 mm. The section of core inside the magnets acts a leakage path for a proportion of the magnet flux, and, hence, as this region is progressively thinned down as the hub diameter increases, this leakage path begins to magnetically saturate. Figure 2.14 shows the finite element predicted flux density distribution in the rotor at the rated current density for a hub diameter of 120 mm with the 165 mm diameter rotor. The nature of permanent magnet excitation is such that a magnet acts neither as a constant flux source nor a constant source of magneto-motive force. Hence, increasing the reluctance of the leakage path via saturation and a reduced cross-section tends to result in an increasing proportion of the magnet flux crossing the working airgap, hence promoting additional torque production. Hence, from an electromagnetic perspective, there is a meaningful benefit in increasing the hub diameter towards 122 mm. Furthermore, significant mass reductions could be realized if the hub was manufactured from a lightweight metal or composite and/or if features such as spokes or holes were incorporated. This finding provides a potential method to enhance the electromagnetic performance but also introduces several potential further work like decreasing the maximum rotating speed or using better materials with higher yield strength to allow higher hub diameter which would be beneficial electromagnetic properties of the machine.

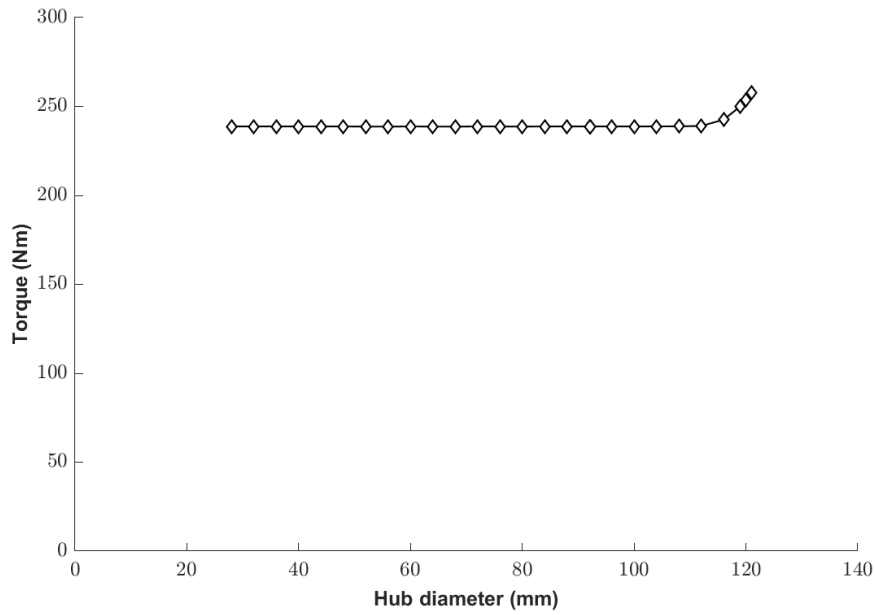


Figure 2.13 Predicted torque for a 165mm diameter rotor as a function of rotor core inner diameter at a current density of 10 A/mm² rms (slot fill factor of 0.45)

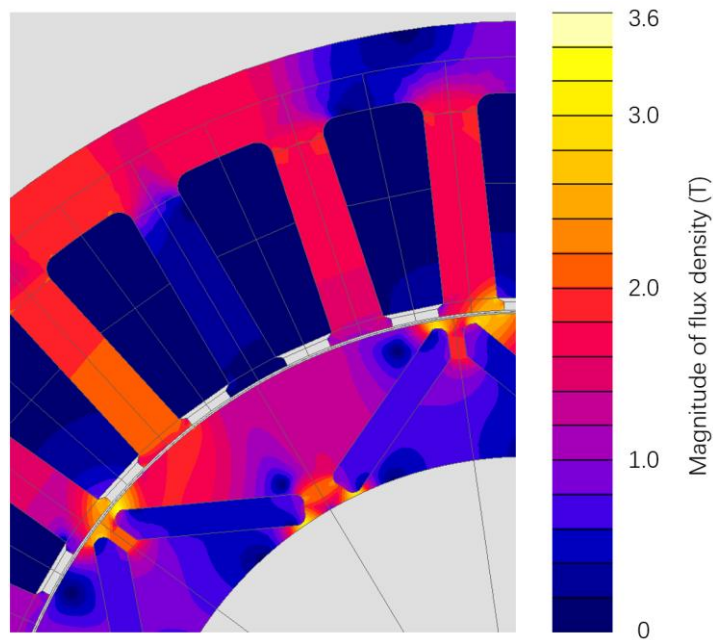


Figure 2.14. Finite element predicted flux density distribution in a 165mm diameter rotor with a shaft diameter of 120mm at full load torque of 253Nm.

However, alongside these electromagnetic and mass considerations, it is necessary to establish the mechanical stress implications of increasing the hub diameter. In the general analytical expressions of the stress in a rotating ring, the hoop stress at the outer edge of the ring of a given outer diameter increases as the bore diameter is increased. Hence, it is to be expected that the hoop stress in the magnet bridge regions of the rotor core will further increase as the bore diameter is increased.

Figure 2.15 shows the predicted peak stress at 12,000 rpm in the 165 mm diameter rotor, which has the optimum values of h_1 and h_2 in Table 4 as a function of the hub diameter. As is apparent, there is the expected increase in the peak stress as the hub diameter is increased. Since the original design with a shaft diameter of 30.5 mm is just under the limiting design stress of 240 MPa, it is to be expected that almost all designs with a larger hub diameter will exceed the stress limit. The calculated stress in Figure 2.15 is shown at four different shaft-to-rotor-core interference levels, from the original 25 μm up to 60 μm . Since the radial growth of the core increases as the hub diameter is increased, there is an upper limit on the hub diameter for a given interference, beyond which the rotor core separates from the hub; e.g., for the original 25 μm , the rotor core lifts off the hub at 12,000 rpm for shaft diameters greater than ~ 58 mm. Even if the stress could be accommodated for in the 165 mm diameter rotor, it would be necessary to increase the interference to at least 35 μm . This additional interference would further exacerbate the stress levels in the rotor core.

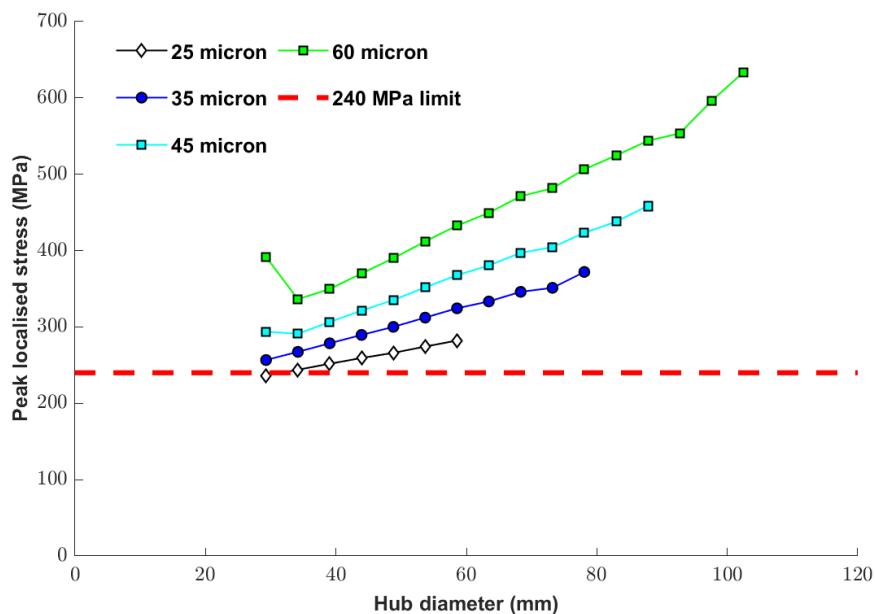


Figure 2.15 Variation in the finite element predicted peak localised stress in the 165 mm diameter rotor core at 12,000 rpm as a function of hub diameter for different diametrical interference fits from 25 μm to 60 μm (240 MPa design stress limit shown as dashed line)

Although almost all the rotor designs in Figure 2.15 exceed the design stress limit at 240 MPa, it is possible to calculate the limiting speed for each design for an imposed peak stress of 240 MPa. Figure 2.16 shows the resulting calculated variations in the maximum rotational speed as a function of the hub diameter and interference for a 165 mm diameter rotor.

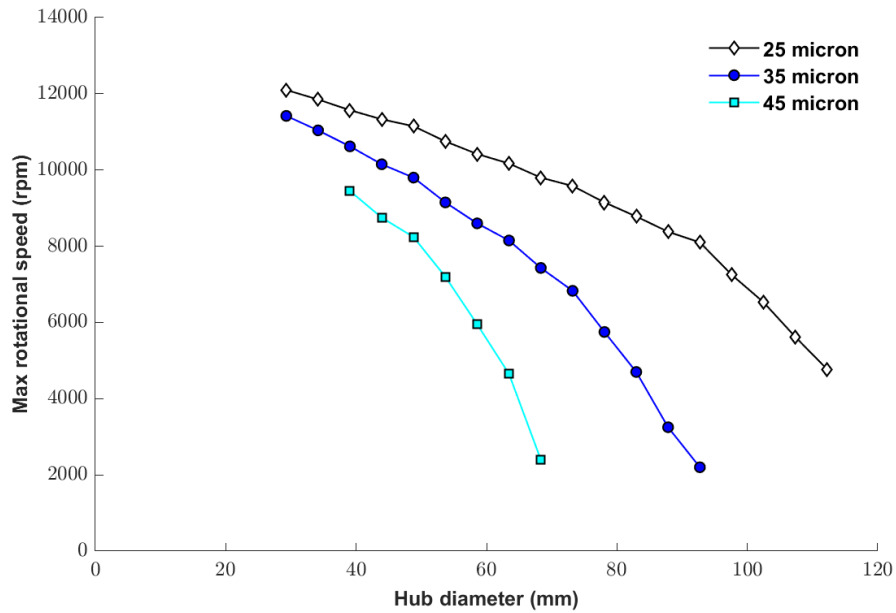


Figure 2.16 Variation in the maximum allowable speed for a 165 mm diameter rotor core to remain within a 240 MPa design stress limit for four levels of interference

The predicted von Mises stress distribution in the rotor is shown in the close-up in Figure 2.17 for the particular case of a hub diameter of 78 mm with an initial interference of 35 μm , from which it can be seen that the problem region is again in the bridge regions near the ends of the individual magnet pieces.

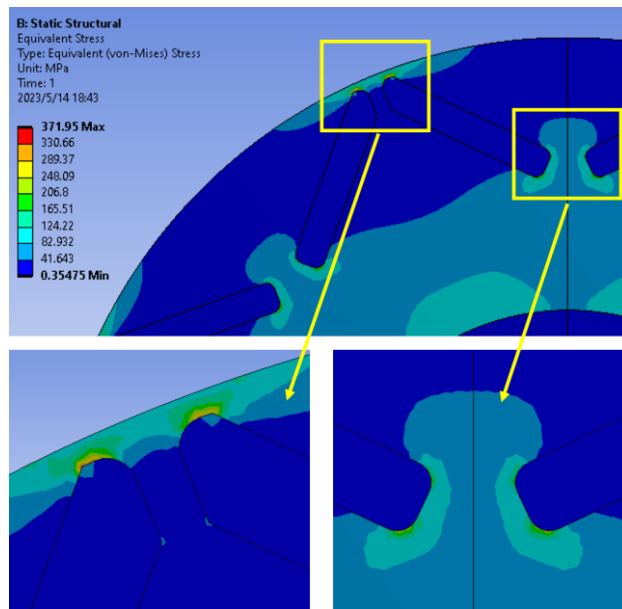


Figure 2.17 Close-up of finite element predicted peak stress distribution in the 165 mm diameter rotor core at 12,000 rpm for a hub diameter of 78 mm

2.3.6 Influence of magnet shape

The analyses performed up to this point considered magnet poles with profiled detailing at the ends. It was noted earlier in this paper that this profiling was incorporated in an attempt to minimize the localized stress concentrations near the outer edges of the magnets while also minimizing flux leakage. However, this intricate detailing will inevitably increase manufacturing cost and slightly reduce magnet utilization unless the detailing is incorporated through a near-net-shape process. To quantify the performance dividend of incorporating this detailing, a series of further mechanical finite element calculations were performed for a 165 mm diameter rotor with plain rectangular blocks of magnets with the two different rotor core apertures shown in Figure 2.18. In both cases, the magnet was simply truncated at the ends of the parallel section of the original magnet profile. In the first case shown in Figure 2.18a, the region previously occupied by the profiled end of the magnet was simply filled by extending the rotor core into this region. In the second variant in Figure 2.18b, the same region was filled with a non-magnetic filler material, which in practice would be a fibre-loaded epoxy resin or putty, such as HysolEM 300T-KL or Dolphon CV-1108. In both cases, the same 30.5 mm diameter shaft as in the original design in Figure 2.6 was used, and the optimal combination of h_1 and h_2 in Table 2.5 was adopted. The mechanical properties of the non-magnetic filler used in the rotor in Figure 2.18b will have some influence on the overall stress distribution within the rotor core. To cover the likely range of physical properties exhibited by various loaded resins and putties, a series of simulations were performed assuming that the non-magnetic filler was assigned inclusive combinations of elastic moduli between 2 GPa and 8 GPa and densities between 1200 and 1800 kg/m³. The resulting range of stresses for these different combination of non-magnetic filler properties was rather narrow, with, as expected, the marginally lowest stress of 245 MPa encountered with the lowest density and highest modulus filler and the highest stress of 261 MPa for the highest density and lowest filler.

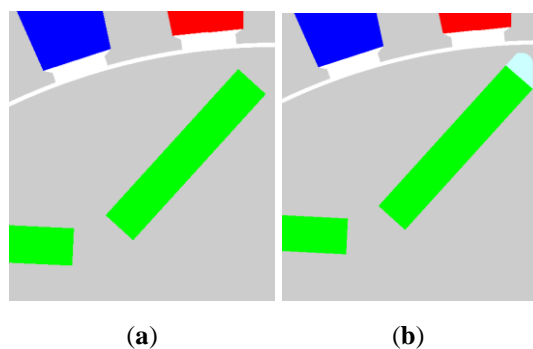
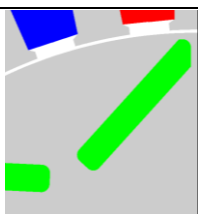
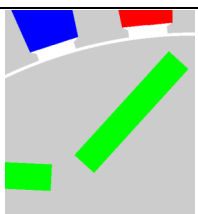
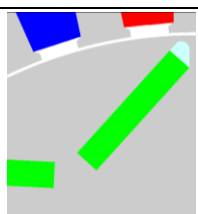


Figure 2.18 Alternative arrangement of magnet poles. **(a)**. Void from profiled end incorporated into rotor core. **(b)**. Void from profiled end filled with non-magnetic filler.

The resulting comparison of the predicted electromagnetic torque between the profiled magnet in Figure 2.6 and the various rectangular magnets is summarized in Table 2.6 for the case of a shaft sized according to the scaling factor in Table 2.3 and a diametric interference fit of 25 μm . As is apparent, the profiled magnet geometry in Figure 2.6 has the highest predicted torque with a particularly notable advantage over the magnet arrangement in Figure 2.18a.

Table 2.6 Comparison of predicted electromagnetic torque and maximum localized stress for different magnet profiles.

	Magnet in Figure 2.6	Magnet in Figure 2.18a	Magnet in Figure 2.18b
			
Torque (Nm)	239	213	230
Maximum stress at 12,000 rpm (MPa)	240	229	245–261 *

*—range for combinations of different filler materials modelled.

However, the arrangement in Figure 2.18a simply replaces the profiled end of the magnet with additional rotor core material, leaving the rectangular magnet at the same location as the rectangular region of the profiled magnet. This inevitably increases flux leakage within the rotor but also serves to reduce the stress in the rotor core due a thickening of the bridging regions. Hence, a more meaningful comparison can be achieved by displacing the rectangular magnet outwards towards the rotor surface, as shown in Figure 2.19. This tends to reduce the leakage flux within the rotor at the outer edge at the expense of an increased localized mechanical stress. To this end, the rectangular magnet in Figure 2.18a is progressively moved outwards while maintaining the same value of β (defined previously in Figure 2.7) until the same peak stress of 240 MPa is achieved.

The dimensions of the magnet piece itself remain fixed. The resulting rotor geometry is shown in Figure 2.19, with the magnet moved 1.06 mm along the line shown. This rotor design has an electromagnetic torque of 205 Nm, which is lower than the original rectangular magnet block design in Figure 2.18a. Although displacing the same magnet block outwards derives some benefits in terms of reducing flux leakage through the bridge regions of the rotor core

near the airgap, it does result in an increase in the separation at the inner edges of the two magnets that make up a pole, i.e., the equivalent of dimension h_2 in Figure 2.7. The additional leakage flux through this wider region more than offsets the reduced flux leakage through the outer bridge regions, thus reducing the overall torque.

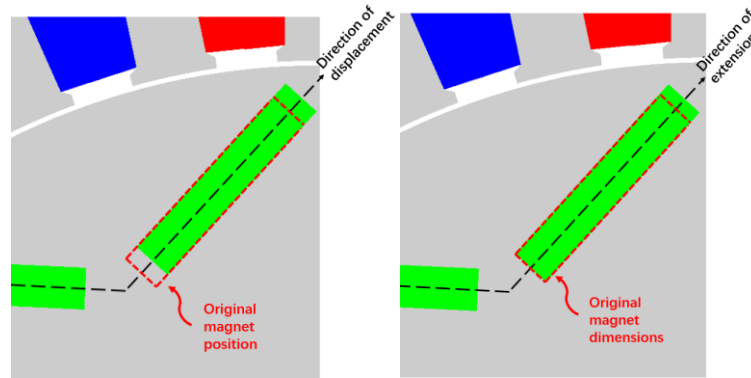


Figure 2.19 Close-up of rectangular magnet blocks showing the direction of displacement and extension from the original magnet position

In an attempt to improve the performance of rotors with plain rectangular magnet blocks, the separation at the inner edges of the two magnets that make up a pole, i.e., the equivalent of dimension h_2 in Figure 2.7, is maintained at its original value of 4.6 mm, and the magnet is simply extended into the region near the outer surface rather than displacing the fixed magnet size. This extension to the rectangular magnet block increases its mass, and, hence, it would be expected that the amount of extension that can be applied before reaching the 240 MPa design stress limit will be less than the displacement of 1.06 mm established previously with the fixed magnet size. For the same stress limit of 240 MPa, the magnet can be extended in the direction shown by 0.53 mm. Figures 2.20 and 2.21 show the finite element predicted flux density distribution and von Mises stress distribution at 12,000 rpm for this case of an extended rectangular magnet block, respectively. This extension of the magnet block results in an electromagnetic torque of 218 Nm, which is still 21 Nm short of the 239 Nm achieved by the profiled magnets in Figure 2.6. Hence, the intricate detailing around the edge of the profiled magnets in Figure 2.6 results in a ~10% higher torque on a like-for-like basis compared to a plain rectangular block. Bringing the design with the rectangular blocks up to the same torque rating could be achieved with a 10% increase in the stack length and, hence, the mass of the active materials. Further detailed cost modelling would be required to establish whether, in volume production, the intricately profiled magnet could be manufactured within the cost saving margin associated with the 10% reduction in the volume of the active material required.

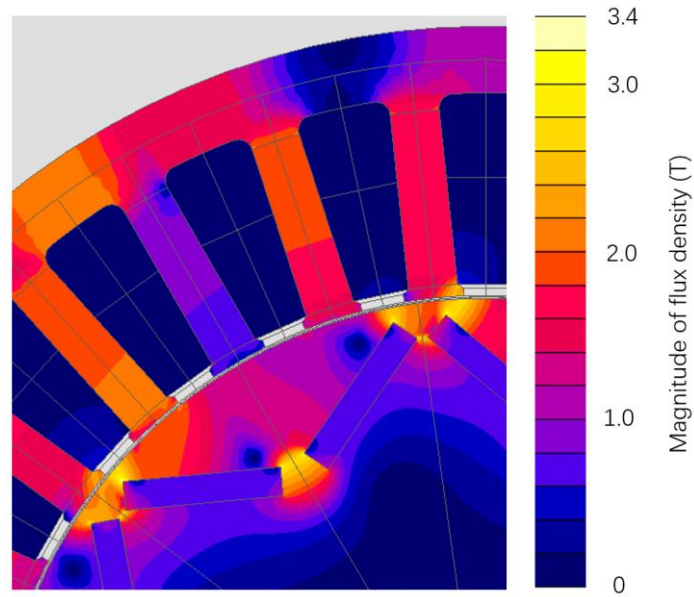


Figure 2.20 Predicted flux density distribution for the 165 mm rotor design with an extended rectangular magnet block.

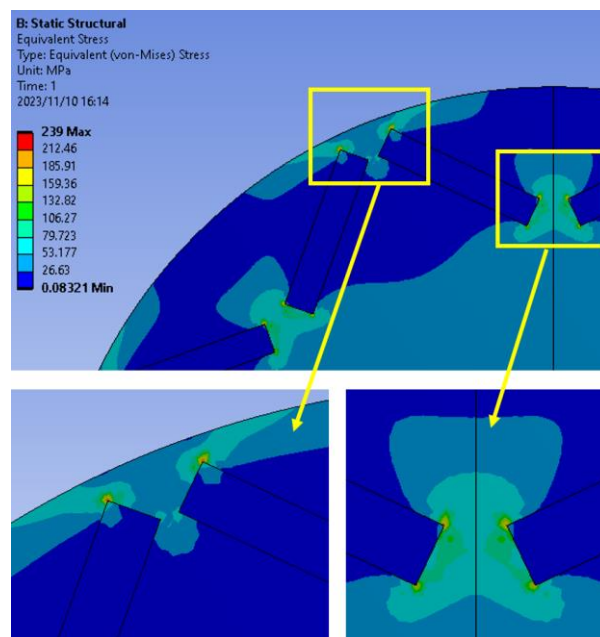


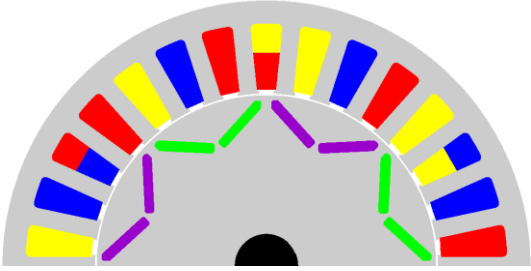
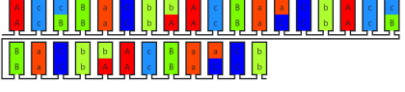
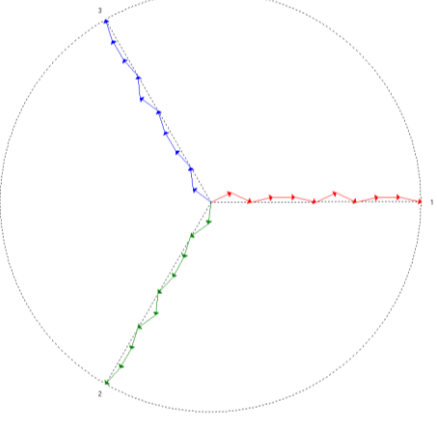
Figure 2.21 Predicted von Mises stress distribution for the 165 mm rotor design with an extended rectangular magnet block

2.4 Summary of final design

This study has established an optimised 100kW IPM machine design with a rotor diameter of 165mm resulting in an active mass of 42.3kg with corresponds to $\sim 2.4\text{kW/kg}$. A summary of the key dimensions of the final optimised machine design is shown in Table 2.7.

Table 2.7 Details of two studied IPM machine

30 slots, 8 poles

Layout	
Rotor diameter	165 mm
Stator diameter	256.7 mm
Axial length	103.4 mm
Peak current	326.2 A
Slot area (per slot)	410.0 mm ²
Slot area (total for machine)	12,300 mm ²
Slot fill factor	0.45
Turns per slot	8
Current density	10 A/mm ²
Winding layout	
Connection	Three-phase star
Winding factor	0.951
Winding phasor diagram	

Reference

- [1] N. Bianchi, S. Bolognani, and F. Luise, “Potentials and limits of high-speed PM motors,” *IEEE Trans. Ind. Appl.*, vol. 40, no. 6, pp. 1570–1578, 2004, doi: 10.1109/TIA.2004.836173.
- [2] A. Binder and T. Schneider, “High-Speed Inverter-Fed AC Drives.”
- [3] A. Yu and G. W. Jewell, “Systematic design study into the influence of rotational speed on the torque density of surface-mounted permanent magnet machines,” *J. Eng.*, vol. 2019, no. 17, pp. 4595–4600, 2019, doi: 10.1049/joe.2018.8204.
- [4] E. C. Lovelace, T. M. Jahns, T. A. Keim, and J. H. Lang, “Mechanical design considerations for conventionally laminated, high-speed, interior PM synchronous machine rotors,” *IEEE Trans. Ind. Appl.*, vol. 40, no. 3, pp. 806–812, 2004, doi: 10.1109/TIA.2004.827440.
- [5] [Online], “Project ELLI,” https://www.amrc.co.uk/files/document/471/1648484969_AMRC_MACH_MAIN_AW.pdf.
- [6] A. Binder, T. Schneider, and M. Klohr, “Fixation of buried and surface-mounted magnets in high-speed permanent-magnet synchronous machines,” *IEEE Trans. Ind. Appl.*, vol. 42, no. 4, pp. 1031–1037, 2006, doi: 10.1109/TIA.2006.876072.
- [7] A. Wang, Y. Jia, and W. L. Soong, “Comparison of Five Topologies for an Interior Permanent-Magnet Machine for a Hybrid Electric Vehicle,” vol. 47, no. 10, pp. 3606–3609, 2011.
- [8] Z. Han, H. Yang, and Y. Chen, “Investigation of the rotor mechanical stresses of various interior permanent magnet motors,” *Proc. - 12th Int. Conf. Electr. Mach. Syst. ICEMS 2009*, pp. 9–14, 2009, doi: 10.1109/ICEMS.2009.5382987.
- [9] J. Ma and Z. Q. Zhu, “Optimal Split Ratio in Small High Speed PM Machines Considering Both Stator and Rotor Loss Limitations,” *CES Trans. Electr. Mach. Syst.*, vol. 3, no. 1, pp. 3–11, 2019, doi: 10.30941/CESTEMS.2019.00002.
- [10] N. Leuning, B. Schauerte, and K. Hameyer, “Interrelation of mechanical properties and magneto-mechanical coupling of non-oriented electrical steel,” *J. Magn. Magn. Mater.*, vol. 567, no. November 2022, p. 170322, 2023, doi: 10.1016/j.jmmm.2022.170322.
- [11] J. Qiu and M. Zhou, “Analytical solution for interference fit for multi-layer thick-walled cylinders and the application in crankshaft bearing design,” *Appl. Sci.*, vol. 6, no. 6, pp. 13–16, 2016, doi: 10.3390/app6060167.

[12] R. G. Budynas and J. K. Nisbett, *Shigley 's Mechanical Engineering Design*. 2023.

Chapter 3: High frequency switching effects in PM machines

3.1 Introduction

The prediction of the iron loss in electrical is reasonably well developed with numerous proposed models [1], [2] and case studies [3], [4]. Finite element post-processors to calculate iron loss from a series of time-stepped magnetostatic field solutions over an electrical cycle are now available as a tool within many commercial finite element packages. However, these models tend to have an idealised representation of material properties which generally do not account for the effects of manufacturing processes such as laser cutting [5], blanking [6] and stress [7].

In addition, many of these models rely on a simplified representation of the machine current, often limited to sinusoidal currents with possibly some harmonics. However, almost all current waveforms in high performance machine drivetrains are produced by power electronic convertors and additional iron losses are generated by the ripple current components which come from the high frequency switching behaviour of the converter. This additional iron loss from high frequency switching effects will cause the machine temperature rise to increase at a given output power compared with the ideal sinusoidal current input. For many types of machines a de-rating of 20% or more is applied for machine during inverter operation [8]. Hence, one of the main factors to incorporate into any iron loss calculations is the effect of high frequency ripple.

This chapter is concerned with development of a method to calculate flux density waveforms in every individual element of a finite element mesh which include representative high frequency switching effects. A schematic of the overall method is shown in Figure 3.1. It combines the use of magnetostatic finite element models the machine at the fundamental frequency to determine electric circuit parameters and the fundamental frequency flux density waveforms with a SIMULINK circuit simulation to predict the high frequency components of the current waveform and hence flux density.

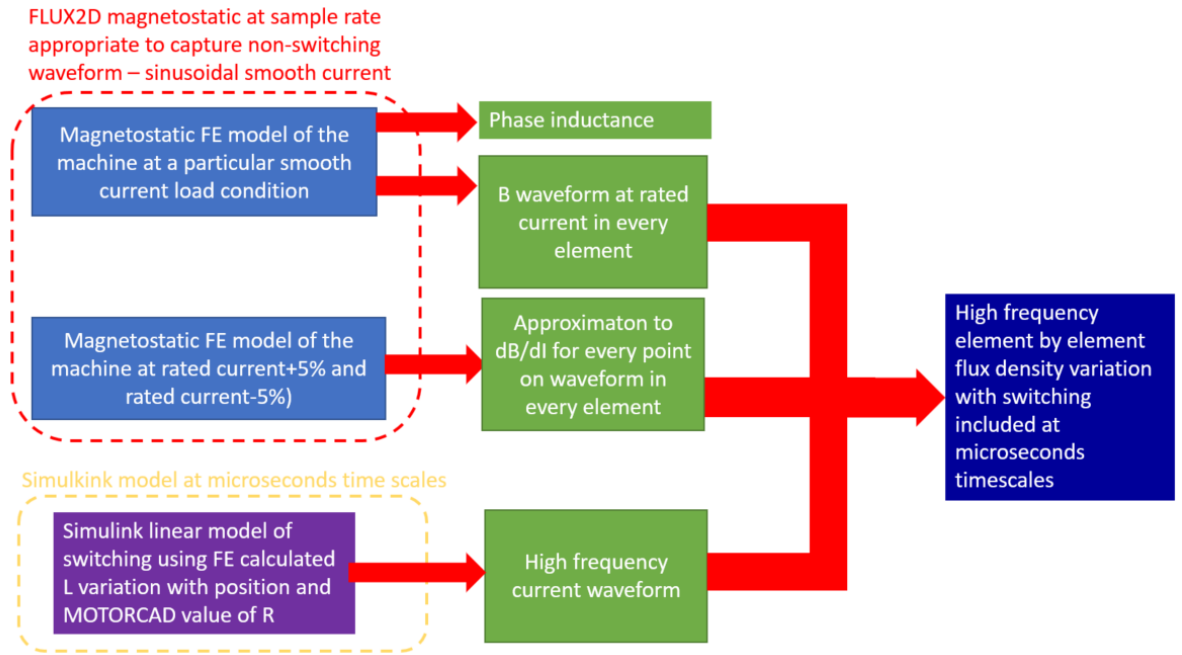


Figure 3.1 Schematic of methodology for predicting flux density waveforms in each element of a finite element mesh which contain high frequency switching effects

3.2 Calculation of machine electrical parameters

3.2.1 Prediction and representation of self-inductance and mutual-inductance

For PMSM machine, the phase self-inductance can be expressed as [9]:

$$L_{ph} = \frac{N_{ph}\Phi_{ph}}{I_{ph}} \quad (3.1)$$

In order to calculate the self-inductance of the phase, it is necessary to separate out the flux-linkage due to the current itself from the contributions to the overall flux-linkage from the remaining phases and from the permanent magnet excitation. It is also important to recognise that the self-inductance can vary as a function of rotor position (due to saliency) and the magnitude of the phase current (due to magnetic saturation). The calculation of the machine electrical parameters is based on the finite element package Altair FLUX2D, which could detail illustrate the inductance variations of IPM machine with position and current.

In principle, the calculation of the self-inductance component of the flux can be done by enforcing zero current in the remaining phases and removing the rotor magnets from the model and replacing them with unmagnetized blocks with a relative magnetic permeability of 1.05.

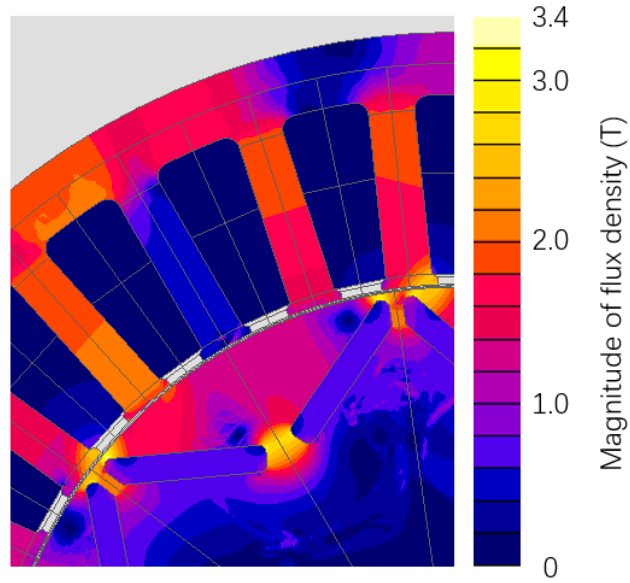
Although this provides a simple method for isolating the contribution of the self flux-linkage it does not represent the actual flux conditions in the stator and rotor cores and hence the effective magnetic permeability.

The calculation of mutual inductance has similar issues of ensuring representative permeability through the core while only having the excitation of interest present in order to separate out the mutual flux-linkage. One widely used method to resolve these issues is the use of a frozen permeability method.

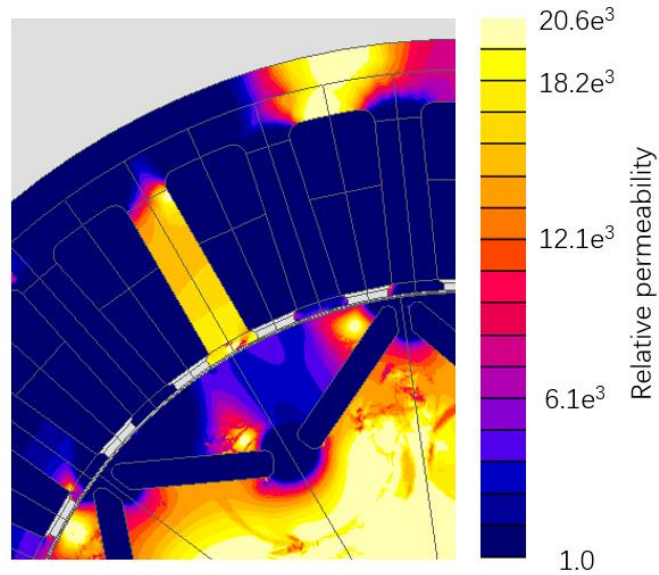
The frozen permeability method involves setting up realistic flux levels in the machine for each step during one electrical cycle and capturing the permeability of each individual finite element in the stator and rotor cores for each time step. A normal non-linear simulation with permanent magnet excitation and the standard three-phase currents flowing is performed and the permeability in the stator and rotor cores is stored for each individual element at each time step. The permeability map at a particular rotational angle is then used to fix the permeability at each time step for a simulation over one electrical cycle in which a fixed DC current is fed into the phase of interest depending on whether the self or mutual inductance are being calculated. Unlike a normal finite element simulation with a non-linear core material in which the permeability is modified through iteration of the field solution, the permeability in the core elements remains fixed (or frozen) for that particular time step. This method allows both the normal operating core conditions to be represented while also being able to attribute all the flux-linkage of a given winding to the DC current introduced into the simulation.

This is a 30 slot, 8 pole salient IPM machine which is equipped with a fractional slot winding as shown previously in Figure 2.6 of chapter 2. This machine exhibits half-symmetry in its electromagnetic behaviour and hence a 180° finite element model is required to represent the machine. The 30 slot machine is equipped with 10 coils per phase with 4 series turn per coil (made up of 20 parallel strands).

Figure 3.2 (a) and 3.2 (b) show a typical field distribution and corresponding relative permeability distribution in the machine under normal simulation conditions, in this particular case for a rotor angle of 8° and rated current of 230.7 A rms, while Figure 3.3 shows the predicted field distribution at this same rotor angle but with frozen permeability map of Figure 3.2b and a DC current of 5A in phase A only. It is worth noting that since the permeability is fixed in this solution, any value of DC current would yield the same inductance value.



(a)



(b)

Figure 3.2 Flux density distribution and relative permeability of D165 IPM machine supplied with rated on-load current

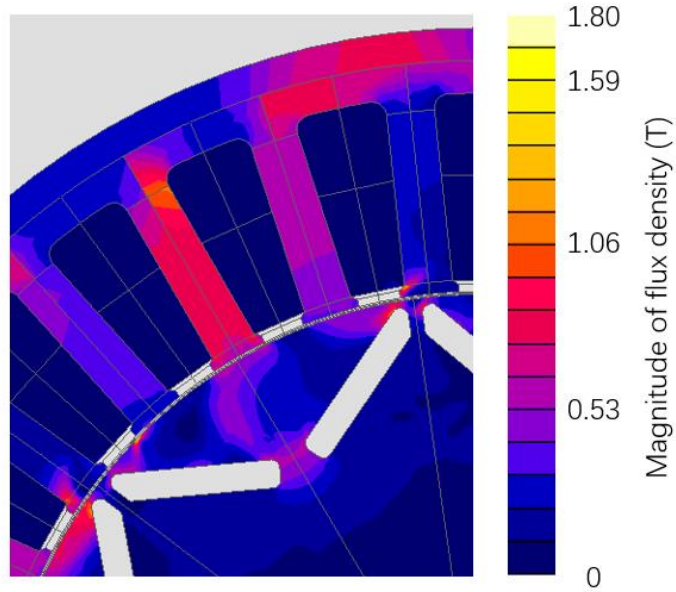
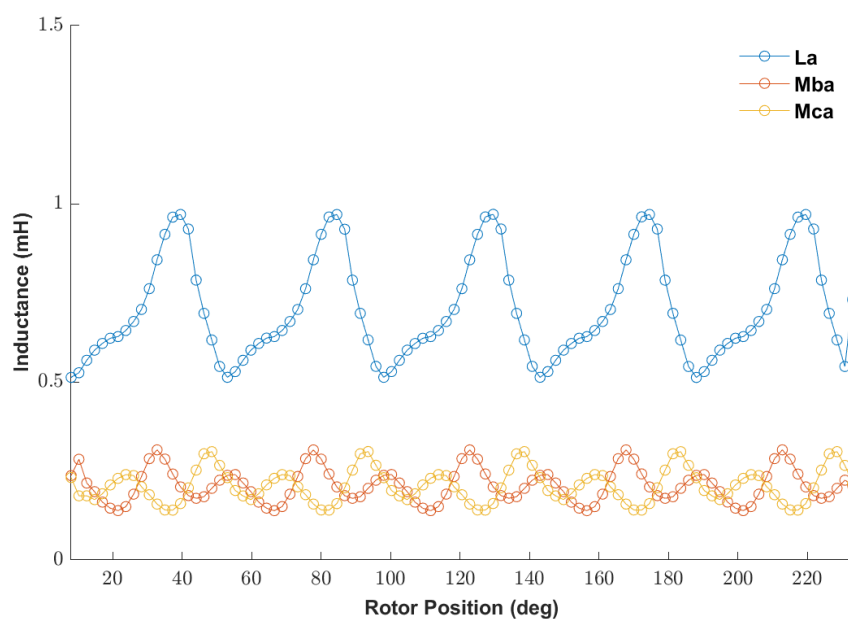
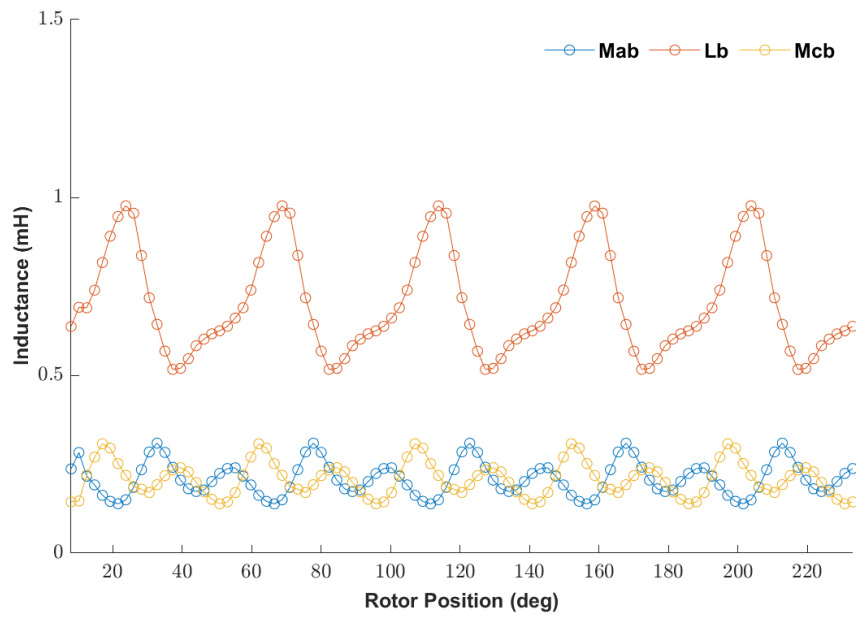


Figure 3.3 Flux density distribution of D165 IPM machine only supplied with 5 A DC current for phase A

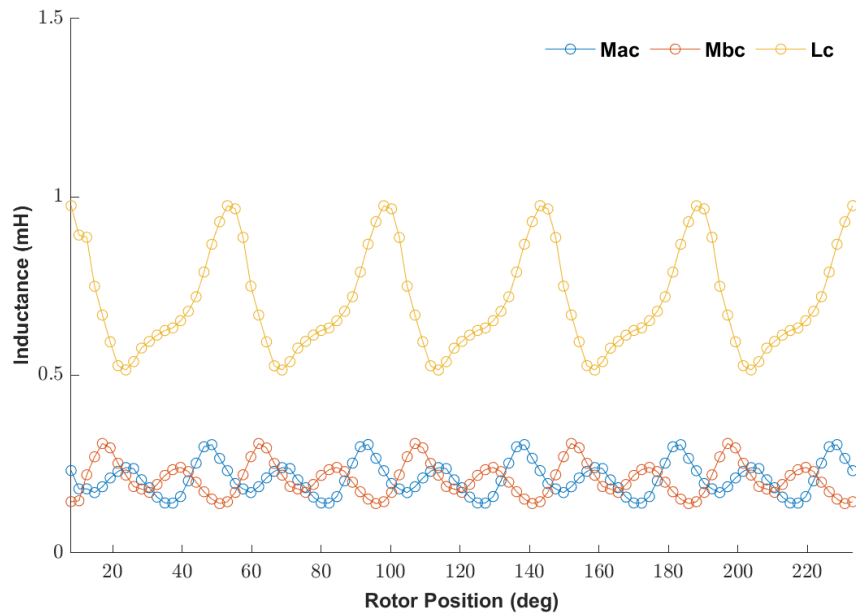
The variations in the self and mutual inductances with rotor mechanical angle predicted for phases A, B and C with this method are shown in Figure 3.4. The characteristics for phase B and phase C take the same form but with angular offsets of 29° (mech) and 14° (mech) respectively. For this salient machine with fractional slot winding, the minimum phase self-inductance is 0.51 mH and maximum inductance is 0.97 mH. The minimum mutual inductance is 0.14 mH and maximum inductance is 0.31 mH.



Phase A



Phase B



Phase C

Figure 3.4 Calculated variation in self and mutual inductance using the frozen permeability method

Having calculated the self and mutual inductances at this fine angular resolution, much of this detailed information would be lost by aggregating these results into a d-axis and q-axis model in SIMULINK even though this would suit standard library block representations of brushless machines in SIMULINK. The effect of the fine detail of inductance changes could have an influence on ripple current and hence the full inductance versus rotor angle characteristics of Figure 3.4 were represented in the SIMULINK system model using a series

of look up tables. There are nine, one-dimensional look-up tables used in the SIMULINK model. Each has the rotor angle as the only input and a single output which is in one of L_a , L_b , L_c , M_{ba} , M_{ca} , M_{ab} , M_{cb} , M_{ac} or M_{bc} .

3.2.2 Prediction and representation the phase resistance

The winding of this particular IPM machine design has 4 series turns per slot made up of 20 parallel strands. An idealised representation of this winding from the MOTORCAD package is shown in Figure 3.5. The winding has an effective slot packing factor of 51% which results in each individual strand having a diameter of 1.3 mm. The MOTORCAD calculated resistance per phase is 0.1625Ω using the end-winding approximation method adopted in MOTORCAD [10].

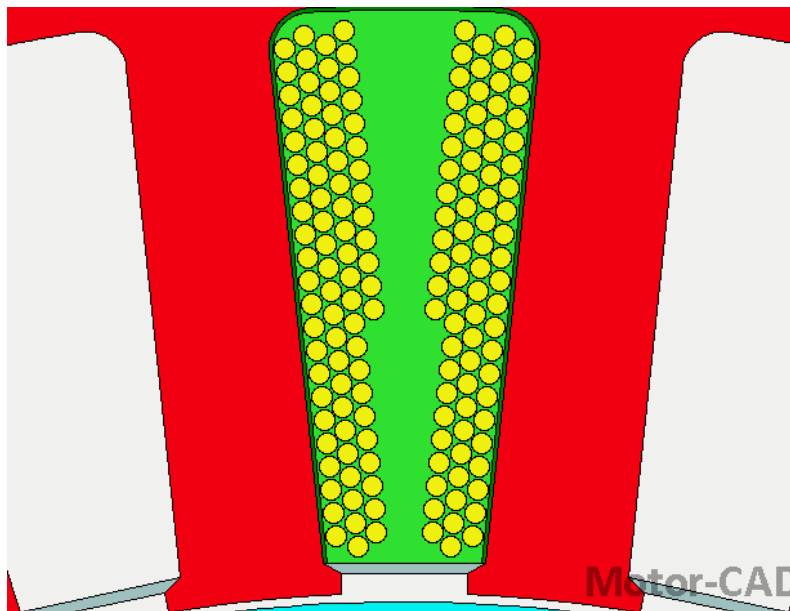


Figure 3.5 MOTORCAD generated conductor arrangement in a single slot (4 turns of 20 parallel strands of 1.3 mm diameter circular wire)

3.2.3: Prediction and representation of the open-circuit back-EMF waveform

The system block-diagram representation of the overall machine and converter includes a look-up table which represents the back emf. Figure 3.6 shows the predicted induced back emf phase voltage (line to neutral) for each of the 3 star-connected phases calculated using the open-circuit method.

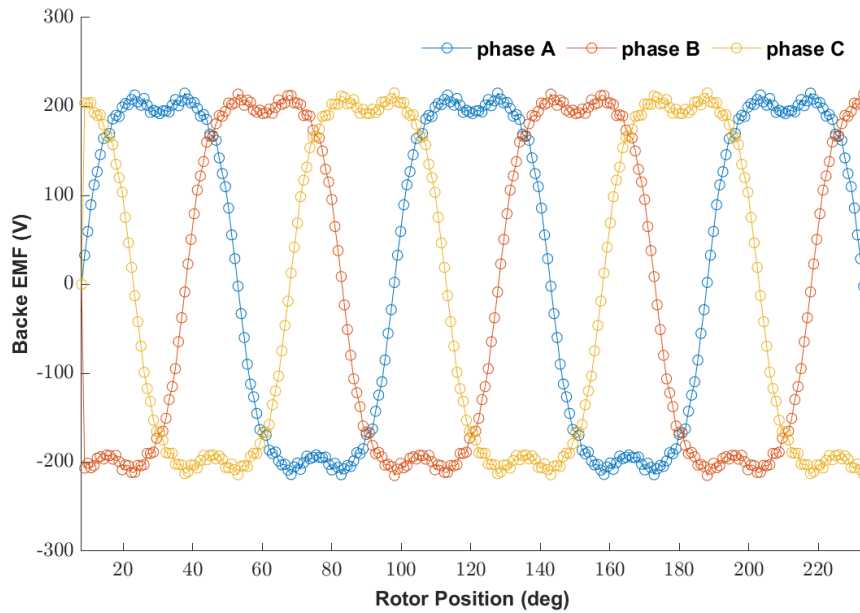


Figure 3.6 Finite element predicted line to star-point back emfs calculated at 4,000 rpm

3.3 Simulation model for a PMSM driven by a hysteresis band current controlled converter

3.3.1 Overall drive architecture

The current control method selected for this study is a simple hysteresis band control strategy. Hysteresis band control strategies are not as widely used as pulse-width modulated (PWM) methods. However, they control the current ripple amplitude directly rather than controlling the duty ratio for a specific frequency, and so hysteresis control is convenient for specifying a give implementation in terms a single parameter which makes a systematic study more straightforward and transparent. Figure 3.7 shows a typical model for a three-phase hysteresis current band control drive system diagram with an AC machine.

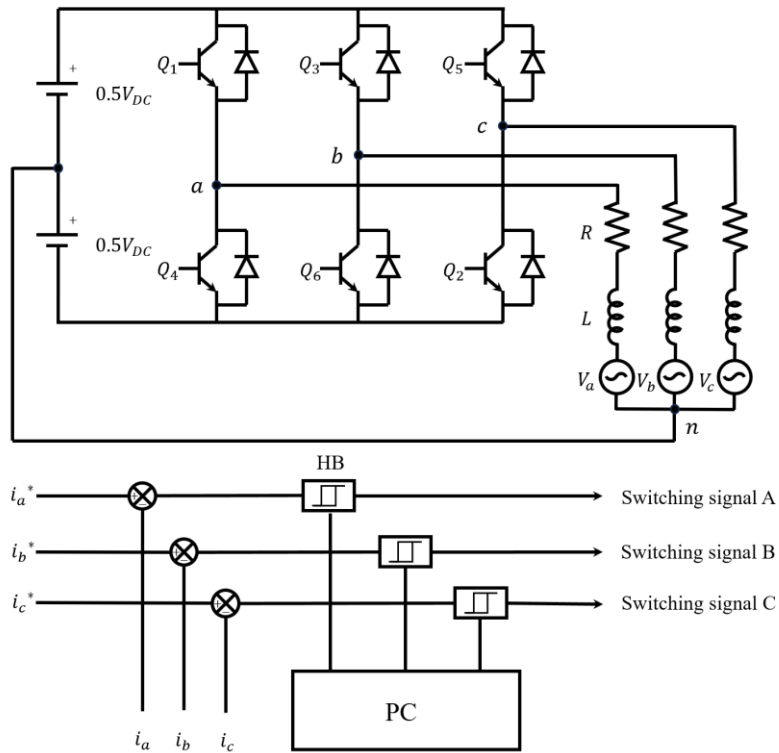


Figure 3.7 Three-phase hysteresis current band control drive system with an AC machine

3.3.2 Operating principles of hysteresis band controllers

The basic operation of a hysteresis controller can be explained with reference to the schematic waveform shown in Figure 3.8. During the period of t_1 , the machine winding is connected via a converter switch positive voltage equal to the half the DC link voltage V_{dc} . This will cause the winding current to rise at a rate determined by the voltage overhead at that instant, i.e. $V-E$, and the inductance of the winding at that rotor position. When the magnitude reaches the top of the band, i.e. the upper dashed line in Figure 8, this is detected by a comparator in the control circuit and the voltage applied to the machine winding is reversed, causing the current to start dropping at similar rate until it reaches the bottom of the hysteresis band and the voltage is again reversed.

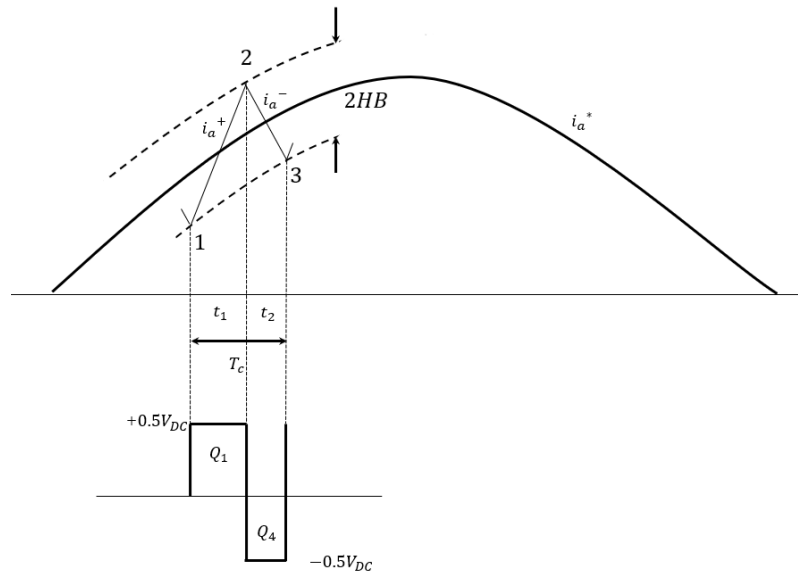


Figure 3.8 Principles of operation of a hysteresis current band controller assuming star connection

3.3.3 System model

A SIMULINK block diagram of the entire converter and machine system under consideration is shown in Figure 3.9. The DC link voltage adopted was 600V DC, which was implemented in the model as two 300V DC voltage source in series. The main sub-systems in this model other the various display elements are:

- Phase-legs of the power converter (dashed orange section)
- Hysteresis current controller (dashed light blue section)
- Mutually coupled voltage (dashed yellow section)
- Back-emf representation (dashed green section)
- Self-inductance representation (dashed purple section)

In most cases, the sub-systems are per-phase models and are duplicated for each of the 3 phases in the model.

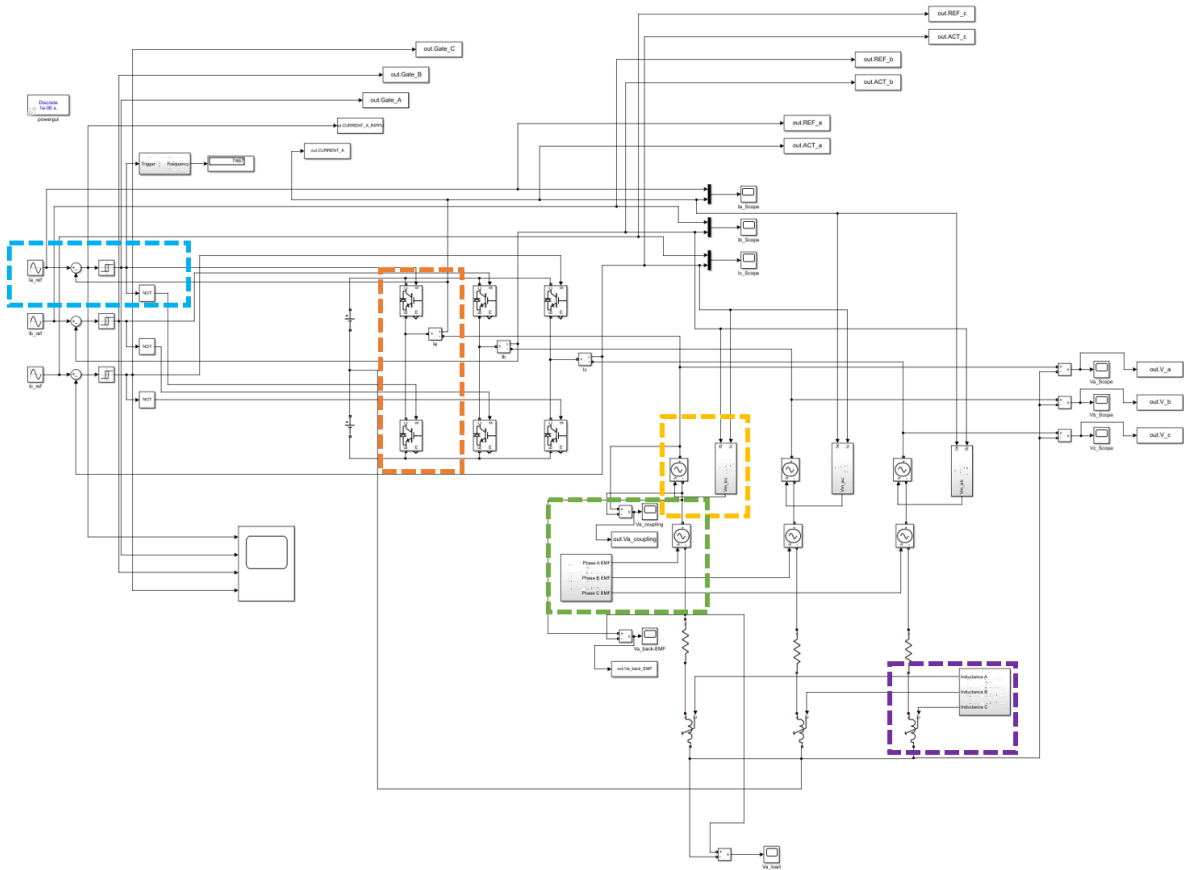


Figure 3.9 SIMULINK hysteresis band current band controller and inverter

3.3.3.1 Switching signal generation sub-system

The representation of the sub-system that generates the switching signal to control the on-off state of the inverter switched is shown in Figure 3.10. For this series of simulations at rated current, the demand signal is given by an ideal sinusoidal current (with respect to rotor position and hence time at a fixed speed) with a peak value of 326.2A. The actual predicted machine current is sensed in the model and fed back into the hysteresis current band controller for comparison against the demand current with hysteresis comparators with adjustable hysteresis bands.

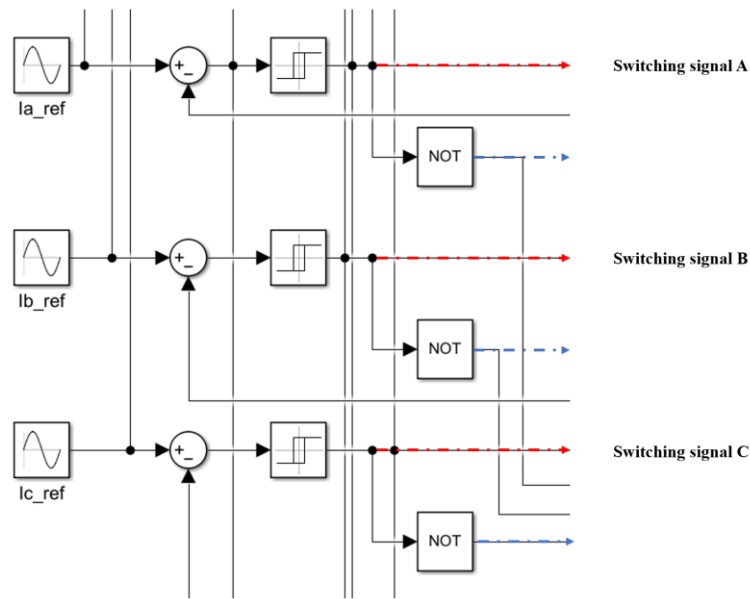


Figure 3.10 Block diagram model of the switching signal generator

3.3.3.2 Calculation of mutually coupled voltage

Taking the example of phase A, and considering the voltage contribution from the mutual inductance M_{AB} and M_{AC} , the induced voltage can be expressed as:

$$V_{muA} = M_{AB} \frac{dI_B}{dt} + M_{AC} \frac{dI_C}{dt} \quad (3.2)$$

The sub-system which implements this voltage equation is Figure 3.11. The 1-D look up tables are fed with rotor position to generate the correct mutual inductance for that position.

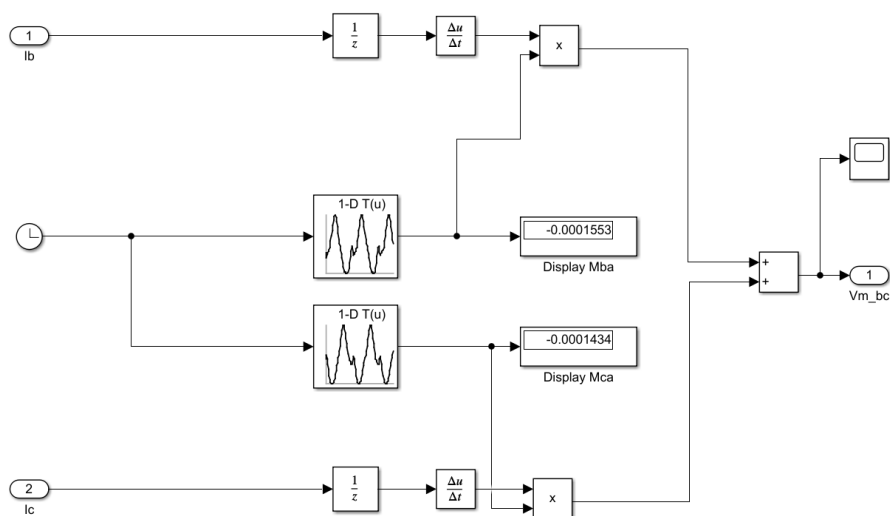


Figure 3.11 SIMULINK sub-system for calculating mutually coupled voltages in phase A caused by coupling from phase B and C

3.3.3.3 Back-emf generator

The 1D look-up table generated from the FE simulations using the method described in section 3.2.3 was used in the sub-system shown in Figure 3.6. In this case, the emf waveform is specific to the rated speed of 4,000 rpm and is hence represented as a voltage versus time look-up table. Each back-emf generator has an input of time (and the output is the actual emf voltage). The block diagram used to implement this process is shown in Figure 3.12. This could be modified if multiple speeds were being considered by normalising the time and voltage inputs of the look-up and table and adding speed as an input.

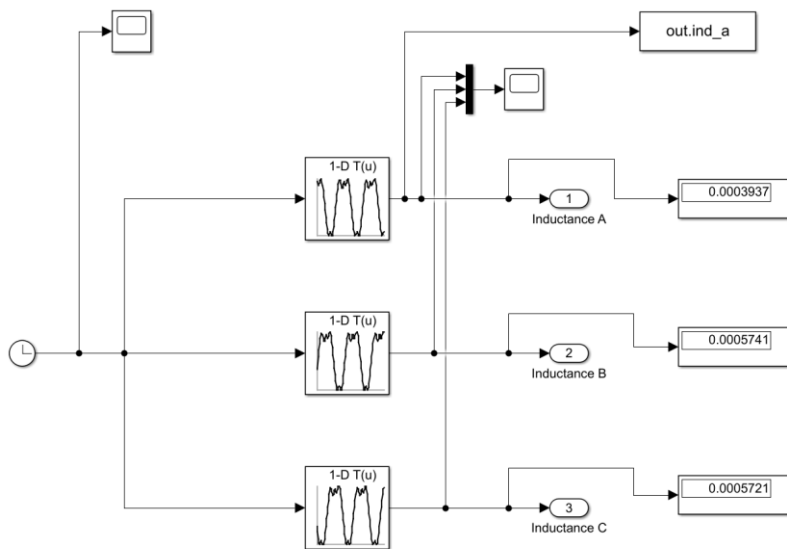


Figure 3.12 Three-phase back-emf generator

3.4 Significance of machine star-point connection

3.4.1 Introduction to star-point grounding

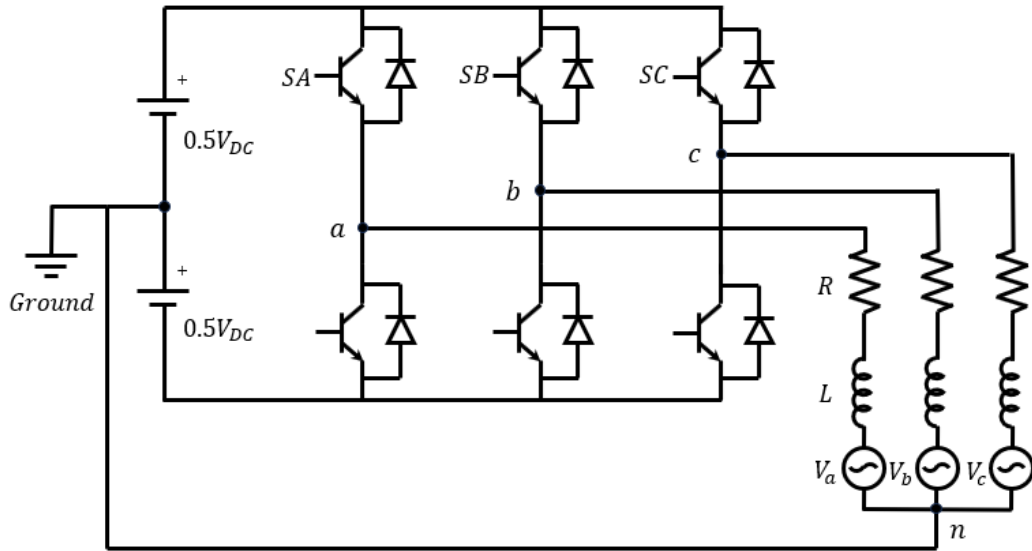
An important factor in the representation of the electrical machine in this model is whether the star point of the machine is grounded or floating, since either is a possible connection depending on the practice in an industry or application. This is a critical factor in the behaviour of a hysteresis controller as it affects the degree of coupling between phases. In all hysteresis current band control, the switching frequency is not a controlled quantity but depends on the width of the hysteresis band and the inductance of the winding. However, in star-connected three-phase systems, another factor that influences the switching behaviour in each individual phase leg is whether the star-point is grounded or floating. This is a consequence of the

imbalance in three phase systems in converter drives where the individual phase connections are connected to either one of the DC link voltage rails during the switching sequence. Hence, the operation of machine will involve intervals of any two of the phases being connected to the positive voltage rail with the remaining phase connected to the negative and vice-versa during other intervals during normal operation. The effect that this imbalance has on the voltage applied to a phase winding machine depends on whether the star-point is grounded or floating [9].

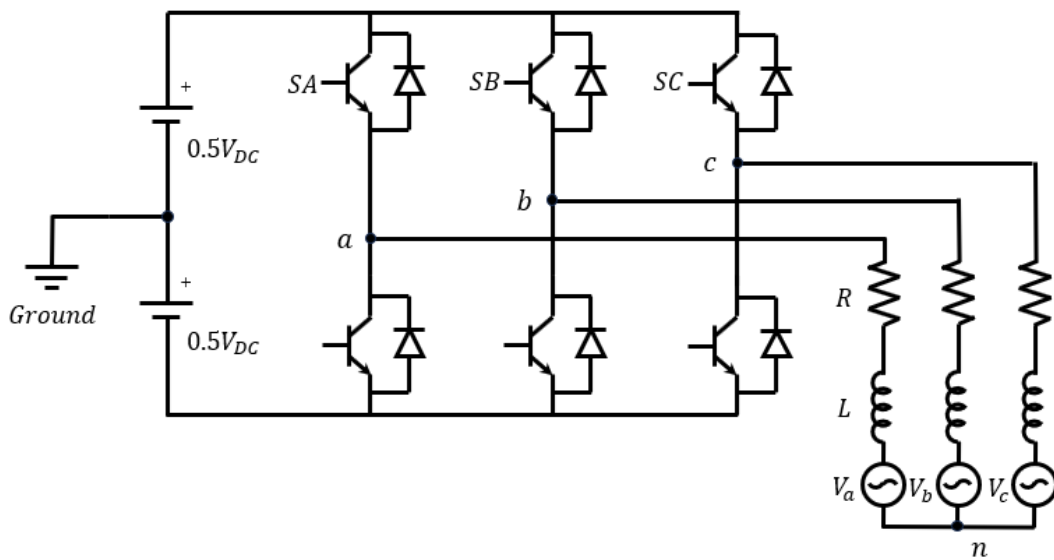
3.4.2 Grounded star connection

When the star point of the machine is grounded, the voltage applied across any of the three phase is restricted to being $\pm \frac{1}{2}V_{DC}$ and the line to star-point voltage of a phase is not affected by the switching state of the other two phases. The voltage in the phase depends only on its own switching state.

Taking the voltage of phase A as example and considering the simplified converter representation in Figure 3.13. When the switching signal to control the top bridge inverter switch phase A is set to '1', this switch is conducting and the output of phase A is connected to the positive voltage rail. During this interval, the lower switch is provided by a complementary '0' signal. With a '0' control signal applied, the lower switch in phase A is conducting and hence for this combination of control signals to the 2 switches, phase A of the machine winding has one end directly connected to a $+\frac{1}{2}V_{DC}$ voltage rail and the other end connected to a grounded star point, and hence the applied voltage for the phase is $\frac{1}{2}V_{DC}$. Similarly, when the switching signal for the two switches in phase A are reversed, a $-\frac{1}{2}V_{DC}$ voltage source, so the applied voltage for phase A is $-\frac{1}{2}V_{DC}$. The full switching table and resulting applied voltages for a grounded star-point is shown in Table 3.1.



(a)



(b)

Figure 3.13 Simplified representation of a three phase converter with (a) grounded star-point and (b) floating star-point

Table 3.1 Switching table for a three-phase converter with a grounded star-point

<i>Switching State of top switch (lower switch has complementary)</i>			<i>Applied voltage</i>		
<i>SA</i>	<i>SB</i>	<i>SC</i>	V_A	V_B	V_C
1	1	1	$\frac{1}{2}V_{DC}$	$\frac{1}{2}V_{DC}$	$\frac{1}{2}V_{DC}$
0	0	0	$-\frac{1}{2}V_{DC}$	$-\frac{1}{2}V_{DC}$	$-\frac{1}{2}V_{DC}$
1	1	0	$\frac{1}{2}V_{DC}$	$\frac{1}{2}V_{DC}$	$-\frac{1}{2}V_{DC}$
1	0	1	$\frac{1}{2}V_{DC}$	$-\frac{1}{2}V_{DC}$	$\frac{1}{2}V_{DC}$
1	0	0	$\frac{1}{2}V_{DC}$	$-\frac{1}{2}V_{DC}$	$-\frac{1}{2}V_{DC}$
0	0	1	$-\frac{1}{2}V_{DC}$	$-\frac{1}{2}V_{DC}$	$\frac{1}{2}V_{DC}$
0	1	1	$-\frac{1}{2}V_{DC}$	$\frac{1}{2}V_{DC}$	$\frac{1}{2}V_{DC}$
0	1	0	$-\frac{1}{2}V_{DC}$	$\frac{1}{2}V_{DC}$	$-\frac{1}{2}V_{DC}$

3.4.3 Floating star connection

When the star-point of the machine is allowed to float, the applied voltage at one end of the phase winding takes the same value $\pm\frac{1}{2}V_{DC}$ in the same way as the grounded star-connection. However, the star-point voltage will fluctuate as different combinations of the phases are connected to the positive rail and negative rails. Hence, the voltage difference across any one of the machine phases will vary not only with the voltage applied by its own phase leg at one end but also the fluctuations of the floating star-point, which in many cases can be caused by switching events in the other phases. It is this coupling between phases via the fluctuating star-point voltage that introduces some complicated behaviours into the hysteresis controller.

The switching table and applied voltages for the case of a floating star point are shown in Table 3.2.

Table 3.2 Switching table for a three-phase converter with a floating star-point

<i>Switching State of top switch (lower switch has complementary)</i>			<i>Applied voltage</i>		
<i>SA</i>	<i>SB</i>	<i>SC</i>	<i>V_A</i>	<i>V_B</i>	<i>V_C</i>
1	1	1	0	0	0
0	0	0	0	0	0
1	1	0	$\frac{1}{3}V_{DC}$	$\frac{1}{3}V_{DC}$	$-\frac{2}{3}V_{DC}$
1	0	1	$\frac{1}{3}V_{DC}$	$-\frac{2}{3}V_{DC}$	$\frac{1}{3}V_{DC}$
1	0	0	$\frac{2}{3}V_{DC}$	$-\frac{1}{3}V_{DC}$	$-\frac{1}{3}V_{DC}$
0	0	1	$-\frac{1}{3}V_{DC}$	$-\frac{1}{3}V_{DC}$	$\frac{2}{3}V_{DC}$
0	1	1	$-\frac{2}{3}V_{DC}$	$\frac{1}{3}V_{DC}$	$\frac{1}{3}V_{DC}$
0	1	0	$-\frac{1}{3}V_{DC}$	$\frac{2}{3}V_{DC}$	$-\frac{1}{3}V_{DC}$

3.5 Prediction of current waveforms with switching effects

3.5.1 Grounded star-point

Since the current ripple which produces the high frequency iron loss is caused by the individual switching events, it is important to look in detail at the behaviour of the machine on the timescales of switching events noting that the converter is modelled using ideal switches and does not account for any non-linear behaviour during the switch transition. Figure 3.14 shows a close-up of the switched voltage applied to phase A during 1.5 electrical cycles of the

reference machine design operating at 4,000 rpm at its rated current of 326.2 A with a hysteresis band of ± 16.3 A. As shown, this machine operates from an ideal 600V DC link and hence the voltage switches between +300 V and -300 V in response to the action of the hysteresis band controller because of grounded star-point. The grounded star-point means that the applied voltage is defined only by the voltage at the terminal end of the phase.

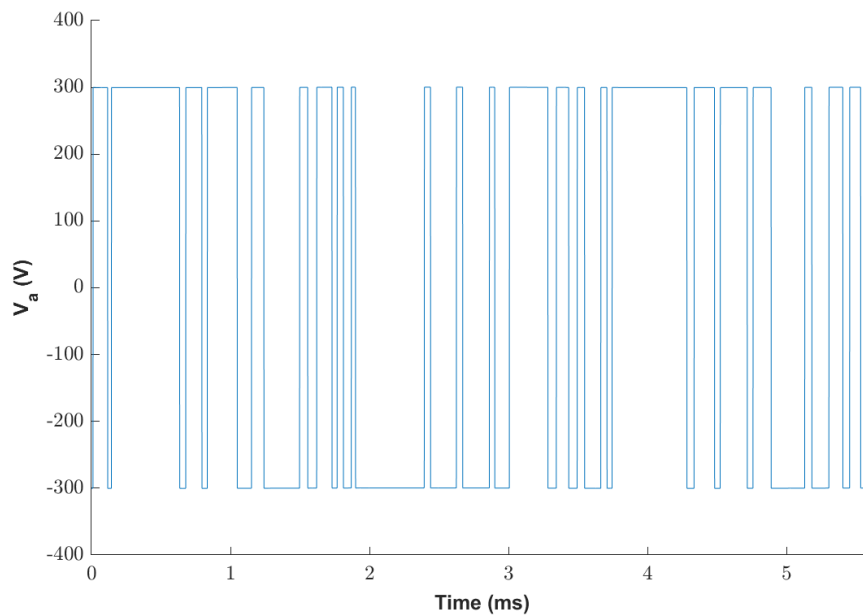


Figure 3.14 Phase A voltage (line to star-point) waveform for grounded star connection in a machine operating at 4,000rpm at rated current with a hysteresis band of ± 16.3 A

Figure 3.15 shows the predicted current waveform over 1.5 electrical cycles for a hysteresis band set at $\pm 5\%$ of the peak current which corresponds to ± 16.3 A. This simulation was performed at the rated speed of 4,000 rpm which corresponds to an electrical frequency of 267 Hz. The reference demand current waveforms are three sinusoidal waveforms with peak amplitude of 326.2 A. The converter is connected to a pair of 300V DC voltage sources to provide a 600V link. The total simulation duration is 2.5 electrical cycles, with the first full cycle removed from these traces to eliminate the start-up transient.

Also shown in Figure 3.15 is the current error in phase A which is acted on by the controller (i.e., error = demand current – actual current). Adopting this controller error definition means that a current that is greater than the demand and heading towards the top of the hysteresis band generates a negative controller error and vice versa. Hence the bounding thresholds on the controller current errors are the opposite way around to the top and bottom hysteresis bands. The error signal shows that there are intervals during the simulation in which

the current falls outside the range of the hysteresis band, e.g. 0.2 - 0.53 ms into the waveform. In this interval the actual current is below the lower hysteresis band (i.e., generating a positive current error which is above the upper threshold). Although the converter leg in phase A has taken the correct action by turning on the top switch, the current remains outside the band because of the coupled voltage contribution from the mutual flux linkage from phases B and C. This behaviour can be explained by considering equation (3.3) which shows that depending on the magnitude of the phase back E_{ph} and the mutually coupled voltages from the other phases $V_{coupling}$ the rate of change of inductance can be negative even when a positive voltage is applied to the phase by turning on the upper switch. Since this chapter mainly focuses on the effects of the ripple current to flux density within the stator core, so the switching loss generated by the converters in the control system will be investigated as further work.

$$\frac{di}{dt} = \frac{V - E_{ph} - V_{coupling}}{L_{ph}} \quad (3.3)$$

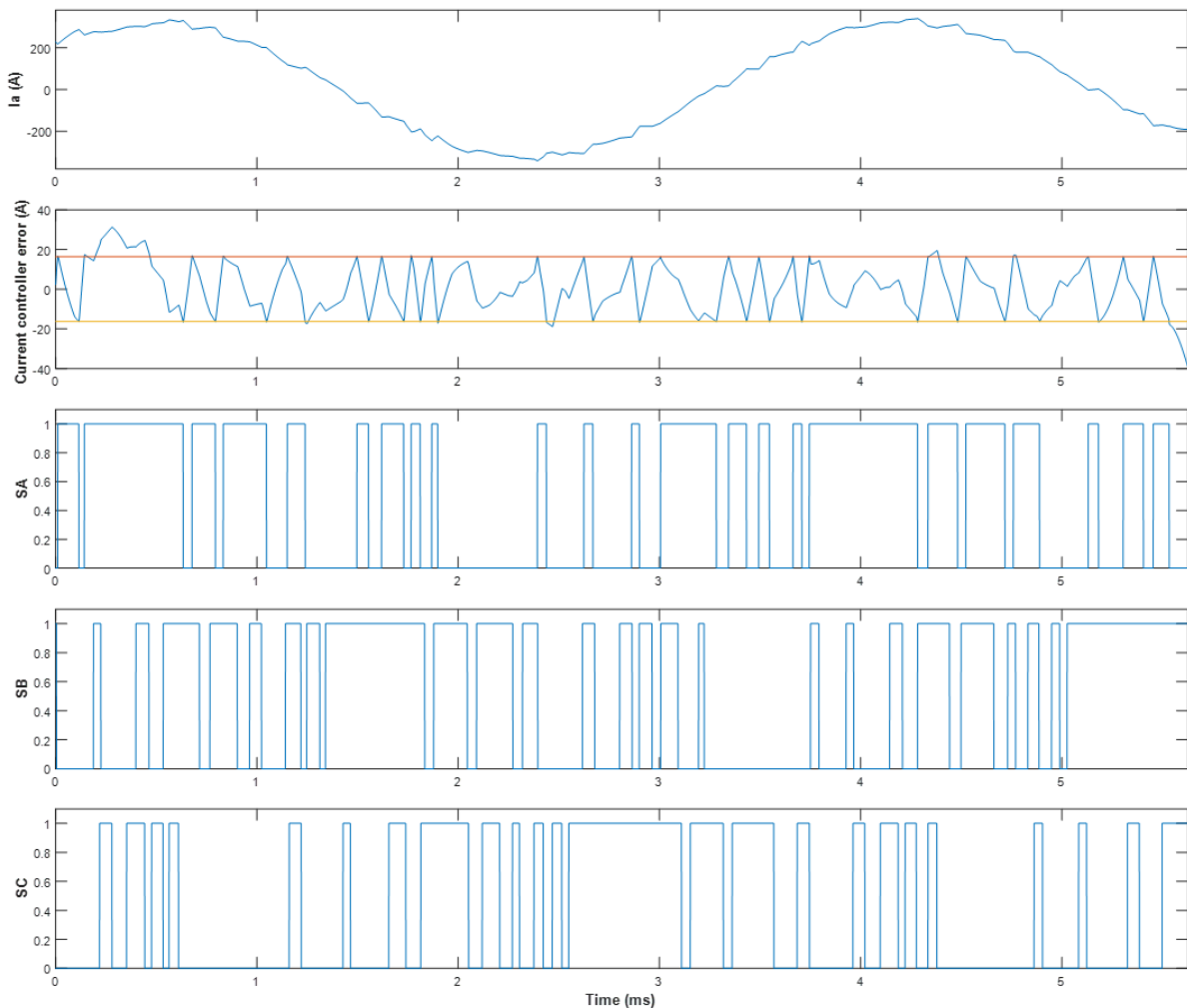


Figure 3.15 Phase A current, controller current error in phase A and corresponding switching signals for a grounded star-point

Figure 3.16 shows the ideal sinusoidal demand and the predicted hysteresis controller waveforms for three different hysteresis band widths at 4,000rpm. As shown, there are several intervals with very few switching events, e.g. and intervals in which the current falls even when the actual current is below the demand waveform. As shown by equation 3.3, this behaviour is influenced by the magnitudes of the current, the back emf and the DC link voltage.

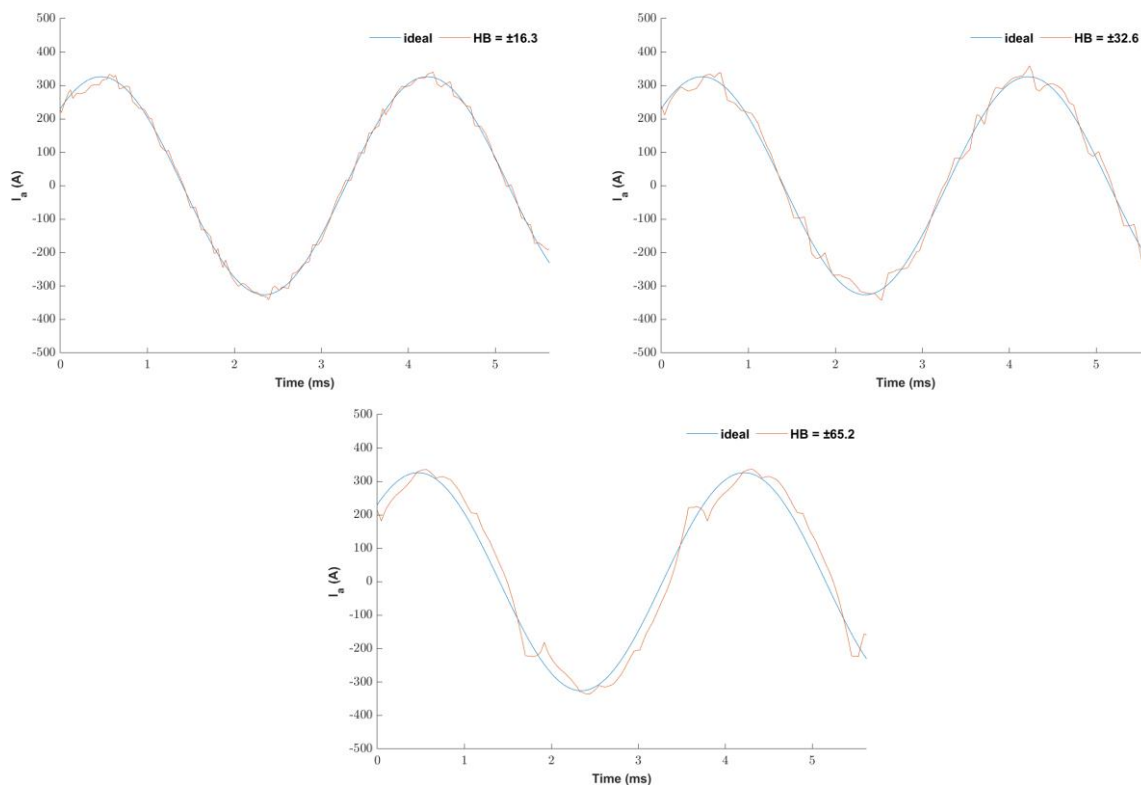


Figure 3.16 Predicted phase A currents with a grounded star point with different hysteresis band magnitudes of $\pm 5\%$ ($\pm 16.3 A$), $\pm 10\%$ ($\pm 32.6 A$) and $\pm 20\%$ of peak ($\pm 65.2 A$)

As demonstrated, even for the simpler case of a grounded star-point, the high frequency ripple current which is present in the output current waveform is far more complicated than a simple symmetrical sawtooth added onto the sinusoid. Since the magnitude of the high frequency eddy currents are determined by the rate of change of flux density and hence current, capturing the detailed behaviour from a full system simulation will be more accurate than an idealised symmetrical representation of the ripple. This section develops a method based on SIMULINK to generate representative switching current waveform in IPM machine with very short time steps from finite element simulation based on standard time-step durations. Moreover, these current waveforms reflect the inductance variations with position and current which are important in modelling IPM machines.

3.5.2 Floating star-point

Figure 3.17 shows the phase A current waveform along with the current controller error and the switching events in the 3 phases. Over the first 5 ms of the trace, there are only 17 switching events in phase A.

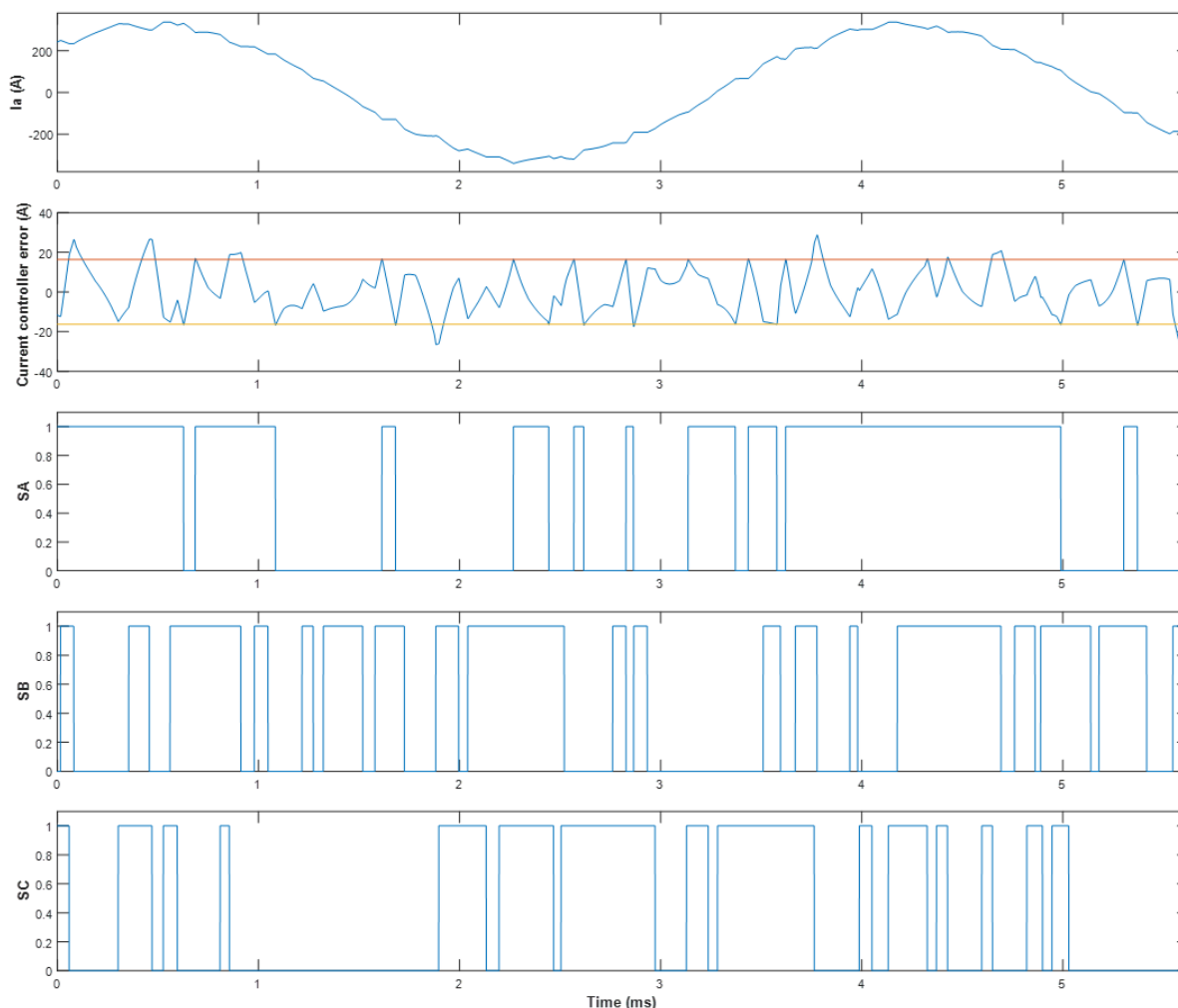


Figure 3.17 Phase A current, controller current error in phase A and corresponding switching signals for a floating star-point

Figure 3.18 shows the predicted phase A current waveforms for hysteresis bands of 5%, 10% and 20% of the peak current while Figure 3.19 shows the corresponding phase A voltage waveform (line to star-point) for the particular case of a hysteresis band of $\pm 5\%$. There are 5 instances in which the current controller error is greater than the upper error threshold (which corresponds to the actual current dropping below the lower hysteresis band level) and only two instances in which the current controller error is below the lower error threshold. Looking in detail at the first 0.5 ms of the simulation, it can be seen the phase A switching signal remains

at 1, which corresponds to the top switch being turned on. This is correct course of action for the controller as it attempts to prevent the actual current from dropping below the lower hysteresis band (which corresponds to the current controller error exceeding the upper threshold). However, it is unable to prevent the current controller error from going above the threshold. This is partly because the switching events in phases B and causing the phase voltage in phase A to change around 200 V and 400 V (i.e. 1/3 and 2/3 of the 600V DC link). The transient behaviours that not strictly varying between the 200 V and 400 V are mainly results from the coupling voltage, back emf and non-linearity properties of the inductance of this salient machine.

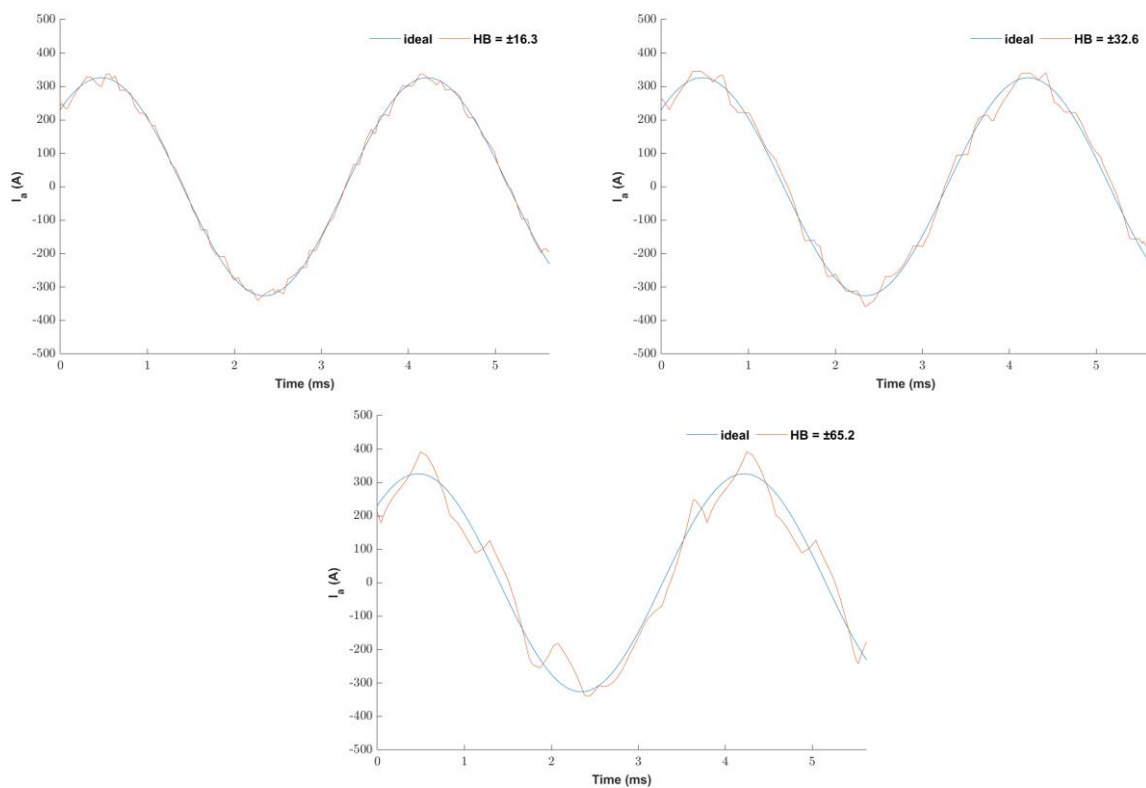


Figure 3.18 Predicted phase A currents with a floating star-point with different hysteresis band magnitudes of $\pm 5\%$ ($\pm 16.3 A$), $\pm 10\%$ ($\pm 32.6 A$) and $\pm 20\%$ of peak ($\pm 65.2 A$)

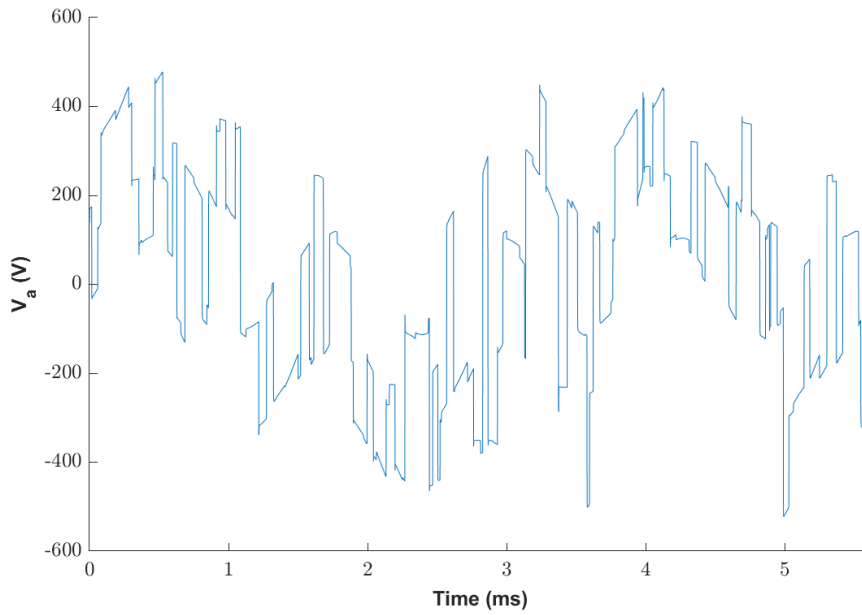


Figure 3.19 Phase A voltage waveform (line to star-point) for a hysteresis band of $\pm 5\%$ (± 16.3 A)

The voltage overhead which can drive the current in the correct direction to maintain the current within the hysteresis band can be estimated by subtracting the instantaneous back emf the mutually coupled voltage from the applied voltage waveform shown previously in Figure 3.19. The resulting waveform is shown in Figure 3.20 for the case of a $\pm 5\%$ hysteresis band. As can be seen, during the first 0.5ms, the net voltage is ~ 300 V which explains the reduced dynamic performance of the controller.

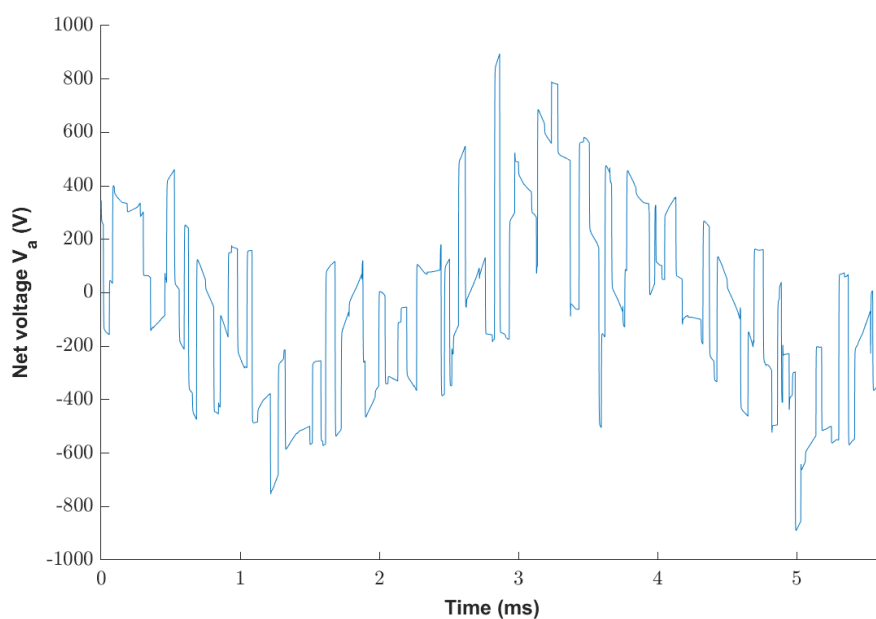


Figure 3.20. Net voltage waveform across phase A for a hysteresis band of $\pm 5\%$ (± 16.3 A)

As was the case with the grounded star-point, the behaviour of the converter is very significant in determining the high frequency components in the current waveform and that in order to get useful input to an iron loss model that has realistic representation of practical waveforms it is necessary to combine the loss model with a circuit simulation.

3.6 Calculation of high frequency flux density waveforms

The SIMULINK model described in section 3.3.3 can be used to calculate the high frequency switching components in the machine current waveforms. However, to calculate the effect of the high frequency current ripple on the iron loss, it is necessary to calculate the flux density waveforms in every element of the stator and rotor cores. One possible method would be to perform finite element field solutions with very short time steps. In the case of the FLUX2D finite element packages used in this thesis, this could be done with the FLUX/SIMULINK coupling tool. However, in to capture accurate flux density waveforms using this direct method it would be necessary to perform several finite element solutions within each switching event. This would involve a very high number of finite element solutions within an electrical cycle, possibly many thousands which would be prohibitive in terms of computation time.

An alternative method which has been used in this study is to make use of the fact that the high frequency ripple current set by the hysteresis band, tends to be small compared to the fundamental. The method performs three finite element simulations over one electrical cycle. The first is for the current waveform without the high frequency switching waveform. The next two simulations are for the same rated waveform but with +5% of the peak added and the third with -5% of the peak subtracted as shown in Figure 3.21 for the case of a sinusoidal rated current of 326.2 A peak at 4,000rpm. These three simulations are carried out with time steps that typically generate field solutions at intervals of a few degrees of electrical angle. In the waveforms shown, simulations were performed every 3.6° electrical.

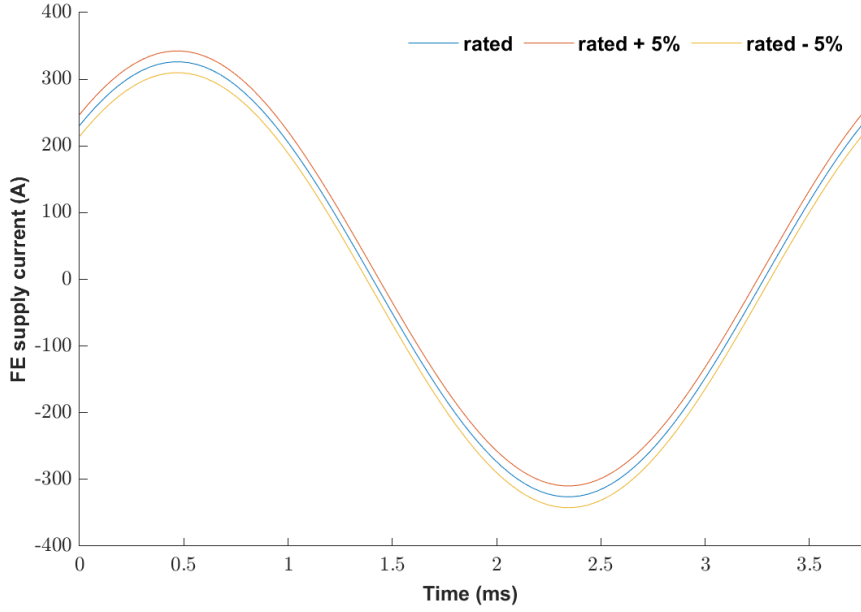


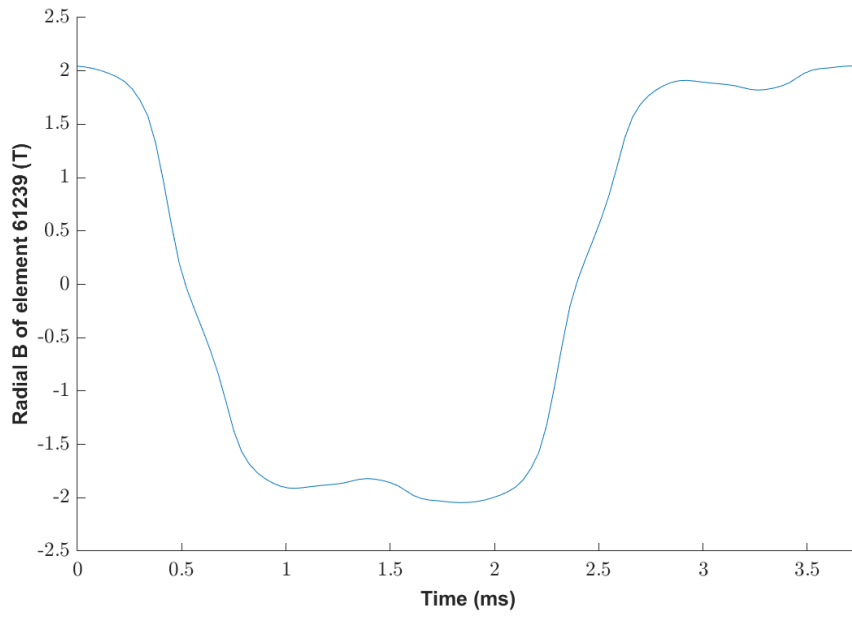
Figure 3.21 Three current waveforms used for the finite element simulations

These three simulations are then post-processed to produce for each mesh element in the stator core at each time step a value of flux density and an estimate of $\frac{dB}{dI}$ based on the following approximation:

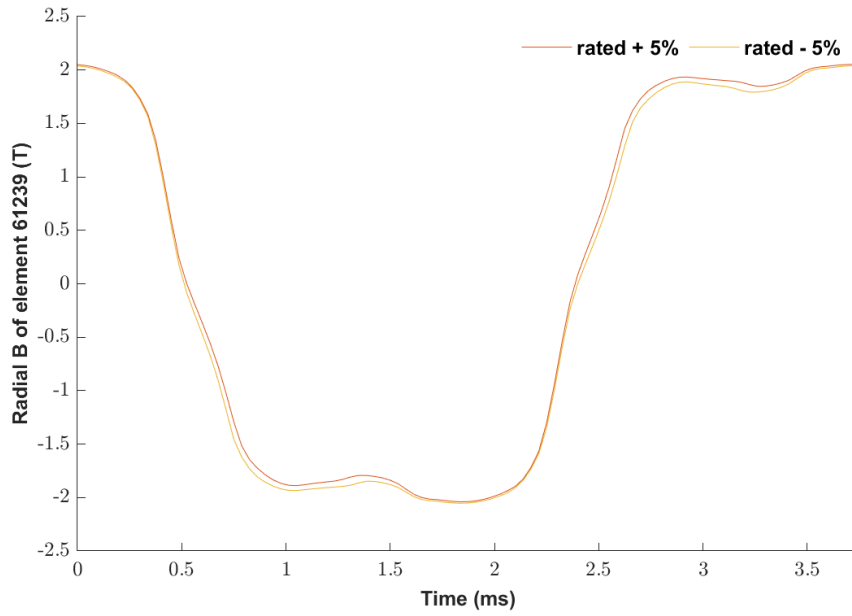
$$\frac{dB_{ij}}{dI_j} \approx \frac{B_{ij}(I + \Delta I) - B_{ij}(I)}{\Delta I} \quad (3.4)$$

For each element in the mesh, the flux density waveform predicted for the rated current can have a ripple component added by simply scaling the SIMULINK predicted high frequency current by the $\frac{dB}{dI}$ value, assuming that this remains constant during the finite element simulation time step.

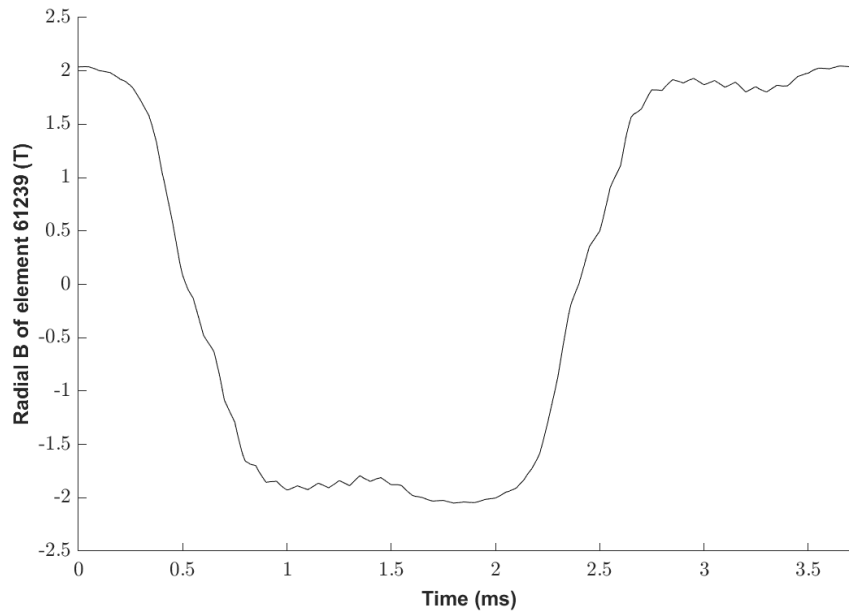
As an example, Figure 3.22(a) shows the variation in flux density from the three finite simulations for element 61239 which is the middle of the stator tooth. The calculated $\frac{dB}{dI}$ waveform for this element calculated from the simulations is shown in Figure 3.22(b) while Figure 3.22(c) shows the calculated flux density waveform in this element for the simple case of a 10 kHz symmetrical 5% ripple.



(a) Flux density waveform for rated current density waveform



(b) $\frac{dB}{dt}$ waveforms calculate from finite element simulations



(c) Calculated flux density waveform

Figure 3.22 Example of the calculation method for adding high frequency switching effect to element-by-element flux density waveforms

This method is based on a linearised perturbation model but does have the very significant advantage of a much lower computational requirement, with only 100s or so finite element simulations required. Once these three simulations have been performed, this finite element field data can be used for many different cases of switching conditions without the need for more finite element simulations.

In general, this chapter focuses on developing a method to calculate flux density waveforms in every individual element of a finite element mesh which considering the high frequency switching effects. Several tasks are finished viz magnetostatic finite elements simulations based on Altair FLUX2D at the fundamental frequency to calculate machine parameters and fundamental flux density waveforms, high frequency switching current waveform prediction based on SIMULINK and post processing for the flux density exported from finite element software based on MATLAB, which allow to calculate flux density waveforms under different switching conditions. In addition, the modelled switching current waveforms illustrate that even for the simple hysteresis controller, the current behaviour is different from sawtooth superimposed onto the demand waveform with many fewer switching events that might be expected.

Reference

- [1] D. Kowal, P. Sergeant, L. Dupre, and L. Vandebossche, "Comparison of iron loss models for electrical machines with different frequency domain and time domain methods for excess loss prediction," *IEEE Trans. Magn.*, vol. 51, no. 1, 2015, doi: 10.1109/TMAG.2014.2338836.
- [2] A. Krings and J. Soulard, "Overview and Comparison of Iron Loss Models for Electrical Machines," *J. Electr. Eng.*, vol. 10, no. May 2010, pp. 162–169, 2010.
- [3] J. Rens, L. Vandebossche, and O. Dorez, "Iron loss modelling of electrical traction motors for improved prediction of higher harmonic losses," *World Electr. Veh. J.*, vol. 11, no. 1, pp. 1–14, 2020, doi: 10.3390/WEVJ11010024.
- [4] Z. Q. Zhu *et al.*, "Evaluation of Iron Loss Models in Electrical Machines," *IEEE Trans. Ind. Appl.*, vol. 55, no. 2, pp. 1461–1472, 2019, doi: 10.1109/TIA.2018.2880674.
- [5] X. Chen, H. Wu, J. D. Ede, G. W. Jewell, L. M. Jones, and H. Ghadbeigi, "A model to account for magnetic permeability changes resulting from edge damage caused by laser cutting in a high performance cobalt-iron alloy," 2023.
- [6] R. Cui, S. Li, and J. He, "Effect of blanking on magnetic and mechanical properties of non-oriented electrical steel," *Procedia Manuf.*, vol. 50, no. 2019, pp. 22–25, 2020, doi: 10.1016/j.promfg.2020.08.005.
- [7] D. Miyagi, K. Miki, M. Nakano, and N. Takahashi, "Influence of compressive stress on magnetic properties of laminated electrical steel sheets," *IEEE Trans. Magn.*, vol. 46, no. 2, pp. 318–321, 2010, doi: 10.1109/TMAG.2009.2033550.
- [8] A. Boglietti, P. Ferraris, and M. Lazzari, "Power derating for inverter fed induction motors," *Conf. Rec. - IAS Annu. Meet. (IEEE Ind. Appl. Soc.)*, vol. 1, pp. 55–61, 1994, doi: 10.1109/ias.1994.345499.
- [9] A. YU, "An Investigation of torque density and losses in high-speed permanent magnet machines," 2018.
- [10] Motor-CAD Software, "Motor-CAD Winding temperature model calibration using Finite Element module," no. November, 2020.

Chapter 4 Iron loss prediction in electrical machines

4.1 Conventional iron loss prediction models for electrical machines

The previous chapter has described methods for generating flux density waveform for every element within the stator core of an electrical including, including the representation of the high frequency switching effects. The final stage in the prediction of the iron loss in a machine is to translate each individual flux density waveform into an equivalent loss density and then combine these via a weighted sum and scale to produce an overall loss.

Many methods have been developed for predicting iron loss in electrical machines given the flux density waveforms throughout the stator core. Almost all of these methods are based on separating the loss into a number of different components. The most commonly used loss separation model in electrical machines research in recent years are variations on the model proposed by Bertotti [1]–[4] in which the loss is separated into hysteresis loss, excess loss and classical eddy current loss.

4.1.1 Hysteresis loss

Hysteresis loss is caused by the Barkhausen jumps, which cause a change in the localised domain structure as individual magnetic domains start to align with the applied field. The loss associated with these numerous Barkhausen jumps is the potential energy difference before and after the jump [5]. When the applied magnetising field strength waveform has no harmonics or minor reversals within the waveform, the region of iron which is exposed to this field follows a single hysteresis loop, and example of which is shown in Figure 4.1. The hysteresis loss density (W/kg) per cycle is equal to the area enclosed within the loop. Equation (4.1) has been shown to produce good agreement with experiments loss measurements for flux density waveforms with no harmonic flux-reversal [6]:

$$P_h = k_h f B_m^{\alpha_h} \quad (4.1)$$

Where k_h and α_h are the material-specific coefficients established from a series of experimental measurements. The frequency and peak flux density are f and B_m respectively. It is worth noting that this equation can be applied to non-sinusoidal flux density waveforms providing there are no reversals in the waveform.

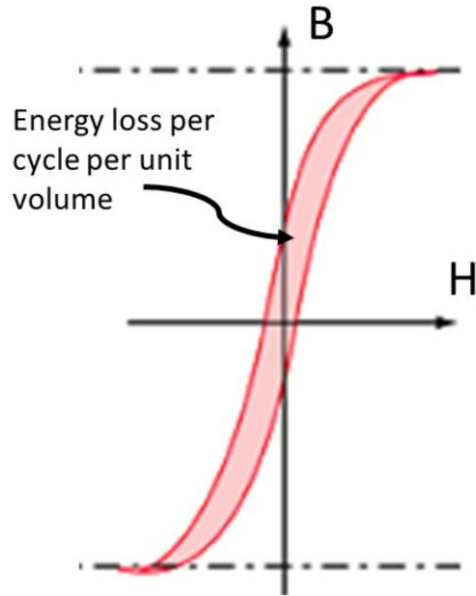


Figure 4.1 Typical hysteresis loop (with no minor loops) for a soft magnetic material

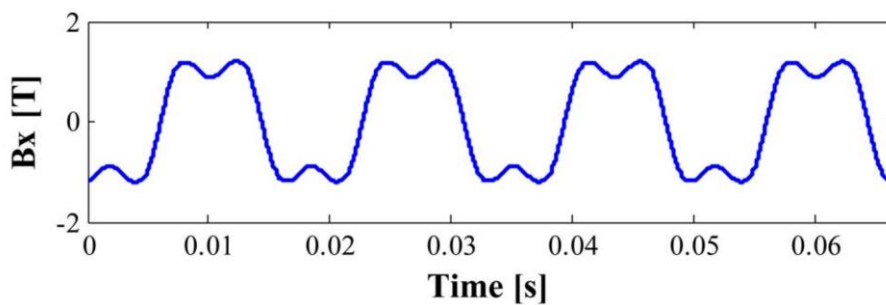
When the flux density waveform has flux reversals which generate minor loops as shown in the example in Figure 4.2, the following correction can be applied [7].

$$P_h = K(B_m) \times P_h(B_m) \quad (4.2)$$

In above equation,

$$K(B_m) = 1 + \frac{0.65}{B_m} \sum_{i=1}^{N_{mlp}} \Delta B_i \quad (4.3)$$

Where N_{mlp} is the number of the minor loops and ΔB_i is the flux density variation during the excursion around a minor loop.



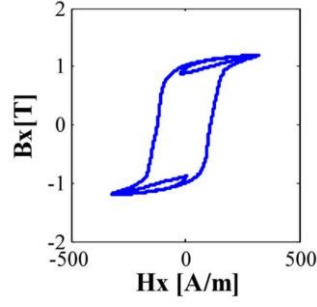


Figure 4.2 Example of flux density waveform with two flux reversal per cycle and the corresponding major and minor hysteresis loops (Source: [8])

4.1.2 Excess loss prediction model

As part of the work on loss separation proposed by Bertotti [1]–[4], the concept of excess loss was introduced which was based on domain wall eddy current effects. The eddy current counter field is mainly caused by the domain wall movement. According to Williams model [9], the eddy counter field of the moving wall is described by:

$$H_e = \frac{8M_s \sigma d}{\pi^3} \left(\sum_{\text{odd } n} \frac{1}{n^3} \right) v = \sigma G_w \dot{\phi}_w \quad (4.4)$$

where $\dot{\phi}_w$ is the flux rate provided by the domain wall movement, and M_s is the saturation magnetisation. The parameter G_w can be expressed as:

$$G_w = \frac{4}{\pi^3} \left(\sum_{\text{odd } n} \frac{1}{n^3} \right) \approx 0.136 \quad (4.5)$$

For n_w individual activated domain walls at a given time, then:

$$n_w \dot{\phi}_w = S \frac{dB}{dt} \quad (4.6)$$

Where S is the cross-section area of lamination and B is the average flux density. According to equations (4.4) and (4.6):

$$H_e = \frac{\sigma G_w S}{n_w} \frac{dB}{dt} \quad (4.7)$$

and

$$P_e = \frac{\sigma G_w S}{n_w} \left(\frac{dB}{dt} \right)^2 \quad (4.8)$$

From equation (4.8) it can be seen that the excess loss is inversely proportional to the parameter n_w , which is the number of the number of the individual activated domains at a given time. Hence, when n_w tends to infinity, the excess loss tends to zero. Similarly, magnetic objects instead of domain walls, equation (4.7) and (4.8) become:

$$H_e = \frac{\sigma G_{mo} S dB}{n_{mo} dt} \quad (4.9)$$

and

$$P_e = \frac{\sigma G_{mo} S}{n_{mo}} \left(\frac{dB}{dt} \right)^2 \quad (4.10)$$

In above equations, G_{mo} is damping factor which depends on the shape and internal structure of the magnetic object and n_{mo} represents the number of the active magnetic objects. The parameter \hat{n} can be used to illustrate the structural and dynamic characteristics of the magnetic objects:

$$\hat{n} = n_{mo} \frac{G_w}{G_{mo}} \quad (4.11)$$

Hence, \hat{n} is the effective number of the magnetic objects and equations (4.9) and (4.10) become:

$$H_e = \frac{\sigma G_w S dB}{\hat{n} dt} \quad (4.12)$$

and

$$P_e = \frac{\sigma G_w S}{\hat{n}} \left(\frac{dB}{dt} \right)^2 \quad (4.13)$$

Equation (4.12) and (4.13) illustrate that if $\hat{n} = f(H_e)$ is known, and neglecting the skin effect, the excess loss can be calculated for an arbitrary flux density waveform. Bertotti found that from experiments with many iron-based soft magnetic materials, that $\hat{n} = f(H_e)$ follow linear law [1], [2]:

$$\hat{n} = \hat{n}_o + \frac{H_e}{V_o} \quad (4.14)$$

Where V_o is the parameter that can be obtained in experiments. Equation (4.11) could be written as:

$$\hat{n} \approx \frac{H_e}{V_o} \quad (4.15)$$

For non-oriented material, the instantaneous excess loss can be written as:

$$p_e = \sqrt{\sigma G_w S V_o} \left| \frac{dB}{dt} \right|^{\frac{3}{2}} \quad (4.16)$$

The average loss over a one electric cycle for an arbitrary waveform is therefore given by:

$$P_e = \frac{\sqrt{\sigma G_w S V_o}}{T} \int_T \left| \frac{dB}{dt} \right|^{\frac{3}{2}} dt \quad (4.17)$$

For the particular case of a sinusoidal flux density variation equation (4.17) becomes:

$$P_e = 8.67 \sqrt{\sigma G_w S V_o} f^{\frac{3}{2}} B_m^{\frac{3}{2}} \quad (4.18)$$

The only unknown parameter in equation (4.17) and (4.18) is V_o , which could be established from experimental measurements on material samples. However, it has been noted that the value of V_o depends on the maximum induction and so a single value will not necessarily provide a good representation over a range of different operating conditions [1], [2].

4.1.3 Classical resistance-limited model for predicting eddy current loss

The classical resistance-limited eddy current model is a straightforward and widely used method for the calculation of eddy currents in the post-processing of magneto-static finite element predictions of flux density in the cores of electrical machines. It assumes the eddy currents do not cause any significant skin effect and hence has an upper frequency limit beyond which it will tend to overestimate the eddy current loss. This frequency limit depends on both material properties and component dimensions. When there is significant skin-effect, the eddy current is said to be inductance limited and the classical resistance limited model tends to overestimate eddy current loss in this operating regime.

The resistance-limited model also assumes that the material is homogeneous and so neglects effects of domain structure [5]. The classical equation for resistance limited one-dimensional eddy current can be derived for the idealised lamination model of Figure 4.3. The assumption of one-dimensional eddy currents is based on the case that $d \ll L$ and that the flux density vector \vec{B} is in the z direction. Due to $d \ll L$ and \vec{B} is along the z axis, so the induced electric field vector \vec{E} is dominated by the x component.

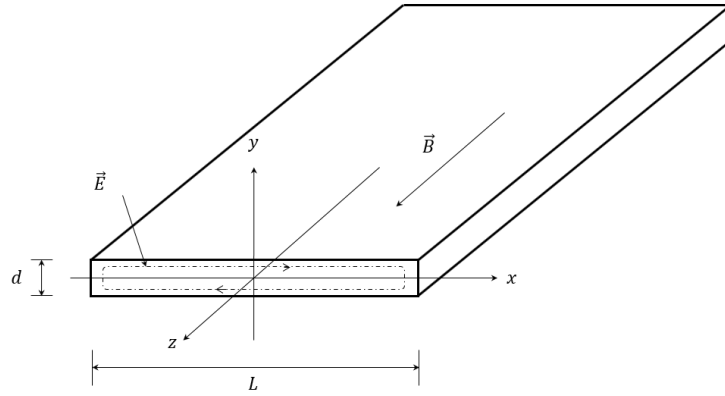


Figure 4.3 Representative lamination model for one-dimensional eddy current flow
(Source:[5])

The vectors representations of the B and E can be written as:

$$B = 0\vec{i} + 0\vec{j} + B\vec{k} \quad (4.19)$$

$$E = E_x\vec{i} + 0\vec{j} + 0\vec{k} \quad (4.20)$$

Where \vec{i} , \vec{j} and \vec{k} and the unit vectors of the Cartesian coordinate separately. According to Maxwell's equation:

$$\text{curl}E = -\frac{\partial B}{\partial t} \quad (4.21)$$

Combining equations (4.19), (4.20) and (4.21):

$$\frac{\partial E_x}{\partial y} = \frac{\partial B_z}{\partial t} \quad (4.22)$$

In low frequency condition, the skin effect can be neglected. So, B is constant throughout the cross-section of the lamination. Then from equation (4.22):

$$E_x = \left(\frac{dB_z}{dt}\right)y + c \quad (4.23)$$

Where c is a constant of integration.

For low frequency conditions, the continuity of current equation can be expressed as:

$$\text{div}\vec{j} = 0 \quad (4.24)$$

The eddy current J is related to the electric field E by:

$$J = \sigma E \quad (4.25)$$

Where σ is the lamination electrical conductivity. According to equation (4.24) and (4.25):

$$\text{div}E = 0 \quad (4.26)$$

Therefore, the path line of the eddy current and electric field is closed. And the path line at $y = y_0$ will reverse direction when $x = \pm\infty$ and have an opposite direction at $y = -y_0$. Hence, the symmetry requirement becomes:

$$E_x|_{y=y_0} = -E_x|_{y=-y_0} \quad (4.27)$$

According to equation (4.23) and (4.27) then $c = 0$.

The local eddy current power loss density is given by:

$$p_c(t) = \sigma E_x^2 \quad (4.28)$$

Hence, the spatial average is given by:

$$\bar{p}_c(t) = \frac{1}{d} \int_{-\frac{d}{2}}^{\frac{d}{2}} p_c(t) dy \quad (4.29)$$

According to equation (4.23) and (4.28):

$$\bar{p}_c(t) = \frac{\sigma d^2}{12} \left(\frac{dB}{dt} \right)^2 \left(\frac{W}{m^3} \right) \quad (4.30)$$

The average value for an electrical cycle is:

$$P_c(t) = \frac{\sigma d^2}{12\delta T} \int_T \left(\frac{dB}{dt} \right)^2 dt \left(\frac{W}{kg} \right) \quad (4.31)$$

The above equation can be applied to any arbitrary waveform. For the specific case of a sinusoidal flux density variation, the eddy current loss density simplifies to:

$$P_c = \frac{\sigma d^2 \pi^2}{6\delta} f^2 B_{max}^2 \quad (4.32)$$

4.1.4 Total loss calculation

The total core loss density can be calculated by a summation of the three loss components over one electrical cycle:

$$P(t) = k_h f B_m^{\alpha_h} \left(1 + \frac{0.65}{B_m} \sum_{i=1}^{N_{mlp}} \Delta B_i \right) + \sqrt{\sigma G_w S V_o} \frac{1}{T} \int_T \left| \frac{dB}{dt} \right|^{\frac{3}{2}} dt + \frac{\sigma d^2}{12\delta T} \int_T \left(\frac{dB}{dt} \right)^2 dt \left(\frac{W}{kg} \right) \quad (4.33)$$

This equation requires the setting of several material specific coefficient which are derived from measurements of loss as a function of flux density and frequency, including quasi-static hysteresis loss measurements. Table 4.1 shows the coefficients for NO20 Silicon iron from [10].

Table 4.1 Material coefficients for NO20

	Value for NO20 Silicon Iron
k_h	0.0172
α_h	1.21
$\sqrt{\sigma G_w S V_o}$ (often lumped into k_{exc})	2.5e-4
σ	1923077
d	2e-4 m
δ	7650 kg/m ³

4.2 Iron loss prediction for high frequency switching

4.2.1 Idealised saw-tooth current ripple test case

The first test case considered for the machine operating at 4,000 rpm and rated torque (i.e. with a phase current peak of 326.2 A) with a series of idealised 10 kHz triangular saw-tooth current ripple superimposed onto the 266.7 Hz sinusoidal current in this 8 pole machine. This results in 37-38 cycles of high frequency switching per cycle of the fundamental. Figure 4.4 shows the fundamental together with the various saw-tooth ripple addition and a close up of the region around 0.5 ms in which the ripple components are clearer. Each of these current waveforms were used in combination with the element-by-element predicted variations of flux

density for the nominal sinusoidal and the calculated dB/dI variation described using the method in section 3.6 of Chapter 3. It is worth noting that the finite element solutions required to calculate the dB/dI only needs to be established once for a given load current (in this case a peak of 326.2 A). The simulation different ripple levels simply use this one finite element characterisation to add on the appropriate estimated high frequency flux density variation.

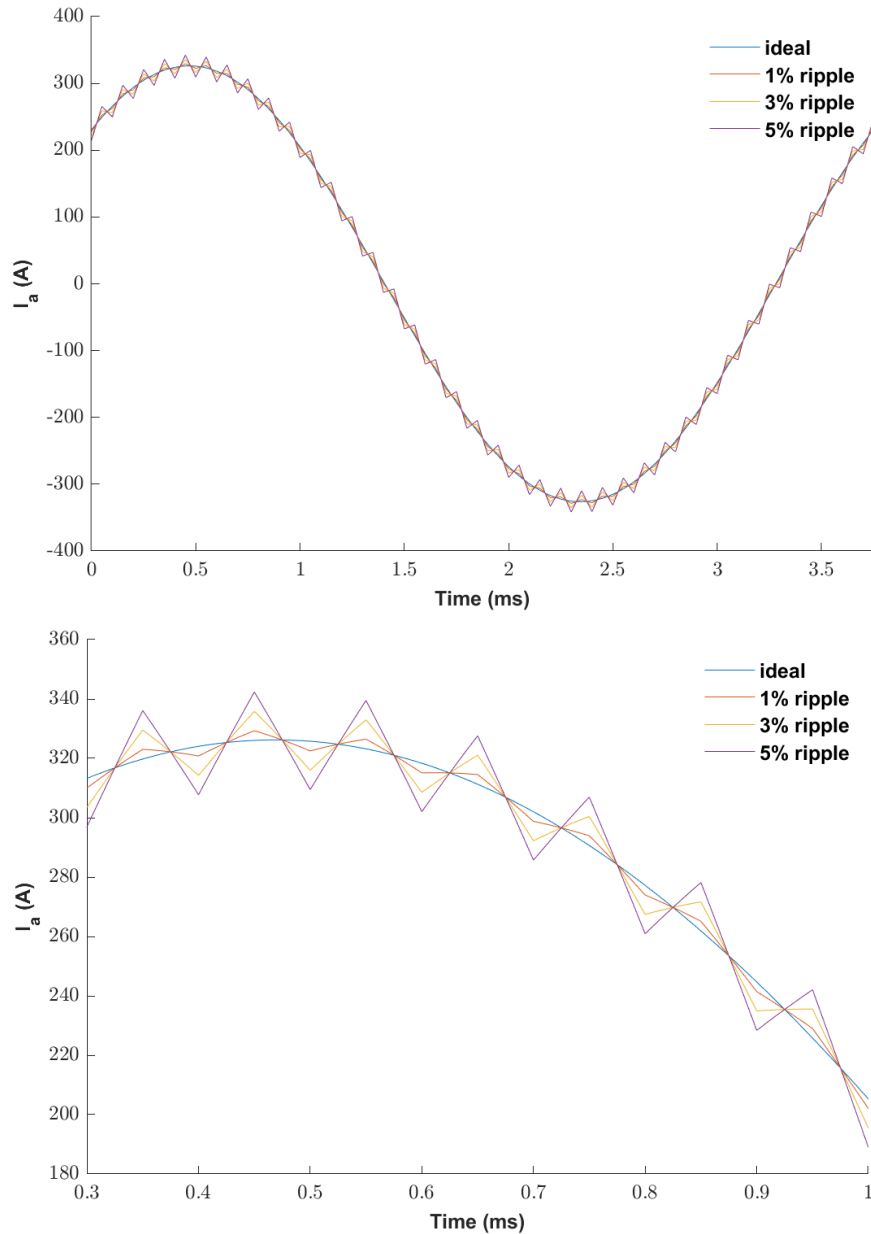
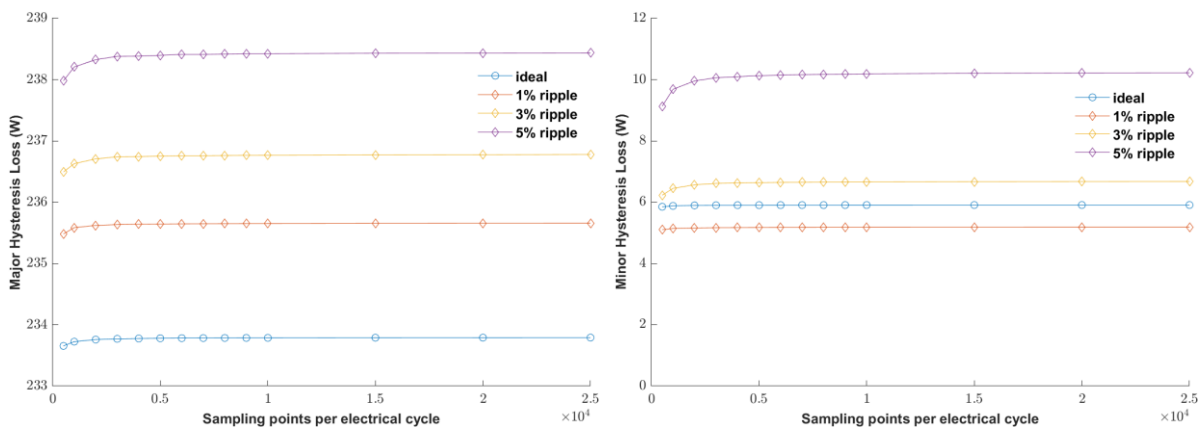


Figure 4.4 Idealised reference current waveforms for the first test case

The methodology described in chapter 3 was used to generate element-by-element flux density variations at a range of different number of sample rates within an electrical cycle and the individual components of loss for the total machine were calculated at these different sampling rates. The resulting variations in calculated loss with the number of sampling points

is shown in Figure 4.5. All the loss components settle down by 5,000 sampling points per electrical cycle, although arguably from a practical point of view, there is very little change in loss beyond 2,000 sampling points per cycle. There are several interesting points shown by this data:

- There is an increase in the major hysteresis loss of $\sim 5\text{W}$ to 238W as the ripple is increased. Since the major hysteresis loss is only a function of the peak flux density during a cycle, this increase is a result of the phasing between the ripple and the peak of the sinusoidal current combining to increase the peak flux density as shown previously in the close-up of the current waveforms in Figure 4.4. The level of increase will be highly dependent on the phase relationship between the ripple and the fundamental
- Although there are no small reversals in the pure sinusoidal current there is still some predicted minor loop loss in the no-ripple case due to harmonics introduced in the flux density waveforms by features such as spatial harmonics in the armature field and magnetic saturation effects. This shows the importance of using finite element field calculations as localized flux density waveforms can contain different harmonics to the machine current.
- A 5% saw-tooth ripple in the current results in an increase in total loss to 112% of the value for the pure sinusoid. In this case, the loss is dominated by the major hysteresis loss which is only affected to small degree by the ripple.
- A 5% saw-tooth ripple in the current results in an increase in the classical eddy current loss to $\sim 140\%$ of the value for the pure sinusoid.



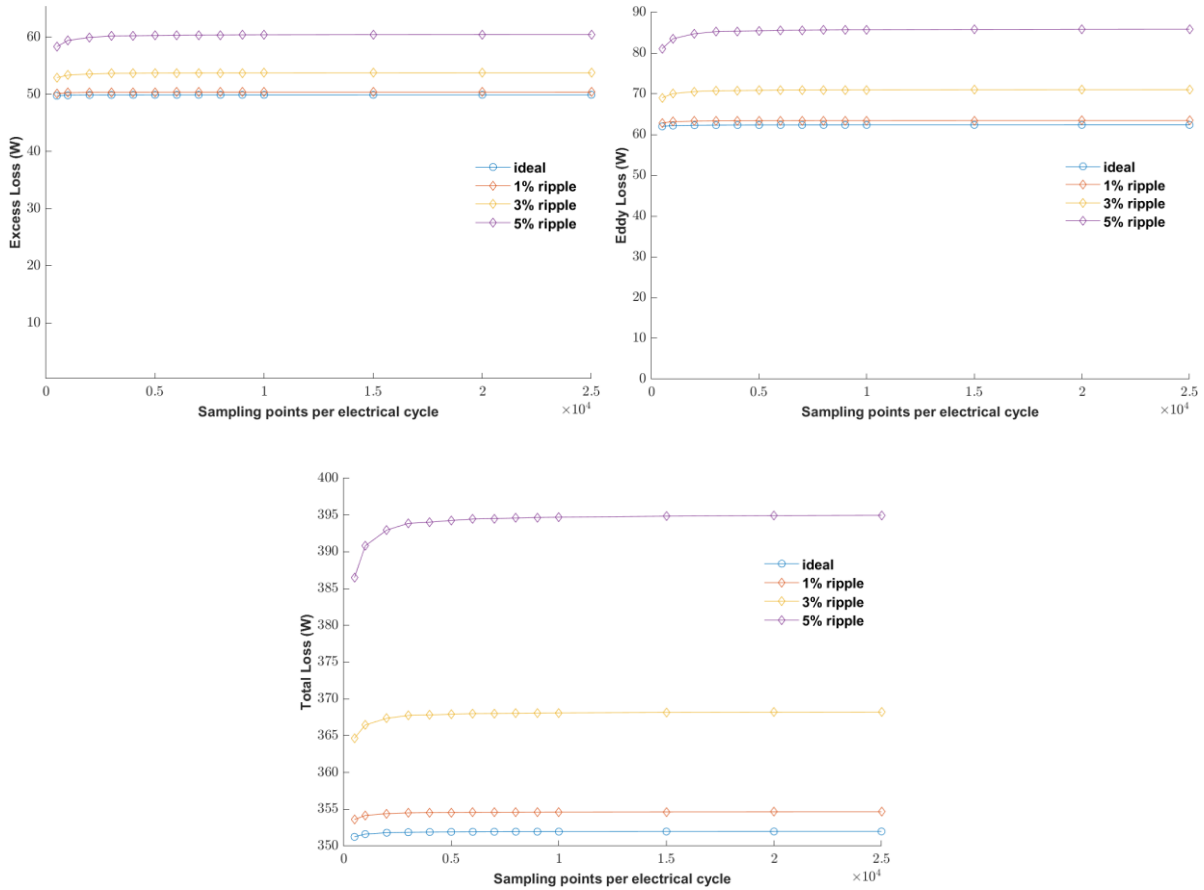


Figure 4.5 Variation in calculated components of loss and total loss with increasing number of sampling points per fundamental electrical cycle

4.2.2 Grounded star connection electrical machine

The next set of cases considered was the reference machine operating at rated current at 4,000rpm with $\pm 1\%$, $\pm 3\%$ and $\pm 5\%$ hysteresis bands. In this case, the star-point is grounded. The current waveforms for these hysteresis bands and a pure sinusoid with a peak of 326.3A is shown in Figure 4.6 along with a close-up of the region around the positive peak of the sinusoid. As was the case with several of the current waveforms in chapter 3, the ripple current is far more complex than the simple symmetrical waveforms investigated in the previous chapter. The number of switching events per electrical cycle for the $\pm 1\%$, $\pm 3\%$ and $\pm 5\%$ hysteresis bands are 149, 52 and 33 respectively. The Figure 4.7 presents the predicted switching signal for phase A in the reference machine with grounded star-point operating at rated current and 4,000 rpm for hysteresis bands of $\pm 1\%$, $\pm 3\%$ and $\pm 5\%$, which shows the effects of the hysteresis band viz switching frequency will drop with the increasing of the hysteresis band.

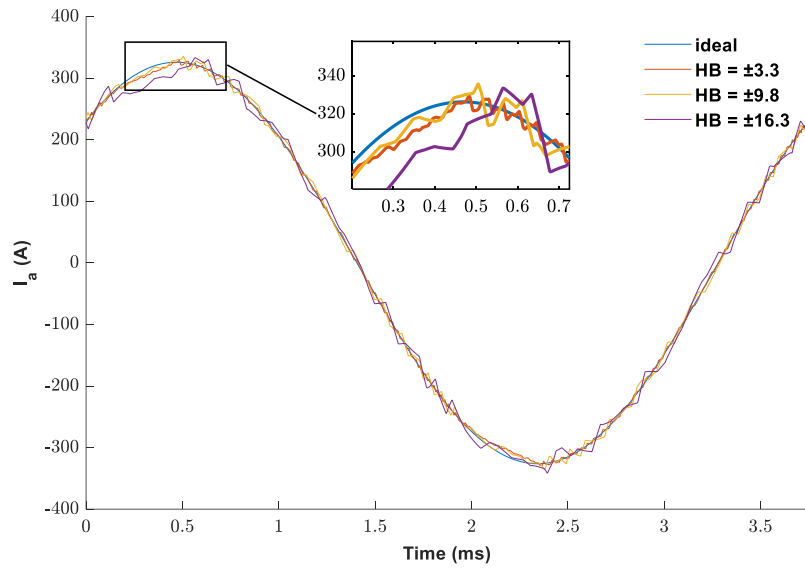


Figure 4.6 Predicted current for phase A in the reference machine with a grounded star-point operating at rated current and 4,000 rpm for hysteresis bands of $\pm 1\%$, $\pm 3\%$ and $\pm 5\%$

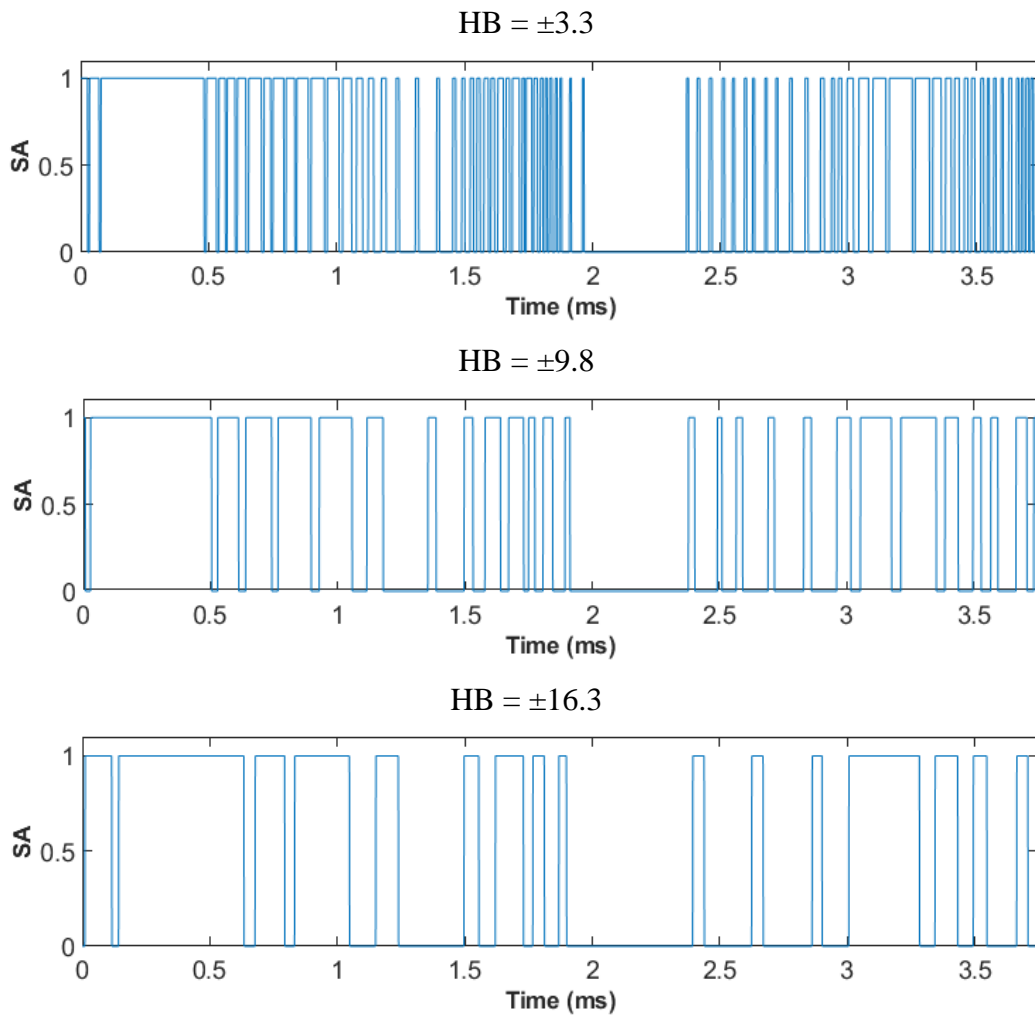
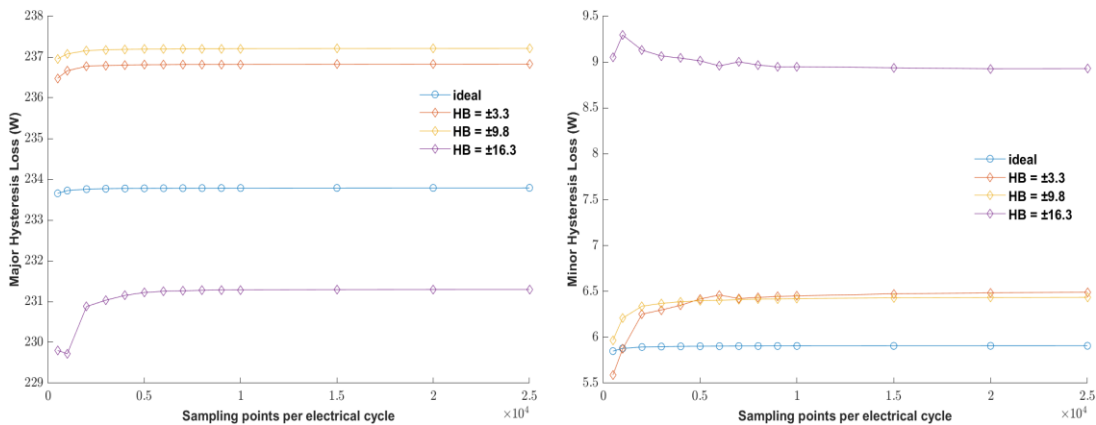


Figure 4.7 Predicted switching signal for phase A in the reference machine with grounded star-point operating at rated current and 4,000 rpm for hysteresis bands of $\pm 1\%$, $\pm 3\%$ and $\pm 5\%$

The methodology described in chapter 3 was again used to generate element-by-element flux density variations at a range of different number of sample rates within an electrical cycle. The resulting variations in calculated loss with the number of sampling points is shown in Figure 4.8. There are several interesting features of these loss predictions:

- The overall loss settles down to its final level after ~ 7000 sample points per electrical cycle for all cases. As would be expected, the smallest hysteresis band, which has the highest switching frequency, requires the most sample points.
- The total loss with the $\pm 5\%$ hysteresis band increases to 104% of the value for the pure sinusoid. This is lower than the $\pm 5\%$ symmetrical sawtooth in the previous section. This is due to the fact that there are intervals during the waveform, e.g. around the zero crossing in which the current tracks the sinusoidal demand waveform with little switching action.
- The difference between the various hysteresis bands is smaller than the saw-tooth example in the previous section since the switching frequency reduces with the increasing hysteresis band.



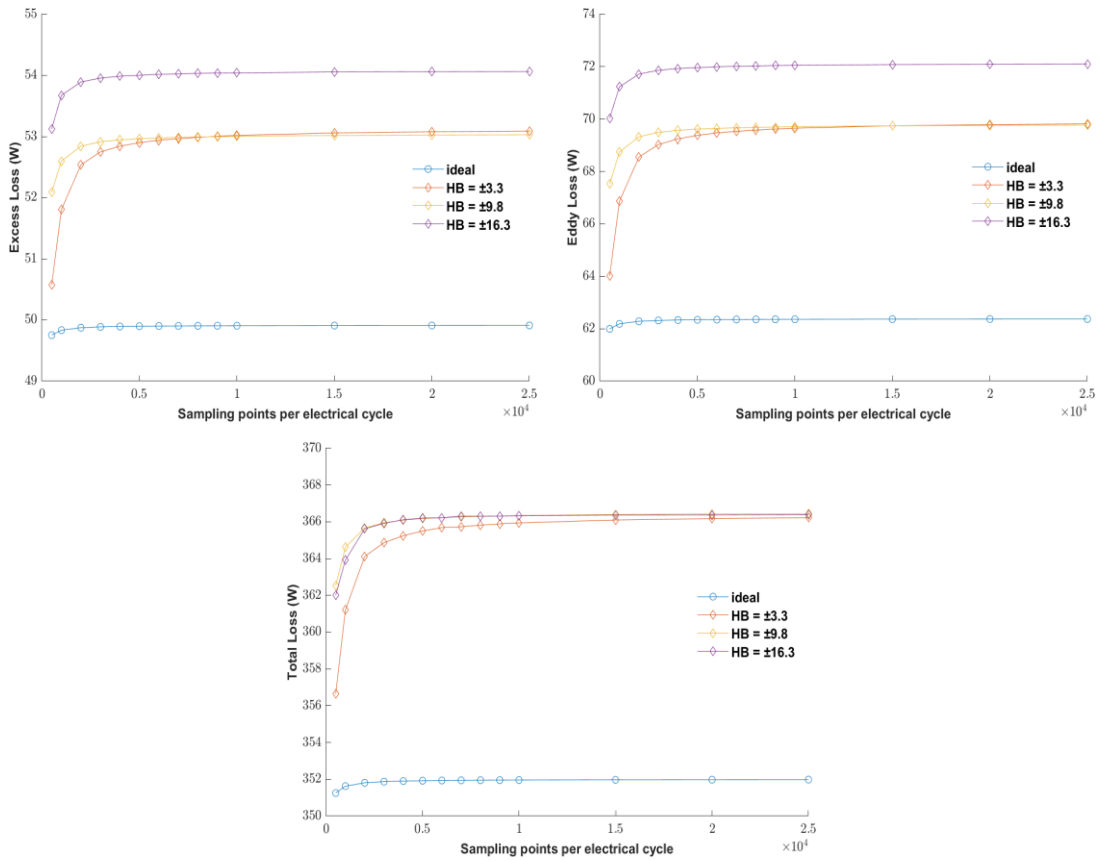


Figure 4.8 Variation in calculated components of loss and total loss with increasing number of sampling points per fundamental electrical cycle

4.2.3 Floating star connection electrical machine

The final set of cases considered was the reference machine operating at rated current at 4,000 rpm with $\pm 1\%$, $\pm 3\%$ and $\pm 5\%$ hysteresis bands but with a floating star-point. The current waveforms for these hysteresis bands and a pure sinusoid with a peak of 326.2 A is shown in Figure 4.9. along with a close-up of the region around the positive peak of the sinusoid. The Figure 4.10 presents the predicted switching signal for phase A in the reference machine with floating star-point operating at rated current and 4,000 rpm for hysteresis bands of $\pm 1\%$, $\pm 3\%$ and $\pm 5\%$, which shows the effects of the hysteresis band viz switching frequency will drop with the increasing of the hysteresis band.

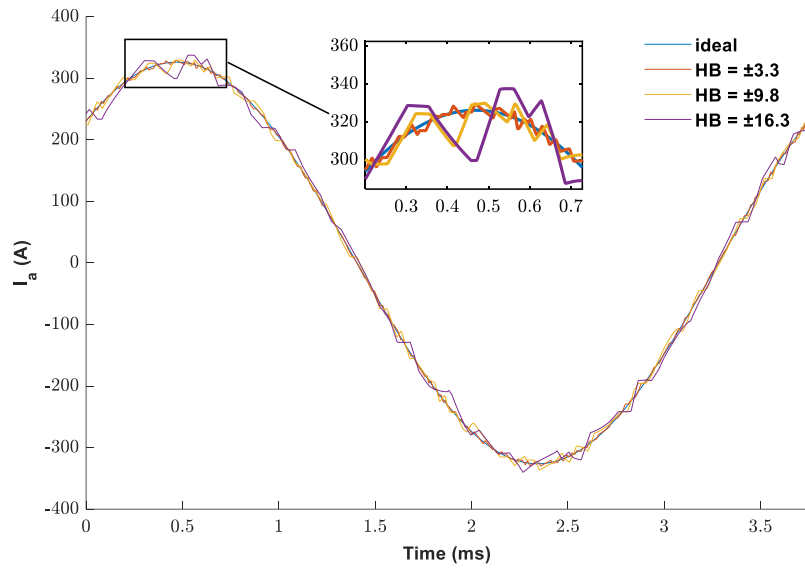


Figure 4.9 Predicted current for phase A in the reference machine with a floating star-point operating at rated current and 4,000rpm for hysteresis bands of $\pm 1\%$, $\pm 3\%$ and $\pm 5\%$

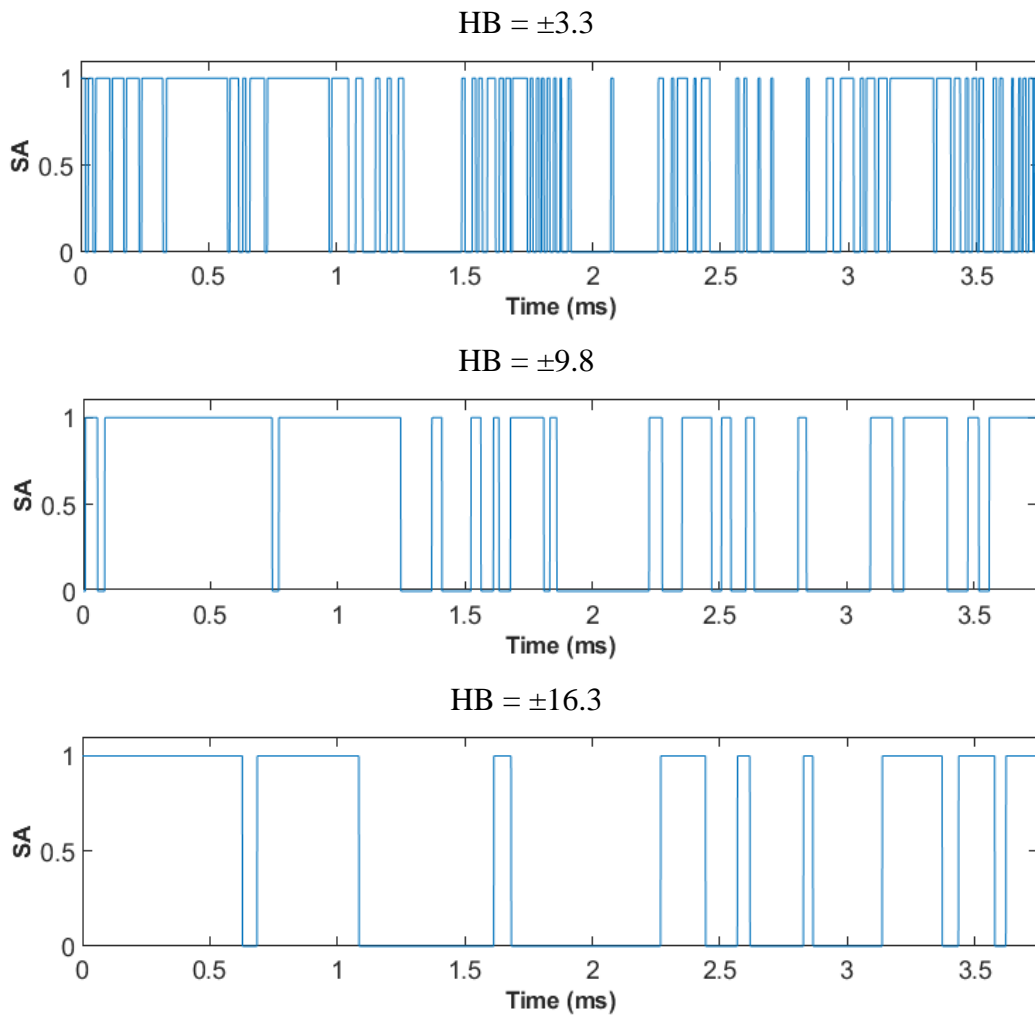


Figure 4.10 Predicted switching signal for phase A in the reference machine with floating star-point operating at rated current and 4,000 rpm for hysteresis bands of $\pm 1\%$, $\pm 3\%$ and $\pm 5\%$

The same process as the previous sections was used to generate the variation of loss components with sample number per cycle. In this case, the number of samples required to achieve a settled overall loss is lower. It is also noticeable that the highest loss is produced by the $\pm 3\%$ hysteresis band in this floating ground case rather than the $\pm 5\%$ band for the grounded case. There is a bigger variation in loss.

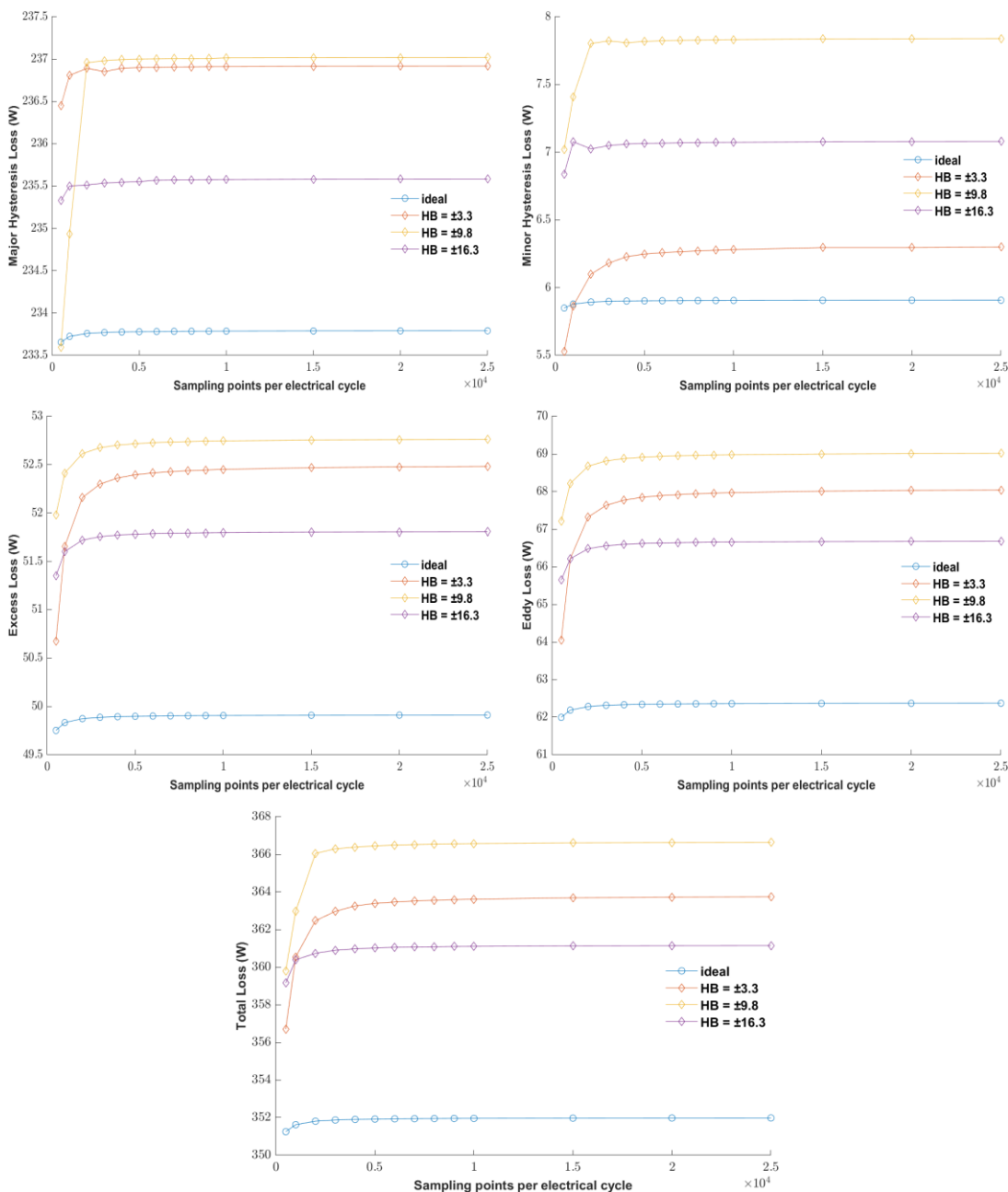


Figure 4.11 Variation in calculated components of loss and total loss with increasing number of sampling points per fundamental electrical cycle

4.3 Summary

This chapter has introduced the methods used for calculating the iron loss in an electrical machine given a series of flux density versus time waveforms in each element of the core. A summary of the total predicted loss for the 12 different combinations of conditions simulated is shown in Table 4.2. This shows that for this series of operating conditions and noting that the major loop hysteresis loss is a significant contributor to the loss, the increases in loss caused by switching frequency is not especially large and that there is no fixed trend with the behaviour of the converter being important.

Table 4.2 Total predicted loss for the 12 different combinations of conditions simulated

	Symmetrical Saw Tooth	Grounded star- point	Floating star- point
Pure sinusoid	352.0 W	352.0 W	352.0 W
±1% hysteresis band	354.7 W	366.2 W	363.7 W
±3% hysteresis band	368.2 W	366.4 W	366.6 W
±5% hysteresis band	395.0 W	366.4 W	361.1 W

Reference

- [1] G. Bertotti, “General Properties of Power Losses in Soft Ferromagnetic Materials.,” *IEEE Trans. Magn.*, vol. 24, no. 1, pp. 621–630, 1987, doi: 10.1109/20.43994.
- [2] G. Bertotti, “Physical interpretation of eddy current losses in ferromagnetic materials. II. Analysis of experimental results,” *J. Appl. Phys.*, vol. 57, no. 6, pp. 2118–2126, 1985, doi: 10.1063/1.334405.
- [3] G. Bertotti, “Some considerations on the physical interpretation of eddy current losses in ferromagnetic materials,” *J. Magn. Magn. Mater.*, vol. 54–57, no. PART 3, pp. 1556–1560, 1986, doi: 10.1016/0304-8853(86)90926-1.
- [4] K. Atallah and D. Howe, “The calculation of iron losses in brushless permanent magnet dc motors,” *J. Magn. Magn. Mater.*, vol. 133, no. 1–3, pp. 578–582, 1994, doi: 10.1016/0304-8853(94)90627-0.
- [5] K. Atallah, “Iron Losses in Brushless Permanent Magnet DC Machines,” 1993.
- [6] G. R. Slemon and X. Liu, “Core Losses in Permanent Magnet Motors,” *IEEE Trans. Magn.*, vol. 26, no. 5, pp. 1653–1655, 1990, doi: 10.1109/20.104480.
- [7] “A simple method of estimating the minor loop hysteresis loss in thin laminations,” *J. D. Lavers*, vol. 88, no. 5, pp. 309--352, 1978.
- [8] N. Alatawneh and P. Pillay, “The minor hysteresis loop under rotating magnetic fields in machine laminations,” *IEEE Trans. Ind. Appl.*, vol. 50, no. 4, pp. 2544–2553, 2014, doi: 10.1109/TIA.2014.2300155.
- [9] H. J. Williams, W. Shockley, and C. Kittel, “Studies of the propagation velocity of a ferromagnetic domain boundary,” *Phys. Rev.*, vol. 80, no. 6, pp. 1090–1094, 1950, doi: 10.1103/PhysRev.80.1090.
- [10] J. J. H. Paulides, G. W. Jewell, and D. Howe, “An evaluation of alternative stator lamination materials for a high-speed, 1.5 MW, permanent magnet generator,” *IEEE Trans. Magn.*, vol. 40, no. 4 II, pp. 2041–2043, 2004, doi: 10.1109/TMAG.2004.832172.

Chapter 5: Iron loss calculation considering skin effect

5.1 Introduction

Chapter 4 described a modelling approach based on combining a-priori finite element characterisation of the machine with a SIMULINK model of a converter and the machine to predict the flux density waveforms in every element including the contribution from converter switching ripple. Once the individual element flux density waveforms were calculated, the method used a reasonably standard loss separation model to predict the iron loss. However, the loss separation model is based on the classical eddy current component calculation which assumes resistance limit eddy currents and no skin-effect within the laminations. The simple analytical expression for the classical eddy current component in equation (4.32) of chapter 4 assumes that the eddy current density is uniform throughout the lamination. This is a widely adopted assumption in core loss modelling with relatively few studies attempting to account for the presence of any non-uniform distribution of field and hence eddy currents throughout the lamination [1]. This may be an entirely reasonable assumption for fundamental frequency flux variations and the first few harmonics, but there is uncertainty over whether this represents high frequency switching effects. It is normal industry practice in industrial machines to de-rate motors by 20%+ for inverter operation to accommodate this uncertainty [2].

Due to the combination of the direction in which the core is laminated and the field excitation, high frequency skin-effect in individual laminations is a fully three-dimensional problem. However, a practical machine consists of many hundreds or thousands of laminations and each of these would need to be finely meshed to capture skin-effect, the resulting full 3D model is likely to be too large to build and solve with present computer capability, although ultimately this would be the best means of capturing the full behaviour.

This chapter is concerned with the development and evaluation of a method which combines the two-dimensional finite element based modelling approach developed in chapter 4 for predicting the effect of high frequency switching waveforms with a further post-processing step that uses a one-dimensional, non-linear finite difference method to solve the diffusion equation that governs eddy current flow in laminations.

A study by Yamakazi [3] proposed a 1D post-processing method for finite element field solution which was deployed after solving the main magnetic field distribution along the

direction of the lamination thickness for each element, then estimating the iron loss with a computationally efficient method. A more complicated method has also been reported by Yamakazi [4], which considered eddy current and hysteresis effects of the lamination and feeding the corresponding reaction field into the main FEM analysis for each element. However, this method required access to the source code of the solver to modify the calculation process and extreme high computation time due to the coupling of fields and convergence issues [5]. Bottauscio directly integrated a 1D analytical diffusion equation into a FEM package to avoid the coupling effects between the 1D and 2D issues so as to reduce computation time [6].

Finite difference methods have been used to deal with the non-linear magnetisation behaviour within the lamination. These methods mathematically separated the lamination into multiple layers with constant flux and current density [7], [8]. These hybrid numerical / analytical strategies can be used in the main FEM package as post-processing tools. For system with linear magnetic materials and hence constant magnetic permeability, then flux distribution and corresponding iron loss could be predicted by closed-form analytical equations [9], [10]. However, this method tends to predict relatively higher skin effects because of the material saturation condition is not considered. There is a study based around a physics-based iron loss model for prediction of iron loss within electrical machine laminations, which calculates an equivalent magnetic permeability according to the mean flux density in the lamination[11].

This chapter focusses on a post-processing method to estimate the effect of flux redistribution caused by skin effects within the thin lamination on the prediction of iron loss in the electrical machines.

5.2 Diffusion equation models for predicting eddy currents in a thin lamination

5.2.1 Formulation of the general form of the diffusion equation

The diffusion equation is the fundamental equation that can be used to predict the distribution of eddy currents within a lamination. This can be derived from first principles as follows for the case of materials that exhibit linear magnetisation characteristics, i.e. a fixed magnetic permeability. The flux density at any point in a problem domain can be expressed as:

$$B = \mu_0(H + M) \quad (5.1)$$

For the case of a material that exhibits a linear magnetisation characteristic then:

$$M = \chi_m H \quad (5.2)$$

Where χ_m is the magnetic susceptibility and equation and leads to:

$$B = \mu_0(1 + \chi_m)H = \mu_0\mu_r H \quad (5.3)$$

Starting from the Maxwell's equation which expresses the vector form of Faraday's law:

$$\text{curl } E = -\frac{\partial B}{\partial t} = -\frac{dB}{dH} \frac{\partial H}{\partial t} \quad (5.4)$$

The magnetic field strength \vec{H} can be expressed in terms of the current density J using:

$$\text{curl } H = J \quad (5.5)$$

Applying the standard constraint:

$$\text{div } B = 0 \quad (5.6)$$

The induced current density and the magnetic flux density can be related to the electric field strength and the magnetic field strength using equations (5.7) and (5.8) respectively.

$$J = \sigma E \quad (5.7)$$

$$B = \mu H \quad (5.8)$$

The following constraint can be applied to the eddy current density:

$$\text{div } J = 0 \quad (5.9)$$

Taking the curl of equation of (5.5) and substituting in the electrical field strength for the eddy current density yields:

$$\text{curl curl } H = \text{curl } \sigma E \quad (5.10)$$

which can be rewritten as

$$\text{grad div } H - \nabla^2 H = \sigma \text{curl } E + (\text{grad } \sigma) \times E \quad (5.11)$$

$$\text{div } \mu H = \mu \text{div } H + H \cdot \text{grad } \mu = 0 \quad (5.12)$$

dividing through by the permeability yields:

$$\text{div } H = -H \cdot \frac{1}{\mu} \text{grad } \mu \quad (5.13)$$

which leads to:

$$\nabla^2 H = \sigma \frac{dB}{dH} \frac{\partial H}{\partial t} - \text{grad} \left(H \cdot \frac{1}{\mu} \text{grad} \mu \right) - \frac{1}{\sigma} (\text{grad} \sigma) \times \text{curl} H \quad (5.14)$$

This results in the general case of the diffusion equation which is the fundamental building block for eddy current analysis:

$$\nabla^2 H = \sigma \mu_0 \mu_r \frac{\partial H}{\partial t} \quad (5.15)$$

5.2.2 Solution of complex diffusion equation

For some geometries and excitations, the diffusion equation can be simplified to a point where a closed-form analytical solution can be derived. For the case of sinusoidal time-varying fields, the time derivate of the magnetic field strength can be expressed using a complex exponential form:

$$H = H e^{-j\omega t} \quad (5.16)$$

$$\frac{\partial}{\partial t} = j\omega \quad (5.17)$$

Substituting into the diffusion equation and assuming a single fixed value of material permeability, results in:

$$\nabla^2 H = j\omega \mu \sigma H \quad (5.18)$$

Analytical solutions to this equation can be established for problems with some level of simplification of the geometry of excitation. The problem of interest for iron loss prediction is the simplified one-dimensional eddy current model for thin lamination. Figure 5.1 shows the simplified model of a transformer core made up from a stack of laminations.

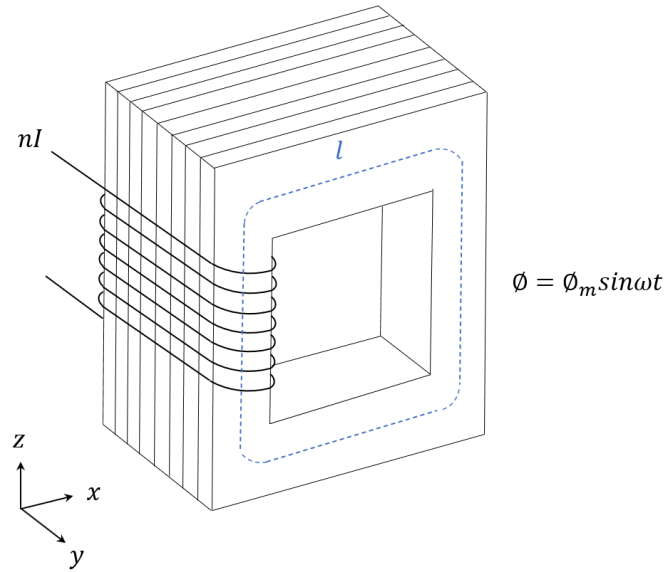


Figure 5.1 Simplified transformer lamination model

Since the dimensions of the lamination in the z and x directions are much greater than in the y -direction (usually by many orders of magnitude) the problem of localised eddy current flows can be simplified as a 1-D problem shown in Figure 5.2.

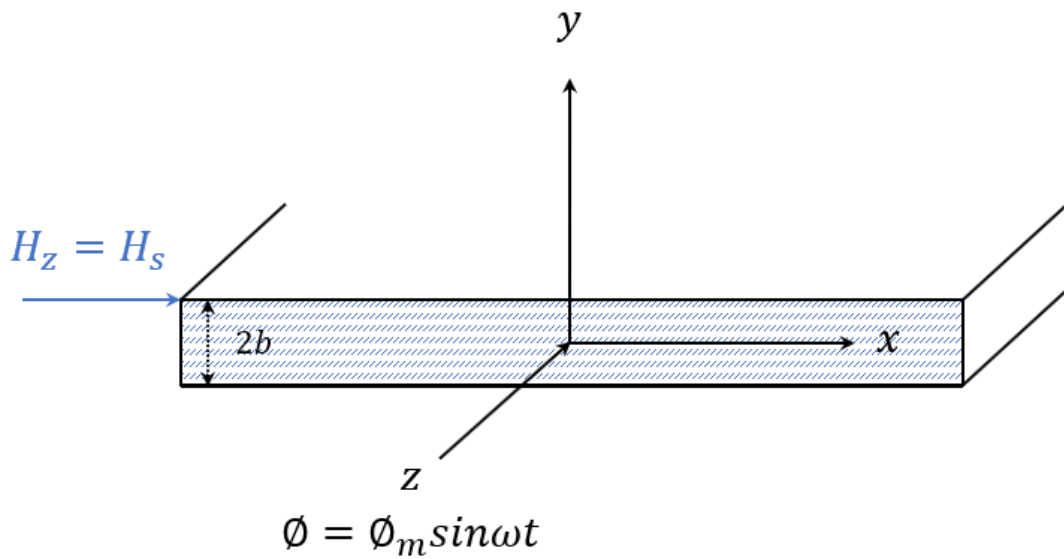


Figure 5.2 Simplified one-dimensional model of a lamination of thickness $2b$

For this 1-D problem, in which the applied magnetic field only has a z -component, then the diffusion equation reduces to:

$$\frac{\partial^2 H_z}{\partial y^2} = \sigma \mu \frac{\partial H_z}{\partial t} \quad (5.19)$$

Assuming the applied field is sinusoidal time-varying magnetic field then:

$$H_z = H_z e^{j\omega t} \quad (5.20)$$

For sinusoidal time-varying magnetic field, using equation (5.20), equation (5.19) becomes:

$$\frac{\partial^2 H_z}{\partial y^2} = j\omega\mu\sigma H = \alpha^2 H_z \quad (5.21)$$

where:

$$\alpha^2 = j\omega\mu\sigma \quad (5.22)$$

For the complex number, there is:

$$\sqrt{j} = \frac{1+j}{\sqrt{2}} \quad (5.23)$$

Defining the skin depth as δ , which is written as:

$$\delta = \sqrt{\frac{2}{\omega\sigma\mu}} \quad (5.24)$$

Therefore, the parameter α can be written as:

$$\alpha = \frac{(1+j)\sqrt{\omega\sigma\mu}}{\sqrt{2}} = \frac{1+j}{\delta} \quad (5.25)$$

The general solution of the equation (5.21) is shown with equation (5.33), where K_1 and K_2 are the coefficients to be determined from the problem specific boundary conditions.

$$H_z = K_1 e^{\alpha y} + K_2 e^{-\alpha y} \quad (5.26)$$

Applying each of the boundary conditions to the general solution provides a means of generating the solution form specific.

At $y = b$, the magnetic field strength takes a surface value H_s :

$$H_z = H_s = K_1 e^{\alpha b} + K_2 e^{-\alpha b} \quad (5.27)$$

At $y = -b$, the magnetic field strength takes the same surface value H_s :

$$H_z = H_s = K_1 e^{-\alpha b} + K_2 e^{\alpha b} \quad (5.28)$$

By implication, $K_1 = K_2$ and hence:

$$H_s = K_1 (e^{\alpha b} + e^{-\alpha b}) \quad (5.29)$$

So,

$$K_1 = \frac{H_s}{e^{\alpha b} + e^{-\alpha b}} = K_2 \quad (5.30)$$

which leads to:

$$H_z = K_1 e^{\alpha y} + K_2 e^{-\alpha y} \quad (5.31)$$

$$\varphi = \varphi_m \sin \omega t \quad (5.32)$$

This results in the final expression for the variation of the magnetic field strength with time and location in the lamination:

$$H_z = H_s \frac{(e^{\alpha y} + e^{-\alpha y})}{(e^{\alpha b} + e^{-\alpha b})} e^{j\omega t} = H_s \frac{\cosh \alpha y}{\cosh \alpha b} e^{j\omega t} \quad (5.33)$$

Equation (5.33) describes the magnetic field distribution within the lamination. The nature of the variation in this equation results in a reduction in magnetic field strength H and a phase shift in the H with increasing depth into the lamination. The attenuation of the H and phase shift growing will be accumulated with the increasing depth.

5.3 Three-dimensional finite element modelling of a reference lamination

5.3.1 Model configuration

In order to provide a benchmark against which various solutions to the diffusion equation can be compared, 3D finite element analysis was used to predict the variation in field and eddy current density in a representative rectangular strip of lamination. This section describes the 3D FE model used to verify the analytical model of eddy currents. This 3D model was based on a 0.2mm thick lamination, with the thickness oriented along the z axis as shown in Figure 5.3. The length in the y direction is 30mm and width in the x direction is 10mm. Several different magnetic representations of the material in the model were used to investigate

different aspects of the model. The Figure 5.4 shows the variation in skin depth verse frequency up to 10 kHz for a 0.2 mm thick lamination. Considering the relative permeability of the NO20 is varying with the applied magnetic field strength, so only plot the skin depth verse frequency for a fix relative permeability of 5000 to represents the tendency. The electrical conductivity using the manufacturer specified data of 1.9×10^6 S/m. Also show in Figure 5.4, when the frequency is 600 Hz, the corresponding skin depth is 0.21 mm and with the increasing of the frequency up to 10 kHz, the skin depth drops to 0.05 mm, which provide a reference for mesh size selection. Considering the frequency of applied magnetic field is 10 kHz and its corresponding skin depth for a fixed relative magnetic permeability of 5000 and an electrical conductivity of 1.9×10^6 S/m is 0.05mm, so using 5 mesh elements to capture the reaction field, so the mesh size along the z axis is 0.01 mm.

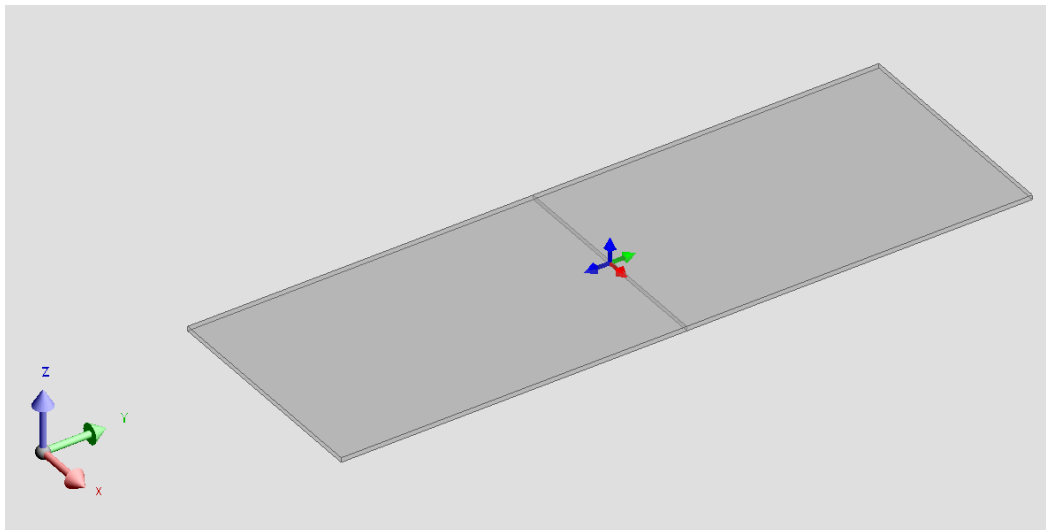


Figure 5.3 Geometry of the lamination piece used in the 3D finite element modelling

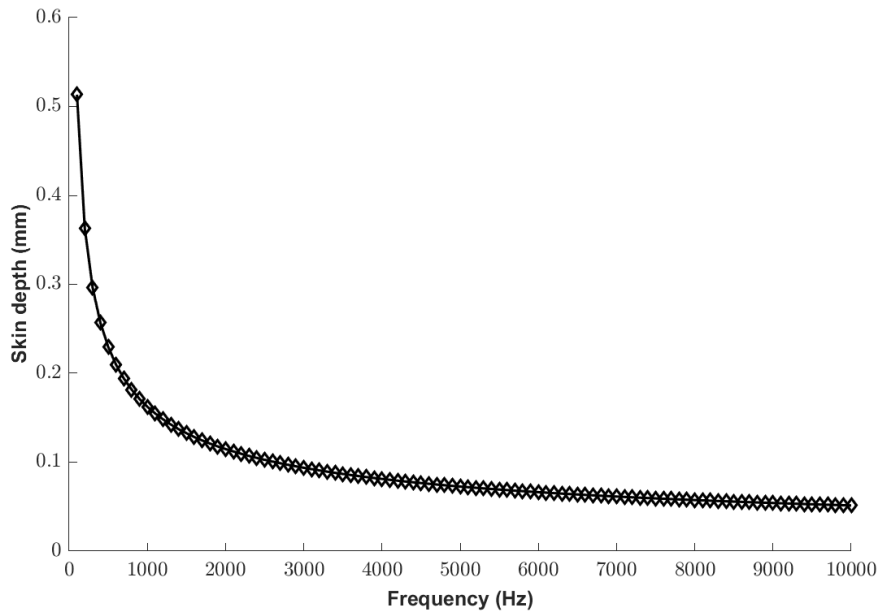


Figure 5.4 Variation in skin depth with frequency up to 10 kHz for a 0.2 mm thick lamination with a fixed relative magnetic permeability of 5000 and an electrical conductivity of 1.9×10^6 S/m

The lamination region was meshed using a regular mesh of rectangular elements, with mesh sizes of 0.2 mm, 0.6 mm and 0.01 mm in the x , y and z directions respectively as shown in Figure 5.5 and Figure 5.6.

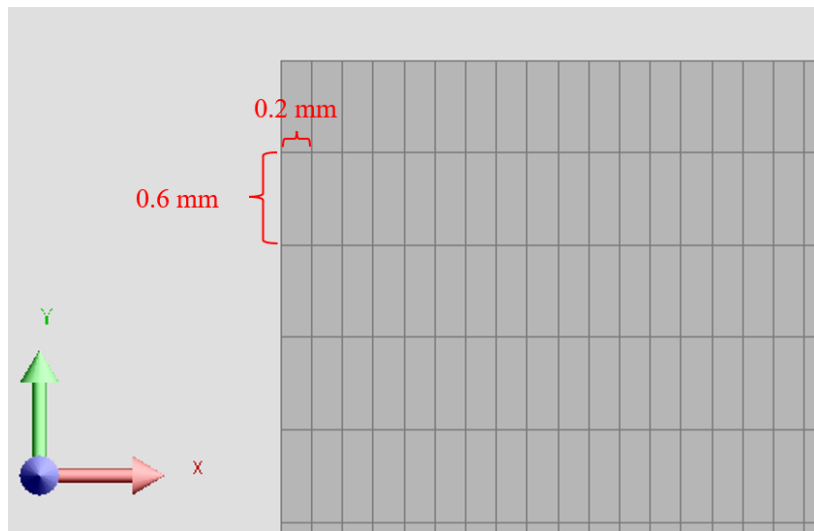


Figure 5.5 Mesh detail on the surface of the lamination, i.e. in x and y direction

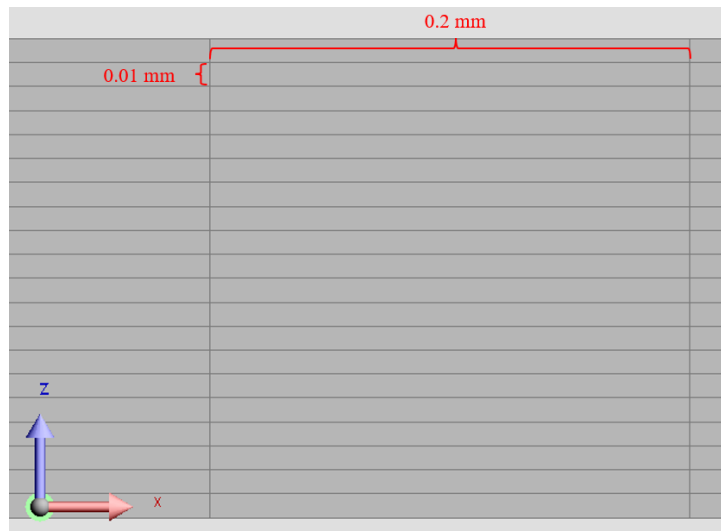


Figure 5.6 Mesh detail on a section through the lamination, i.e. in x and z direction

The time varying magnetic field is applied by a low profile coil which is tightly wrapped around the lamination as shown with Figure 5.7. The current in the main section of the coil flows in the x -direction as also shown. This is a theoretical model and hence there was no need to operate the coil at a realistic current density giving complete freedom over the height of the coil section. In an attempt to produce as near a z -direction aligned field, the thickness of the coil was set to 0.1 mm.

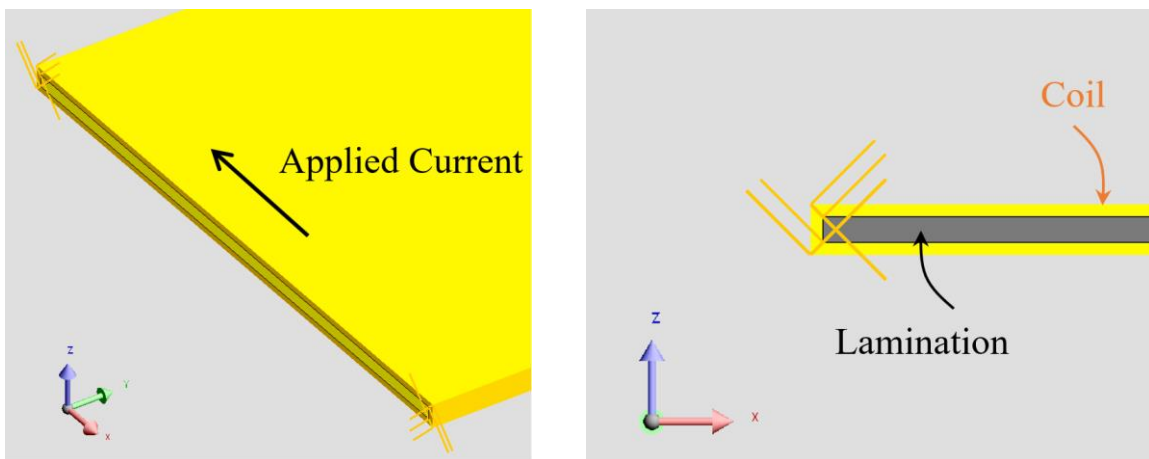


Figure 5.7 Coil geometry used to apply the field current direction of the 3D thin lamination model

5.3.2 Magnetostatic calculations

The finite model was first solved using a time-stepped solution with the properties of the lamination set to a linear characteristic with a relative permeability of 5000 and an electrical conductivity of zero. This simple first calculation which generated a series of magnetos-static

field distributions was used to understand the spatial variation in the imposed magnetic field strength and hence flux density across the lamination strip and the relationship between the coil current and the magnitude of the applied magnetic field in the centre of the strip. As discussed previously, this is a highly idealised representation of the coil and the actual current required is of no significance. A series of 101 time-stepped calculations were performed spanning 2 electrical cycle. For consistency this simulation was performed with an excitation frequency of 10 kHz, but since the solutions are magneto-static there is no direct dependence on the frequency.

Figure 5.8 shows the predicted magnetic field strength across the outer surfaces at the time instant that corresponds to the positive peak of the applied current while Figure 5.9 shows the magnetic field strength at the same instant, but in this case on a cut-plane through the middle of the lamination. As would be expected given the coil and sample geometry there is a significant variation in magnetic field strength across the sample. However, since the purpose of the 3D model is to provide a reference model for the 1D eddy current representations, the cut section along the midline provides a large region of near uniform magnetic field strength and near 1D eddy current flow.

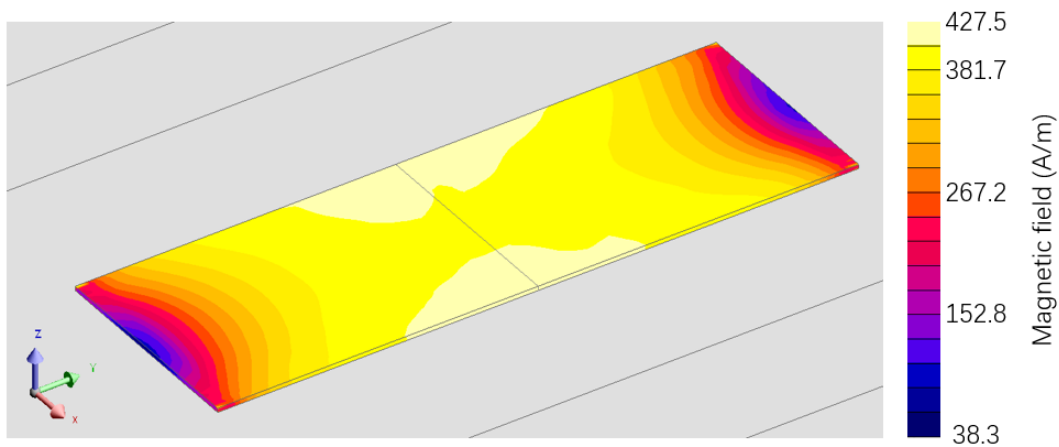


Figure 5.8 Finite element predicted magnetic field strength distribution on the surface of the lamination

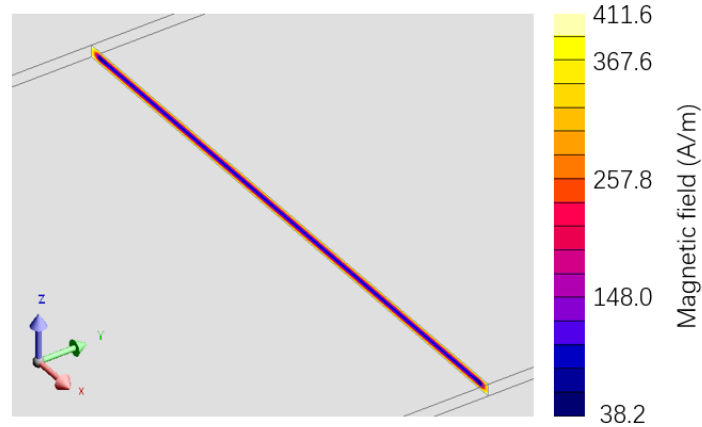


Figure 5.9 Finite element predicted magnetic field strength distribution on a cut-plane on mid-line of the lamination

5.3.3 Transient time-stepped eddy current calculations

The 3D model was simulated with the lamination relative magnetic permeability set to a fixed value of 5000 and the electrical conductivity set to its manufacturer specified value of 1.9×10^6 S/m. The coil was supplied with a 10 kHz sinusoidal current with a peak magnitude of 100 A in 5 series turns. The simulation duration was 0.2 ms which corresponds to two electrical cycles. A total of 101 time-steps were used to cover this 0.2 ms simulation. The finite element predicted variation in the magnetic field strength at a point half-way along the mid-line of the lamination is shown in Figure 5.10. As will be evident in Figure 5.10, there is a small transient start-up effect which largely settles down within half of an electrical cycle. The peak value of the surface magnetic field strength is 566 A/m.

The variation in the magnetic field strength through the thickness of the lamination (i.e. from $z = -0.1$ mm to $+0.1$ mm) as a function of time is shown in Figure 5.11. As would be expected, there is a drop of in the magnitude of the magnetic field away from the surface ($z = 0$ mm corresponds to the mid-point of the lamination thickness). As would be expected, there is also a phase shift with depth that is not so evident in the surface plot but will be compared with analytical models later in this chapter.

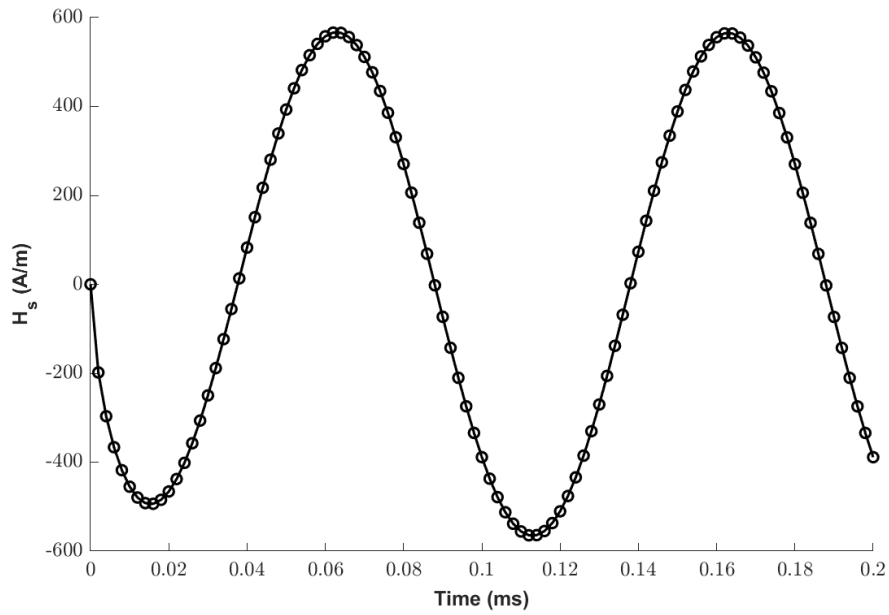


Figure 5.10 Time varying surface magnetic field distribution H_s waveform over two electrical cycles for a 10 kHz sinusoidal coil current with a peak magnitude of 566 A for a lamination with a fixed relative magnetic permeability of 5000 and an electrical conductivity of 1.9×10^6 S/m

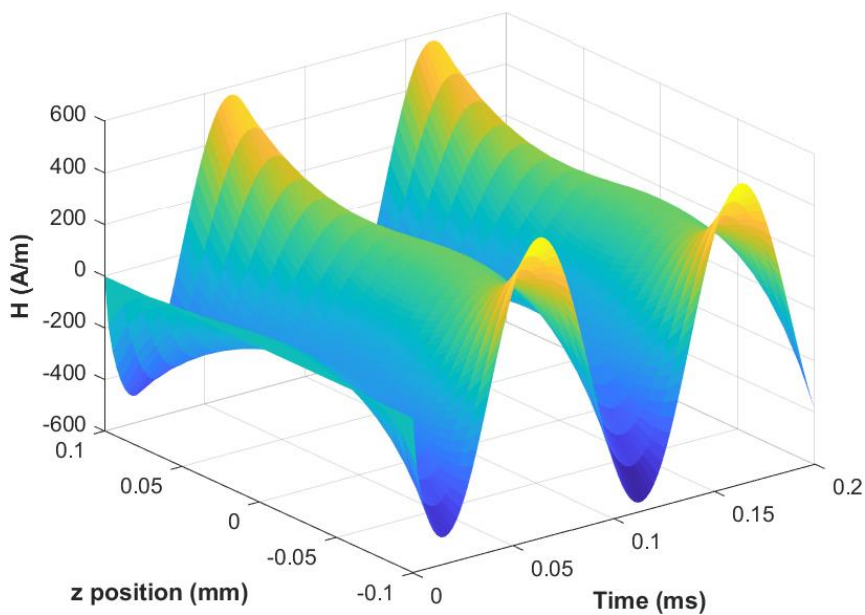


Figure 5.11 Variation in magnetic field through the lamination thickness and time as the central point of the lamination over two electrical cycles for a 10 kHz sinusoidal coil current with a peak magnitude of 100 A for a lamination with a fixed relative magnetic permeability of 5000 and an electrical conductivity of 1.9×10^6 S/m

5.4 Analytical solution of the diffusion equation for linear magnetic materials

5.4.1 Direct use of the diffusion equation for predicting one-dimensional eddy current field redistribution

According to the analytical solution of the diffusion equation for steady-state sinusoidal excitation shown below, the variation of the magnetic field strength with depth into the lamination can be calculated for a given values of surface value magnetic field strength, H_s :

$$H_z = H_s \frac{\cosh \alpha y}{\cosh \alpha b} e^{j\omega t} \quad (5.34)$$

Specifying a value of H_s is far from straightforward in terms of matching to a particular applied flux or magnitude of an external source of mmf. The first test of the analytical model is for the simplified case of a specified input value of H_s . For direct comparison with the finite element simulation discussed in section 5.3 above, the finite element calculated value of H_s for the second electrical cycle shown previously in Figure 5.10.

The first analytical method used, which can only be used for linear magnetic materials, is to directly apply equation (5.33) for varying values of y and that $y = 0$ corresponds to the centre of the lamination. At 10 kHz, a fixed relative permeability of 5000 and an electrical conductivity of 1.9×10^6 S/m, the value of α is $1.9 \times 10^4 + i1.9 \times 10^4$. Substituting this into equation (5.33) and noting that the lamination thickness of 0.2 mm gives a value for b of 0.1 mm, yields the variation in the magnitude of the magnetic field strength with depth shown in Figure 5.12 for the same surface magnetic field strength, H_s , of 566 A/m. Also shown in Figure 5.12 are values of magnetic field strength extracted from the finite element simulation described in section 5.3.3 at 10 even-spaced increments of depth. As shown, there is good agreement.

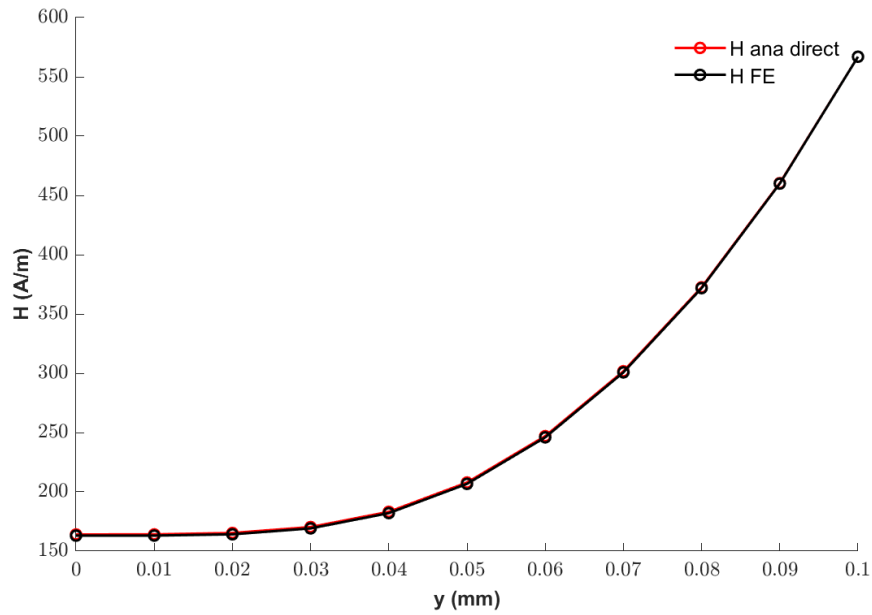


Figure 5.12 Variation in the peak magnetic field strength with depth for 10 kHz sinusoidal variation in magnetic field strength peak magnitude of 566 A/m for a 0.2 mm thick lamination with a fixed relative magnetic permeability of 5000 and an electrical conductivity of 1.9×10^6 S/m

5.4.2 Layered analytical solution to diffusion equation

Although the direct use of equation (5.33) yields a continuous analytical solution, it can only be used for a fixed value of permeability. A first stage to developing a model that can account for non-linear materials is to develop a layered model. The first version of this layered model was based on linear magnetic properties to ensure that the basic method could be compared with the previous analytical and finite element calculations. The lamination which has an overall thickness of $2b$ is divided into a number of layers as shown in Figure 5.13. In this case, the lamination is divided into 20 layers, numbered using the convention shown. The thickness of each layer h_l is given simply by $h_l = b/10$. For the case of 10 layers, there are 11 boundary lines between the centre of the lamination and the outer edge as also shown.

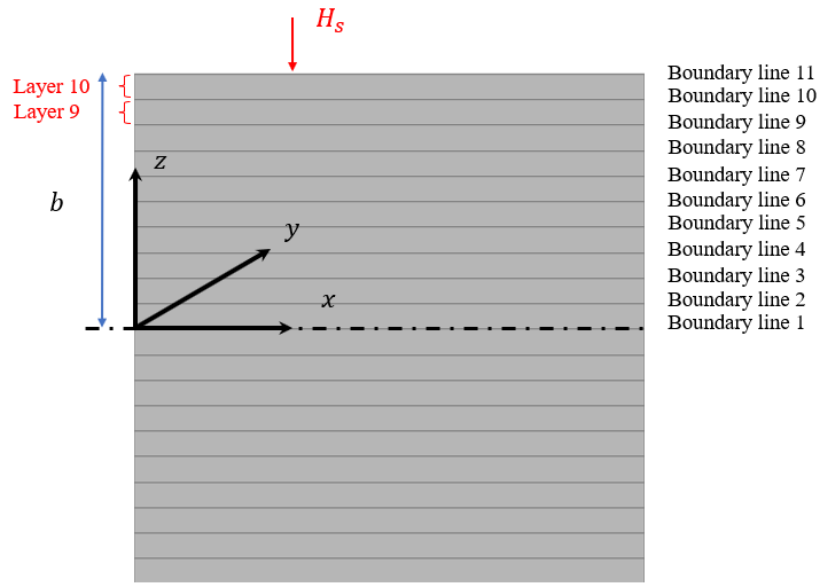


Figure 5.13 Numbering convention for layers and boundary lines in one half of an electrical steel lamination

The method adopted is to treat each layer as a separate region and apply the diffusion equation layer-by-layer while updating the surface value of the magnetic field strength to be the value at the bottom of the previous layer. In this first case, the permeability is kept fixed in each layer, but it is already clear that the different layers could take different values of permeability as they are only coupled to each other by the cascading of the surface magnetic field strength value. As an example, starting at layer 10 (outer layer) and applying the diffusion equation using the value of H_s at boundary 11 (outer surface), the magnitude of H at boundary 10 can be calculated using the following equation noting that the half thickness of the lamination as seen from the surface is $10h_l$ and that $y = 0$ corresponds to the centre of the lamination:

$$H_{10} = H_s \frac{\cosh \alpha 9h_l}{\cosh \alpha 10h_l} \quad (5.35)$$

This process can be repeated to calculate the value for H_9 using:

$$H_9 = H_{10} \frac{\cosh \alpha 8h_l}{\cosh \alpha 9h_l} \quad (5.36)$$

By performing this process for each successive layer, the variation of the magnetic field strength with depth can be calculated. Figure 5.14 shows the predicted variation of the magnetic field strength for the layered model along with the corresponding variations predicted for direct

use of the diffusion equation and the 3D finite element model. In all cases, the excitation frequency is 10 kHz, the magnetic relative permeability is fixed at 5000 and the electrical conductivity is 1.9×10^6 S/m.

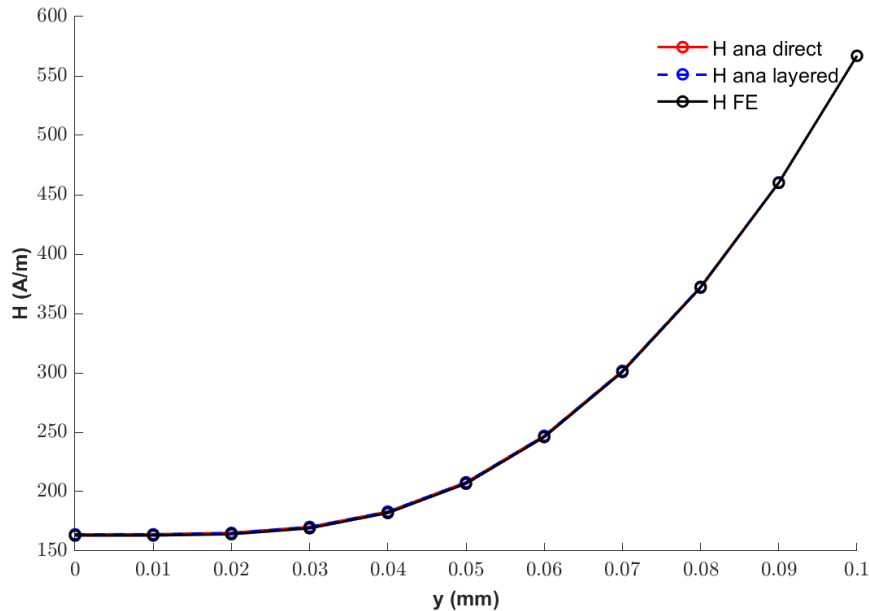


Figure 5.14 Variation in magnetic field strength with depth for 10 kHz sinusoidal variation in magnetic field strength peak magnitude of 566 A/m for a 0.2 mm thick lamination with a fixed relative magnetic permeability of 5000 and an electrical conductivity of 1.9×10^6 S/m

It is also possible to extract the phase shift between successive layers using zero crossing point of flux density variation waveform for all layer within the thin lamination. Figure 5.15 and Figure 5.16 shows the predicted amplitude and phase shift variation of the flux density for linear material that magnetic relative permeability is fixed at 5000.

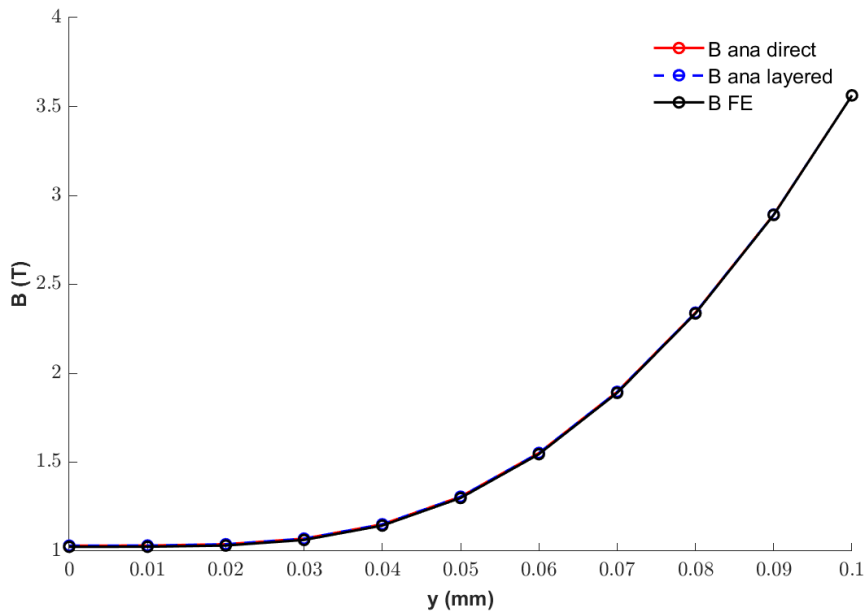


Figure 5.15 Amplitude variations of the flux density within the thin lamination for linear material

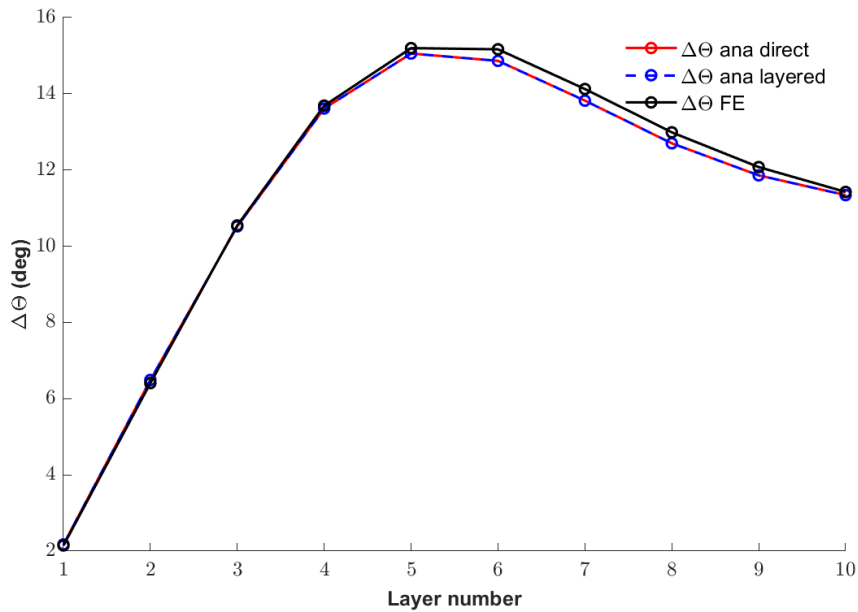


Figure 5.16 Flux density phase shift between the top and bottom point of a layer for linear material

5.4.3 Modelling non-sinusoidal excitation through harmonics in linear materials

The analytical methods presented up to this point have been based on a sinusoidal variations in the surface magnetic field strength. It is possible to apply these methods to more complex waveforms by superposition of the individual harmonic components. However, this

superposition based approach is reliant on the material being magnetically linear. As an example, a current waveform was constructed with same fundamental magnitude of 100 A peak combined with 3rd, 5th and 7th harmonics of magnitudes 20%, 15% and 10% respectively. In each case, there is no phase offset between the harmonics and the fundamental. The resulting current waveform is shown in Figure 5.17. This current waveform which has a fundamental frequency of 10 kHz and hence harmonic content up to 70 kHz was used as input to the 3D FE model for the case of a lamination with a fixed magnetic relative permeability of 5000 and an electrical conductivity of 1.9×10^6 S/m. The resulting surface magnetic field strength waveform over two complete cycles is shown in Figure 5.18. As would be expected give the time-stepped nature of the finite element simulation, there is some transient start-up effects in the first cycle which settle down rapidly so that the second cycle is very near to a steady-state condition.

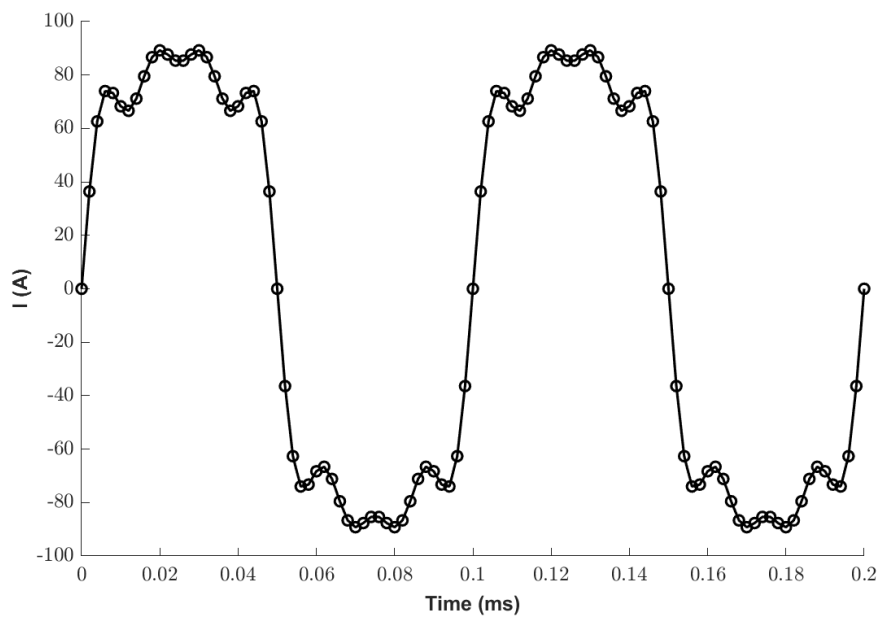


Figure 5.17 Coil excitation current for the finite element model with 100A, 10kHz fundamental and 20%,15% and 10% addition of 3rd, 5th and 7th harmonics

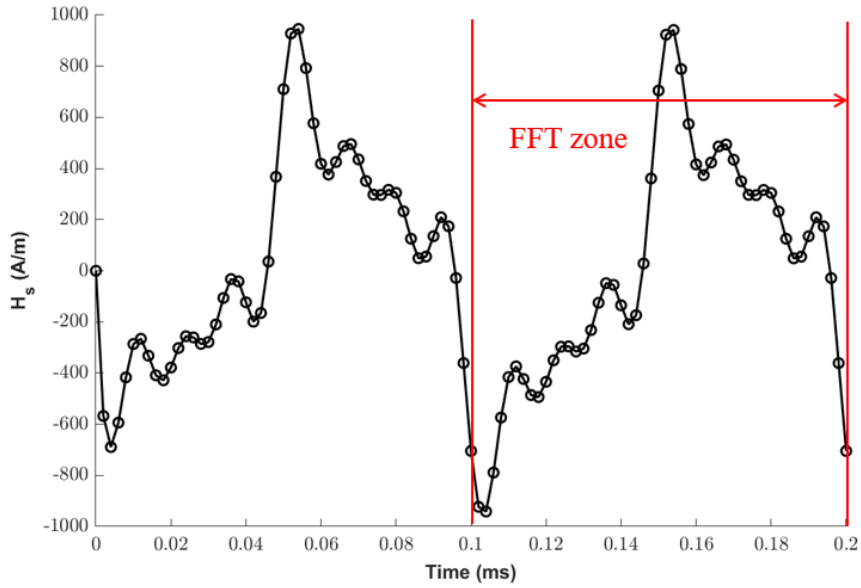


Figure 5.18 3D finite element predicted surface magnetic field strength for the current waveform of Figure 16

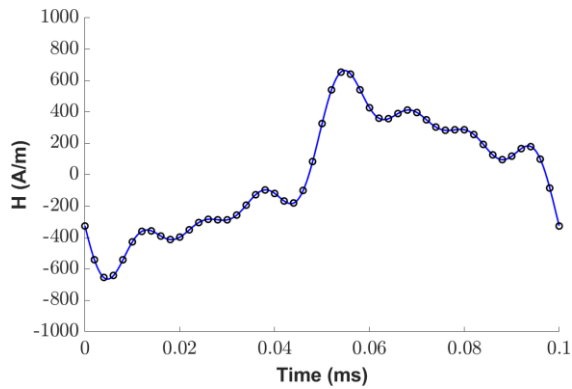
The harmonic spectrum of the surface magnetic field strength waveform was calculated using a standard FFT algorithm in MATLAB. The FFT was taken over the second cycle only using a cosine function (with appropriate re-setting of the reference phase angle to the start of that cycle) in an attempt to eliminate the influence of the start-up transient which is present in the first cycle. The results from the cosine FFT calculation are shown in Table 5.1.

Table 5.1 Cosine FFT calculation results for figure 17

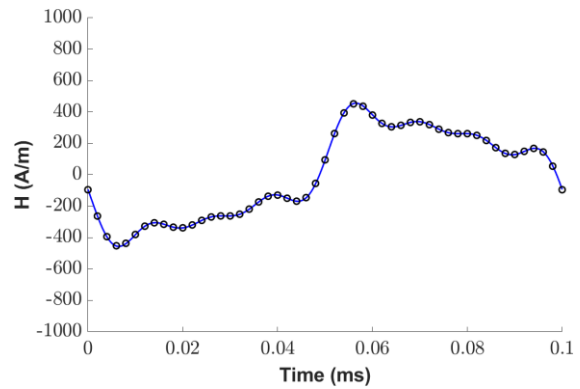
	Harmonic			
	Fundamental	3rd	5th	7th
Magnitude	565.4A/m	194.5A/m	183.0A/m	141.2A/m
Phase shift relative to fundamental	0 rad	0.074 rad	0.108 rad	0.137 rad

The layer based analytical model with the same fixed magnetic relative permeability of 5000 and electrical conductivity of 1.9×10^6 S/m was applied to each harmonic in turn and the overall waveform in each reconstructed by addition of the harmonic with due account of phase. A comparison between the magnetic field strength waveforms in each layer predicted by the 3D finite element model and by superposition of the layer model is shown in Figure 5.19. As will be seen, there is excellent agreement between the two methods in terms of both

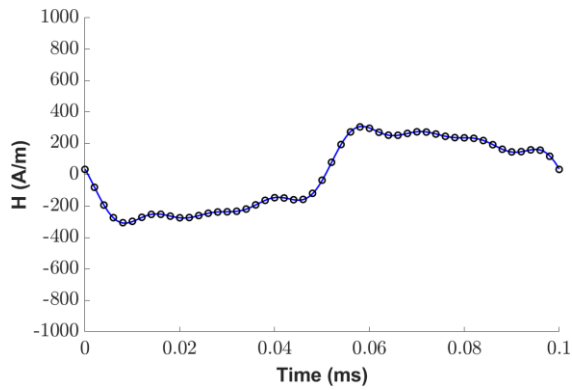
magnitude and phase. This demonstrates the ability of the layered analytical model to predict eddy current redistribution within a lamination for non-sinusoidal waveforms for the case of a linear material.



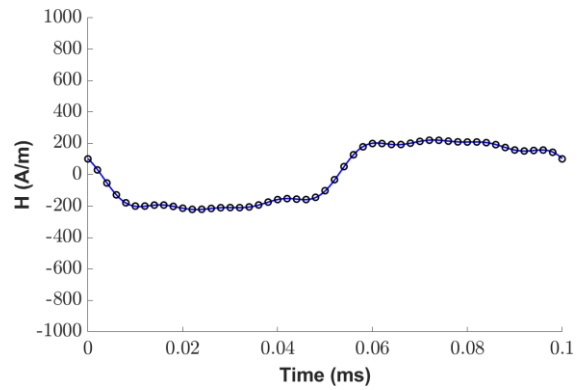
Boundary line 10



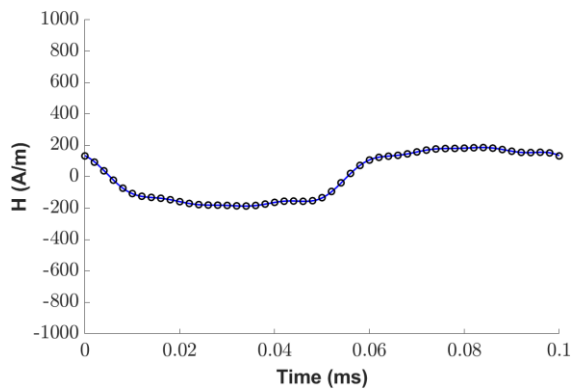
Boundary line 9



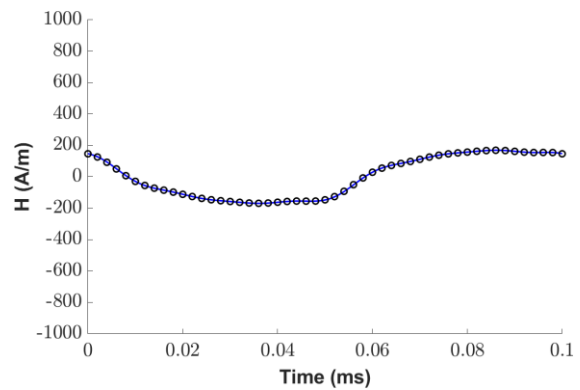
Boundary line 8



Boundary line 7



Boundary line 6



Boundary line 5

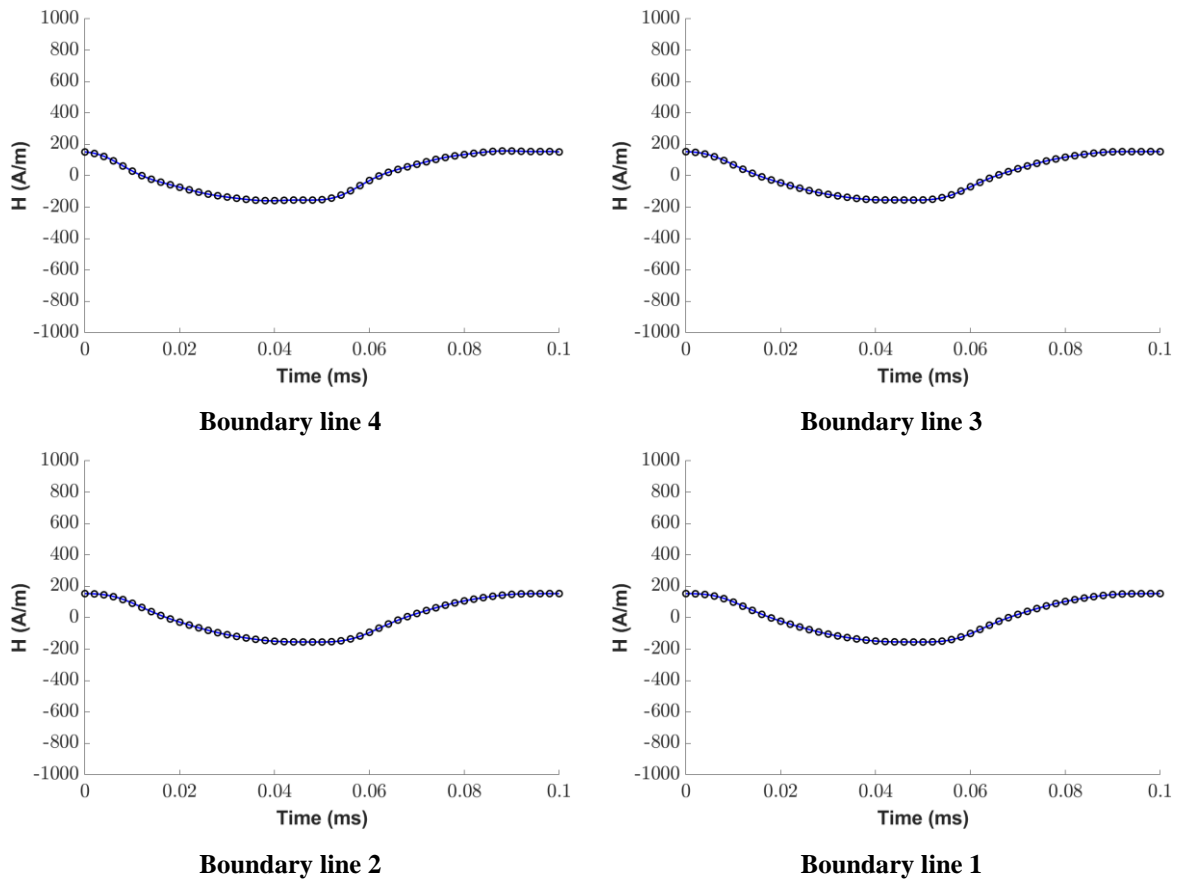


Figure 5.19 Comparison of magnetising field strength in different boundary lines predicted by finite element (\circ) and harmonic analytical layer model (—)

5.5 Non-linear solution of the diffusion equation

The layered model in principle provides a means of changing the permeability in different layers and hence offers a route to modelling the non-linear and saturating behaviour of electrical steels. Non-linearity plays an important role in the distribution of eddy currents. In general, the concentration of flux near the surface which is observed in the case of linear materials will tend to be less pronounced with saturating materials since saturation will tend to force the flux deeper into the lamination. Figure 5.20 shows the initial magnetisation curve for the NO20 grade of Silicon iron used in this thesis. A close up of the magnetisation curve up 1000 A/m is shown in Figure 5.21 along with the variation of relative permeability which shows the large range of values taken by the relative permeability up 1000A/m.

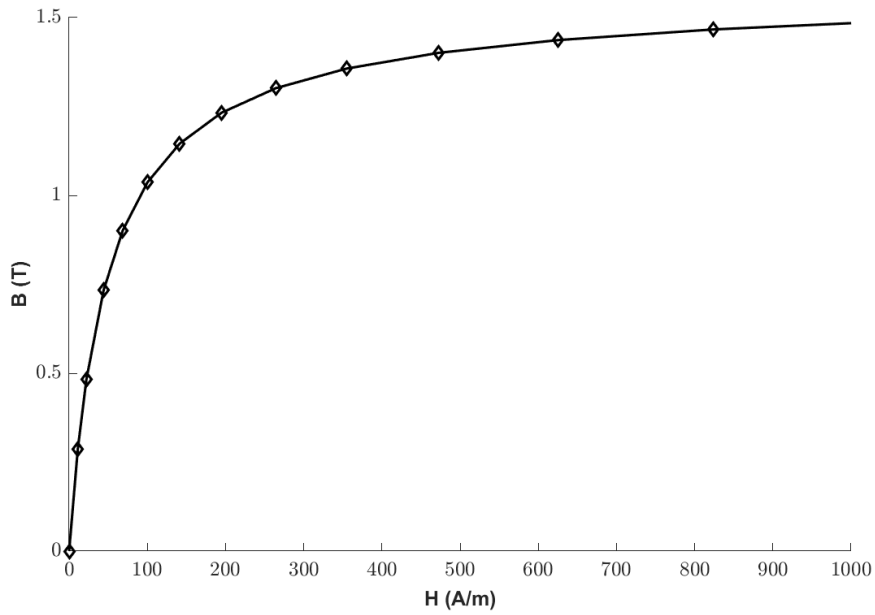


Figure 5.20 Magnetisation characteristics of NO20 Silicon iron

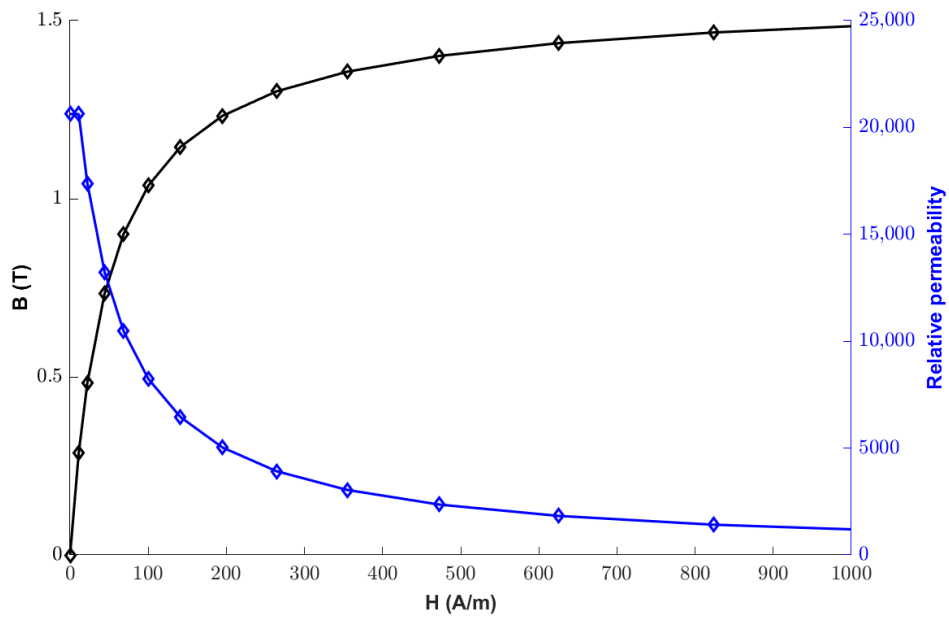


Figure 5.21 NO20 magnetisation curve and variation in relative permeability up to 1000A/m

A 3D finite element simulation was performed with the magnetisation curve of Figure 5.20 used to represent the NO20 lamination which was also assigned the manufacturer specified electrical conductivity of 1.9×10^6 S/m. The 5 turn coil in the finite element model was supplied with a sinusoidal, 10 kHz current with a peak magnitude of 100 A. This current magnitude is sufficient to ensure magnetic saturation conditions within the lamination. The finite element predicted H waveform that this generates on the surface of the lamination is shown in Figure 5.22. This has a much greater deviation from a sinusoid compared to the

corresponding waveform for the linear material case shown previously in Figure 5.10. This surface magnetic field strength variation has a peak magnitude of 907 A/m which higher than that for the linear material with the same peak current.

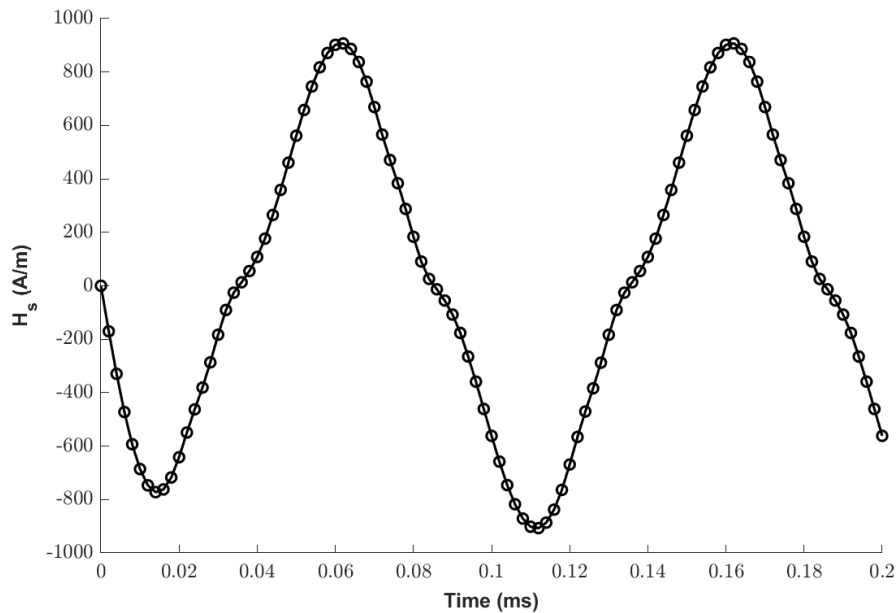


Figure 5.22 Finite element time varying surface magnetic field distribution H_s waveform within two electrical period

Figure 5.23 shows the finite element predicted flux density waveforms in the 11 boundary lines between one surface of the lamination and the centre for the same simulation that generated the surface magnetic field distribution H_s waveform shown above in Figure 5.22. It is worth noting that these flux density waveforms have magnitudes are in the range where saturation is a significant factor as shown previously in the magnetisation curve for NO20 in Figure 5.20. As can be seen, there is a progressive phase shift with depth, but there is only a small attenuation of the flux density. There is some evidence of a change in shape, and this demonstrates that the non-linear case is far more complicated than the linear case, with significant deviations from sinusoidal waveforms, not only on the surface but also with increasing depth. For the particular conditions shown the peak flux density drops from 1.5 T on the surface to 1.4 T at the centre of the lamination.

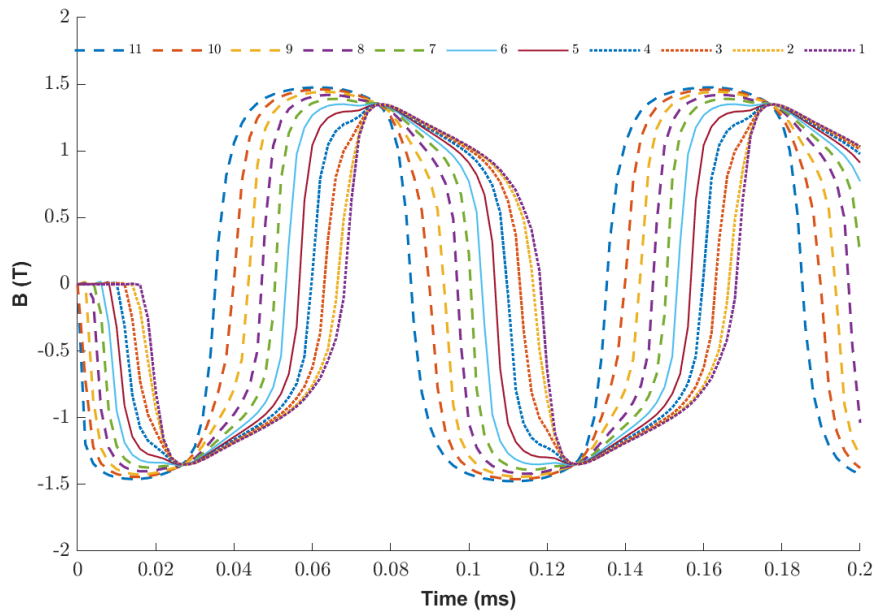


Figure 5.23 3D finite element predicted flux density waveforms in each of the 11 layers between the surface and the centre of the lamination

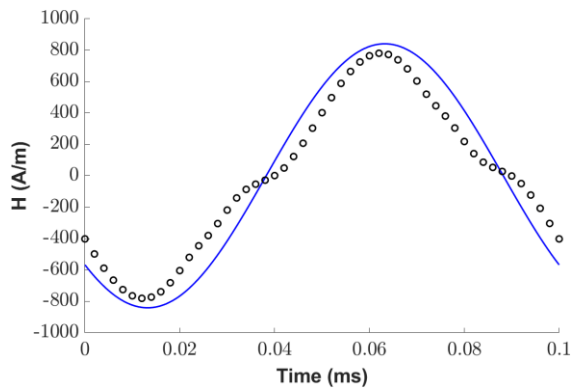
The non-sinusoidal form of the surface magnetic field strength waveform of Figure 5.22 makes it difficult to model the same conditions with the analytical model, which is limited to sinusoidal variations. The method using harmonics cannot be used in the non-linear case as it relies on superposition. Since the solution is based on a complex steady state excitation (as represented by $e^{j\omega t}$) only one value of permeability is used for the sinusoidal waveform – i.e. the permeability does not vary during the waveform. Hence, a single value of permeability must be used in each layer, and a value based on the peak magnetic field strength would seem to be the most appropriate single value.

The procedure adopted for each layer in the analytical model is to start with the permeability from the layer above and calculate the magnetic field strength at the next layer boundary line by direct solution of the diffusion equation. The permeability is then adjusted based on the calculated mean magnetic field strength in the layer, which is generally lower than the magnetic field strength in the layer above. This new value of permeability is then used in a further calculation of the magnetic field using the diffusion equation and the process repeated until convergence is achieved. In general, convergence was achieved with 2-3 iterations.

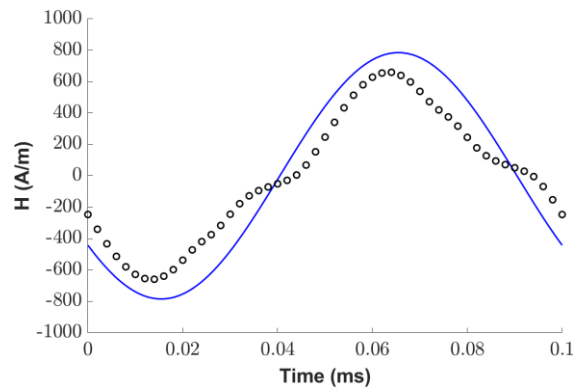
Two magnitudes of time varying surface magnetic field strengths H_s with different peak amplitudes of 907 A/m and 261 A/m have been used in this section as these correspond to operation into saturation and operation in largely unsaturated conditions. Starting with a 10 kHz sine wave with the higher peak value of 907A/m, Figure 5.22 shows the time variation of

the magnetic field strength calculated by the finite element model and the analytical layer model in which the non-linear behaviour of NO20 magnetisation curve (shown previously in Figure 5.20) was used.

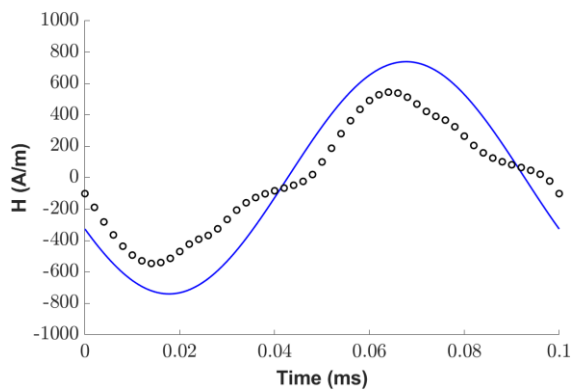
As shown by Figure 5.24, there are significant differences in the magnitudes and phase shift between these two models. This is not surprising given that the analytical model must approximate the surface magnetic field strength with a sinusoid and relies on a single value of permeability based on the peak of the magnetic field strength. The analytical model predicts a reduction in the peak magnitude of the magnetic field strength from 907 A/m at the surface to ~660A/m at the centre of the lamination. This results in a relative permeability increase from 1295 to 1740.



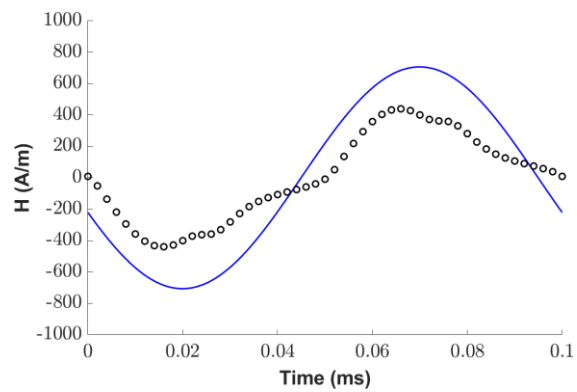
Boundary line 10



Boundary line 9



Boundary line 8



Boundary line 7

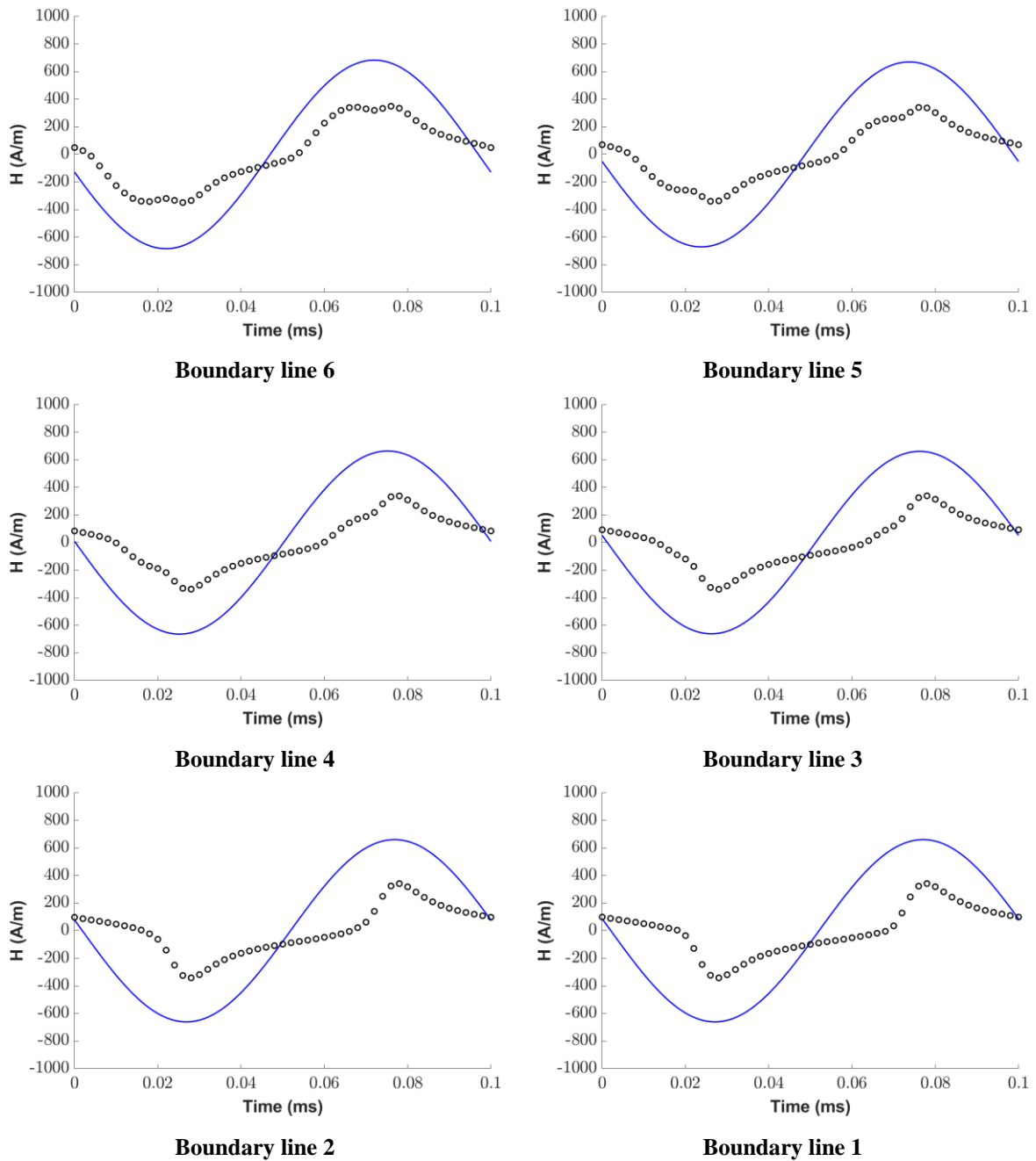


Figure 5.24 Comparison of magnetising field strength in different boundary lines predicted by finite element (\circ) and harmonic analytical layer model (—)

In the previous linear models, the flux density waveforms in the lamination have simply been scaled versions of the magnetic field strength because of the fixed permeability. However, in the non-linear case, the H and B waveforms can be quite different as shown in Figure 5.25 which shows flux density waveforms calculated by both the 3D FE model and the layer analytical non-linear model in layers 10 and 1.

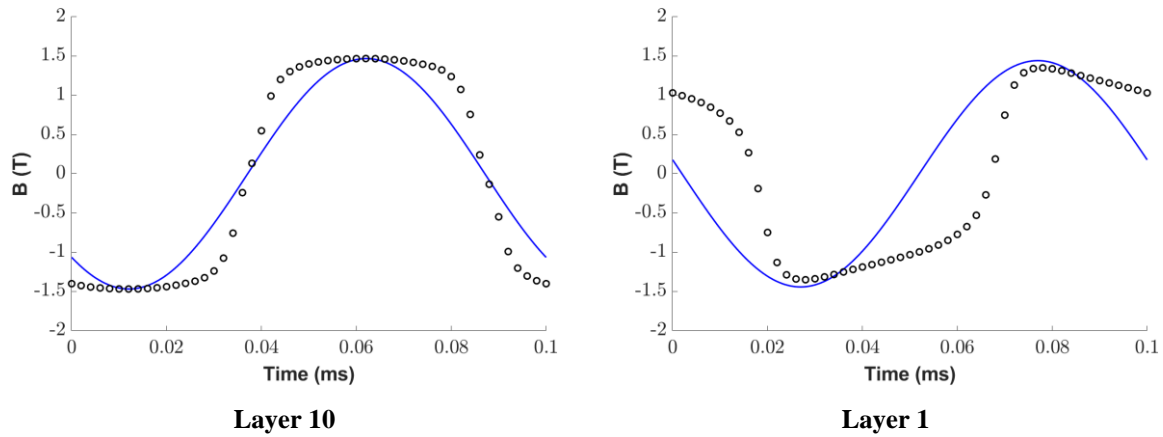


Figure 5.25 Comparison of flux density in layers 10 and 1 predicted by finite element (\circ) and harmonic analytical layer model (—)

The same 3D finite element simulation was used but with a same peak current of 100 A in the reduced 2-turn coil, again for a 10 kHz sinusoidal current waveform. The time variation in the surface flux density, H_s , is shown in Figure 5.26. This has a peak magnitude of 261 A/m and although it still contains some distortion compared to the pure sinusoidal current applied, it is less pronounced than in the earlier case with a peak H_s magnitude of 907 A/m.

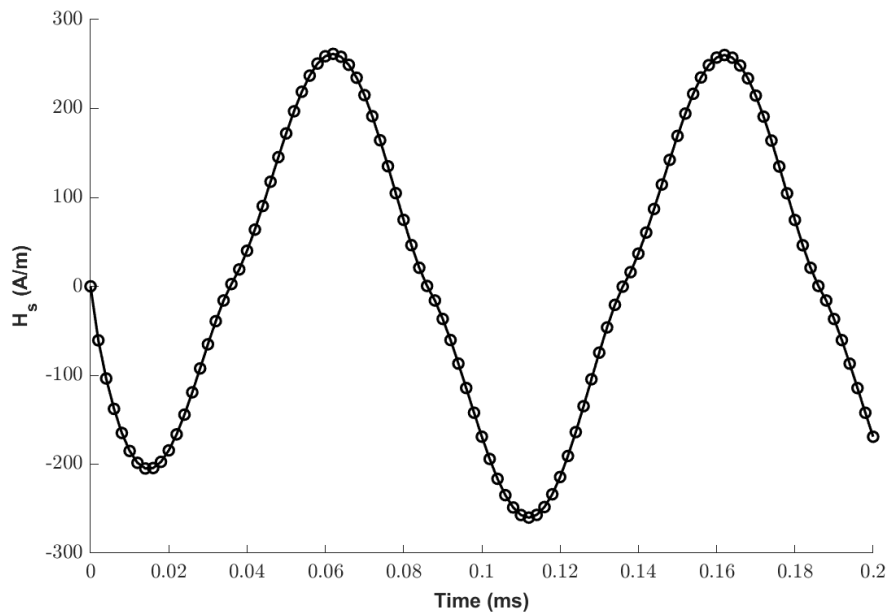
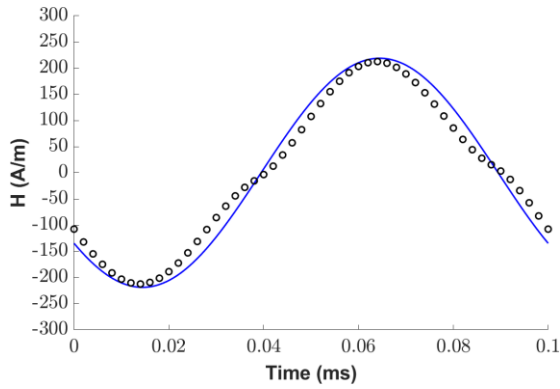


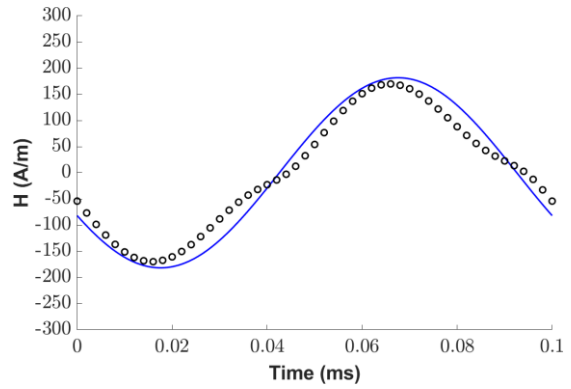
Figure 5.26 3D finite element predicted surface magnetic field strength H_s waveform with a reduced coil current

Figure 5.27 shows the variation in the magnetic field strength throughout the lamination predicted by 3D finite element analysis and the layer analytical model with non-linear

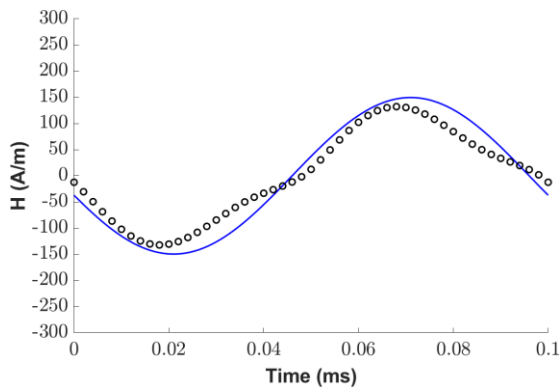
permeability for a peak surface magnetic field strength of 261A/m. Although there is some improvement in the ability of the analytical layer model to match the waveforms predicted by 3D FE, there are still significant differences.



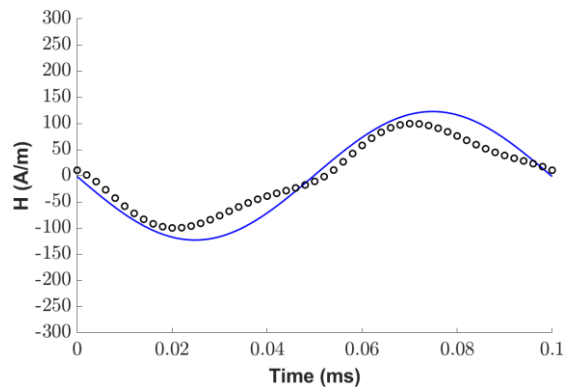
Boundary line 10



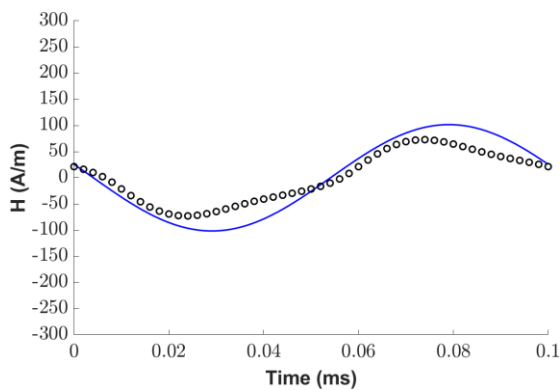
Boundary line 9



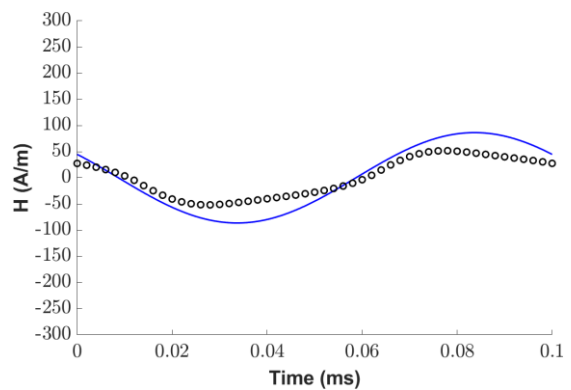
Boundary line 8



Boundary line 7



Boundary line 6



Boundary line 5

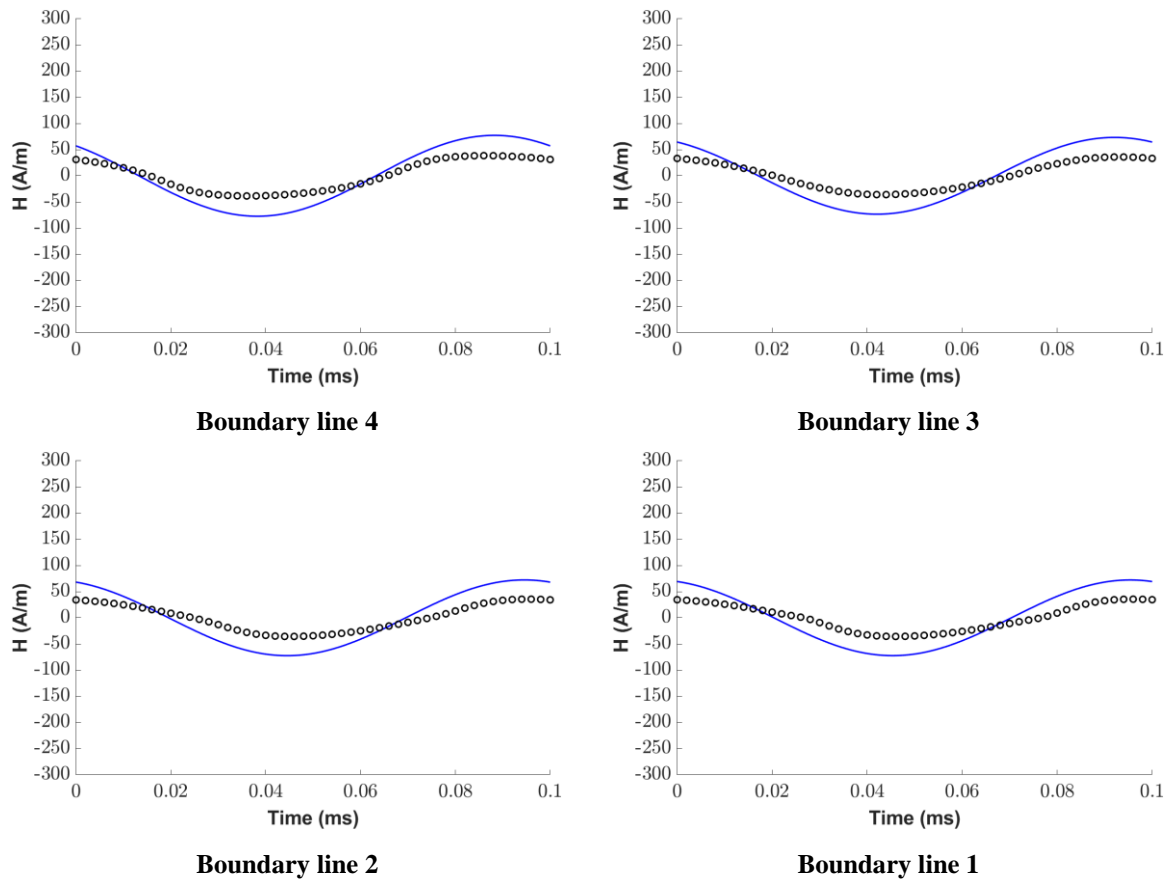


Figure 5.27 Comparison of magnetic field strength in boundary line 10 and 1 predicted by finite element (\circ) and harmonic analytical layer model (—) for 10 kHz, 261 A/m peak surface magnetic field strength

This section has shown that extending the analytical model to non-linear magnetisation characteristics for non-sinusoidal surface magnetic field strengths results in poor agreement with finite element analysis. This is due to a combination of each layer in the analytical model having a single value of permeability (which can be different to other layers) with no time variation in the permeability and the fact that the excitation is sinusoidal. Since the general requirements for a post-processing tool is a need to accommodate arbitrary non-sinusoidal waveforms, it seems that analytical solution methods for the diffusion equation, although useful for linear materials, cannot deal with non-linear materials at a reasonable level of accuracy.

5.6 Finite difference time-stepped method for a one-dimensional numerical post-processing model

To remove the limitations of both sinusoidal excitation and linear materials, it is necessary to move to a time-stepped method which combines the layer model with a finite difference time-stepped solution of the diffusion equation.

5.6.1 The finite difference method

For the one-dimensional system, which is shown in Figure 5.28, when the conductor has a uniform electrical conductivity, the z component of the time-varying magnetic field is governed by the diffusion equation.

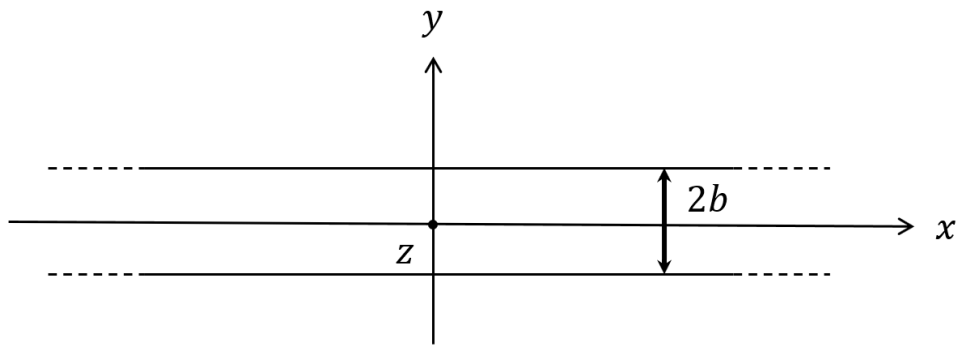


Figure 5.28 1-D system for thin lamination model

The diffusion equation is:

$$\frac{\partial^2 H}{\partial y^2} = \sigma \frac{\partial B}{\partial H} \frac{\partial H}{\partial t} \quad (5.37)$$

In a finite-difference scheme, the discrete variable $H_{i,k}$ only depends on the space and time nodes defined by the coordinate.

$$y = (i - 1)h \quad (5.38)$$

$$t = (k - 1)p \quad (5.39)$$

Where h is the separation between the two successive mesh points in space; p is the time interval between the two successive variables H_i .

For convenience, it is common to define:

$$\beta = \sigma \frac{dB}{dH} \quad (5.40)$$

with β initially regarded as a constant value.

Using the Taylor series for second order space derivate for node i, k , yields:

$$\left. \frac{\partial^2 H}{\partial y^2} \right|_{i,k} = \frac{H_{i+1,k} - 2H_{i,k} + H_{i-1,k}}{h^2} + O(h^2) \quad (5.41)$$

The first term of the right-hand expressions is a second-order correct finite-difference analogue of the derivative. Expanding the expression about node $(i, k + 1)$ yields a similar expression.

Expanding about node (i, k) gives the time derivative, which can be expressed as:

$$H_{i+1,k} = H_{i,k} + p \left. \frac{\partial H}{\partial t} \right|_{i,k} + \frac{p^2}{2} \left. \frac{\partial^2 H}{\partial t^2} \right|_{i,k} + \dots \quad (5.42)$$

Hence,

$$\left. \frac{\partial H}{\partial t} \right|_{i,k} = \frac{H_{i,k+1} - H_{i,k}}{p} - \frac{p}{2} \left. \frac{\partial^2 H}{\partial t^2} \right|_{i,k} + \dots \quad (5.43)$$

Expanding about node $(i, k + 1)$ yields:

$$\left. \frac{\partial H}{\partial t} \right|_{i,k+1} = \frac{H_{i,k+1} - H_{i,k}}{p} + \frac{p}{2} \left. \frac{\partial^2 H}{\partial t^2} \right|_{i,k+1} + \dots \quad (5.44)$$

The first term of the right-hand expression for equation (5.50) and (5.51) is a first-order analogue of the time derivative. Basing the finite-difference analogue of equation (5.44) on expansion about node (i, k) yields:

$$\frac{1}{h^2} (H_{i+1,k} - 2H_{i,k} + H_{i-1,k}) = \frac{\beta}{p} (H_{i,k+1} - H_{i,k}) \quad (5.45)$$

which yields

$$H_{i,k+1} = rH_{i+1,k} + (1 - 2r)H_{i,k} + rH_{i-1,k} \quad (5.46)$$

For writing convenience, then have:

$$r = \frac{p}{\beta h^2} \quad (5.47)$$

When the analogy is expanded based on the node $(i, k + 1)$, yields the following equation:

$$H_{i+1,k+1} + \left(-2 - \frac{1}{r}\right)H_{i,k+1} + H_{i-1,k+1} = -\frac{1}{r}H_{i,k} \quad (5.48)$$

The time-stepping solution of equation (5.48) can be solved using a Crank-Nicholson method. Alternately using simply explicit and implicit equations to successive time rows. So, according to equation (5.52), all nodes on time row $(k + 1)$ can be obtained. For all nodes on time row $(k + 2)$, equation (5.48) can be written as:

$$H_{i+1,k+2} + \left(-2 - \frac{1}{r}\right)H_{i,k+2} + H_{i-1,k+2} = -\frac{1}{r}H_{i,k+1} \quad (5.49)$$

$$H_{i+1,k+1} + 2\left(-1 - \frac{1}{r}\right)H_{i,k+1} + H_{i-1,k+1} = -H_{i+1,k} + 2\left(1 - \frac{1}{r}\right)H_{i,k} - H_{i-1,k} \quad (5.50)$$

For Crank-Nicolson equation,

$$\beta = \sigma \frac{dB}{dH} = \frac{\sigma a}{(a + b|H|)^2} \quad (5.51)$$

$$r_{i,k} = \frac{p}{2h^2\beta_{i,k}} = \frac{p(a + b|H_{i,k}|)^2}{2\sigma ah^2} \quad (5.52)$$

$$r_{i,k+\frac{1}{2}} = \frac{p}{h^2\beta_{i,k+\frac{1}{2}}} = \frac{p(a + b|H_{i,k+\frac{1}{2}}|)^2}{\sigma ah^2} \quad (5.53)$$

A useful way of illustrating the Crank-Nicolson method is shown in Figure 5.29. All nodes represent sequential calculation points in time and space (depth into the lamination in this 1D formulation). It is worth noting that the Crank-Nicolson uses a half-time-step progression, which means the time interval between two successive time node is $\frac{p}{2}$.

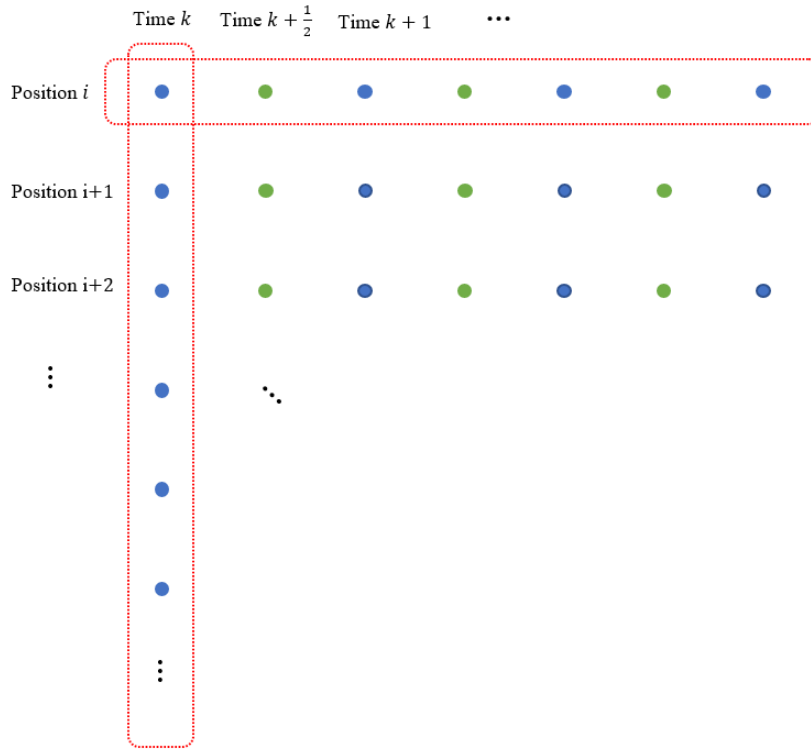


Figure 5.29 Time and spatial nodes for FD method

5.6.2 Test case for finite difference method on a linear problem

The first case of the 1D finite difference method which was simulated was based on a fixed relative permeability of 5000 in a lamination with an electrical conductivity of 1.9×10^6 S/m. Although this is a simple case that can be modelled with direct use of the analytical solution of the diffusion equation described in previous sections, it provides a good first test of the implementation of the finite difference algorithm. The input to the model was a defined surface magnetic field strength waveform. For finite difference scheme, the parameter β , which features in equation (5.51), is constant and takes a value of 1.2×10^4 .

To initiate the finite difference method all the nodes which are spaced through the thickness of the lamination at an initial time k are given initial magnetic field strength values of zero. For the spatial node that corresponds to surface of the lamination, the surface magnetic field H_s was set to the appropriate value from the waveform of Figure 5.30 for the given time step. The nature of the finite difference model is that the surface values gradually propagate through the nodes which span the thickness of the lamination and hence there is an initial transient start-up phase in the calculation.

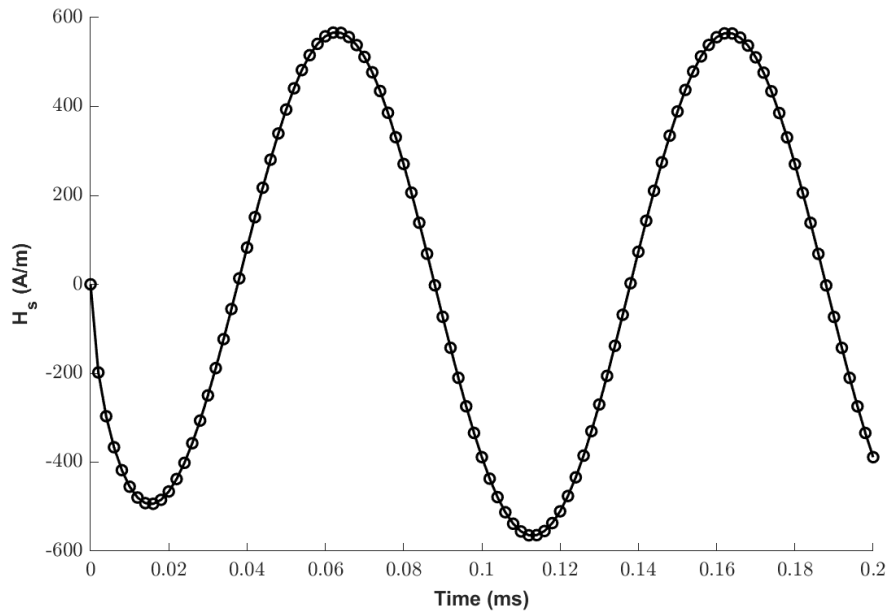


Figure 5.30 Time varying surface magnetic field distribution H_s waveform with amplitude of 566 A/m and frequency of 10000 Hz.

Figure 5.31 shows a comparison between the finite difference and the 3D finite element variations in flux density at the surface of the lamination and the center of lamination, i.e., at $z=0$ mm. In the finite difference solution, the magnetic field strength was scaled to an equivalent flux density with the relative permeability of 5000. As shown, there is good agreement between the two methods, both in terms of the attenuation of the magnitude of the flux density from the surface into the interior of the lamination and the phase shift.

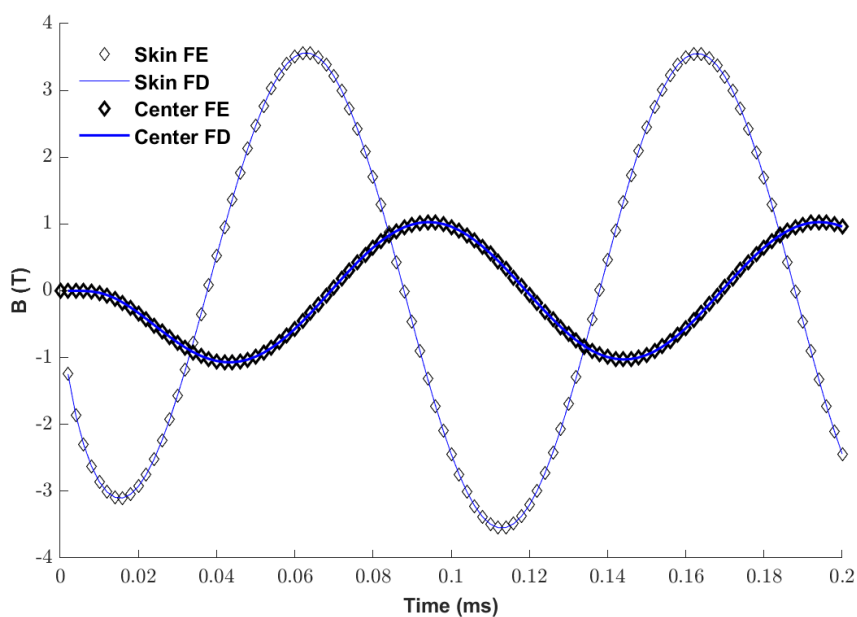
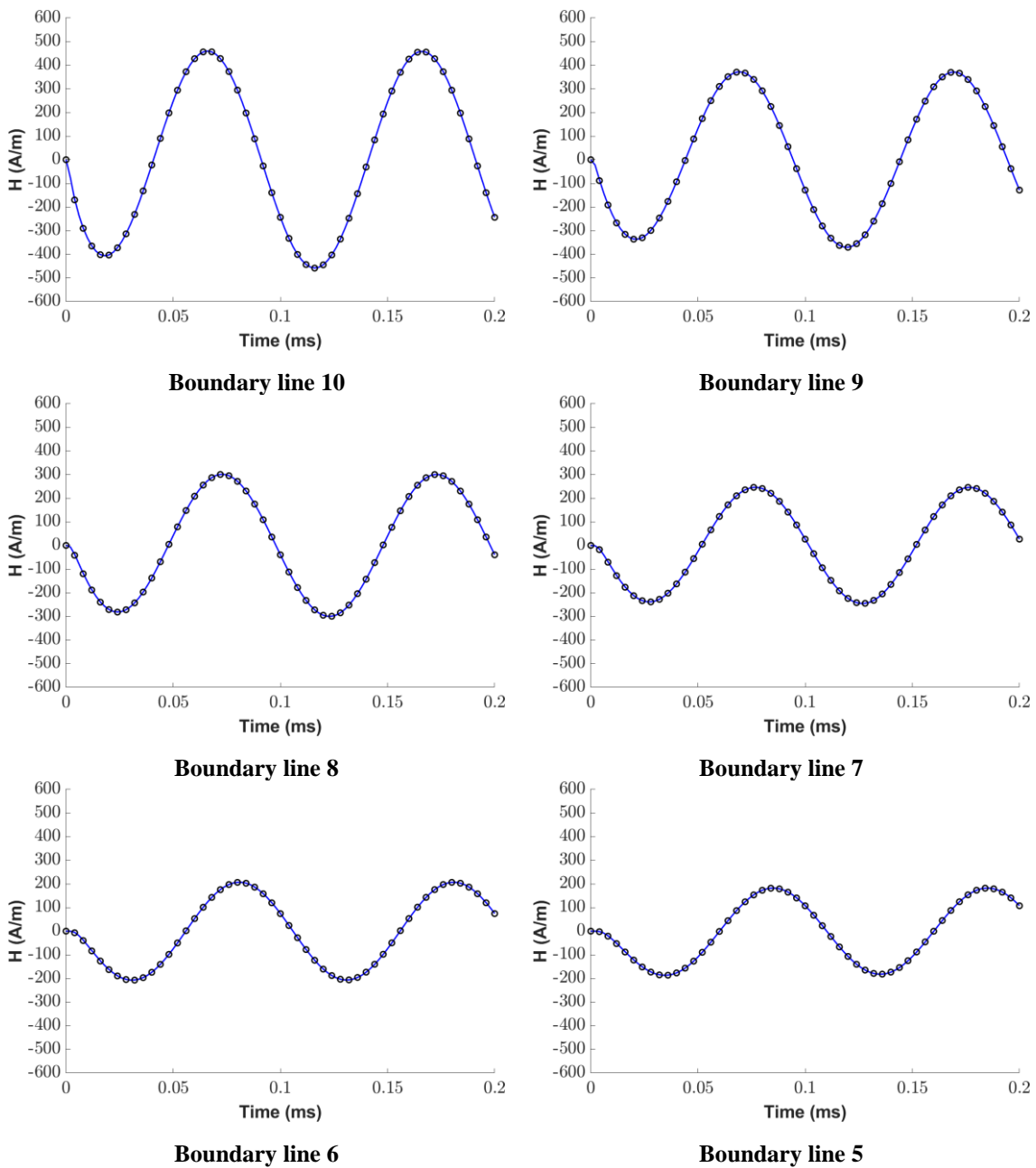


Figure 5.31 Finite difference and the 3D finite element variations in flux density at the surface of the lamination and the center of lamination

Figure 5.32 shows a comparison between the magnetic field strength waveforms calculated using the 3D finite element model and the finite difference approach described in this section. As would be expected, there is a gradual decrease in the magnitude of the peak magnetic field strength and an increasing phase shift. Also shown in Figure 5.32 is the more prominent initial transient behaviour in the deeper regions of the laminations.



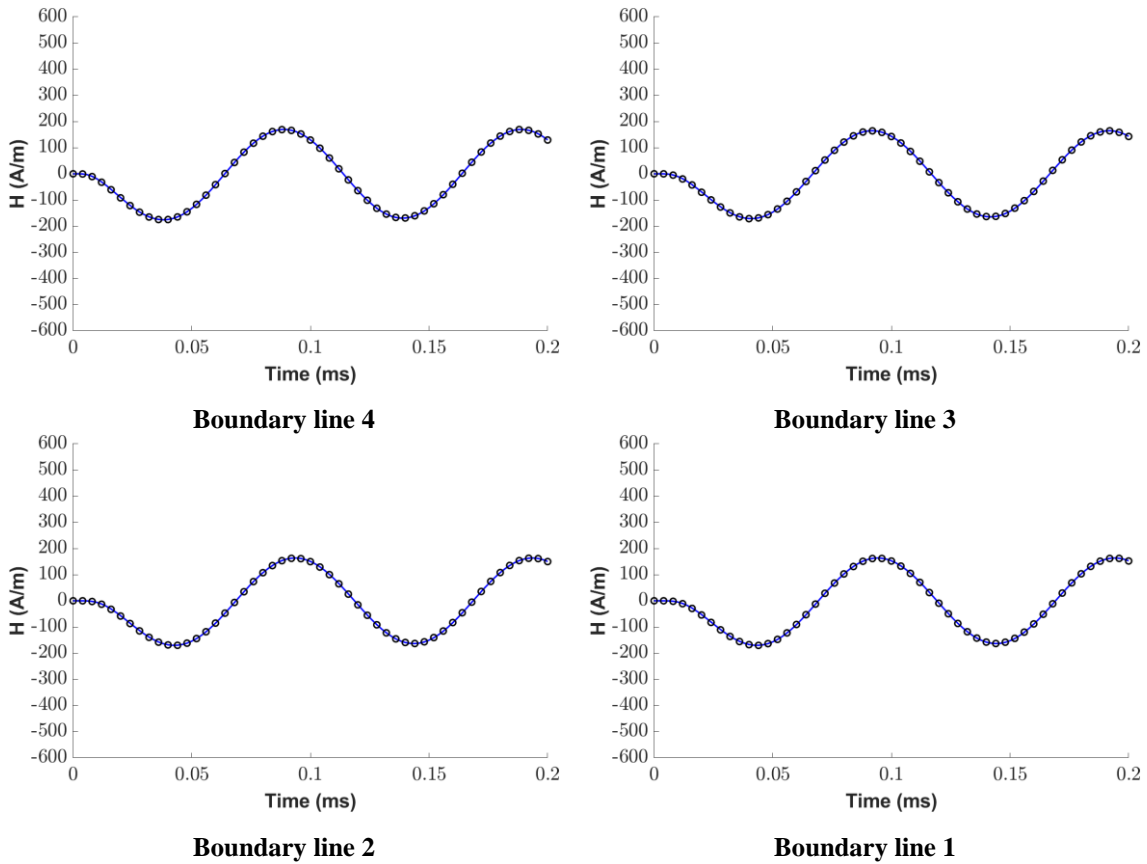


Figure 5.32 Calculated magnetic field strength waveforms throughout the lamination

predicted by 3D finite element analysis (\circ) and finite difference post-processing method (—) (linear permeability of 5000, electrical conductivity of 1.9×10^6 S/m and an excitation frequency of 10kHz)

5.7 Development of the non-linear finite difference one-dimensional post-processing method

This section will further develop the finite difference scheme described above to predict the magnetic field re-distribution in the z direction of the lamination with a non-linear magnetisation characteristic. In the non-linear material, the relative permeability μ_r is not constant, and hence in the finite difference scheme, the parameter β is variable and must be updated for each spatial node and time step.

The surface node at each time step is the boundary condition node and is progressively given the values shown in Figure 5.33. This is the 3D finite element non-linear predicted surface flux density waveform (based on NO20 characteristic of Figure 5.20) which acts as the

reference excitation for the first validation of the finite difference method. This has a peak amplitude of 907 A/m and fundamental frequency of 10,000 Hz.

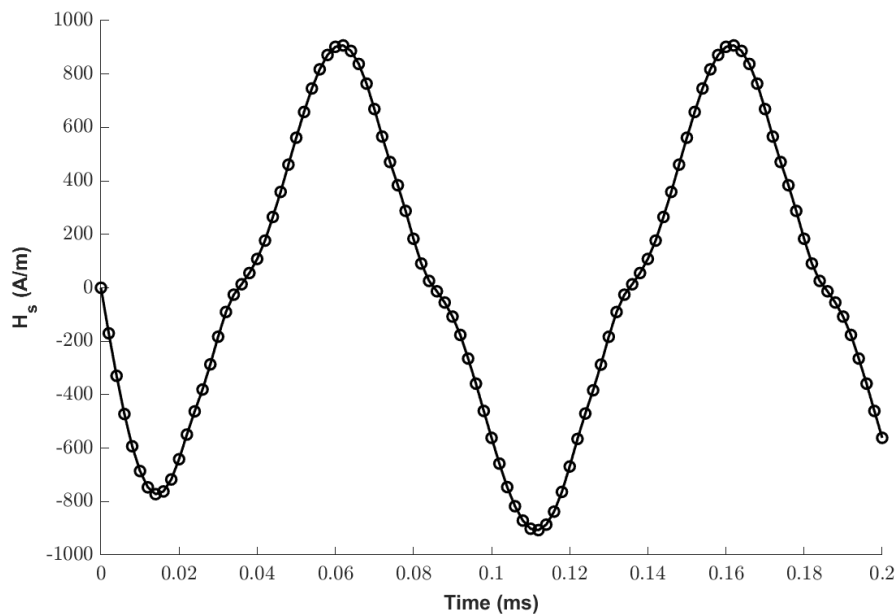


Figure 5.33. Time varying surface magnetic field distribution H_s waveform

At start of the finite difference calculation, the magnetic field strength at all the spatial nodes is set to zero, which will result in the magnetic permeability for the first set of calculations being the initial permeability of the *NO20* magnetisation characteristic shown previously in Figure 5.21. The value adopted for this is $\mu_{ini} = 0.0259 \text{ Hm}^{-1}$ which corresponds to a relative permeability of 20,627.

The procedure adopted is that for the first time-step, the field at the first node below the surface (numbered 10) is calculated using equation (5.50), initially using the value of the initial magnetic permeability, μ_{ini} . This value of H for the 1st node is then cascaded down through the nodes at increasing depth until values of H for the first time-step are obtained for all nodes which cover half the lamination depth. The finite difference procedure then progresses through each time-step updating the value of permeability at each spatial node based on the calculated magnetic field strength.

One feature of all time stepped methods is the discontinuity which occurs at the start of the simulation which results in some transient behaviour. Depending on the damping, it can take a number of cycles before the field settles down to the steady-state value. As shown previously in this chapter, the 3D finite element time-stepped simulations involve some level of transient start-up, but this tends to settle down within one cycle. For the finite element

simulations, the initial permeability is set to $\mu_{initial} = \mu_{max} = 0.0259$ (corresponds to a relative permeability of 20,627) which is the value from the *NO20* curves shown previously in Figure 5.21.

In the implementation used there is no iteration of the permeability at each time as the finite difference method progresses. The permeability from the previous time step is carried forward. This means that the time step must be chosen carefully to ensure that the change in permeability between successive steps. For example, for the H_s waveform shown the previously in Figure 5.33, then Figure 5.34 shows a comparison of the finite element predicted magnetic field strength waveform at the centre of the lamination with finite difference simulations having 150, 1000 and 3750 steps per electrical cycle. As shown, the 150 step finite difference results in a large difference from the finite element simulation while there is excellent agreement for the 3750 steps per cycle case.

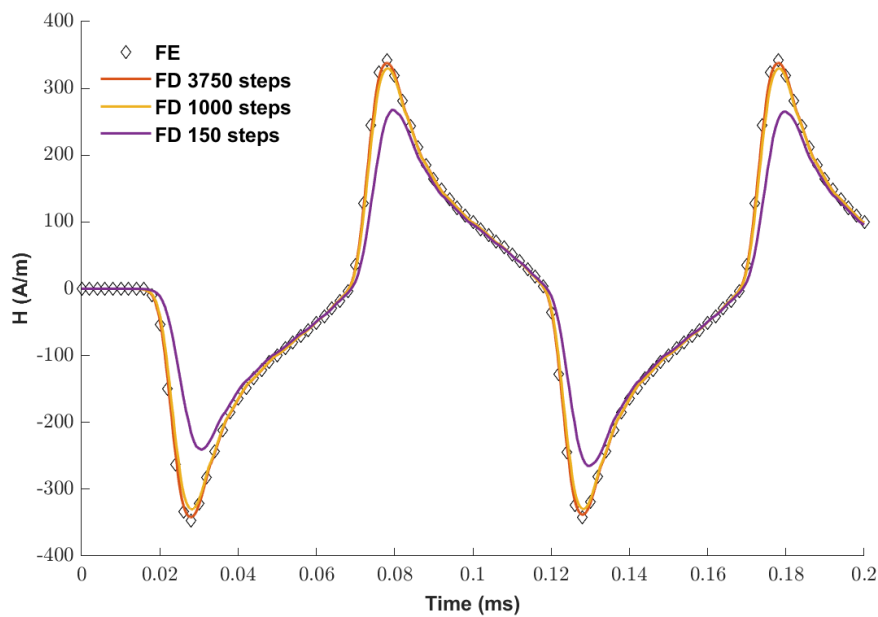
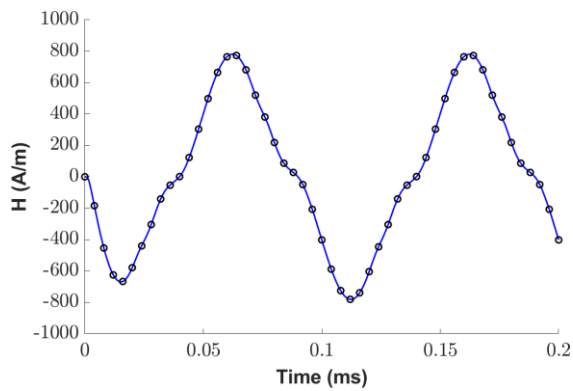


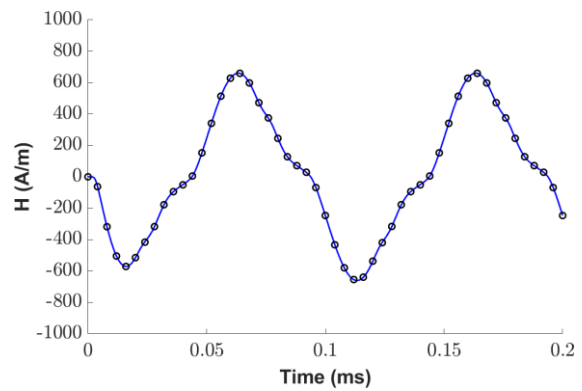
Figure 5.34 Comparison of the finite element predicted magnetic field strength waveform at the centre of the lamination with finite difference simulations having 150, 1000 and 3750 steps per electrical cycle

Figure 5.35 shows a comparison between the finite element and finite difference predicted variations in magnetic field strength at increasing depth into the lamination for the H_s waveform shown the previously in Figure 5.33. This finite difference simulation was performed with 3750 steps per electrical cycle. As shown, there is excellent agreement between both methods despite the presence of significant magnetic saturation as demonstrated in Figure

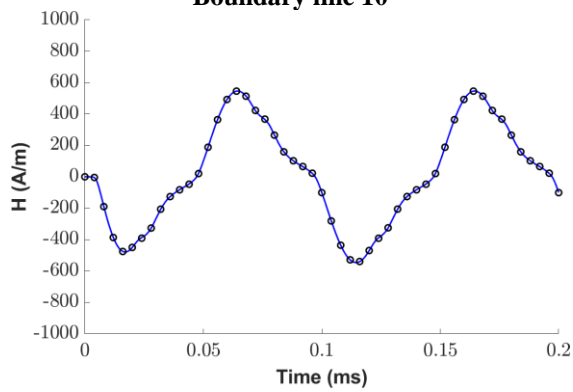
5.36 which shows a comparison between the finite difference and the 3D finite element variations in flux density at the surface of the lamination and the center of lamination, i.e., at $z=0\text{mm}$.



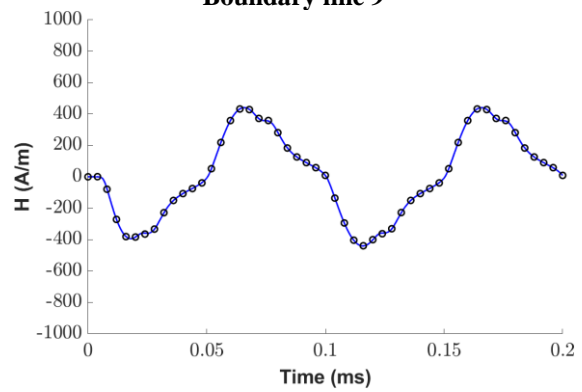
Boundary line 10



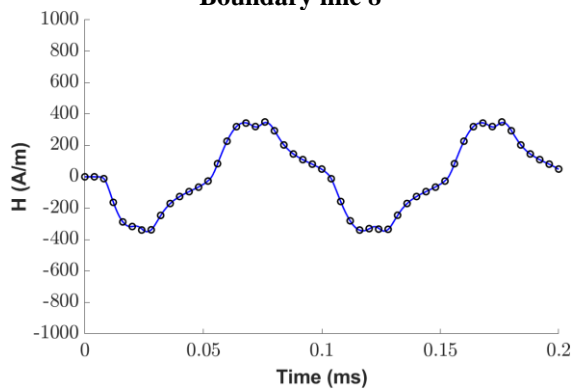
Boundary line 9



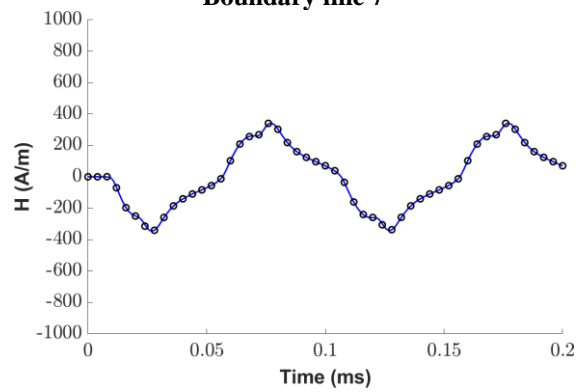
Boundary line 8



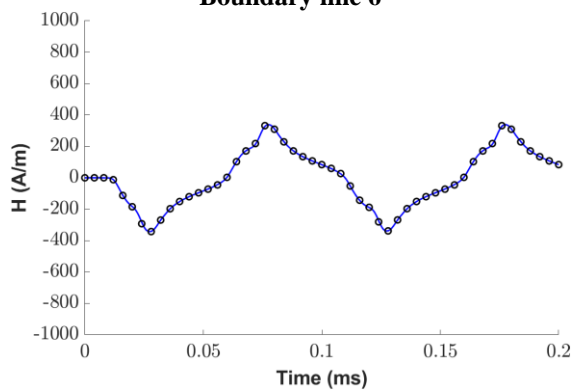
Boundary line 7



Boundary line 6



Boundary line 5



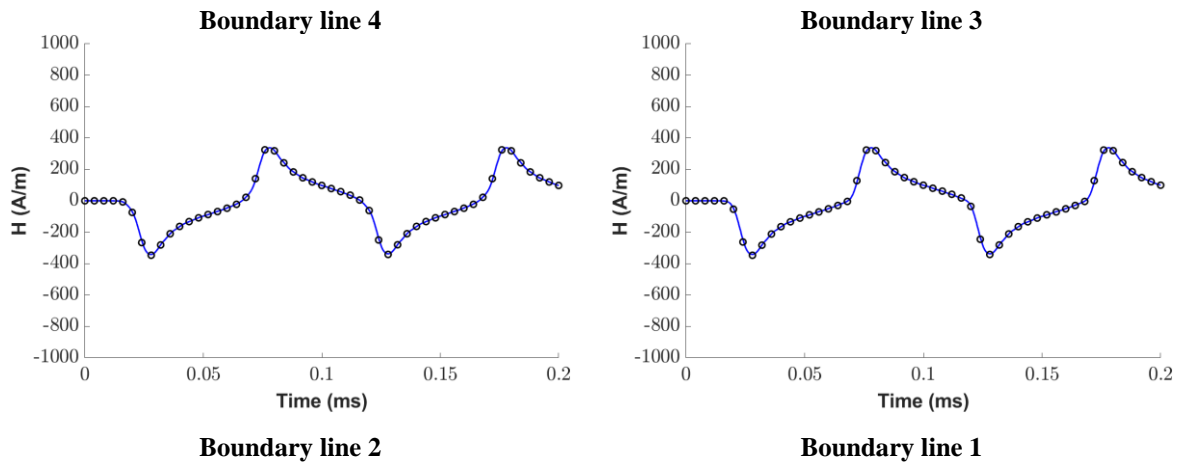


Figure 5.35. Comparison of finite element (\circ) and finite difference (—) simulations of an NO20 lamination exposed to the magnetic field strength waveform of Figure 34

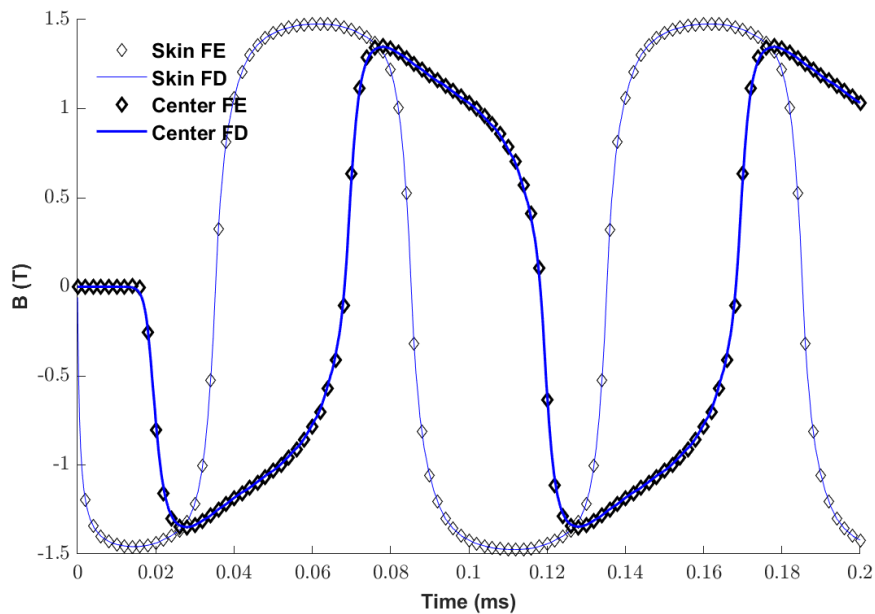


Figure 5.36. Finite difference and the 3D finite element variations in flux density at the surface of the lamination and the center of lamination

5.8 Establishing surface magnetic field strength for a 1D finite difference eddy current model from flux density waveforms

The finite difference implementation in section 5.7 was used with a known surface magnetic field strength waveform as an input. The aim of the overall methodology which is developed in this chapter is to take element-by-element flux density variations from a 2D magneto-static model of the full electrical machine and apply the 1D eddy current model to

that element. The 2D finite element model of the full electrical machine is a time-stepped magnetostatic simulation which does not include the effect of eddy currents in the solution and so there is no reaction field from the eddy currents. Hence, there is an inconsistency between the flux density waveforms generated from the machine level finite element model and the net flux in the lamination which is predicted by the 1D finite element model. This inconsistency cannot be resolved without including a representation of the eddy current within the lamination in the machine level finite element simulation. However, the aim of this study was to develop a post-processing tool to use with a commercial finite element package and so it is necessary to consider approximations for representing the flux density input to the finite difference model.

The method adopted in this study is to take the 2D calculated magnetostatic flux density waveform and convert this via the magnetisation curve of the core material (NO20 in this case) to a corresponding magnetic field strength waveform and directly assign this as the surface magnetic field strength H_s . This approach means that skin effect is accounted for in the iron loss calculation, but the reaction field is not accounted for in the setting of H_s from the magneto-static finite element simulations at machine level.

The impact of this approximation can be demonstrated by considering the case of the flux density variation in element in the front a stator tooth during the full rated torque operation of the baseline machine at 4,000rpm. The variation in the flux density which is a region subjected to complicated flux variations as the rotor magnets pass by is shown in Figure 5.37. As can be seen, this element is operating below saturation. The corresponding variation in the magnetic field strength calculated using the magnetisation curve of NO20 is shown in Figure 5.38. There is some evidence of the hysteresis controller introducing some high frequency ripple into the flux density waveform. It should be noted that the flux variation in the stator core has a significant contribution from the permanent magnet flux and hence a 5% ripple in the current does not translate into anything approaching 5% of the flux density. The finite difference predicted flux density waveforms with depth into the lamination in Figure 5.39. This shows the attenuation and phase shift of the flux density with depth into the lamination and the screening effect of the eddy currents which limit the noticeable high frequency ripple to the top few layers of the model. Towards the centre of the lamination, the flux density waveforms are smoother due to screening and the small skin depth of the high frequency components of the field.

The mean of the flux densities in each layer gives an estimate of the flux in the element and can be compared with the flux based on a uniform flux density in the lamination. For this particular element in the mesh the flux density waveform from the 2D magnetostatic finite element analysis and the mean flux density which results from the 1D finite difference model

is shown in Figure 5.40. As will be apparent, for this waveform which includes a representative 10 kHz ripple flux in the element is only $\pm 5\%$ of the magneto-static value. Hence, although the finite difference model provides a way of representing the redistribution of flux due to high frequency flux density variations and hence more accurately represent high frequency loss components, the magnetostatic solution of the field distribution provides a reasonable representation of the overall flux variation in the element, noting that in many machines the magnitude of the overall flux density is dominated by the low frequency components. Hence, aspects of performance such as torque will not be affected to any significant degree although the high frequency skin effect behaviour can be captured.

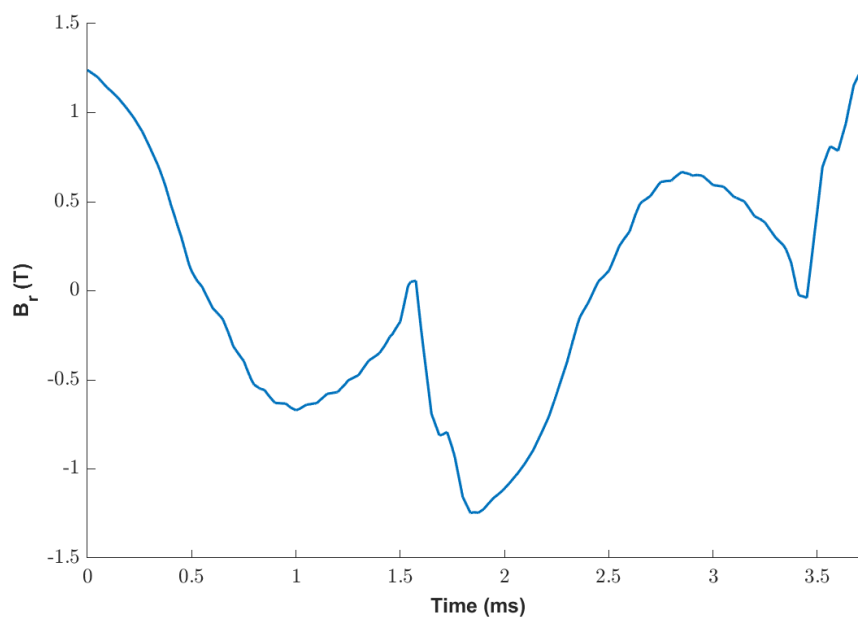


Figure 5.37 Finite element predicted waveform of radial component of flux density for an element in the front of the stator tooth with the baseline machine operating at rated torque and 4,000 rpm with an idealised symmetrical current hysteresis band of $\pm 5\%$

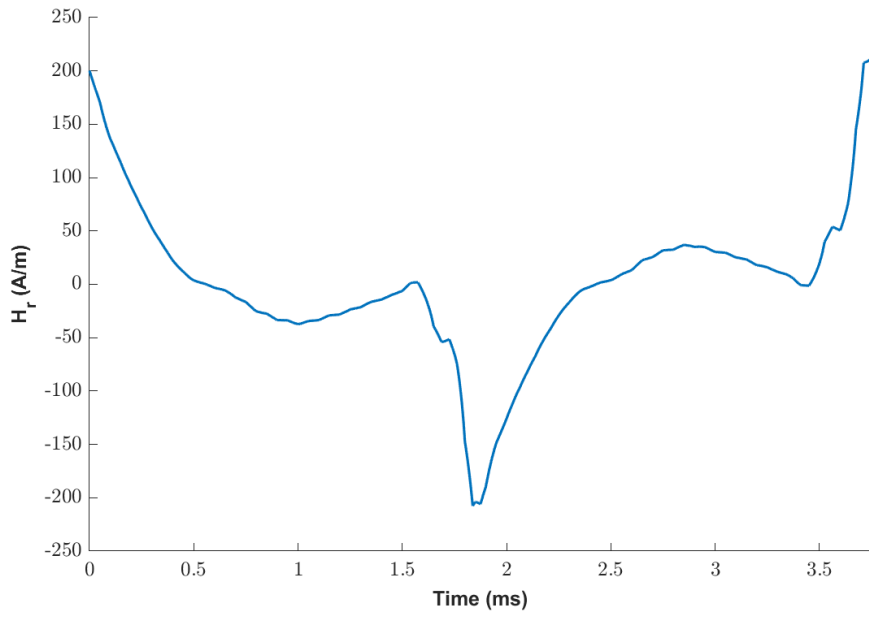


Figure 5.38 Corresponding magnetic field strength to the flux density waveform of Figure 5.36

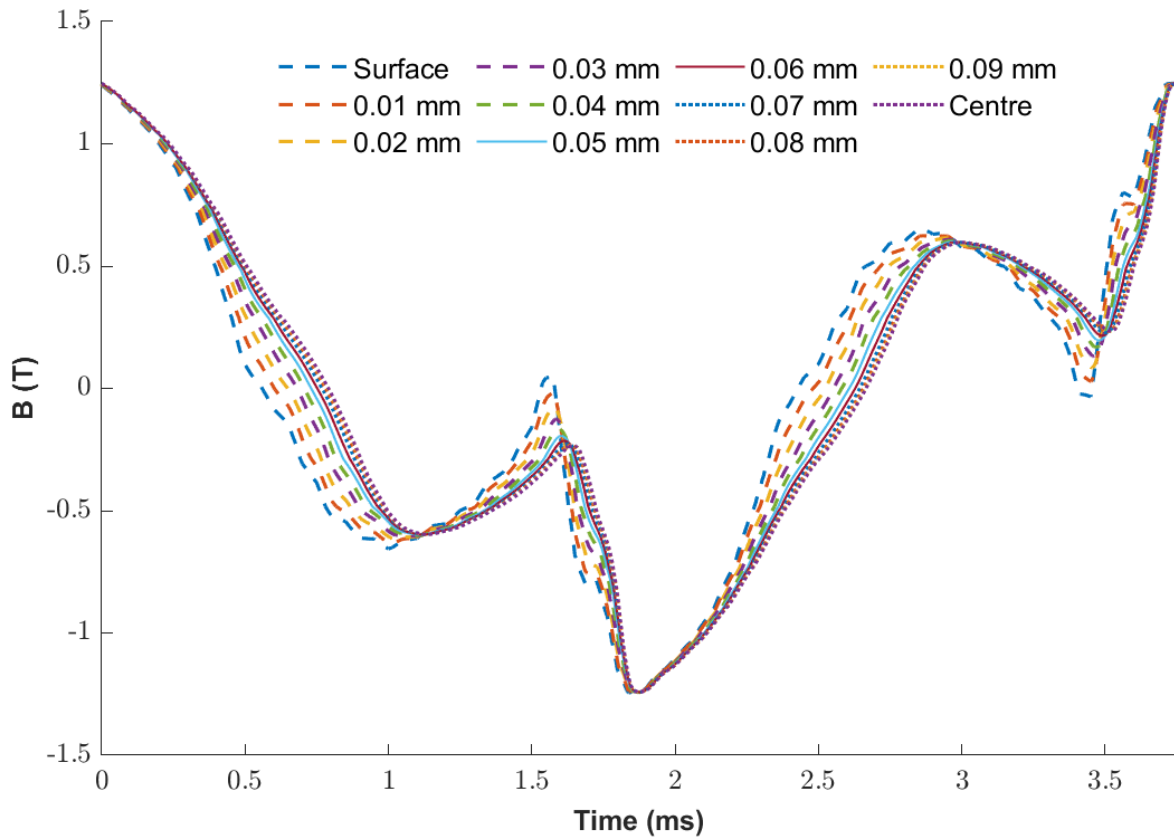


Figure 5.39 Finite difference 1D model predictions of the variation in magnetic flux density with depth into the lamination

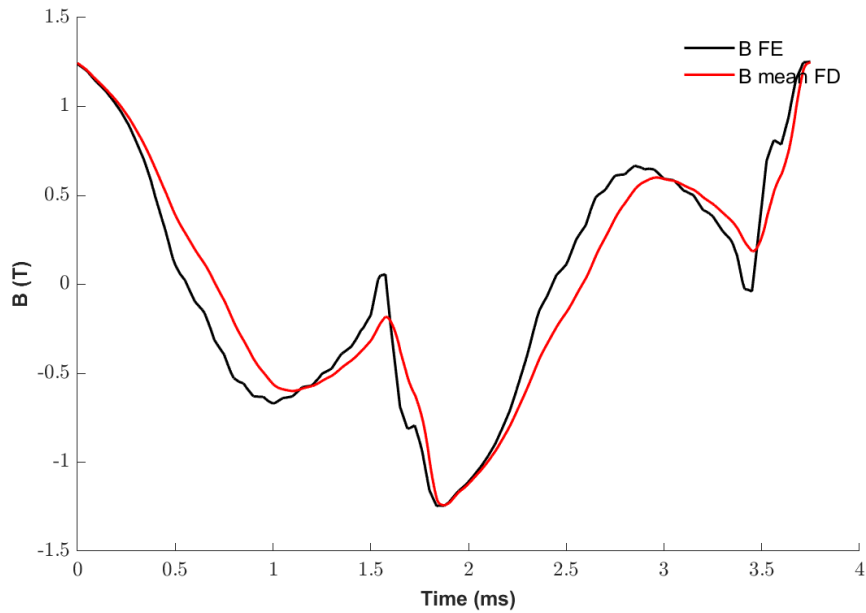


Figure 5.40 Comparison between original flux density waveforms with flux density waveform generated by taking the mean of the flux densities predicted by the 1D finite difference model at different depths into the lamination

5.9 Machine level iron loss calculations including the effects of high frequency switching and skin effect.

5.9.1 Introduction

The sections above have developed a post-processing method to account for skin-effect in laminations and applied it on a single element. This section is concerned with extending its use to a full machine at a range of speeds. As well as using the 1D finite difference method described in this chapter, two additional calculations were performed using a classical eddy current loss model. In the first method, the flux density waveforms are generated by the time-stepped finite element model with sinusoidal current. In the second method, the flux density waveforms are again generated by time-stepped finite element model with sinusoidal current but have a high frequency ripple added by the method described in chapter 3. These three calculations were performed to separate out the effect of including the effect of high frequency ripple in the flux density waveforms and accounting for skin effect.

5.9.2 Machine details and operating conditions

The loss calculations were first performed at rated torque at the rated speed of 4,000rpm for the final D165 IPM machine whose specification was summarised in section 2.4 of chapter

2. The pure sinusoidal current waveform used in the 2D time-stepped finite element model of the machine is shown in Figure 5.41 along with the corresponding waveform from the SIMULINK simulation with switching generated by a $\pm 5\%$ and $\pm 10\%$ hysteresis band controller. In this case, only the case of Grounded star-point was considered.

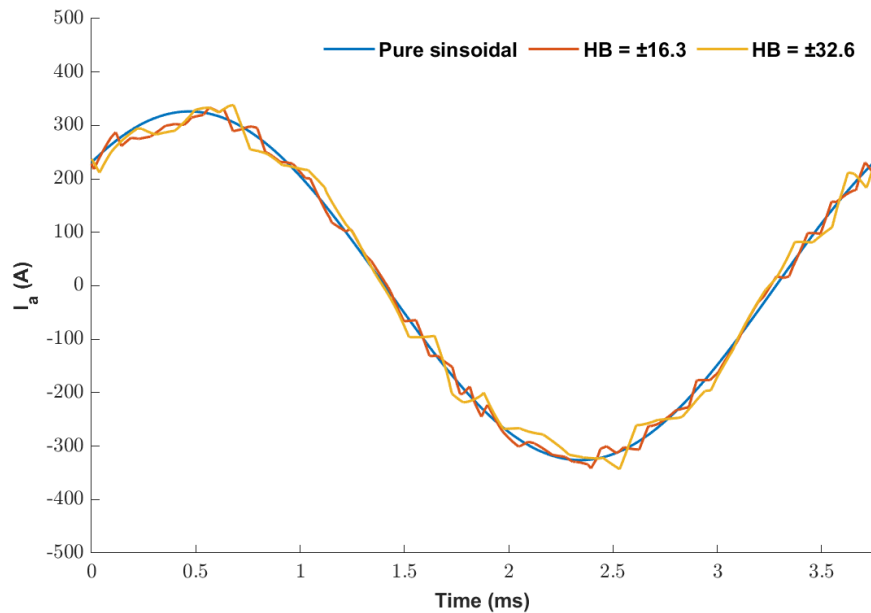


Figure 5.41 Pure sinusoidal current and hysteresis bands ($\pm 5\%$ and $\pm 10\%$) at 4,000rpm

The resulting predictions of iron loss for this operating point of rated torque at 4,000rpm with a hysteresis band of $\pm 5\%$ are summarised in Table 5.2. As can be seen there is some difference in loss when the skin effect is added into the model even at this modest speed.

Table 5.2 Summary of predicted iron loss at 4,000rpm and rated torque ($\pm 5\%$ hysteresis band)

Methodology	Pure sinusoidal current + resistance limited eddy current iron loss	Hysteresis controlled current waveform + resistance limited eddy current iron loss	Hysteresis controlled current waveform + 1D finite difference iron loss
Hysteresis loss (incl. minor loops)	240.0 W	240.4 W	242.3 W
Hysteresis major loop	234.1 W	231.4 W	236.8 W
Hysteresis minor loop	5.9 W	9.0 W	5.5 W
Excess loss	50.0 W	54.1 W	53.5 W
Eddy current loss	62.5 W	72.1 W	81.7 W
Total loss	352.4 W	366.6 W	377.5 W

Table 5.3 Summary of predicted iron loss at 4,000rpm and rated torque ($\pm 10\%$ hysteresis band)

Methodology	Pure sinusoidal current + resistance limited eddy current iron loss	Hysteresis controlled current waveform + resistance limited eddy current iron loss	Hysteresis controlled current waveform + 1D finite difference iron loss
Hysteresis loss (incl. minor loops)	240.0 W	243.0	242.6
Hysteresis major loop	234.1 W	235.4	236.3
Hysteresis minor loop	5.9 W	7.7	6.3
Excess loss	50.0 W	52.8	52.9
Eddy current loss	62.5 W	69.4	78.8
Total loss	352.4 W	365.3	374.2

The results in Table 5.2 and Table 5.3 are unexpected since it is usually the case for sinusoidal flux densities that accounting for skin effect will tend to reduce the eddy current loss for a given surface flux density. The detailed behaviour in terms of loss can be observed by considering an element in the middle of the stator tooth. The flux density waveforms in this particular element as function of depth are shown in Figure 5.42 for the case of $\pm 5\%$. The associated eddy current losses density in each layer for this particular element is summarised in Table 5.4. For comparison, the classical resistance-limited eddy current loss density for this element is 11.79W/kg for a 0.01 mm equivalent layer. As would be expected, the loss near the surface of the 1D finite difference calculated waveform are very close to the classical eddy-current loss. However, since the only major change in the flux density waveform is an increase in the rate of change around zero crossing, then it is to be expected that the loss increases with depth rather than decreases as might be expected from pure sinusoid.

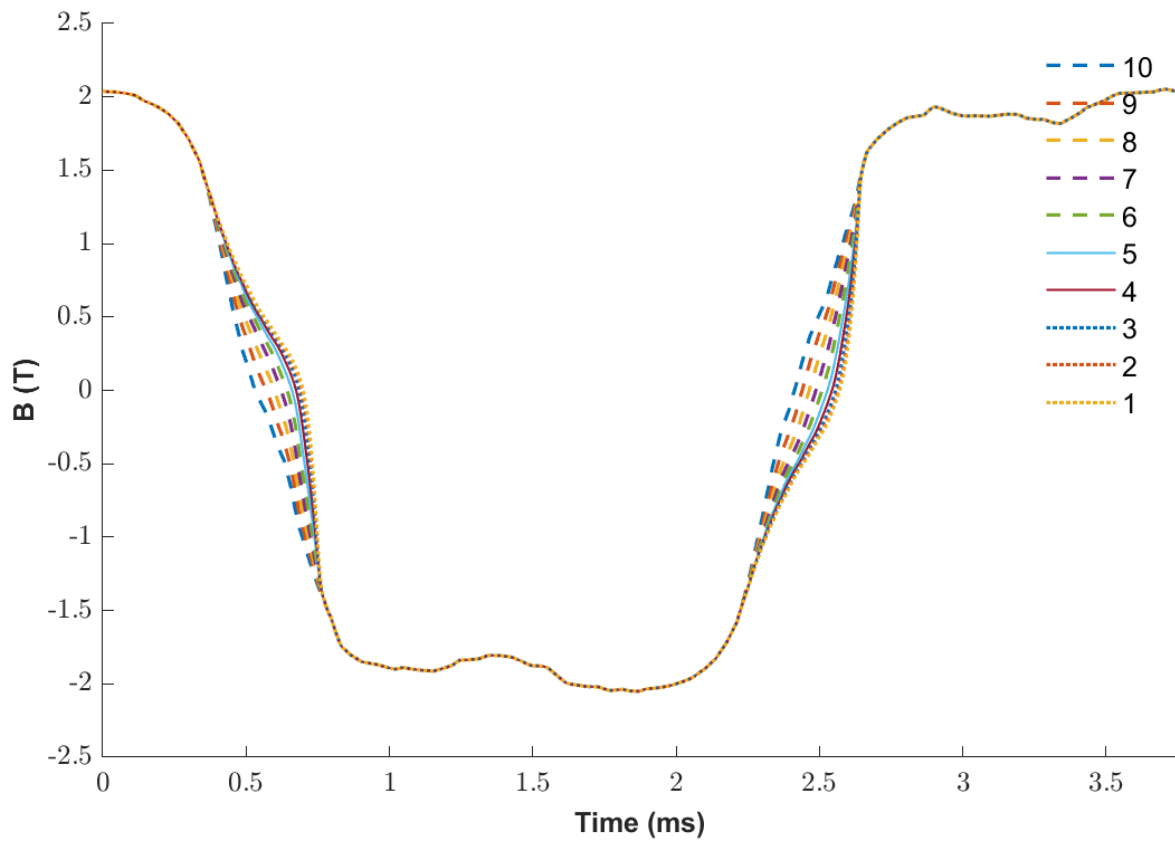


Figure 5.42 Finite difference 1D model predictions of the variation in magnetic flux density with depth into the lamination

Table 5.4 Associated eddy current losses density in each layer for selected element

Layer	Loss density (W/kg)
10	11.53
9	11.34
8	11.54
7	12.07
6	12.90
5	14.02
4	15.44
3	17.13
2	18.82
1	19.93

5.10 Summary

This chapter has developed a method for predicting the loss in the core of an electrical machine which takes account of skin effect and field redistribution within individual laminations. Several methods based on the diffusion equation of eddy current are investigated and applied within the lamination level. A full 3D time-stepped model of single lamination was used as the reference for comparing the accuracy of different models. The results have shown that layer method of analytical model could procedure flux density re-distribution within the laminations for linear materials but have a significant error in processing non-linear material cases due to varying permeability of non-linear materials. A 1D finite difference model have been developed with shows excellent agreement with 3D finite element analysis for a specified surface magnetic field strength variation. The overall iron loss at machine level is calculated by integrating high frequency switching effects and skin effects within the laminations with time-domain iron loss calculation method. This chapter detail illustrates the full methodology from finite element characterisation of the machine parameters, calculation of element-by-element localised flux densities and rates of change of flux density with stator current, through a SIMULINK model to generate element-by-element flux density waveforms with representative switching and culminating in Matlab based post-processor which includes a 1D finite difference model. It has been shown that in an electrical machine the effect on the overall iron loss of accounting for high frequency switching events is modest due to the dominant role of the permanent magnet excitation.

Reference

- [1] K. Atallah, “Iron Losses in Brushless Permanent Magnet DC Machines,” 1993.
- [2] A. Boglietti, P. Ferraris, and M. Lazzari, “Power derating for inverter fed induction motors,” *Conf. Rec. - IAS Annu. Meet. (IEEE Ind. Appl. Soc.*, vol. 1, pp. 55–61, 1994, doi: 10.1109/ias.1994.345499.
- [3] K. Yamazaki and N. Fukushima, “Torque and loss calculation of rotating machines considering laminated cores using post 1-D analysis,” *IEEE Trans. Magn.*, vol. 47, no. 5, pp. 994–997, 2011, doi: 10.1109/TMAG.2010.2089501.
- [4] K. Yamazaki and Y. Sakamoto, “Electromagnetic Field Analysis Considering Reaction Field Caused by Eddy Currents and Hysteresis Phenomenon in Laminated Cores,” *IEEE Trans. Magn.*, vol. 54, no. 3, pp. 1–4, 2018, doi: 10.1109/TMAG.2017.2749247.
- [5] J. Rens, L. Vandenbossche, and O. Dorez, “Iron loss modelling of electrical traction motors for improved prediction of higher harmonic losses,” *World Electr. Veh. J.*, vol. 11, no. 1, pp. 1–14, 2020, doi: 10.3390/WEVJ11010024.
- [6] O. Bottauscio and M. Chiampi, “Analysis of laminated cores through a directly coupled 2-D/1-D electromagnetic field formulation,” *IEEE Trans. Magn.*, vol. 38, no. 5 I, pp. 2358–2360, 2002, doi: 10.1109/TMAG.2002.803573.
- [7] S. E. Zirka, Y. I. Moroz, P. Marketos, and A. J. Moses, “Viscosity-based magnetodynamic model of soft magnetic materials,” *IEEE Trans. Magn.*, vol. 42, no. 9, pp. 2121–2132, 2006, doi: 10.1109/TMAG.2006.880685.
- [8] P. Rasilo, W. Martinez, K. Fujisaki, J. Kyyra, and A. Ruderman, “Simulink model for PWM-supplied laminated magnetic cores including hysteresis, eddy-current, and excess losses,” *IEEE Trans. Power Electron.*, vol. 34, no. 2, pp. 1683–1695, 2019, doi: 10.1109/TPEL.2018.2835661.
- [9] H. Zhao, C. Ragusa, O. De La Barriere, M. Khan, C. Appino, and F. Fiorillo, “Magnetic Loss Versus Frequency in Non-Oriented Steel Sheets and Its Prediction: Minor Loops, PWM, and the Limits of the Analytical Approach,” *IEEE Trans. Magn.*, vol. 53, no. 11, pp. 18–21, 2017, doi: 10.1109/TMAG.2017.2701299.
- [10] C. Beatrice *et al.*, “Broadband magnetic losses of nanocrystalline ribbons and powder cores,” *J. Magn. Magn. Mater.*, vol. 420, pp. 317–323, 2016, doi: 10.1016/j.jmmm.2016.07.045.

- [11] M. Ibrahim and P. Pillay, "Core loss prediction in electrical machine laminations considering skin effect and minor hysteresis loops," *IEEE Trans. Ind. Appl.*, vol. 49, no. 5, pp. 2061–2068, 2013, doi: 10.1109/TIA.2013.2260852.

Chapter 6: Experimental testing and validation

6.1 Introduction

The research presented up to this point has involved simulation and post-processing analysis. In order to provide verification of the loss models developed, this chapter describes some loss measurements on a test sample of core material and the construction of the reference electrical machine design demonstrator.

6.2 Toroidal core testing with sinusoidal excitation

6.2.1 Measurement equipment for sinusoidal excitation

To provide direct and well-controlled experimental reference measurements against which to compare the iron loss models developed in chapters 4 and 5, a series of measurements with sinusoidal excitation were performed on a toroidal ring sample of NO20 Silicon iron laminations. The measurement of magnetisation curves and iron loss was performed using a Laboratorio Electrofisica AMH-1K soft magnetic measurement system. This is a high precision instrument which contains the controlled excitation source and the measurement hardware. It includes a PC controlled data acquisition system and a software controller. It is capable of performing soft magnetic material measurements up to 1kHz in line with the requirements of IEC 60404-4 and IEC 60404-6 standards. The instrument is shown in Figure 6.1 along with a block diagram.

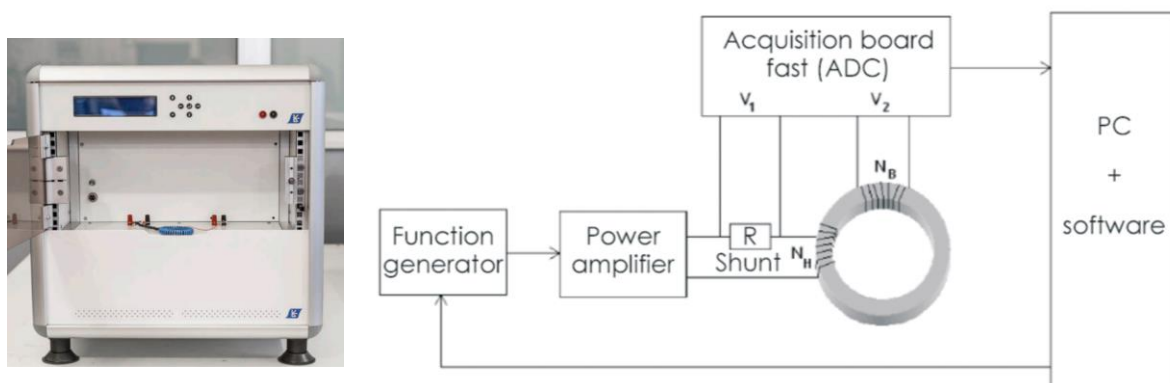


Figure 6.1 Laboratorio Electrofisico AMH-1K high resolution soft magnetic measurement (Source: [1], [2])

6.2.2 Sample winding

The lamination stack is wound with two coils which act as the drive coil which is connected to the excitation source and a search coil. These can be regarded as the primary and open-circuit secondary windings. The search coil is close-fitting coil of fine wire which is wrapped onto the stack which has had a thin layer of insulating tape applied. The drive coil is wound on top of the search coil, in most cases after a further layer of tape. The drive coil is made up of thicker wire can carry the current required to achieve the desired excitation levels. The mean path length of the flux path in the toroid, l_m , can be estimated using:

$$l_m = \pi \frac{(D_o + D_i)}{2} \quad (6.1)$$

If the number turns number of the drive coil is N_H , the magnetising field strength for a particular current is given by:

$$H = \frac{N_H i}{l_m} \quad (6.2)$$

The search coil measures the induced voltage which is proportional to the rate of change of flux in the toroidal stack.

$$e_B = -N_B \frac{d\phi}{dt} \quad (6.3)$$

The flux in the sample can be calculated using:

$$\phi = - \int V_2 dt \quad (6.4)$$

Although the effective height of magnetic material in the toroid, h , could be obtained by measuring the lamination thickness and scaling up by the number of laminations, a more accurate value of h can be obtained from a measurement of the overall stack mass, m , using:

$$h = \frac{4m}{\rho\pi(D_o^2 - D_i^2)} \quad (6.5)$$

The cross-sectional area A of the sample for a total magnetic material height is given by:

$$A = \frac{(D_o - D_i)}{2} h \quad (6.6)$$

The flux density in the sample can be calculated from the measured flux using:

$$B = \frac{\phi}{N_B A} \quad (6.7)$$

Since the search coil voltage is directly proportional to the excitation frequency and the magnitude of the flux density, the range of input voltages to the data acquisition can be large. In order to ensure good resolution at low frequencies and avoid damaging the input channels through over-voltage at high frequencies, the AMH-1K has a series of fixed ratio attenuators which can be added in response to prompts from the software to keep the voltage within a range as the frequency and flux density are increased. Figure 6.2 shows a typical connection arrangement with and without an attenuator in place.



a. Directly connected (low induced V_2)

b. Connected with a resistive attenuator
(high induced V_2)

Figure 6.2 Search coil connections with and without attenuator

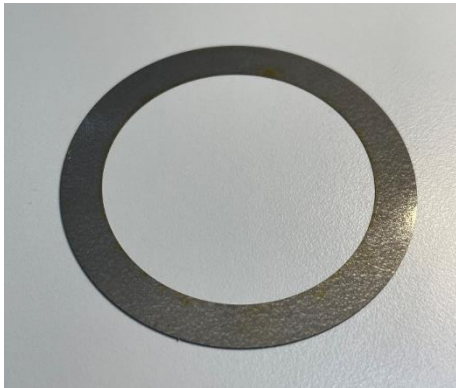
6.2.3 Preparation of test sample

The toroidal sample used in this test was made from a stack of 35 NO20 Silicon-iron laminations which are 0.2mm thick. These were produced by wire EDM which is recognised as the cutting method for thin laminations which introduces the least edge damage. The main dimensions of the toroid sample are summarised in Table 6.1. The process from a single lamination to the finished measurement sample is shown in Figure 6.3. The stack of laminations was wrapped with a Kapton tape and a tight-fitting search coil with 30 turns was wound on top of the tape. This number of turns was chosen by adopting the AMH-1K recommended guidance for a Silicon-iron samples of this size [3]. A drive coil consisting of 40 turns of 1.0 mm diameter wire was then wound on top of the search coil, again following the equipment manufacturer recommendations for the number of turns.

Table 6.1 NO20 toroid sample parameters

Parameter	Value
Inner diameter	50.0mm
Outer diameter	64.94mm
Nominal lamination thickness	0.21mm
Number of laminations in stack	35
Stack mass	71.8g
Density	7600 kg/m ³

Step 1



Step 2



Step 3



Step 4



Step 5



Figure 6.3 Toroid sample construction steps

6.2.4 Method for predicting losses in the toroid sample

Inferring material properties from measurements on a toroidal sample assumes that there is a single magnetic working point throughout the sample. This is based on the assumption of a uniform magnetising field strength in the material which is based on the mean path length and the number of Ampere-turns in the coil. In practice, the magnetising field strength varies between the inner diameter (where it is a maximum) to the outer diameter. In order to minimise the error from this approximation of a uniform magnetising field strength, the IEC 60404-4 and IEC 60404-6 standard for measurement of material properties sets out a preferred ratio of outer to inner diameter of <1.25 [3].

For this series of tests, the purpose is not to characterise the dimension independent material properties but to perform a series of tests on a test-piece in which the excitation is known. A more representative test for the post-processing method which has been developed to calculate loss at a machine level is to consider the toroid as a series of nested sub-rings which can be considered as having some similarities to elements in a finite element in a mesh. An illustration of this approach, in which the toroid is split for calculation purposes into 6 sub-rings is shown in Figure 6.4. It is important to note that this does not involve any modification to the lamination ring itself, it is simply a discretisation of the region for calculation.

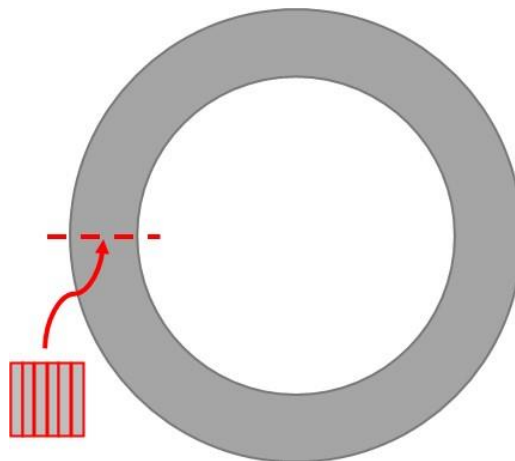


Figure 6.4 Division of the toroidal sample into 6 equal sub-rings for calculation purposes

The main challenge in this sub-division is that the flux density waveform which acts as input to the model is based on an average flux density across the full width of the sample. Hence, using this approach, there is only a single value of magnetising field strength that can be derived from the NO20 magnetisation curve. However, it is well known that the magnetising field strength varies between the inner and outer edge, simply because the path length is

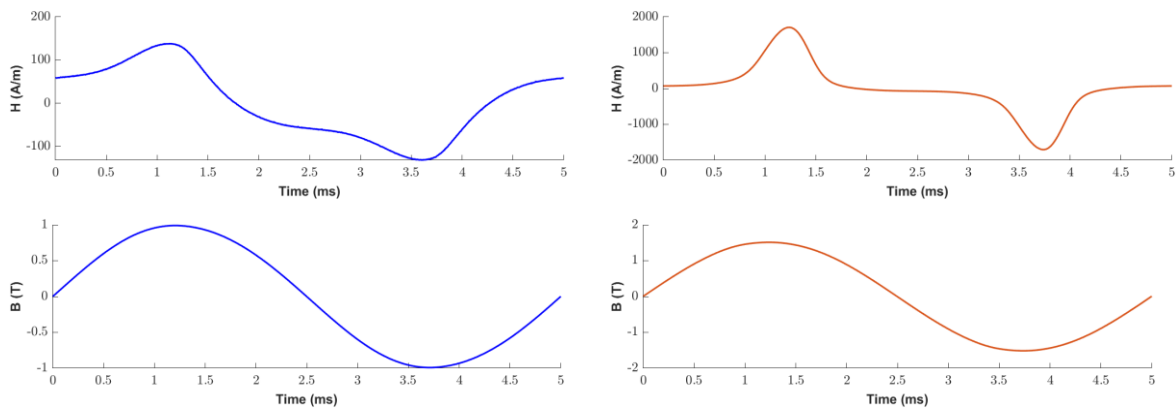
changing. To account for this inconsistency, the magnetising field strength in the n^{th} ring is approximated by:

$$H_n = \frac{D_{mean}}{D_n} H_{mean} \quad (6.8)$$

Having calculated the loss density in each sub-ring it is necessary to weight these contributions to give an overall effective loss density for the toroid, which is the value that is compared to measurements. This weighting of contributions from each sub-ring is based on the mass fraction of that ring to the overall mass of the toroid sample. In the predictions of loss presented in this chapter, 6 sub-rings (each 1.25mm wide) were used to represent the actual toroid and the predicted loss density is the weighted mean of these loss densities.

6.2.5 Loss measurements with sinusoidal excitation

Figure 6.5 shows the measured B and H waveforms for 200Hz sinusoids with peak flux densities of 1.0T and 1.5T while Figure 6.6 shows the resulting measured hysteresis loops.



(a) 200Hz sinusoid with 1.0T peak

(b) 200Hz sinusoid with 1.5T peak

Figure 6.5 Measured B and H waveforms for 200Hz sinusoidal excitation

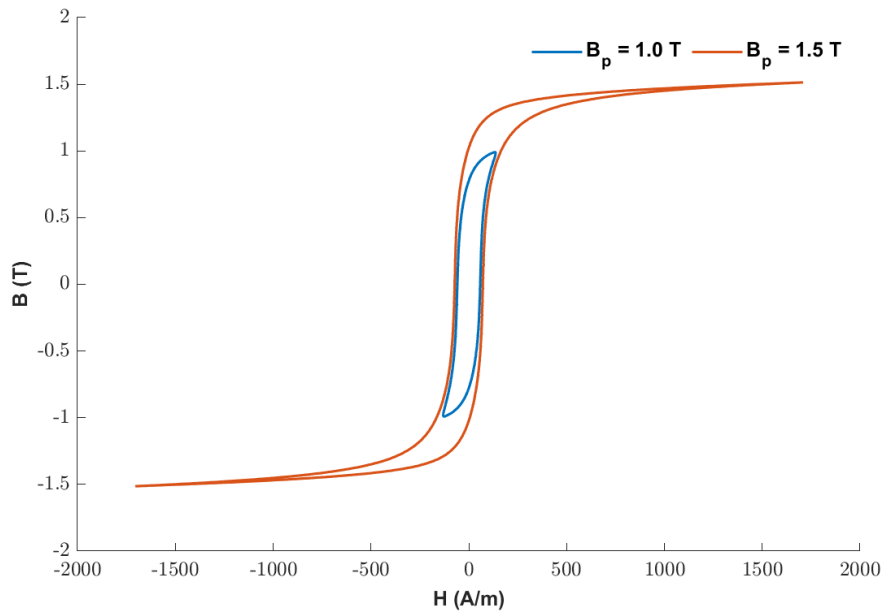


Figure 6.6 Measured hysteresis loops for 200Hz sinusoidal excitation

This process was repeated with 200Hz steps in frequency up to 1kHz. The resulting measured loss as a function of frequency are shown in Figure 6.7 along with predictions of loss based on the classical resistance-limited eddy currents and the finite-difference eddy current model with skin effect which is based on converting measured flux density waveform into magnetic field strength through NO20 magnetisation curve as the input for the surface magnetic field strength.

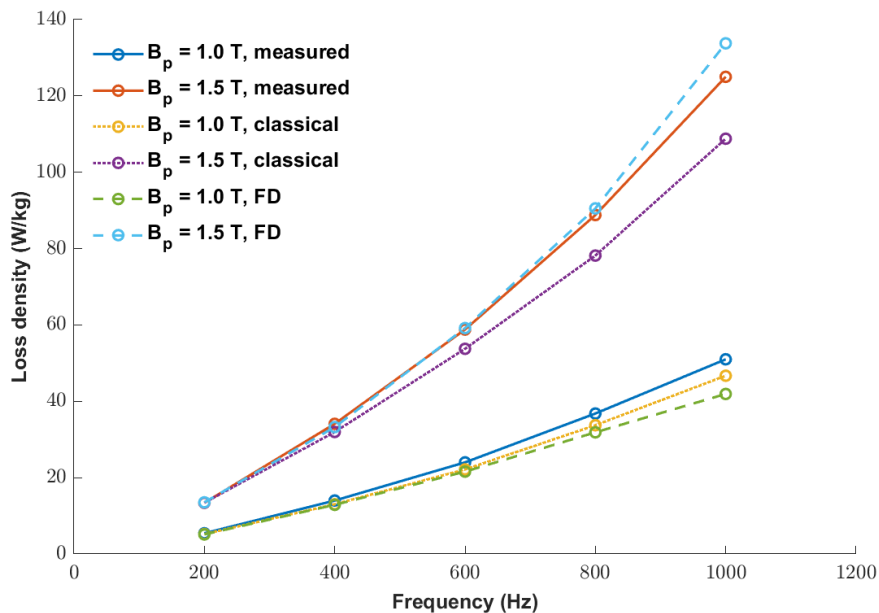


Figure 6.7 Comparison of measured loss and predictions with classical and skin effect models

As will be seen, at 1.5T and from 600Hz upwards, there is a significant difference between the classical eddy current model and the measured loss and skin effects models, with the finite difference model showing good agreement with measurements. This behaviour is not observed in the 1.0T measurements where the loss predicted by classical eddy current model tracks the measurement better and is higher than the skin effect loss. In general, it is expected that the iron loss predicted by a classical model would be higher than a skin depth based model, although shown in these results, the behaviour becomes more complex with the presence of significant saturation where the permeability within the skin depth drops significantly.

6.3 Toroidal core testing with switching waveform

6.3.1 Test apparatus

To provide controlled switching waveforms for loss measurements, a custom test-rig was assembled. The overall set-up is shown in Figure 6.8 along with a block diagram of the arrangement. Since the aim of this testing was to generate representative switching waveforms and measure the loss, there was no requirement to have closed-loop control for sinusoidal excitation. Although the switching strategy considered in chapter 2 was hysteresis control, the H bridge modules (Infineon BLDCSHIELDIFX007TTOBO1 operating with a 15 V DC link) and the controller were configured for PWM control. Since the current waveforms measured with this rig provided the input current waveforms for the loss models, the difference between a hysteresis controller and a PWM controller is not important. A National Instruments Compact-Rio controller was used to generate PWM signals for the H-bridge drivers with adjustable demand waveform and modulation.

The circuit includes an additional in-line inductor (PCV-2-105-02L CCI 0649 with an inductance of 10.3 mH) to improve the current waveform in terms of producing representative ripple. The current was measured using a pico TA018 current probe. The search coil emf and current probe output were measured using a 12-bit resolution Yokogawa DL850V Scopecorder. The measured waveforms were downloaded for further analysis and to provide input to the loss models.

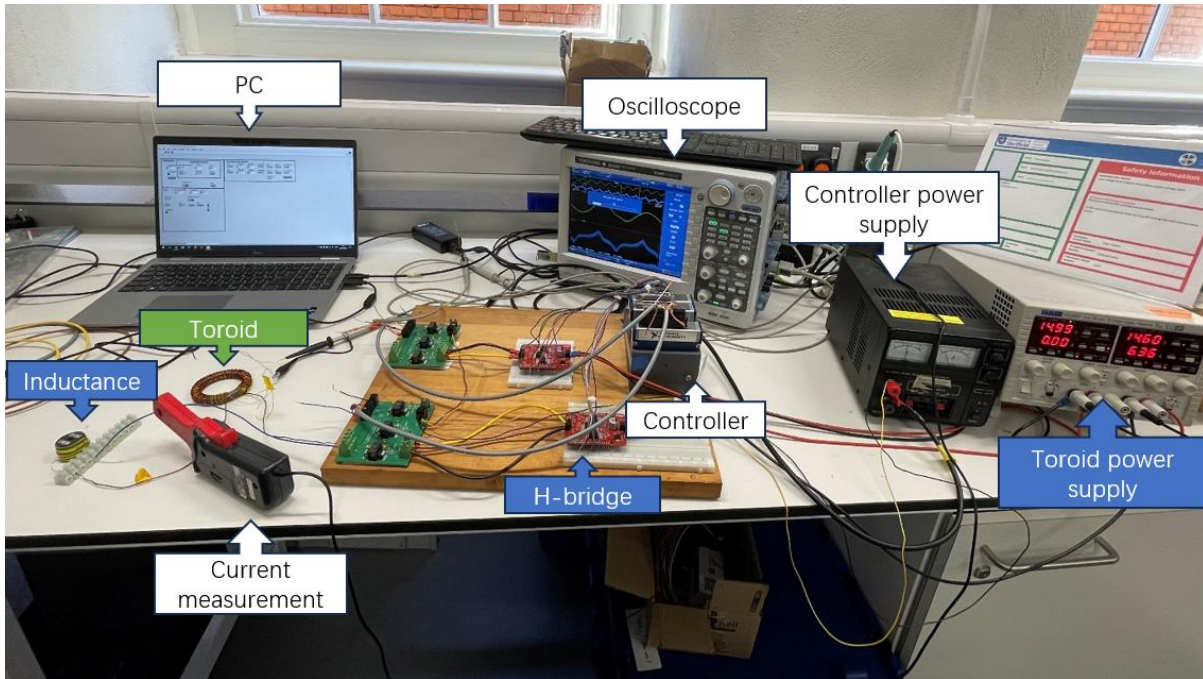


Figure 6.8 Test overall set-up

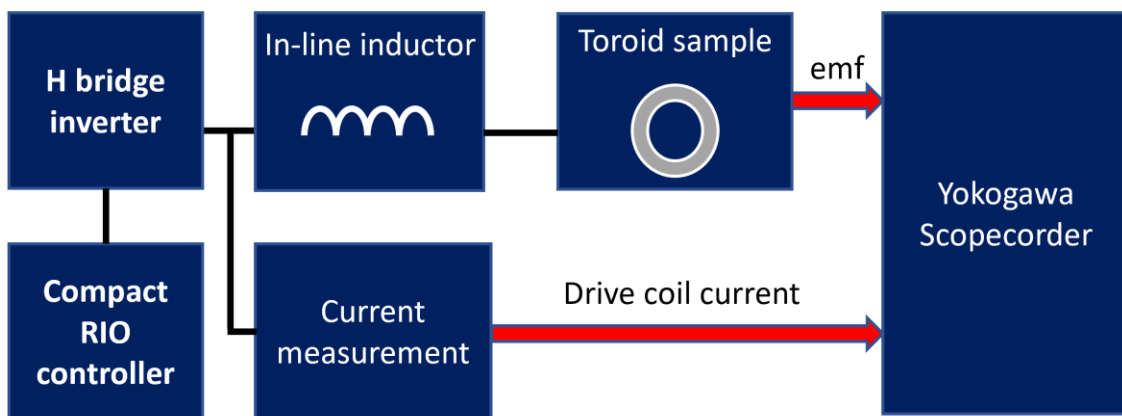


Figure 6.9 Switching waveform test rig

Figures 6.10 and 6.11 shows typical measured current and search coil voltage for the toroidal sample at $V_{dc}=15V$, PWM frequency 5 kHz, fundamental frequency 200 Hz condition with 0.2 and 1.0 modulation indices respectively.

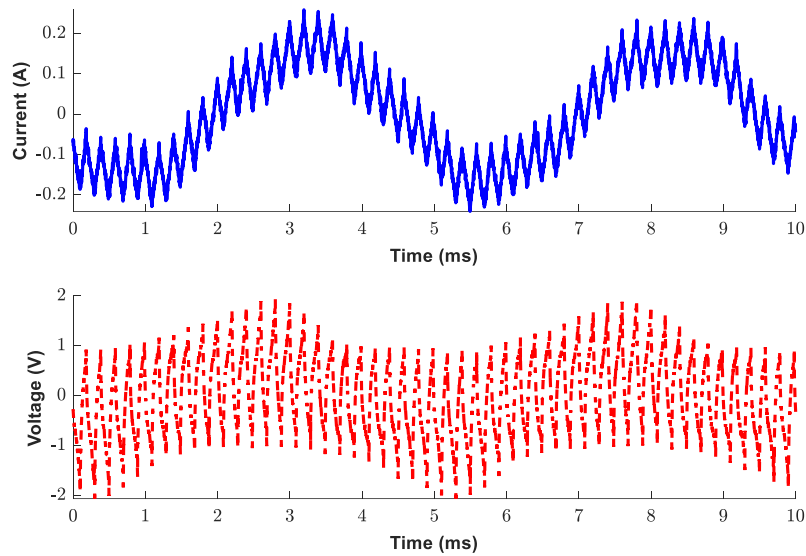


Figure 6.10 Typical measured current and search coil voltage ($V_{dc}=15V$, PWM frequency 5 kHz, fundamental frequency 200 Hz and modulation index 0.2)

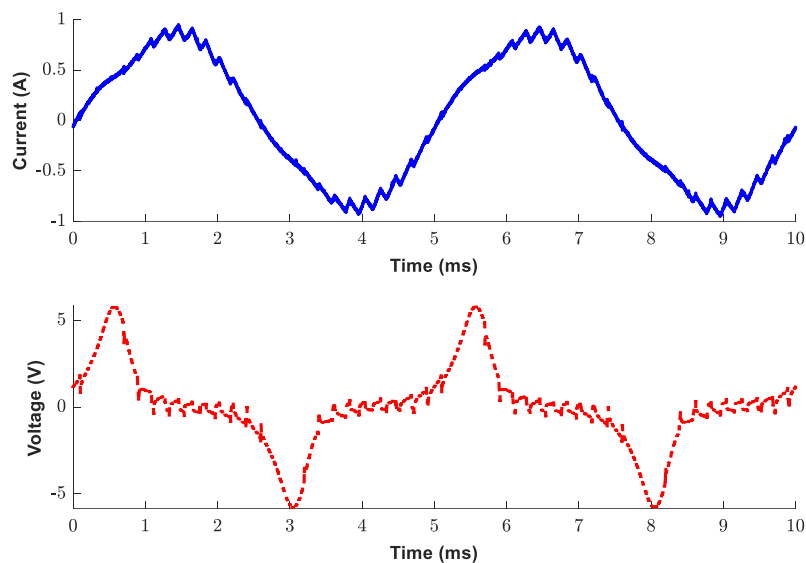


Figure 6.11 Typical measured current and search coil voltage ($V_{dc}=15V$, PWM frequency 5 kHz, fundamental frequency 200 Hz and modulation index =1)

6.3.2 Calculating loss density from the measured waveforms

The core loss per unit mass from measurements on this sample can be calculated from the instantaneous power which is transferred into the toroidal sample. The combination of the current measurement on the drive coil and the search coil voltage captures the input power to the core but does not include the drive coil resistive losses which would be included in the input power if the measurement of terminal voltage was taken at the drive coil input to the toroid.

For a drive coil with N_s turns and a search coil with N_B turns, the average electrical input power into the sample over one cycle is given by:

$$P_e = \frac{1}{T} \int_0^T \frac{N_H}{N_B} e_s i_d dt \quad (6.9)$$

The correction of $\frac{N_H}{N_B}$ is required to account for the fact that the drive and sense coils have a different number of turns in the toroid used. The loss density can be obtained by dividing the electrical input power by the mass of the sample. For a toroidal sample this is given by:

$$m = \frac{\pi}{4} (D_o^2 - D_i^2) N_l h_l \rho \quad (6.10)$$

Hence, the average of loss per kg can be obtained from

$$P_{fe} = \frac{P_e}{m} \quad (6.11)$$

Taking the example of a 200Hz, 1T peak sinusoidal demand waveform with a 5kHz PWM frequency. The measured drive coil current waveform and search coil emf waveform for this particular case are shown in Figures 6.12 and 6.13 respectively while Figure 6.14 shows the flux density waveform generated by integration of the search coil emf. The DC offset caused by the absence of an initial condition for the integration was removed by forcing the waveform to be symmetrical about zero.

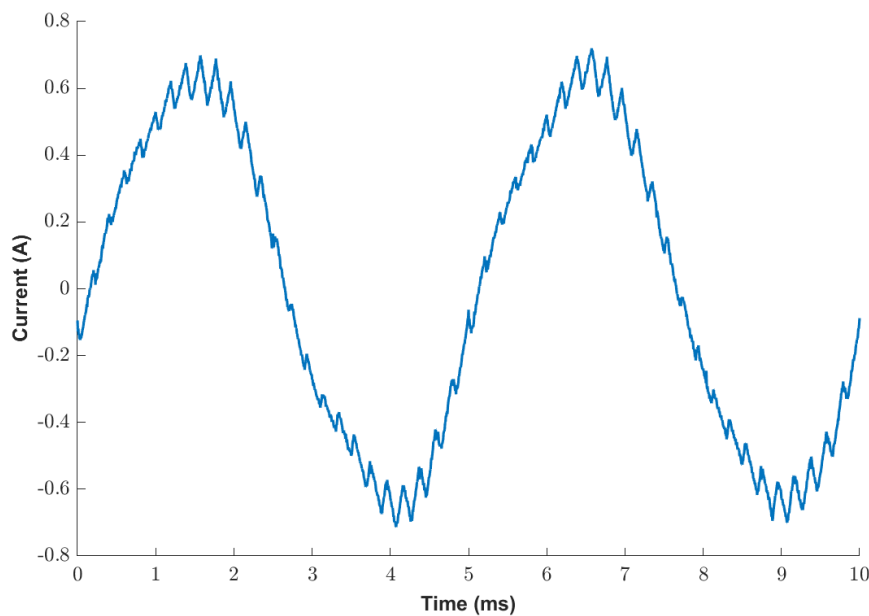


Figure 6.12 Measured current waveform in 40 turn drive coil

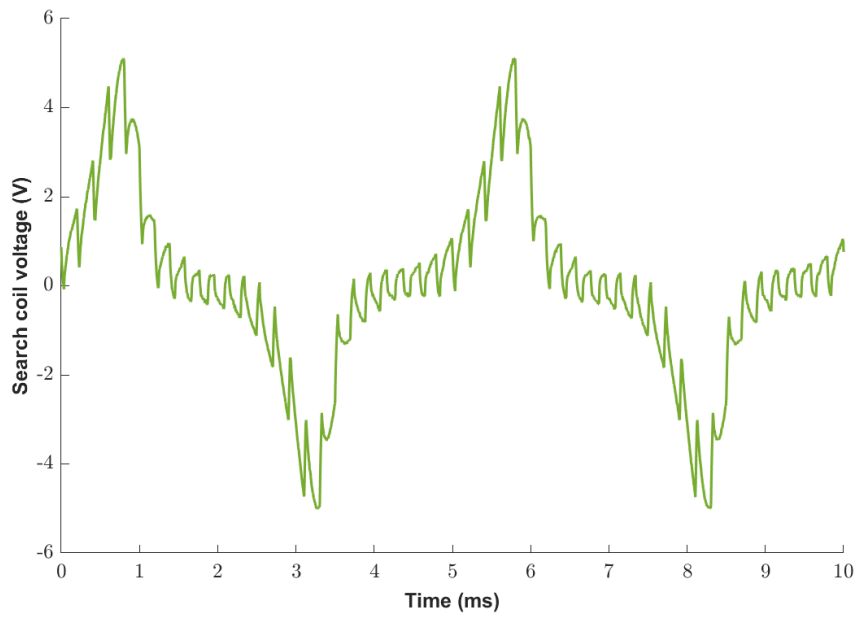


Figure 6.13 Measured search coil voltage waveform in 30 turn search coil

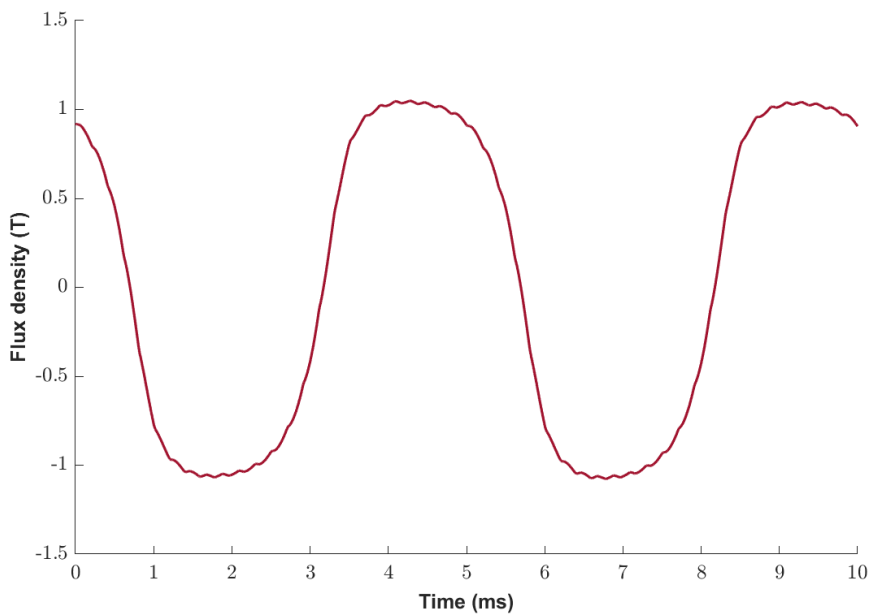


Figure 6.14 Flux density waveform derived by integration of the search coil emf

Figure 6.15 shows the instantaneous electrical power, i.e. product of the measured drive coil current and search coil emf. This contains both reactive and real power and hence it is necessary to integrate the instantaneous power over one complete electrical cycle to obtain the real power, since the reactive power sums to zero over a complete electrical cycle.

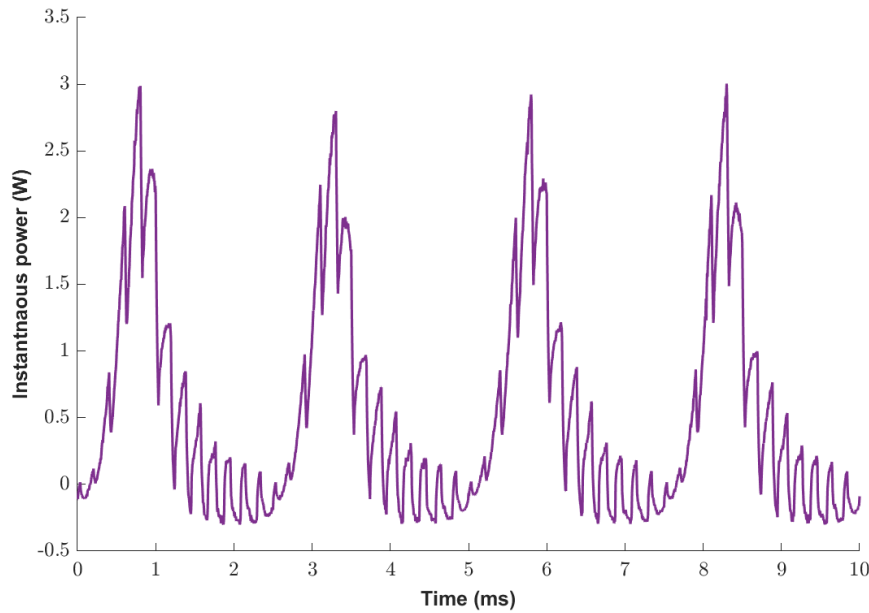


Figure 6.15 Instantaneous power loss

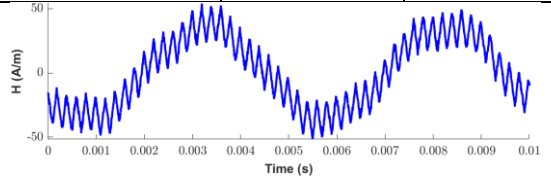
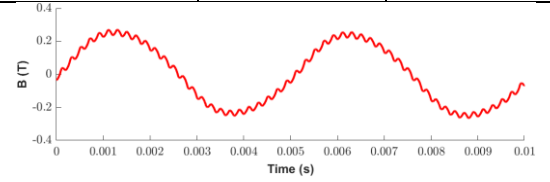
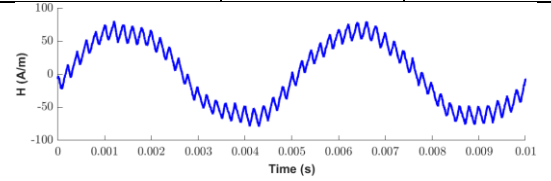
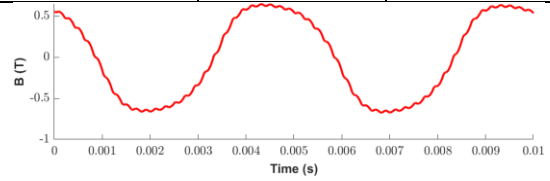
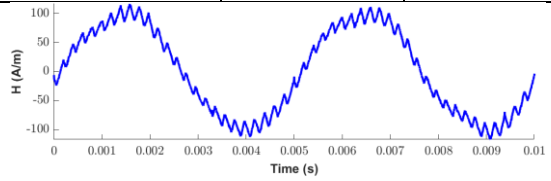
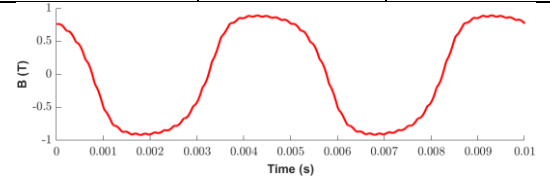
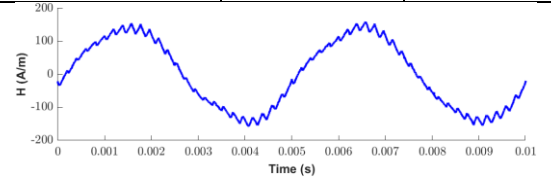
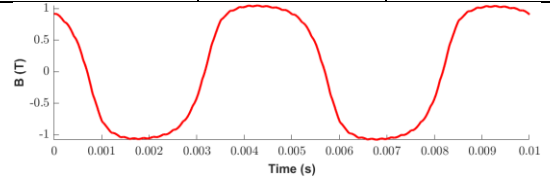
The application of equations 6.10 and 6.11 to the instantaneous power gives a loss density of 7.45/kg. The predicted loss for this case is 9.35 W for loss separation method with classical eddy current loss model and 9.06 W for loss separation method with FD skin effect model.

A series of waveforms with different PWM frequency and modulation index were generated and the current and search coil voltage captured. These measured waveforms were used to calculate the loss density using the method above and converted to B and H waveforms through the integration and scaling detailed in section 6.2. The B waveform was used with the classical resistance limited eddy current model of chapter 4 to predict the loss density. The measured B waveform was also used to generate a surface H waveform using the NO20 magnetisation curve shown previously in chapter 5 to predict loss with the finite difference eddy current loss prediction of chapter 5 which includes eddy current re-distribution and skin effect. Table 6.2 contains a summary of the results for 4 cases.

As can be seen in all cases, the finite difference skin effect model is close to the measured loss than the classical eddy current loss, notably in the case1. However, there are significant differences, of the order up to 25% between the measured and skin effect model even though it is an improvement on the classical eddy current loss. It is worth noting that the presence of high frequency switching events in the waveform also affects the minor loop loss. It was discussed in section 6.2.4 that the toroid is sub-divided into a series of sub-rings for calculation purposes and that this results in an assumed magnetic field strength spatial variation between the inner and outer edges. The significance of this approximation on the results can be

considered using case 1 as an example. The range of loss densities ranges from 0.961W/kg at the outer edge to 1.196 W/kg at the inner edge which is to be expected given the increase magnetising field strength with the shorter path length. The weighting of these losses by volume fraction of the total toroid is 18.5% and 14.8%. The possible reasons for the remaining discrepancies between the finite difference skin effect model and the measured results are discussed in the conclusions of chapter 7.

Table 6.2 Summary of the results for 4 cases with different peak amplitude of flux density

	Fundamental frequency	PWM frequency	Peak flux density	Measured loss density	Classical eddy current loss density	FD skin effect loss density
Case 1	200Hz	5kHz	0.27T	0.79W/kg	2.46W/kg	1.07W/kg
						
Case 2	200Hz	5kHz	0.65T	3.12W/kg	4.75W/kg	3.76W/kg
						
Case 3	200Hz	5kHz	0.89T	5.40W/kg	7.25W/kg	6.68W/kg
						
Case 4	200 Hz	5kHz	1.05 T	7.45W/kg	9.35W/kg	9.06W/kg
						

6.4 Manufacture of a demonstrator IPM machine

Instead of building a dedicated demonstrator for experimental validation, an opportunity came about to provide the reference design in chapter to the ELLI research programme at the Advanced Manufacturing Research Centre for them to build the machine. This research programme was concerned with developing a demonstrator electric drive-train to showcase novel manufacturing techniques. The reference design of the machine established in chapter 2 has a rotor outer diameter of 165mm and a traditional steel shaft diameter of 31.25 mm (scaled up from the 25 mm set for the smallest 135 mm rotor diameter design). One novel feature of the proposed ELLI demonstrator machine was the use of the hollow composite rotor shown in Figure 6.16. This is a two-part carbon-fibre composite rotor in which the adhesive bonded flanges on each half act as a key way. In order to incorporate this novel rotor hub into the demonstrator, it was necessary to increase the inner diameter of the rotor core from 31.25mm to 100 mm. As shown previously in chapter 2, this increase will have negligible effect on the electromagnetic torque but will limit the maximum rotational speed. In this case, the maximum speed is reduced from 12,000 rpm to 6887 rpm. It is recognised that this reduction in the maximum speed involves a change in electrical frequency, but these compromises were accepted given the long lead-time and costs of building two rotors and the fact that the reduced speed would still allow testing at the base speed of 4,000 rpm.



Figure 6.16 Novel hollow carbon-fibre shaft and hub

The rotor core and permanent magnets, which have exactly the same profiled shape as those shown previously in chapter 2 were mounted on the carbon fibre hub as shown in Figure 6.17. Unfortunately, in the fitting one of the last sets of magnets into the aperture, a mistake was made and one magnet was omitted. This was not uncovered until the glue had set and

efforts to remove the magnets caused irreparable damage to the core. The damage was such that a full rebuild of the rotor was required, including sourcing new magnets and core laminations. This set back the main ELLI project and could not be completed within the timeframe of the research reported in this thesis. The wound stator, which was fixed into an additive manufactured case is shown in Figure 6.18. It remains an objective to test this machine when the new rotor becomes available as detailed until future work in chapter 7.

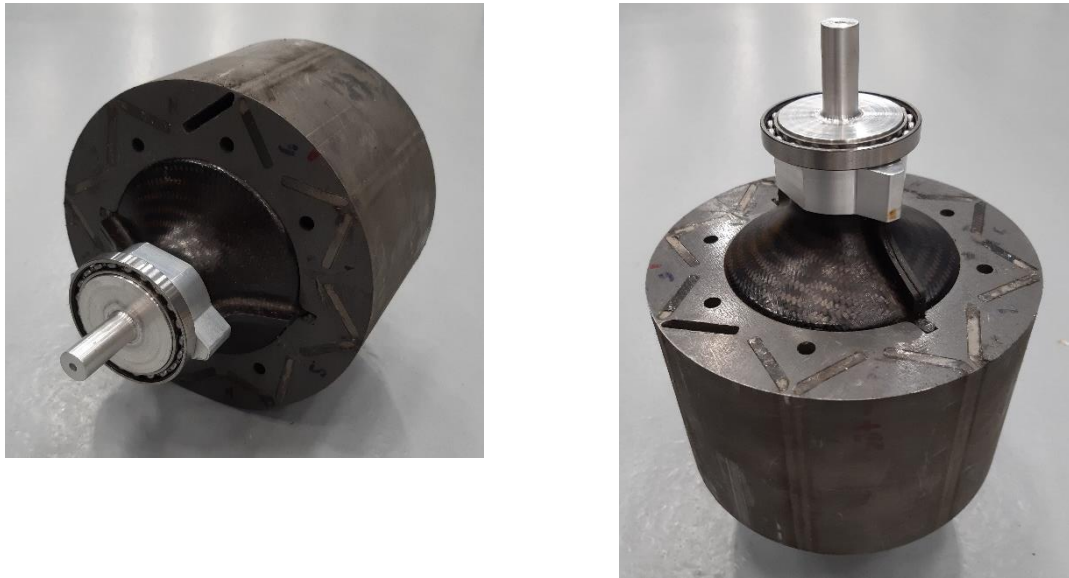


Figure 6.17 Demonstrator rotor seen from non-damaged end



Figure 6.18 Stator of V-shaped IPM machine

6.5 Summary

This chapter mainly focuses on providing verification of the developed iron loss calculation model in chapter 5, including toroidal sample preparation, loss measurement with sinusoidal excitation and loss measurement with switching waveform. For loss under sinusoidal excitation, higher saturation level of the toroidal sample will introduce significant differences between the classical eddy current model and the measured loss and skin effects model, with the finite difference model showing good agreement with measurements. This complex behaviour is caused by significant saturation where the permeability within the skin depth drops significantly. As for loss under switching waveform, the finite difference skin effect model is close to the measured loss than the classical eddy current loss and it is worth noting that the presence of high frequency switching events in the waveform also affect the minor loop loss.

Reference

- [1] [Online], “AMH-1K Permeameter: characterize rings and strips at high resolution in DC and AC,” *<https://www.laboratorio.elettrofisico.com/measuring-equipment/soft-magnetic-materials/amh-1k-permeameter/>*. .
- [2] Laboratorio Elettrofisico, “AMH-SERIES - SOFT MAGNETIC MATERIALS,” pp. 1–7.
- [3] Laboratorio Elettrofisico user manual, “ Neon Magnetizing & Measuring Equipment,” 2019.

Chapter 7: Conclusions and Future Work

7.1 Main conclusions

The research reported in this thesis has focussed on high fidelity mechanical and iron loss modelling for IPM machines designed for EV traction. The thesis has described several research activities which cover a wide range of different types of analysis including mechanical stress analysis, SIMULINK modelling of switching effects, analytical and numerical solution of the diffusion equation. Several of these investigations have been supported by extensive use of 2D and 3D finite element electromagnetic analysis of both magneto-static and magneto-dynamic cases.

The combined electromagnetic and mechanical optimisation in chapter 2 showed the complex trade-off between mechanical stress and torque density in IPM machines. The study showed that mechanical constraints for typical EV speed and power specifications can result in an optimal diameter in IPM machines beyond which the normal tendency in electrical machines for torque density to continually increase with size is reversed. The study also highlighted the importance of the mechanical properties of the electrical steels for the rotor and that higher strength steels would lead to an indirect improvement in the torque density due to the ability to accommodate thinner sections within the rotor geometry and hence reduce flux leakage within the IPM rotor. The study culminated in an optimized 100kW IPM machine design with a rotor diameter of 165mm resulting in an active mass of 42.3kg with corresponds to $\sim 2.4\text{kW/kg}$. It is worth noting that the specific findings in terms of torque density and operating speed range are somewhat specific to the specification of a design stress limit of 240MPa and a current density of 10A/mm^2 rms.

The switching waveform modelling in chapter 3 demonstrated that even with a simple hysteresis controller, the waveforms depart from a simple sawtooth superimposed onto the demand waveform with may fewer switching events that might be expected. It is also worth noting that the change in eddy current loss was in some cases, surprisingly low. This can be explained by recognising that the machine operating points used were at or around base speed and that the winding for the machine had been designed to match the available supply at the base speed. Hence, the voltage overhead, which determines the rate of rise current during a switching event, results in current waveforms in which the rate of change of current (which ultimately determines the additional eddy current loss) is not especially different from that in some regions of the fundamental waveform. Hence, the departure of the actual current from

the demand waveform and hence the number of switching events per cycle in some of the current waveforms of chapter 3 are surprisingly small. This behaviour is complicated by the effect of the mutual coupling and varying star-point voltage (in the case of the ungrounded case). However, chapter 3 illustrates that a hysteresis controller, which only responds when the current falls outside a range, offers some benefits in minimising extra iron loss from switching events.

Several approaches for accounting for eddy currents within laminations were investigated in chapter 5. A full 3D time-stepped model of a single lamination was used as the reference for comparing the accuracy of different models. It was shown that whereas analytical approaches to solving the diffusion equation in a layered model can produce excellent agreement with 3D finite element analysis for linear magnetic problems, i.e. with constant fixed permeability, accommodating non-linear material introduces significant errors. A 1D finite difference model has been developed with shows excellent agreement with 3D finite element analysis for a specified surface magnetic field strength variation.

Integrating the finite difference model into a post-processing tool for magneto-static finite element analysis involves an inconsistency and a resulting approximation since the original machine level model does not reflect the presence of any reaction field. However, using the calculated flux density waveform from a magneto-static finite element analysis to generate an approximate surface flux density has been shown to provide a reasonable representation of eddy currents in the lamination. Chapter 5 utilised the full methodology from finite element characterisation of the machine parameters, calculation of element-by-element localised flux densities and rates of change of flux density with stator current, through a SIMULINK model to generate element-by-element flux density waveforms with representative switching and culminating in Matlab based post-processor which includes a 1D finite difference model. This complicated sequence of simulations and calculations resulted in the prediction of the effect of switching on the overall iron loss.

The influence of switching events in terms of increasing core loss have been shown in chapter 5 to be important factor in machine level loss calculation with the resulting increases in loss in the few 10s of percent range under normal operating conditions, although this is likely to be highly dependent on the type of machine. In permanent magnet machines, although there may appear to be significant ripple in the current waveforms, the ripple in the flux density is less pronounced because of the significant contribution of the flux from the permanent magnet excitation to net the flux density variation and the impact of magnetic saturation in may regions of the stator core.

Overall, this thesis has undertaken several studies which improve mechanical and electromagnetic modelling capability for IPM machines and provided significant generic insight into the modelling of lamination eddy currents irrespective of the machine type.

7.2 Key contributions to knowledge

The following are regarded as the key contributions to knowledge from this thesis:

- Detailed illustration of the benefits and trade-offs in a combined electromagnetic and mechanical optimisation of an IPM machine. This work has been published in the World Journal of Electric Vehicles as ‘Combined electromagnetic and mechanical design optimization of interior permanent magnet rotors for electric vehicle drivetrains’ in December 2023
- Found an interesting torque promotion resulted from the increasing of the hub diameter, which caused by the reluctance increasing of leakage path via saturation and reduced cross-section.
- Developed a method for SIMULINK based method for generating representative switching current waveforms in IPM machines with very short time steps from finite element simulations based on standard time-step durations. These current waveforms include full representation of the changes in inductance with position and current which are important in modelling IPM machines. Due to the magnitude of the high frequency eddy currents are determined by the rate of change of flux density and hence current, capturing the detailed behaviour from a full system simulation will be more accurate than an idealised symmetrical representation of the ripple.
- Explored quantitatively several different methods for integrating lamination level eddy currents and skin effect into a practical post-processing method. Whereas bring magneto-dynamic effects into the post-processing of magneto-static solutions involves some compromises and approximations, the overall benefits of this have been shown.
- Developed a MATLAB based post-processor that can work in tandem with commercial finite element packages.

7.3 Future work

There are several aspects of future work which could follow-on from this study:

7.3.1 Experiment validation of iron loss at machine level

The most obvious aspect of this project which requires further work is the re-build of the damaged rotor to allow machine level validation of the performance calculations in chapter 2 and the machine level iron loss predictions of chapter 5.

7.3.2 Experiment validation of mechanical modelling for rotor of high speed IPM machine

The mechanical analysis reported in chapter 2 used well developed methods and published manufacturer material data, but there was no means of experimentally verifying the radial

growth in the rotor at rated speed. This would require a spin test rig which was not available to this project, but chapter 2 has illustrated the interesting trade-offs that could be validated experimentally.

7.3.3 Enhancement to the electromagnetic performance by adjusting hub diameter

The finding reported in chapter 2 gives a potential method to enhance the electromagnetic performance but also introduces concerns about mechanical within the rotor, some further work could be focused on decreasing the maximum rotating speed or using better materials with higher yield strength to allow higher hub diameter, which would be beneficial electromagnetic properties of the machine.

7.3.4 Switching loss modelling of converters

The chapter 2 mainly focuses on developing a method to calculate flux density waveform in every individual element of a finite element mesh, so it only considering of effects of ripple current towards to flux density variations. However, the switching state changes of the converters in the control system will also introduce extra losses, which would be a potential further work.

7.3.5 Enhancement to the eddy current loss model

The main drawback of the model developed in chapter 5 is the difficulty in fitting a magnetostatic field solution to a localised model with accounts for eddy currents and hence a reaction field. This challenge is most evident when setting the surface magnetic field strength for the 1D model as this is the crucial boundary condition. The only rigorous way of resolving this inconsistency is to account for the reaction field in some way in the finite element model. Combining the finite difference model into the finite element model could provide a solution but this would require access to the solver source code.

APPENDIX

PYTHON script to export *B* and *H*

```
import math
import os

Name1 = "LAM_Z"
Name2 = "AIR_Z"

N = 601
time_start = 0
step = 2E-4/600

for i in range(N):

    T = time_start+step*i

    selectCurrentStep(activeScenario=Scenario['SCENARIO_1'],
        parameterValue=['TIME='+str(T)])

    SpatialCurve(name=Name1+'_B_'+str(i),
        compoundPath=CompoundPath['LAM_Z'],
        formula=['Comp(2,B)'])

    CurveSpatial2D[Name1+'_B_'+str(i)].exportTXT(txtFile=Name1+'_B_'+str(i),
        mode='add')

    CurveSpatial2D[Name1+'_B_'+str(i)].delete()

    SpatialCurve(name=Name1+'_H_'+str(i),
        compoundPath=CompoundPath['LAM_Z'],
        formula=['Comp(2,H)'])

    CurveSpatial2D[Name1+'_H_'+str(i)].exportTXT(txtFile=Name1+'_H_'+str(i),
        mode='add')

    CurveSpatial2D[Name1+'_H_'+str(i)].delete()

    SpatialCurve(name=Name2+'_B_'+str(i),
        compoundPath=CompoundPath['AIR_Z'],
        formula=['Comp(2,B)'])

    CurveSpatial2D[Name2+'_B_'+str(i)].exportTXT(txtFile=Name2+'_B_'+str(i),
        mode='add')

    CurveSpatial2D[Name2+'_B_'+str(i)].delete()

    SpatialCurve(name=Name2+'_H_'+str(i),
        compoundPath=CompoundPath['AIR_Z'],
        formula=['Comp(2,H)'])
```

```
CurveSpatial2D[Name2+'_H_'+str(i)].exportTXT(txtFile=Name2+'_H_'+str(i),
mode='add')

CurveSpatial2D[Name2+'_H_'+str(i)].delete()
```

MATLAB script to process exported B and H

```
clear

start_sol = 0;
end_sol = 600;
num_sols = end_sol-start_sol+1;

index=start_sol-1;

f_name1 = 'LAM_Z_B';
f_name2 = 'LAM_Z_H';
f_name3 = 'AIR_Z_B';
f_name4 = 'AIR_Z_H';

for n = 1:num_sols
fname = sprintf('lam data(NO20_saturated)\%s_%d.txt',f_name1,(n+index)); %input
file = fopen(fname,'r');
lines = textscan(file,' %f %f %f %f %f %f',21,'HeaderLines',21);
%skin 21 lines and read the next 20 lines
LineData = cell2mat(lines);
B_lam_data(1:21,n) = LineData(1:21,5);
fclose(file);

clear fname file lines LineData

fname = sprintf('lam data(NO20_saturated)\%s_%d.txt',f_name2,(n+index)); %input
file = fopen(fname,'r');
lines = textscan(file,' %f %f %f %f %f %f',21,'HeaderLines',21);
LineData = cell2mat(lines);
H_lam_data(1:21,n) = LineData(1:21,5);
fclose(file);

clear fname file lines LineData

fname = sprintf('lam data(NO20_saturated)\%s_%d.txt',f_name3,(n+index)); %input
file = fopen(fname,'r');
lines = textscan(file,' %f %f %f %f %f %f',2,'HeaderLines',21);
%skin 21 lines and read the next 2 lines
LineData = cell2mat(lines);
B_air_data(1:2,n) = LineData(1:2,5);
fclose(file);

clear fname file lines LineData

fname = sprintf('lam data(NO20_saturated)\%s_%d.txt',f_name4,(n+index));
file = fopen(fname,'r');
lines = textscan(file,' %f %f %f %f %f %f',2,'HeaderLines',21);
```



```

LineData = cell2mat(lines);
H_air_data(1:2,n) = LineData(1:2,5);
fclose(file);
end

mu0=4*pi*(1e-7);
mur = 5000;
thk = 2e-4;
f = 10000;
omega=2*pi*f;
sigma = 1/(5.2e-7);
skindep=sqrt(2/(omega*sigma*mu0*mur));

delta_t = (2e-4)/600;
t = (0:600)*delta_t;
Hs_air = H_air_data(1,:);
Hs_lam = H_lam_data(1,:);

for i = 1:length(B_lam_data)
    B_lam_mean(i) = mean(B_lam_data(1:21,i));
end

```